

THESIS / THÈSE

DOCTOR OF SCIENCES

Pharmacokinetic modeling and control design for drug dosing

THEMANS, PAULINE

Award date:
2021

Awarding institution:
University of Namur

[Link to publication](#)

General rights

Copyright and moral rights for the publications made accessible in the public portal are retained by the authors and/or other copyright owners and it is a condition of accessing publications that users recognise and abide by the legal requirements associated with these rights.

- Users may download and print one copy of any publication from the public portal for the purpose of private study or research.
- You may not further distribute the material or use it for any profit-making activity or commercial gain
- You may freely distribute the URL identifying the publication in the public portal ?

Take down policy

If you believe that this document breaches copyright please contact us providing details, and we will remove access to the work immediately and investigate your claim.



UNIVERSITY OF NAMUR

FACULTY OF SCIENCES

Pharmacokinetic modeling and control design for drug dosing

A thesis submitted by
Pauline Thémans
in fulfillment of the
requirements for the
degree of Doctor of
Science

Composition of the Jury:

Oscar DELLA PASQUA
Renaud LAMBIOTTE
Alexandre MAUROY (president)
Flora MUSUAMBA TSHINANU (co-advisor)
Pierre WALLEMACQ
Joseph WINKIN (co-advisor, secretary)

July 2021

Cover design: ©Presses universitaires de Namur
©Presses universitaires de Namur & Pauline Thémans
Rue Grandgagnage, 19
B - 5000 Namur (Belgique)

Reproduction of this book or any parts thereof, is strictly forbidden
for all countries, outside the restrictive limits of the law,
whatever the process, and notably photocopies or scanning.

Printed in Belgium

ISBN: 978-2-39029-144-2

Registration of copyright: D/2021/1881/13

University of Namur
Faculty of Sciences
rue de Bruxelles, 61, B-5000 Namur (Belgique)

Pharmacokinetic modeling and control design for drug dosing

by Pauline Thémans

Abstract: Pharmacokinetics (PK) is a field of clinical pharmacology that studies how a drug evolves in the body after administration. Thanks to mathematical modeling, clinical pharmacology is an interesting and promising field of application of control and system theory. We report on the population PK analysis of three case study drugs: hydroxychloroquine in COVID-19 patients, and temocillin and meropenem in patients with severe pneumonia. We developed data-driven models using a mixed-effects approach, meaning that parameters are characterized by a fixed and a random component. We also describe the results of internal and external validations that were performed. These systems are described by linear time-invariant state-space representations. They turn out to be nonnegative and stable, as expected. From these models, the aim is to provide methods for dosing rationale in patients (decision-making aid) based on relevant patient's characteristics (covariates) and on other practical conditions (target exposure for efficacy and pharmacodynamic index, dosing interval, and duration of infusion). Our contributions in this field are the following. (1) A deterministic input-output (I/O) analysis of the system leads to an open-loop control law that enables the computation of an appropriate dosage for the average/nominal patient. This approach is then incorporated into the "worst-case" system based on the monotony of the state trajectories with respect to the clearance. (2) The I/O analysis is used to heuristically design a feedback dosing strategy based on the estimated state. (3) We finally describe an optimal control approach (minimum principle). This approach aims at improving the drug dosing by optimizing a criterion under input and state constraints.

Modélisation pharmacocinétique et conception de lois de commande pour la posologie

par Pauline Thémans

Résumé : La pharmacocinétique est une discipline de la pharmacologie clinique qui étudie le devenir d'un médicament dans l'organisme après administration. Grâce aux modèles mathématiques, la pharmacologie clinique est un champ intéressant et prometteur d'application de la théorie des systèmes et du contrôle. Nous présentons l'analyse pharmacocinétique de population de trois médicaments (cas d'étude) : l'hydroxychloroquine chez des patients COVID-19, et la témocilline et le méropénème chez des patients atteints de pneumonie sévère. Nous avons développé des modèles basés sur des données en utilisant une approche à effets mixtes, ce qui signifie que les paramètres sont caractérisés par une composante fixe et une composante aléatoire. Nous décrivons également les résultats des validations internes et externes. Ces systèmes sont décrits par des modèles d'état linéaires temps-invariants, qui s'avèrent être positifs et stables, comme attendu. À partir de ces modèles, l'objectif est de fournir des méthodes d'ajustement posologique (aide à la décision) en fonction des caractéristiques du patient (covariables) et d'autres conditions pratiques (concentration cible et index pharmacodynamique, intervalle de dosage et durée de perfusion). Nos contributions dans ce domaine sont les suivantes. (1) Une étude entrée/sorties du système conduit à une loi de contrôle en boucle ouverte qui permet de calculer un dosage approprié pour le patient moyen/nominal. Cette approche est ensuite incorporée dans le système du "pire des cas" basé sur la monotonie des trajectoires d'état par rapport à la clairance. (2) L'analyse entrée/sorties est utilisée pour concevoir de manière heuristique une stratégie de dosage par feedback de l'état estimé. (3) Nous décrivons également une approche de contrôle optimal (principe du minimum). Cette approche vise à améliorer le dosage du médicament en optimisant un critère sous des contraintes d'entrée et d'état.

Ph.D. thesis in Science (Thèse de doctorat en Sciences)

Date: 01/07/2021

University of Namur (UNamur)

Department of Mathematics and Namur Institute for Complex Systems (naXys)

Advisors (Promoteurs): Flora MUSUAMBA TSHINANU, Joseph WINKIN

Remerciements

À travers ces lignes, j'aimerais adresser mes plus sincères remerciements à tous ceux sans qui ces six dernières années n'auraient pas été les mêmes, à tous ceux qui ont contribué, de près ou de loin, à la réalisation et à la réussite de ma thèse de doctorat.

Mes premiers remerciements vont naturellement à mes promoteurs, Flora Musumba (AFMPS) et Joseph Winkin (UNamur). Merci pour votre aide considérable, vos nombreux conseils, votre bienveillance et votre soutien. Flora, merci pour tout ce que tu m'as appris depuis huit ans maintenant et pour la confiance que tu m'as accordée. Joseph, merci pour nos longues discussions, scientifiques et humaines, pour ta positivité et ta passion des mathématiques. Merci à vous deux de m'avoir poussée à dépasser mes limites, d'avoir cru en moi et de m'avoir toujours considérée comme votre égale.

Je remercie les membres de mon comité d'accompagnement, Pierre Wallemacq (UCLouvain) et Renaud Lambiotte (University of Oxford et UNamur), ainsi qu'Oscar Della Pasqua (University College London) et Alexandre Mauroy (UNamur) d'avoir accepté d'évaluer mon travail de thèse. Merci à vous pour vos questions, remarques et suggestions de révision qui ont permis d'améliorer le manuscrit. Je remercie particulièrement Alexandre d'avoir présidé le jury. Merci pour ton écoute et tes conseils.

Je tiens également à remercier tous nos coauteurs et collaborateurs qui nous ont notamment fourni les données cliniques et pharmacocinétiques sans lesquelles cette thèse n'aurait pas pu être possible. Merci en particulier à Clotilde Visée, à Nathalie Layios et à Frédéric Fripiat pour nos nombreux échanges scientifiques.

Entreprendre une thèse, c'est aussi commencer une incroyable aventure humaine. Merci à toutes les personnes rencontrées en conférences ou en *summer school* et à mes acolytes du Benelux Meeting qui se reconnaîtront. Merci à tous les collègues, académiques et scientifiques, avec qui j'ai fait un bout de chemin. Et merci à Pascale, à Alice et à Juan de m'avoir soutenue dans les aspects administratifs et techniques, mais surtout de faire du département un lieu de travail convivial et agréable. Merci pour votre efficacité et votre disponibilité.

Réaliser une thèse en tant qu'assistante implique d'assurer des charges didactiques en équipe. Et quelle équipe ! Merci à tous mes collègues scientifiques, anciens et actuels, et en particulier à ceux avec qui j'ai collaboré. Je remercie également les académiques avec qui j'ai directement travaillé et qui ont permis d'enrichir mon expérience professionnelle.

Je tiens à remercier tout particulièrement Delphine et Eve-Aline de m'avoir accueillie avec enthousiasme dès mon arrivée en septembre 2015. Nos premières sorties culturelles et festives n'auront pas tardées. Delphine, merci de m'avoir si bien accompagnée et conseillée, et d'avoir fait de notre bureau un lieu de travail agréable et efficace. Merci pour nos bavardages, au bureau et en dehors, et pour nos confidences. Eve, merci pour notre belle complicité, pour ta bonne humeur et ton côté olé-olé, pour tes conseils et ton soutien sans faille. Merci d'être disponible à toute heure du jour et de la nuit. Merci à toutes les deux d'être des amies plus que des collègues.

Merci à mon grand frère scientifique, Jérémy, de jouer son rôle de merveille depuis six ans. Merci au topo-mate qui m'a appris tellement dans mon métier d'assistante. Merci au docteur de m'avoir fait partager son expérience, de m'avoir conseillée et toujours soutenue. Merci surtout à l'ami pour son écoute et pour nos (trop) longues heures de conversation.

J'adresse également un grand merci à Anthony qui a toujours répondu présent quand j'avais besoin d'un coup de pouce ou d'une relecture. Merci pour nos discussions et pour ton aide précieuse. Merci aussi à Riccardo pour son soutien et sa présence, particulièrement durant la dernière phase de ma rédaction.

Merci à Julien d'être mon collègue et ami depuis bientôt onze ans et d'être toujours disponible quand j'ai besoin d'aide ou de conseils. Merci à Manon pour ses nombreux encouragements et sa compagnie toujours agréable. Merci aussi à Mara d'avoir fait un bout de chemin avec nous et d'avoir contribué à l'ambiance du premier étage par sa bonne humeur. Merci à Ambi d'avoir partagé notre bureau avec enthousiasme et optimisme. Merci à Nicolas et à Martin pour leur humour et leurs jeux de mots qui me font tant rire, mais également pour leur aide quand j'ai besoin de compétences informatiques ou statistiques. Merci à ma souriante copine d'analyse, Candy, notamment pour nos rendez-vous hebdomadaires pendant cette année particulière.

Merci à mes colocataires pour les bons moments passés ensemble, et en particulier à Marion de m'avoir fait partager son expérience d'infirmière sur l'administration du méropénem. Merci à mes amis de l'unif qui se reconnaîtront pour avoir encore été à mes côtés pendant ces six dernières années. Merci à Fanny pour notre belle amitié. Merci pour ton soutien et tes visites à Namur qui m'ont permis de décompresser.

Enfin, merci à mes parents pour leur présence, leur générosité, leurs conseils précieux et leur patience. En particulier, merci de m'avoir supportée pendant ces derniers mois. Merci à ma sœur et à mon beau-frère Quentin pour leur soutien. Merci Noémie de partager tellement de choses avec moi depuis presque trente ans et d'être toujours là pour moi.

À vous tous, merci !

Pauline

Contents

List of abbreviations and notations	1
Introduction	5
I Pharmacokinetic modeling	15
1 Drug pharmacokinetics and mathematical modeling	17
1.1 Mathematical preliminaries	17
1.2 Individual pharmacokinetics	21
1.2.1 Pharmacokinetic profile	21
1.2.2 Absorption	23
1.2.3 Distribution	24
1.2.4 Elimination	25
1.3 Population pharmacokinetic modeling	25
1.3.1 Structural model	25
1.3.2 Pharmacokinetic parameters	30
1.3.3 System analysis	31
1.3.4 Mixed effects model and covariates	35
1.3.5 Residual error model	36
1.3.6 Bayes estimates	36
1.4 Model development	37
1.4.1 Parameter estimation method	37
1.4.2 Likelihood ratio test and covariate selection	39
1.5 Evaluation tools	40
1.6 Physiologically based pharmacokinetic modeling	45

2	Population pharmacokinetic model of hydroxychloroquine in COVID-19 patients	47
2.1	Study design and data	48
2.2	Population model building	50
2.3	Model validation	52
3	Population pharmacokinetic model of temocillin in patients with pneumonia	57
3.1	Study design and data	58
3.2	Population model building	58
3.3	Model internal validation	61
4	Pharmacokinetic models of meropenem in patients with pneumonia	65
4.1	Patient data	66
4.2	Population model	69
4.2.1	Model building	69
4.2.2	Model evaluation	69
4.3	Physiologically based model	76
4.3.1	Structural model	76
4.3.2	System analysis	79
4.3.3	Model parameter estimation	80
4.3.4	Model evaluation	80
4.3.5	Extrapolation in morbidly obese individuals	86
II	Drug dosing	89
5	Simulations and probability of target attainment	91
5.1	Simulations: application to HCQ dosage	91
5.2	PTA-based method for AB dosing	94
5.2.1	Time-dependent antibiotics	94
5.2.2	PTA analysis: application to temocillin dosage	95
6	Open-loop control law	101
6.1	State-space model	101
6.1.1	Input function	102
6.1.2	Input-output analysis	103
6.2	Dose selection for time-dependent AB	108
6.2.1	Input-output formula	108
6.2.2	“Worst-case” analysis	111
6.2.3	Drawbacks and advantages	115
6.2.4	Application to meropenem dosage: a PTA-based comparison	116
6.3	Therapeutic window	117
6.3.1	Input-output formula	117
6.3.2	Area under the concentration-time curve	117

7	State estimation and feedback control law	121
7.1	Discrete-time state estimator	121
7.2	Dose adjustment: heuristic method	123
7.3	Application to meropenem dosage	126
8	Optimal control approach	129
8.1	Continuous-time finite-horizon setting	129
8.2	Discrete-time setting	131
8.2.1	Minimum principle	132
8.2.2	Relaxed constraints	138
8.3	Extension to the continuous-time setting	143
8.4	Further computational explorations	152
	Conclusion & perspectives	159
	Appendices	163
A	External evaluation of the models of meropenem: additional plots	165
A.1	Population model	166
A.2	Physiologically based model	169
B	Resolvent function of the PBPK model: symbolic computations	173
C	Sensitivity analysis on the PBPK model of meropenem	177
D	System response	181
D.1	Context	181
D.2	Zero-state system response	182
D.3	Asymptotic system response	185
E	Sensitivity analysis on the popPK model of meropenem	187
	Bibliography	191

Contents

List of abbreviations and notations

Abbreviations

AB	antibiotic
AUC	area under the (concentration-time) curve
BAL	bronchoalveolar lavage
BSA	body surface area
CI	confidence interval or continuous infusion
Cl _{CR}	creatinine clearance
CO	cardiac output
conc.	concentration
CV	coefficient of variation
EBE	empirical Bayes estimate
ELF	epithelial lining fluid
GFR	glomerular filtration rate
GOF	goodness-of-fit
HCQ	hydroxylchloroquine
ICU	intensive care unit
IIV	interindividual variability
I/O	input-output
IV	intravenous
LRT	likelihood ratio test
LTI	linear time-invariant
MC	Monte Carlo
MIC	minimal inhibitory concentration
NLMEM	nonlinear mixed effects model
OF(V)	objective function (value)
OC	optimal control

List of abbreviations and notations

PBPK	physiologically based pharmacokinetic
PD	pharmacodynamics
PI	prediction interval
PK	pharmacokinetics
popPK	population pharmacokinetic
PTA	probability of target attainment
resp.	respectively
RSE	relative standard error of estimate
s.t.	such that
TDM	therapeutic drug monitoring
TVP	typical value of a parameter
VPC	visual predictive check
w.l.o.g.	without lost of generality
w.r.t.	with respect to
WT	body weight

Notations

c_p	plasma drug concentration [g/L]
c_t	tissue drug concentration [g/L]
K_t or K_p	tissue-to-plasma partition coefficient (penetration ratio)
F	bioavailability
CL	clearance [L/h]
V	volume of distribution [L]
Q	intercompartmental clearance [L/h]
S	scaling factor
$N(0, s^2)$	normal distribution with mean zero and variance s^2
η	normal random variable describing IIV
ω^2	variance of η
ε	normal random variable describing residual error
σ^2	variance of ε
D	dose [g]
T	length of a dosing interval [h]
Δ	infusion duration [h] (length of an administration interval)
c_{\max}	highest concentration on a dosing interval
c_{trough}	lowest concentration on a dosing interval
N_{repl}	number of replicates
n_{sim}	number of simulations (for MC simulations)
t	time variable
x	space variable
y	output variable
\dot{x}	derivative of x with respect to t
\mathbb{R}	set of real numbers
\mathbb{R}^n	set of real vectors of dimension n

\mathbb{R}_+^n	nonnegative orthant of \mathbb{R}^n
\mathbb{C}	set of complex numbers
$\text{Re}(z)$	real part of a complex number z
\bar{z}	conjugate of a complex number z
A^T	transpose of a matrix A
A^*	conjugate transpose of A
$\sigma(A)$	set of eigenvalues of A
$[r]$	integer part of a real number r

List of abbreviations and notations

Introduction

“Ce qui est simple est toujours faux. Ce qui ne l’est pas est inutilisable.”

Paul Valéry

Pharmacokinetics (PK) is a field of clinical pharmacology that studies what happens to the drug following administration. In particular, pharmacokinetics describes the processes of absorption, distribution, and elimination, that characterize the drug exposure (concentrations) over time. PK modeling consists in developing mathematical models in order to quantify the interaction between dose and drug exposure. In the framework we focus on, the systems are described by linear time-invariant (LTI) state-space representations (see Figure I) given, for all $t \geq 0$, by

$$\dot{x}(t) = Ax(t) + bu(t), \quad y(t) = Cx(t) \quad (\text{I.1})$$

where $x \in \mathbb{R}^n$ and $y \in \mathbb{R}^p$ denote the state and output variables, respectively. The system outputs correspond to the drug concentration in plasma and possibly at the site of infection. The state matrix $A \in \mathbb{R}^{n \times n}$ is a stable Metzler matrix (all its off-diagonal elements are nonnegative), $b \in \mathbb{R}^{n \times 1}$ is a nonnegative vector with one and only one nonzero component, and $C \in \mathbb{R}^{m \times n}$ is the output matrix that converts the state vector x in concentrations. The input function $u(\cdot)$ is called the *control* variable. These models can then be used to predict concentration-time profiles, called *pharmacokinetic profiles*.

Thanks to mathematical modeling, clinical pharmacology is an interesting and promising field of application of systems and control theory. Famous examples reported in the literature include automated anesthesia (Bailey and Haddad (2005)) and the artificial pancreas designed to replace the natural blood sugar regulation in patients with diabetes (Haidar (2016), Sereno et al. (2018)). They involve closed-loop control strategies to continuously adjust the dose of a drug. Controllers reported in the literature include proportional-integral-derivative (PID) and adaptive model-based

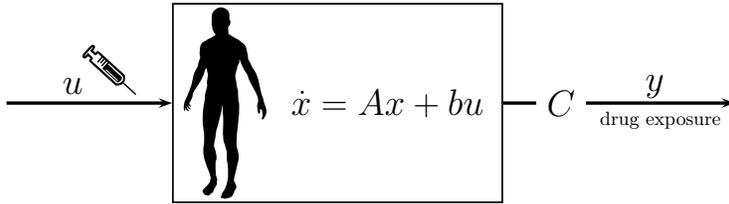


Figure I – State-space representation

controllers, see the book of Haddad et al. (2010)[Chapter 12] and references therein. The adaptive control uses identification methods to estimate the (time-dependent) parameters specific to an individual patient. More recently, we can also identify other control and systems approaches to pharmacology. To cite two of them, in Anelone et al. (2020), authors report an impulsive control strategy with an integral action and a state feedback control for oncolytic virus therapy, and, in Liparulo et al. (2020), a model predictive control (MPC) framework is presented to design an optimal cancer chemotherapy treatment.

In the second part of this work, we perform an input-output analysis and discuss control methods for pharmacokinetic systems (I.1) whose input function is given by a right-continuous piecewise constant function, in line with the administration of the case study drugs. Indeed, in the first part, we present PK analyses of drugs given by intermittent administration of a fixed dose at regular dosing intervals, particularly by intravenous (IV) infusion. In the case of multiple dosing by oral or IV bolus administration, the system input u is the null function and the control must be performed by updating the initial condition. Results regarding the input-output relationship in that particular case are provided in Koch (2012).

Currently, model-based antibiotic (AB) dosing is mostly guided by Monte Carlo simulations and empirical comparison of successive dosing regimens at *population level*. Comparison is performed through an analysis of the probabilities of target attainment (PTA) (see, e.g., Usman et al. (2017) and Ikawa et al. (2010)). While a population-based approach provides a one-fits-all dose, there has been an increasing interest in the *individualization* of antibiotic dosing to ensure that concentrations for clinical cure are achieved (see, e.g., Cotta et al. (2015)). Besides, in Heffernan et al. (2018), authors advocate therapeutic drug monitoring (TDM) and AB dose individualization to minimize resistance emergence.⁽¹⁾ Individual dosing is based, on the one hand, on the patient characteristics that influence the pharmacokinetics of the drug of interest and, on the other hand, on Bayes estimations using well-timed measured concentrations, called TDM concentrations; see, e.g. Sime et al. (2015) and Heffernan et al. (2018). These relevant patient characteristics are called the model *covariates*. Softwares for TDM-guided dosing emerged some year ago, as explained in Parker et al. (2015).

In Dhaese et al. (2019), authors compare eight PK models of meropenem in criti-

⁽¹⁾In this regard, it is crucial to quantify the link between drug exposure and resistance development (see, e.g., Gould and MacKenzie (2002)).

cally ill patients. The predictive performances were evaluated on independent external data collected in intensive care unit (ICU). The models, including parameter estimates and retained covariates, differ across studies and therefore vary considerably in their predictions. This study shows that a population pharmacokinetic (popPK) model must be validated in the target population before using it for dose selection and dosing adjustment (therapeutic drug monitoring). The choice of a model should also be guided by the safety of the drug. Indeed, for time-dependent AB without important toxicity as meropenem, a model which under-predicts drug exposure should be favored.

This work aims to develop PK models and provide model-based methods for dosing rationale (decision-making aid). These methods take into account the covariate (in view of individualized dosing), as well as clinical or practical constraints such as the target concentration for efficacy and the dosing interval. One important challenge is how to take into account the random components included in PK models to describe the interindividual variability (IIV) in parameters and drug concentrations (Figure II).

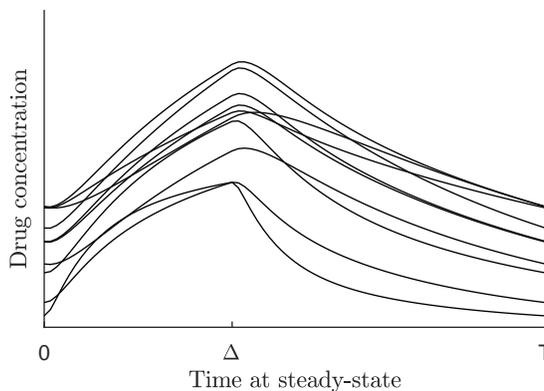


Figure II – Drug exposure over time with interindividual variability (Δ , infusion duration; T , length of the dosing interval)

Context

The development of PK models provides a basis to increase the understanding of drug mechanisms and to improve dosing strategies. Hydroxychloroquine (HCQ) is an antimalarial drug known for its anti-inflammatory properties and showing good treatment responses in autoimmune diseases, particularly systemic lupus erythematosus (Lee et al. (2016)). This drug has been recommended in the Belgian protocol for the COVID-19-disease at the very beginning of the sanitary crisis. A PK model is developed from observed concentrations in COVID-19 patients in Chapter 2. Apart from this particular case study, the present thesis deals with antibiotics used in ICU to treat critically ill patients with severe bacterial infection, including pneumonia. Pneumonia

is still the main cause of infection-related mortality (Kiem and Schentag (2008)). Enterobacteriaceae (Gram-negative bacteria) are responsible for numerous nosocomial infections including hospital-acquired pneumonia (HAP), bloodstream infection and urinary tract infection (Peleg and Hooper (2010)). To protect themselves from antibiotics, antimicrobials develop resistance mechanisms. Some Enterobacteriaceae produce extended-spectrum β -lactamases (ESBLs), that are enzymes able to inactivate commonly used antibiotics such as penicillins. Carbapenems (class of antibiotics) are usually chosen for treatment of severe infections due to ESBL-producing bacteria. However, carbapenem-resistant Enterobacteriaceae (producing enzymes called carbapenemases) are reported and the more this class of antibiotics is used, the more the bacteria are susceptible to develop defense strategies, see, e.g., CDC (2019)⁽²⁾ and Rawat and Nair (2010). These infections are associated with extended hospital stays, a high rate of mortality, and high costs.

Temocillin (penicillin) and meropenem (carbapenem) are β -lactamase-resistant antibiotics, making them interesting drugs in the current area of increasing antimicrobial resistance. As all β -lactam antibiotics, they are *time-dependent* AB, meaning that inhibitory activity and clinical outcome depend on the percentage of time that the (free/unbound) drug concentration exceeds the bacteria minimal inhibitory concentration (MIC)⁽³⁾ ($\%T>MIC$) (Gonçalves-Pereira and Póvoa (2011), Chow et al. (2018)). The latter is called the *pharmacodynamics* (PD) *index*. Increasing concentrations at the site of infection much above the MIC should not improve the bactericidal efficacy of the drug. According to Veiga and Paiva (2018), 50% $T>MIC$ of the dosing interval is usually needed to ensure AB efficacy, and therefore clinical outcome, but 100% $T>MIC$ of the dosing interval should be ensured in immunosuppressed patients. A *PK/PD breakpoint* is a PK/PD target associated with a high probability of success.

PK models of temocillin and meropenem developed in Chapters 3 and 4 are based on measured systemic concentrations, but also on few concentrations sampled at the site of infection. The site of infection is the thin layer of liquid lining the pulmonary alveoli, called *epithelial lining fluid* (ELF). The pulmonary alveoli are cavities located at the extremity of the respiratory tract where gas exchanges take place. The antibiotics reach this site by passive diffusion through the alveolar capillary wall, the interstitial space, and the alveolar epithelial cells (forming a wall called *alveolar epithelium*), as illustrated in Figure III. As the pulmonary capillaries contain large pores, diffusion of molecules from the bloodstream to the interstitial fluid is mainly driven by the concentration gradient of the unbound drug. The extent of the diffusion through the alveolar epithelium depends on the lipophilic and hydrophilic features of the molecule. (Jager et al. (2019)).

When the bacterial infection occurs outside the blood, infection-site concentrations are essential to improve drug dosing. In case of pulmonary infections, AB efficacy depends on its concentration in ELF or in alveolar macrophages for extracellular and intracellular pathogens, respectively. However, ELF concentrations measured by

⁽²⁾CDC stands Centers for Disease Control and Prevention, the national public health agency of the United States.

⁽³⁾MIC is defined as “the lowest concentration of an antibiotic required to inhibit the growth of an organism.” [BSAC website].

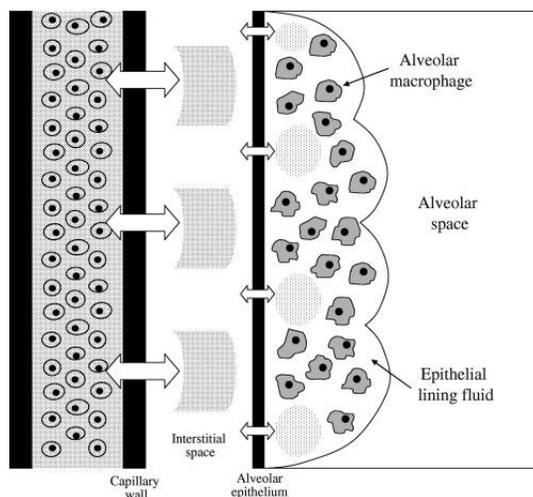


Figure III – Schematic diagram of the blood-alveolar barrier composed of two membranes, the capillary wall and the alveolar wall, that are separated by a fluid-filled interstitial space. Illustration taken from Kiem and Schentag (2008).

bronchoalveolar lavage (BAL) may produce biased data following technical errors such as the contamination by cell lysis or the prolonged dwelling time of fluid during BAL (Kiem and Schentag (2008), Jager et al. (2019)).

Adequate dosing is still a challenging issue in drug development, despite useful and well-established tools. These methods are described and discussed in Musuamba et al. (2017), following a workshop gathering modelers and pharmaceutical regulators on dose finding. The available model-based strategies for AB dosing are empirical techniques based on Monte Carlo simulations to identify clinical PK/PD breakpoints for specific PD targets and modes of administration. This is illustrated in **Chapter 5** (PTA analysis). While most publications mention “dosing optimization”, the methods used do not provide an optimal treatment from a mathematical point of view. In **Chapter 8**, an optimal control approach is discussed, aiming at improving the drug dosing by optimizing a well-defined criterion. This approach represents an important clinical interest, as it could provide the minimal effective dose.

Structure of the thesis

The thesis is divided into two main parts and written to be understandable by an interdisciplinary audience.

The first part is devoted to pharmacokinetic modeling. After an introduction to useful mathematical concepts and drug pharmacokinetics, Chapter 1 describes the main features of the population models. Then, the process for model development, from parameter estimation to internal and external validation, is detailed. Three case

study drugs are presented in Chapters 2-4 :

- hydroxychloroquine (oral administration), in COVID-19 patients;
- temocillin (IV infusion), in ICU patients with nosocomial pneumonia;
- meropenem (IV infusion), in ICU patients with nosocomial pneumonia.

The three cases were chronologically analyzed in the opposite order during my PhD thesis, the meropenem was even already covered in my master's thesis. The order of the presentation is consistent with the following part.

The second part is about the model-based methods for dosing rationale. In Chapter 5, PK simulations are illustrated with the HCQ model and the standard PTA-based strategies is explained and exemplified on the temocillin model. Chapter 6 presents an open-loop control, based on an input-output approach, and shows how it can be incorporated into a worst-case analysis. This is then used in Chapter 7 to heuristically design a feedback dosing strategy. Finally, an optimal control approach for drug dosing is discussed in Chapter 8. The theory developed in the last three chapters is illustrated on numerical toy examples using the popPK model of meropenem.

Contributions

Thanks to fruitful collaborations (see co-authors of the publications listed below), our contributions include the development of pharmacokinetic models from patient level data, including observed concentrations and demographic information. A traditional population model (“top-down”), whose structural model is a mammillary compartmental model, is reported for each case study drug - HCQ **Chapter 2**, temocillin **Chapter 3**, and meropenem **Chapter 4** - in a target population. A physiologically based pharmacokinetic (PBPK) model has also been developed for meropenem. This is a reduced PBPK “bottom-up” model in which some parameters are data-driven (“middle-out” approach).

A comprehensive analysis of the input-output (I/O) relationship has been carried out for a particular class of systems - including the PK systems described by a LTI state-space representation (I.1) - and a particular form of the control function u , in line with the drug administration (Figure IV), see **Appendix D**. This input-output analysis has then been used to suggest an open-loop method for drug dosing, in the nominal case as well as in the “worst case” to take IIV into account (**Chapter 6**). In particular, we have deduced a formula, called *I/O formula*, which expresses the dose D needed to achieve, at steady-state (i.e., asymptotically), $100\%T > MIC$ assuming that, if the model describes the infection-site concentrations, the drug of interest has no clinically relevant time disconnect between systemic and infection-site concentrations. In this open-loop control law, we consider only one degree of freedom (the dose). If other aspects should be taken into account, e.g., prevention of risks of toxicity or reducing the cost, the other input parameters, namely the infusion duration and/or the length of the dosing interval, should also be fine-tuned. In **Chapter 7**, this I/O formula is included in a feedback control, based on the estimated state.

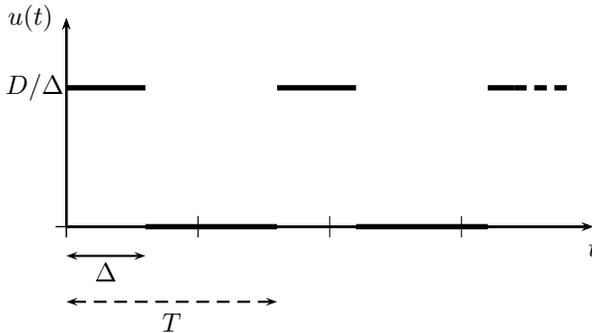


Figure IV – System input function (D , dose; Δ , infusion duration; T , length of the dosing interval)

Finally, we have performed a systematic analysis to develop the minimum principle for the optimal control (OC) problem which consists in minimizing the cost functional

$$J(u) = \int_0^{t_f} u^2(t) dt$$

for the system dynamics

$$\dot{x}(t) = Ax(t) + bu(t)$$

under relaxed input constraints and pure state constraints. The input constraints are said relaxed because there is no requirement for a constant infusion rate during the administration intervals. We have first studied the discrete-time OC problem, in order to guess the form of the continuous-time solution. This is reported in **Chapter 8**.

In short, we believe that the contributions of this thesis cover all the aspects of a pharmacokinetic research question: we derived mathematical models from clinical data and we designed personalized drug dosing strategies in line with the clinical practice

Communications

Posters

- “Modeling, analysis and control of pharmacokinetic system”. August 9, 2017. Uppsala Pharmacometric Summer school, Uppsala, Sweden.
- “Prediction of meropenem exposure: a PBPK approach”. May 29, 2018. PAGE meeting, Montreux, Switzerland.
- “Modeling, analysis and control of pharmacokinetic systems”. September 20, 2018. NaXys kick-off meeting, Namur, Belgium.

Talks

- “Modeling and control of pharmacokinetic systems: application to meropenem”. March 30, 2017. 36th Benelux Meeting on Systems and Control, Spa.
- “Prediction of meropenem systemic and infection site exposure and open-loop control strategy for optimal drug dosing: a PBPK approach”. March 29, 2018. 37th Benelux Meeting on Systems and Control, Soesterberg, The Netherlands.
- “Pharmacokinetic modeling and strategies for drug dosing recommendation: Application to meropenem” (naXys seminar). May 23, 2019. University of Namur, Belgium
- “Strategies of drug dosing based on pharmacokinetic models”. February 4, 2020. Ecole Doctorale FNRS Complex, University of Namur, Belgium.
- “Strategies of drug dosing based on pharmacokinetic models”. March 11, 2020. 39th Benelux Meeting on Systems and Control, Elspeet, The Netherlands.
- “Model-based strategies of drug dosing for pharmacokinetic systems”. July, 2020. (Virtual) 21st IFAC World Congress, Berlin, Germany.

Publications

- P. Thémans, P. Marquet, J. J. Winkin, and F. T. Musuamba. Towards a generic tool for prediction of meropenem systemic and infection-site exposure: A physiologically based pharmacokinetic model for adult patients with pneumonia. *Drugs in R&D*, 19(2):177-189, 2019. doi: [10.1007/s40268-019-0268-x](https://doi.org/10.1007/s40268-019-0268-x).
- P. Thémans, F. T. Musuamba, and J. J. Winkin. Model-based strategies of drug dosing for pharmacokinetic systems. *IFAC-PapersOnLine*, 53(2):16061-16068, 2020. doi: [10.1016/j.ifacol.2020.12.421](https://doi.org/10.1016/j.ifacol.2020.12.421).
- P. Thémans, N. Dauby, L. Schrooyen, F. Lebout, M. Delforge, R. Nasreddine, A. Libois, M.-C. Payen, D. Konopnicki, F. Wuillaume, C. Lescrainier, V. Verlinden, J.-M. Dogné, J. Hamdani, F. T. Musuamba. Model informed dosing of hydroxychloroquine in COVID-19 patients: Learnings from the recent experience, remaining uncertainties and gaps. *Br J Clin Pharmacol*, 2020. doi: [10.1111/bcp.14436](https://doi.org/10.1111/bcp.14436).
- P. Thémans, L. Belkhir, N. Dauby, J.-C. Yombi, J. De Greef, K.A. Delongie, M. Vandeputte, R. Nasreddine, X. Wittebole, F. Wuillaume, C. Lescrainier, V. Verlinden, S. Kiridis, J.-M. Dogné, J. Hamdani, P. Wallemacq, F. T. Musuamba. Population Pharmacokinetics of Hydroxychloroquine in COVID-19 Patients: Implications for Dose Optimization. *Eur J Drug Metab Pharmacokinet*, 45(6), 703-713, 2020. doi: [10.1007/s13318-020-00648-y](https://doi.org/10.1007/s13318-020-00648-y).

- N. Layios, C. Visée, P. Thémans, V. Mistretta, R. Denooz, N. Maes, J. Descy, J. Winkin, FT. Musuamba. Systemic and epithelial lining fluid pharmacokinetics of temocillin in critically ill patients: a study of continuous versus intermittent infusion. (*Submitted*).
- P. Thémans, F. T. Musuamba, and J. J. Winkin. Input-output approaches for personalized drug dosing of antibiotics: application to a pharmacokinetic model of meropenem. Invited chapter in the book entitled *Feedback control for personalized medicine* (Editor: E. Vargas, Publisher: Elsevier, *In preparation*).

Data and code availability

The datasets analyzed during the current thesis work are not publicly available due to confidentiality reasons. Some custom NONMEM, MATLAB and R codes used for modeling and simulations are available on the DDMoRe Model Repository:

- population model of meropenem ([DDMODEL00000301](#)),
- population model of hydroxychloroquine ([DDMODEL00000322](#)).

The NONMEM control stream of the ‘middle-out’ physiologically based model of meropenem and a MATLAB script for external evaluation are available as electronic supplementary material to the related publication.

Any additional MATLAB and R scripts are available from the author on reasonable request.

Part I

Pharmacokinetic modeling

CHAPTER 1

Drug pharmacokinetics and mathematical modeling

This chapter intends to provide the reader with the basic concepts of pharmacokinetics and modeling. Pharmacokinetics is a particular field of clinical pharmacology that studies how a drug evolves after it is administered to an organism. It aims to describe the relationship between the dose of a drug administered to patients and the evolution of drug exposure (concentrations) over time. Pharmacokinetic modeling consists in quantifying the interaction between dose and drug exposure through the development of mathematical models whose parameters are fitted to observed concentrations.

The most commonly used pharmacokinetic models are the population (“top-down”) models and the physiologically based (“bottom-up”) models. While the “top-down” approach is mostly informed by the data for parameter estimation (at population level), the “bottom-up” approach is mostly informed by the mechanistic understanding (at individual level). Therefore, the parameters of a popPK model should be interpreted as virtual volumes and rate constants, while the parameters of a PBPK model represent real volumes and blood flows. In the framework we focus on, the systems are described by linear time-invariant state-space representations with a limited number of compartments, but one could increase in complexity (nonlinear absorption, nonlinear elimination, time varying parameters...).

Before introducing the most important concepts of pharmacokinetics and modeling, we provide the reader with some mathematical preliminaries and notation conventions.

1.1 Mathematical preliminaries

For any vector $v \in \mathbb{R}^l$, $v \geq 0$ (resp. $v \leq 0$) means that all components of v are nonnegative (resp. nonpositive), while $v \gg 0$ (resp. $v \ll 0$) means that all components of v

are positive (resp. negative). The notation $v > 0$ (resp. $v < 0$) means that $v \geq 0$ (resp. $v \leq 0$) and $v \neq 0$ (i.e., at least one component is nonzero). The *nonnegative orthant* of \mathbb{R}^n is the set denoted indifferently by \mathbb{R}_+^n or $[0, \infty)^n$ and is defined by

$$\mathbb{R}_+^n := \{x \in \mathbb{R}^n \mid x \geq 0\}.$$

Definition 1 A vector v (a matrix M , respectively) is said *nonnegative* if all its components (elements, respectively) are nonnegative. It is denoted by $v \geq 0$ ($M \geq 0$, respectively), in line with the previous notations.

In what follows, the conjugate and the real part of a complex number z are denoted \bar{z} and $\operatorname{Re}(z)$, respectively. The conjugate transpose of a matrix $M \in \mathbb{C}^{l \times m}$ is denoted M^* . If M is a real matrix, $M^* = M^T$.

Definition 2 For a given matrix $A \in \mathbb{R}^{n \times n}$, the complex number $\lambda \in \mathbb{C}$ is an *eigenvalue* of A if $\det(\lambda I - A) = 0$.

The set of eigenvalues of a matrix $A \in \mathbb{R}^{n \times n}$ is denoted by $\sigma(A)$. If $\lambda \in \sigma(A)$, there exists a non-zero vector $v \in \mathbb{C}^n$, called *right eigenvector associated to λ* , that satisfies

$$Av = \lambda v.$$

Furthermore, since $\det(\bar{\lambda}I - A^T) = \overline{\det(\lambda I - A)}$, the conjugate $\bar{\lambda}$ is an eigenvalue of A^T . Thus there exists a non-zero vector $w \in \mathbb{C}^n$ such that

$$\begin{aligned} A^T w &= \bar{\lambda} w \\ w^* A &= \lambda w^*. \end{aligned}$$

The vector w is called *left eigenvector associated to λ* .

Proposition 1.1.1 Let a matrix $A \in \mathbb{R}^{n \times n}$. For all $\lambda \in \sigma(A)$ and $t \geq 0$,

$$e^{At} v = e^{\lambda t} v \quad \text{and} \quad e^{A^T t} w = e^{\bar{\lambda} t} w \tag{1.1.1}$$

where v and w are, respectively, the left and right eigenvectors associated to λ .

Proof. By definition, the exponential of A is given by

$$e^{At} = \sum_{k=0}^{\infty} \frac{t^k}{k!} A^k$$

such that

$$e^{At} v = \sum_{k=0}^{\infty} \frac{t^k}{k!} \lambda^k v = e^{\lambda t} v$$

since v is a right eigenvector associated to λ . The second identity of (1.1.1) holds since w is a right eigenvector of A^T associated to $\bar{\lambda}$. \square

Definition 3 A matrix $A \in \mathbb{R}^{n \times n}$ is said *Metzler* if all its off-diagonal elements are nonnegative. Furthermore, A is *compartmental* if A is Metzler and $\sum_{i=1}^n a_{ij} \leq 0$ for all $j \in \{1, \dots, n\}$ (Haddad et al., 2010, Definition 2.10), where a_{ij} denotes the element (i, j) of A (element at the intersection of row i and column j).

Proposition 1.1.2 Let $A \in \mathbb{R}^{n \times n}$. Then A is Metzler if and only if $e^{At} \geq 0$ for all $t \geq 0$.

Proof. see (Chellaboina et al., 2009, Proposition 2).

From now on, let consider a linear time-invariant state-space model

$$\begin{cases} \dot{x}(t) = Ax(t) + Bu(t) \\ y(t) = Cx(t) \end{cases} \quad t \geq 0 \quad (1.1.2)$$

where $A \in \mathbb{R}^{n \times n}$, $B \in \mathbb{R}^{n \times m}$, and $C \in \mathbb{R}^{p \times n}$.

Definition 4 The state-space representation (1.1.2) is a *nonnegative system* if, for all nonnegative initial conditions (i.e., $x(0) \geq 0$) and for all nonnegative admissible input functions $u(\cdot)$ (i.e., $u(t) \geq 0$ for all $t \geq 0$), the state $x(t)$ is nonnegative for all $t \geq 0$.

Lemma 1.1.1 The state-space representation (1.1.2) is nonnegative if and only if A is a Metzler matrix and B is nonnegative ($B \geq 0$).

Proof. see (Haddad et al., 2010, Proposition 4.1).

Definition 5 A *zero-input state trajectory* of the LTI differential system (1.1.2) is the solution $x(\cdot)$ of a Cauchy problem $\dot{x} = Ax$, $x(0) = x_0 \in \mathbb{R}^n$, and is given by $x(t) = e^{At}x_0$, for all $t \geq 0$.

Proposition 1.1.3 If A is diagonalizable, the zero-input state trajectory associated to the initial condition $x_0 \in \mathbb{R}^n$ can be written as a linear combination of exponential functions given by

$$x(t) = \sum_{i=1}^n c_i e^{\lambda_i t} v_i = \sum_{i=1}^n \langle x_0, w_i \rangle e^{\lambda_i t} v_i \quad (1.1.3)$$

where, for all $i \in \{1, \dots, n\}$, $\lambda_i \in \sigma(A)$, and v_i and w_i are the associated right and left eigenvectors. The inner product is defined, for all $x, y \in \mathbb{C}$, by

$$\langle x, y \rangle = y^* x.$$

Proof. This proof is inspired by (Curtain and Zwart, 2020, Lemma 3.2.4). Since $A \in \mathbb{R}^{n \times n}$ is diagonalizable, there exists an invertible matrix V such that

$$A = VDV^{-1}$$

where $D := \text{diag}[\lambda_i]$ and V is the matrix formed by the right eigenvectors, i.e.,

$$V = [v_1 \quad \dots \quad v_n].$$

Let define

$$W := (V^{-1})^*$$

For all $i \in \{1, \dots, n\}$, the vector $w_i := We_i$ denotes the i^{th} column of W , i.e.,

$$W = [w_1 \quad \dots \quad w_n]$$

where $\{e_i : i \in \underline{n}\}$ is the canonical basis. On the one hand, for all $i \in \{1, \dots, n\}$, w_i is the left eigenvector associated to λ_i . Indeed,

$$w_i^* A = e_i^* V^{-1} A = e_i^* V^{-1} V D V^{-1} = e_i^* D W^* = \lambda_i w_i^*.$$

On the other hand, for any vector $x \in \mathbb{C}^n$, $V^{-1}x$ is decomposed in the canonical basis as

$$V^{-1}x = \sum_{i=1}^n \langle V^{-1}x, e_i \rangle e_i$$

such that

$$x = \sum_{i=1}^n \langle V^{-1}x, e_i \rangle Ve_i = \sum_{i=1}^n \langle x, (V^{-1})^* e_i \rangle Ve_i = \sum_{i=1}^n \langle x, w_i \rangle v_i$$

In particular, for all $t \geq 0$,

$$x(t) = e^{At}x_0 = \sum_{i=1}^n \langle e^{At}x_0, w_i \rangle v_i = \sum_{i=1}^n \langle x_0, e^{A^T t} w_i \rangle v_i = \sum_{i=1}^n \langle x_0, w_i \rangle e^{\lambda_i t} v_i$$

using Proposition 1.1.1. □

Remark 1 The sets $\{v_i : i \in \underline{n}\}$ and $\{w_i : i \in \underline{n}\}$ of the right and left eigenvectors, respectively, are biorthogonal: for all $i, j \in \{1, \dots, n\}$,

$$\langle v_i, w_j \rangle = \langle Ve_i, (V^{-1})^* e_j \rangle = \langle e_i, e_j \rangle = \delta_{ij}.$$

Definition 6 The exponential functions $e^{\lambda_i t} v_i$, where $\lambda_i \in \sigma(A)$ and v_i is the associated eigenvector, are called the *modes* of the uncontrolled system $\dot{x} = Ax$.

Definition 7 The *zero-input system response* is the term of $y(\cdot) = Cx(\cdot)$ corresponding to $u(\cdot) \equiv 0$. In fact, the system response is given, for all $t \geq 0$, by

$$y(t) = Cx(t) = \underbrace{Ce^{At}x_0}_{\text{zero-input response}} + \underbrace{\int_0^t Ce^{A(t-\tau)}Bu(\tau)d\tau}_{\text{zero-state response}}$$

The system response $y(\cdot)$ is indifferently called the *output trajectory*. Each component $y_j(\cdot)$ of the output trajectory is a linear combination of the components of the state trajectory.

Definition 8 The state-space representation (1.1.2) is said *internally stable* if there exist $M > 0$ and $\sigma > 0$ such that, for all $t \geq 0$,

$$\|e^{At}\| \leq Me^{-\sigma t}. \quad (1.1.4)$$

Equivalently, whatever the initial condition x_0 , the zero-input state trajectory verifies, for all $t \geq 0$,

$$\|x(t)\| \leq Me^{-\sigma t} \|x_0\|$$

and thus converges towards $0 \in \mathbb{R}^n$ when $t \rightarrow 0$.

Definition 9 A matrix $A \in \mathbb{R}^{n \times n}$ which satisfies (1.1.4) is said *asymptotically stable*.

A matrix A is asymptotically stable if and only if all its eigenvalues have negative real part, i.e., for all $\lambda \in \sigma(A)$, $\text{Re}(\lambda) < 0$.

Lemma 1.1.2 Let A be a Metzler matrix. Then the two following statements are equivalent:

1. A is asymptotically stable
2. there exists $\mu \gg 0$ such that $A^T \mu \ll 0$.

Proof. see (Chellaboina et al., 2009, Proposition 7).

The following result is taken from (Horn and Johnson, 1985, Theorem 8.3.1)

Proposition 1.1.4 (Perron-Frobenius) If A is a Metzler matrix, then the spectral abscissa $\mu(A) := \max \{\text{Re}(\lambda) : \lambda \in \sigma(A)\}$ is an eigenvalue of A associated with a nonnegative eigenvector, i.e., there exists $x > 0$ such that $Ax = \mu(A)x$. This eigenvalue is called *Frobenius eigenvalue* and is denoted by λ_F .

1.2 Individual pharmacokinetics

The pharmacokinetics of a drug is characterized by different phases: **absorption**, **distribution** and **elimination** (including **metabolism** and **excretion**). This is generally denoted by ADME. The writing of this section is mainly based on the book of Rowland and Tozer (2011).

1.2.1 Pharmacokinetic profile

The *pharmacokinetic profile*, also called *concentration-time profile*, is the evolution of the drug concentration with respect to time, due to the processes of administration, absorption, distribution, and elimination. It is known in the pharmacology literature that, with repeated drug administration, the concentration eventually reaches a so-called *plateau*, or *steady state*, where the concentrations at the beginning and at the end of the dosing interval are equal (as illustrated in figures 1.1 and 1.2 for a typical concentration-time profile).

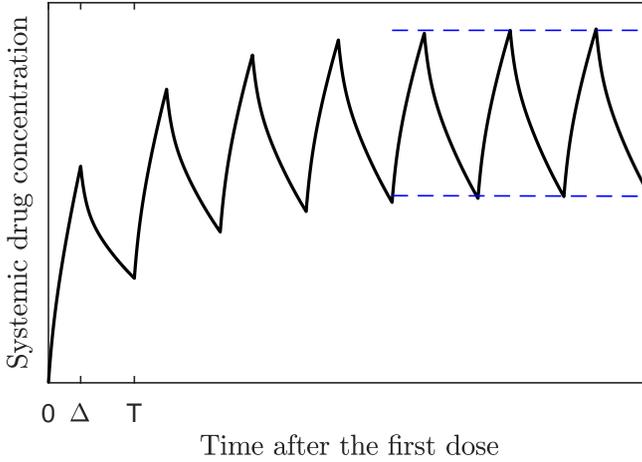


Figure 1.1 – Hypothetical concentration-time curve following a repeated intravenous administration (Δ , infusion duration; T , length of the dosing interval)

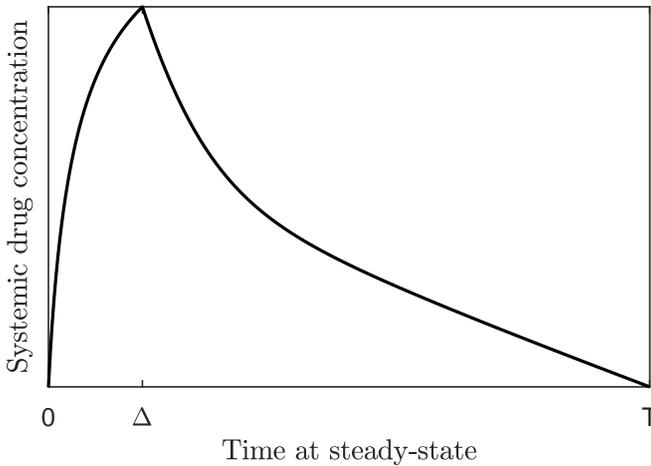


Figure 1.2 – Hypothetical steady-state concentration-time curve (log scale) following a repeated intravenous administration (Δ , infusion duration; T , length of the dosing interval)

1.2.2 Absorption

Absorption is the process by which the drug passes from the site of administration to the site of measurement (blood or plasma). It is considered in the case of extravascular routes of administration (e.g., oral administration). This process can be quantified by the PK parameter of *bioavailability*. Bioavailability is defined as the fraction of the administered dose that reaches the systemic circulation.

The cardiovascular circulation has two components: the systemic circulation and the pulmonary circulation. The pulmonary circulation carries the deoxygenated blood (venous blood) from the heart to the lungs via the pulmonary artery. In the lungs, carbon dioxide is released from the blood and oxygen is absorbed. The oxygenated blood (arterial blood) returns to the heart via the pulmonary vein. Then, the systemic circulation carries the oxygenated blood via the aorta to the rest of the body and then returns the oxygen-depleted blood back to the heart. Oxygen and nutrients diffuse through the blood vessel layers and are transported to the target cells via the *interstitial fluid* (Tortora and Derrickson (2007)). As illustrated in Figure 1.3, the liver is not only supplied by the hepatic artery, but also by the so-called portal vein, which is the blood vessel that carries the blood from the gastrointestinal tract, pancreas and spleen to the liver. The liver receives oxygen-rich blood via the hepatic artery and deoxygenated but nutrient-rich blood via the portal system.

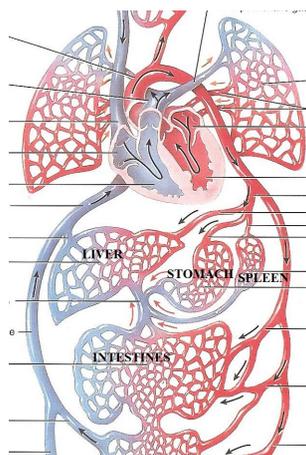


Figure 1.3 – Blood circulation. Red, arterial blood; blue, venous blood. Illustration taken from Tortora and Derrickson (2007).

After extravascular administration, a drug may suffer losses by decomposition or metabolism before reaching the systemic circulation. With oral administration, the main sites of loss are the gastrointestinal tract (stomach and intestines) and the liver. The loss of drug during its first passage through these tissues is called *first-pass loss*. First-pass loss is obviously not restricted to oral administration. But, as the pulmonary first-pass loss is rare, the intra-arterial and intravenous administrations are indifferently referred to as the intravascular or intravenous route (denoted by IV infusion).

1.2.3 Distribution

Distribution is the process by which the (free) drug is distributed to the fluids, tissues and organs. This transfer is reversible. In the body a fraction of the drug is protein-bound. Only the unbound drug is able to diffuse through the vessel and tissue layers. As the free fraction is eliminated or diffused to the tissue, a part of the bound drug becomes free. Protein binding is rapid such that the two forms are assumed to be at equilibrium at all times.

Most drugs are transported by passive diffusion, but other transport processes exist (see Rowland and Tozer (2011)). Passive diffusion is the process by which the drug moves from the most concentrated site to the least concentrated one. Passive diffusion depends on various factors including the drug permeability, the surface, and the gradient of concentrations. It can also be influenced by the severity of the illness (Jager et al. (2019)). Lipophilicity (solubility in lipids) and small size of a drug improve its permeability, and thus facilitates its passage across a membrane.

At *distribution equilibrium*, there exists a constant ratio K_t between plasma and tissue concentrations, called *tissue-to-plasma partition coefficient*, or *penetration ratio*:

$$K_t := \frac{c_t}{c_p} \quad (1.2.1)$$

where c_p and c_t stand, respectively, for plasma and tissue drug concentrations. This is illustrated in Figure 1.4

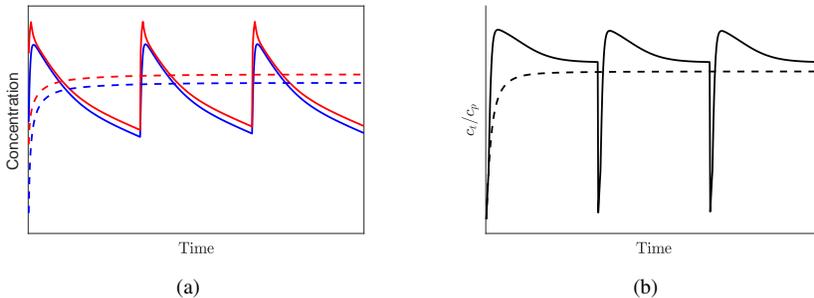


Figure 1.4 – (a) Hypothetical PK profiles after intravenous administration. Red, plasma concentration; blue tissue concentration. (b) Ratio of tissue to plasma concentrations. Continuous curves, intermittent administration; dashed curves, continuous administration.

The *volume of distribution* is the PK parameter that quantifies the amount of drug distributed in the organs and tissues, by relating the drug concentration in the site of measurement (usually plasma) to the amount of drug in the body. The volume of distribution V is then defined by the ratio between the total amount of drug in the body

and the (equilibrium) plasma drug concentration:

$$V := \frac{A}{c_p} = \frac{A_p + A_t}{c_p}$$

where A , A_p , and A_t are the amounts of drug in the body, in the plasma and in the tissues and organs, respectively, and c_p is the plasma drug concentration. This volume is not a physical one, but a apparent one, and corresponds thus to the virtual volume into which the drug should be distributed to account for the total amount of drug in the body if its concentration was everywhere equal to that measured in plasma.

1.2.4 Elimination

Elimination incorporates all the processes by which the drug is eliminated from an organism. The main routes of elimination are the kidneys (by renal excretion) and the liver (by hepatic metabolism and biliary excretion). The notion of *clearance* is used to quantify the elimination processes. Clearance is defined as the virtual volume of plasma cleared of drug per time unit. A distinction can be made between renal and hepatic clearances:

$$CL = CL_R + CL_H$$

where CL , CL_R and CL_H denote the total, renal and hepatic clearances, respectively.

1.3 Population pharmacokinetic modeling

A population pharmacokinetic model aims to describe the PK of a drug of interest at population level, accounting for different sources of variability in drug concentrations. Mammillary compartmental models are the standard structural models in this field. Here, we detail two routes of administration: the intravenous and oral administrations. For IV administration, the site of administration is the plasma. For oral administration, we need to add a so-called *depot compartment*. The oral absorption and the elimination are assumed to be first-order reactions.

1.3.1 Structural model

This section is partly inspired by the PhD thesis Koch (2012). We use a pedagogical approach by progressively increasing the number of compartments.

1.3.1.1 One-compartment model

In a one-compartment model, the organism is assumed kinetically homogeneous: the drug is instantaneously distributed to tissues and organs and the distribution equilibrium is immediately reached for each tissue. This does not mean that the tissue concentrations are equal to the plasma concentration.

Let x_1 be the total amount of drug in the body. The evolution of the drug is described by the following state-space representations:

- with IV bolus injection,

$$\dot{x}_1(t) = -k_e x_1(t), \quad x_1(0) = D$$

where D is the administrated dose,

- with IV infusion,

$$\dot{x}_1(t) = -k_e x_1(t) + u(t), \quad x_1(0) = 0$$

where the input function $u(\cdot)$ corresponds to the rate of infusion of the drug, and

- with oral administration,

$$\begin{cases} \dot{x}_1(t) = -k_e x_1(t) + k_a x_2(t), & x_1(0) = 0 \\ \dot{x}_2(t) = -k_a x_2(t), & x_2(0) = F \cdot D \end{cases}$$

where k_a is the first-order absorption rate constant, $0 < F \leq 1$ denotes the bioavailability, and x_2 is the virtual amount of drug in the additional depot compartment.

In all three cases, k_e is the first-order elimination rate constant. These one-compartment models are represented in Figure 1.5.

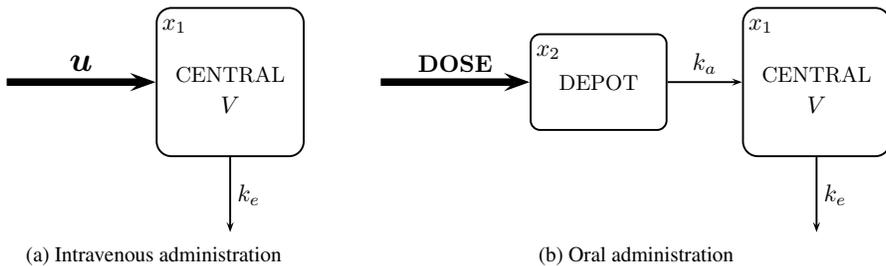


Figure 1.5 – Schematic representations of one-compartment pharmacokinetic models. k_a , absorption rate constant; V , volume of distribution; k_e , elimination rate constant.

1.3.1.2 Two-compartment model

In a two-compartment model, the organism is divided in two compartments that are kinetically homogeneous. The first compartment, called *central compartment*, is identified with the plasma, or the blood, and the well-perfused organs, such as the kidneys, the liver, the lungs, etc. The second compartment, called *peripheral compartment*, corresponds to the rest of the body, not heavily-supplied with blood. Since excretion and metabolism occur mainly via the kidneys and in the liver, respectively, the drug elimination takes place from the central compartment.

Let x_1 and x_2 be the virtual amounts of drug in the central and peripheral compartments, respectively. The evolution of the drug is described by the following state-space representations:

- with IV bolus injection,

$$\begin{cases} \dot{x}_1 = -k_{10}x_1(t) - k_{12}x_1(t) + k_{21}x_2(t), & x_1(0) = D \\ \dot{x}_2 = k_{12}x_1(t) - k_{21}x_2(t), & x_2(0) = 0 \end{cases} \quad (1.3.1)$$

where D is the administrated dose,

- with IV infusion,

$$\begin{cases} \dot{x}_1 = -k_{10}x_1(t) - k_{12}x_1(t) + k_{21}x_2(t) + u(t), & x_1(0) = 0 \\ \dot{x}_2 = k_{12}x_1(t) - k_{21}x_2(t), & x_2(0) = 0 \end{cases} \quad (1.3.2)$$

where the input function $u(\cdot)$ corresponds to the rate of infusion of the drug, and

- with oral administration,

$$\begin{cases} \dot{x}_1(t) = -k_{10}x_1(t) - k_{12}x_1(t) + k_{21}x_2(t) + k_a x_3(t), & x_1(0) = 0 \\ \dot{x}_2(t) = k_{12}x_1(t) - k_{21}x_2(t), & x_2(0) = 0 \\ \dot{x}_3(t) = -k_a x_3(t), & x_3(0) = F \cdot D \end{cases} \quad (1.3.3)$$

where k_a is the first-order absorption rate constant, $0 < F \leq 1$ denotes the bioavailability, and x_3 is the virtual amount of drug in the additional depot compartment.

In all three cases, k_{12} and k_{21} are the distribution rate constants and k_{10} is the first-order elimination rate constant. Using the matrix notation

$$\dot{x}(t) = Ax(t) + bu(t), \quad x(0) = x_0$$

where $x = (x_1 \quad x_2 \quad x_3)^T$, the state matrix of the systems (1.3.1)-(1.3.3) is given by

$$A = \begin{pmatrix} -k_{10} - k_{12} & k_{21} & k_a \\ k_{12} & -k_{21} & 0 \\ 0 & 0 & -k_a \end{pmatrix} \quad (1.3.4)$$

where $k_a \equiv 0$ with IV administration (bolus or infusion). Besides, $b \equiv 0$ with bolus and oral administrations. These two-compartment models are represented in Figure 1.6.

Remark 2 The eigenvalues of A are real. Indeed, two of them coincide with the eigenvalues of the submatrix

$$\tilde{A} = \begin{pmatrix} -k_{10} - k_{12} & k_{21} \\ k_{12} & -k_{21} \end{pmatrix}.$$

Since \tilde{A} is Metzler, the mostright eigenvalue of \tilde{A} is real by Proposition 1.1.4. The second eigenvalue is therefore also real. The third eigenvalues of A is obviously k_a .

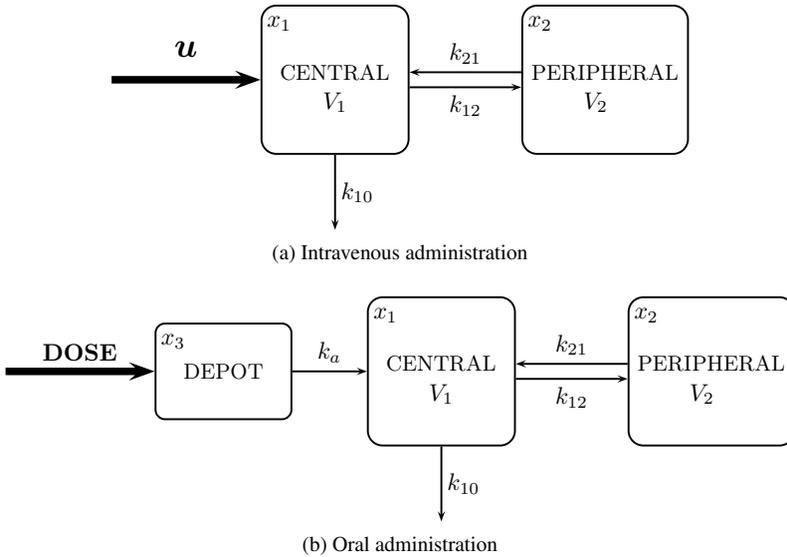


Figure 1.6 – Schematic representation of two-compartment pharmacokinetic models. k_a , absorption rate constant; V_1 , volume of distribution of the central compartment; k_{12} and k_{21} , distribution rate constants; V_2 , volume of distribution of the peripheral compartment; k_{10} , elimination rate constant.

Let λ_1 and λ_2 be the eigenvalues of \tilde{A} . In Koch (2012), the analytical solution of the state trajectory $x_1(\cdot)$ of a two-compartment model with bolus IV injection is calculated using the Laplace transform and is given, for all $t \geq 0$, by

$$x_1(t) = \frac{(x_0)_1(k_{21} + \lambda_1)}{\lambda_1 - \lambda_2} e^{\lambda_1 t} + \frac{(x_0)_1(k_{21} + \lambda_2)}{\lambda_2 - \lambda_1} e^{\lambda_2 t}$$

where

$$\lambda_1, \lambda_2 = \frac{-(k_{10} + k_{12} + k_{21}) \pm \sqrt{(k_{10} + k_{12} + k_{21})^2 - 4k_{10}k_{21}}}{2}$$

The solution of the state trajectory $x_1(\cdot)$ following an oral administration is also provided in Koch (2012).

1.3.1.3 n -dimensional compartmental model

In this paragraph, we unify in one general n -dimensional system the models describing the evolution of the drug with the different routes of administration. Such models consist in one central compartment and $n - 1$ peripheral compartments. Drug is administered into either the central compartment or an additional depot compartment. Then, substance exchange takes place between the central and the peripheral compartments (see Figure 1.7). The central compartment is identified with the plasma and the tissues/organs with which drug distribution is extremely fast. The elimination organs

are included in the central compartment. The peripheral compartments are identified with the tissues into which the drug distributes more slowly. Tissues for which the times to reach distribution equilibrium are similar are lumped together to form a virtual compartment (distribution is slower in the compartment 3 than in the compartment 2, and so on). Drug elimination occurs exclusively from the central compartment.

Absorption, transfer and elimination processes are usually supposed to be first-order reactions, meaning that the rate of reaction is proportional to the amount of drug. They are characterized by (positive) rate constants k_{\bullet} . These constants represent the fraction of drug which moves from one compartment to another or to external environment per time unit. Relationships with the PK notions of volume of distribution and clearance are detailed in Paragraph 1.3.2.

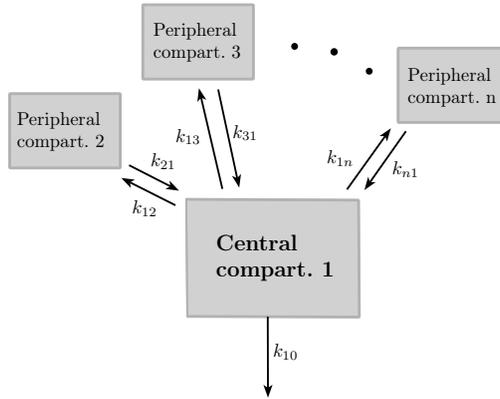


Figure 1.7 – A general n -compartment mammillary model

A n -compartment pharmacokinetic model is described by the following LTI state-space representation:

$$\begin{cases} \dot{x}(t) = Ax(t) + bu(t), & x(0) = x_0 \\ y(t) = Cx(t) \end{cases} \quad t \geq 0 \quad (1.3.5)$$

where

$$A = \begin{pmatrix} -k_{10} - \sum_{j=2}^n k_{1j} & k_{21} & k_{31} & \cdots & \cdots & k_{n1} & k_a \\ k_{12} & -k_{21} & 0 & 0 & \cdots & 0 & 0 \\ k_{13} & 0 & -k_{31} & 0 & \cdots & \vdots & \vdots \\ \vdots & \vdots & 0 & \ddots & \ddots & \vdots & \vdots \\ \vdots & \vdots & \vdots & \ddots & \ddots & 0 & \vdots \\ k_{1n} & 0 & 0 & \cdots & 0 & -k_{n1} & 0 \\ 0 & \cdots & \cdots & \cdots & \cdots & \cdots & -k_a \end{pmatrix} \quad (1.3.6)$$

and

$$b = (1 \quad 0 \quad \dots \quad 0)^T, \quad C = \begin{pmatrix} 1/S_1 & 0 & 0 & \dots & 0 \\ 0 & 1/S_2 & 0 & \dots & 0 \end{pmatrix}. \quad (1.3.7)$$

The absorption rate constant $k_a \equiv 0$ with IV administration (bolus or infusion). The initial condition is given by

$$x_0 = (D \quad 0 \quad \dots \quad 0)^T \quad \text{or} \quad x_0 = (0 \quad \dots \quad F \cdot D)^T$$

for bolus injection and oral administration, respectively, where $0 < F \leq 1$ corresponds to the bioavailability and D is the given dose [g]. The input function $u(\cdot)$ is either the null function, or a piecewise constant function that corresponds to the drug infusion rate [g/h] into the blood.

The parameters k_a and k_{ij} [h^{-1}] are the first-order rate constants and are positive real numbers. Clearly, the matrix $A \in \mathbb{R}^{n \times n}$ is compartmental (see Definition 3). The state vector $x = (x_1 \quad x_2 \quad x_3 \quad \dots \quad x_n)^T \in \mathbb{R}^n$ represents the virtual amount of drug [g] in each compartment. Without loss of generality, x_1 and x_2 correspond to the plasma and the site of infection, respectively. The output vector $y = (y_1 \quad y_2)^T \in \mathbb{R}^2$ represents the drug concentrations [mg/L] in the plasma and at the site of infection. For all $j \in \{1, 2\}$, S_j is a *scaling factor* used to convert a *virtual* amount of drug [g] in a concentration whose unit is consistent with the observations, e.g., [mg/L] (see Owen and Fiedler-Kelly (2014)). Note that the concentrations at the site of infection are not always described by the model. That depends on the available data to adequately estimate the values of the related parameters (S_2, V_2, \dots). In that case, the matrix C becomes $C = (1/S_1 \quad 0 \quad \dots \quad 0)$. When designing a feedback control law for drug dosing, we have to keep in mind that the site of measurement is almost always the plasma (or whole blood), while the controlled/regulated output is either y_1 or y_2 (see Chapter 7).

1.3.2 Pharmacokinetic parameters

The *volume of distribution* (V [L]) is, by definition, the apparent volume in which the drug is distributed to account for the plasma concentration, i.e.,

$$V = \frac{x_1 + x_2 + \dots + x_n}{c_p}$$

where c_p [g/L] is the (unscaled) plasma concentration. The volume of distribution is therefore made of several volumes

$$V = V_1 + V_2 + \dots + V_n, \quad \text{where} \quad V_1 = \frac{x_1}{c_p}, V_2 = \frac{x_2}{c_p}, \dots, V_n = \frac{x_n}{c_p}$$

where V_1 is the virtual volume of the first/central compartment, V_2 is the virtual volume of the second compartment, and so on. They are apparent volumes into which the drug would be distributed if the concentration in the compartment was equal to the plasma concentration c_p . Scaling factors S_j are scaled volumes of distribution

$$S_j = \frac{V_j}{u s v_j}$$

where usv stands for unitless scalar value. They are used to convert amounts in concentrations (e.g., if concentrations are in mg/L and dose in g, $S_1 = V_1/1000$ would permit V_1 to be reported in L). Observe that, at distribution equilibrium,

$$y_2 = \frac{x_2}{S_2} = \frac{x_2}{V_2} usv_2 = c_p \cdot usv_2 = \frac{y_1}{usv_1} usv_2$$

such that the ration usv_2/usv_1 is interpreted as the constant ratio K_t between tissue and plasma concentrations (tissue-to-plasma penetration ratio), i.e.,

$$K_t = \frac{usv_2}{usv_1}. \quad (1.3.8)$$

It expresses the degree of drug distribution into the tissue (Jager et al. (2019)). An estimated unitless scalar usv_2 does not seem to be primarily used in tissue penetration studies. Instead, Monte Carlo simulations are commonly performed to estimate, at population level, the ratio between the areas under the steady-state concentration-time curves (AUCs),⁽¹⁾ see, e.g., Lodise et al. (2011), Frippiat et al. (2015), or even as carried out in N. Layios, C. Visée, P. Thémans, et al. (2021, submitted).

The (*systemic*) *clearance* (CL [L/h]) is, by definition, the virtual volume of plasma cleared of drug per time unit, so that

$$CL = k_{10}V_1.$$

Likewise, the *intercompartmental clearance* (Q_{1i} and Q_{i1} , $i \in \{2, 3, \dots, n\}$, [L/h]) is defined as the virtual volume of distribution released of drug to the linked compartment per time unit, so that

$$Q_{1i} = k_{1i}V_1 \quad \text{and} \quad Q_{i1} = k_{i1}V_i.$$

At distribution equilibrium, the same amount of drug goes from the central to the peripheral compartment and from the peripheral to the central compartment, i.e.,

$$k_{1i}x_1 = k_{i1}x_i$$

or, equivalently,

$$Q_{1i} = Q_{i1} =: Q_i.$$

1.3.3 System analysis

As the state components of (1.3.5) represent amounts of drug, it is expected that the state trajectories stay in the nonnegative orthant of \mathbb{R}^n for all nonnegative initial conditions and nonnegative admissible input functions. Besides, since the drug is eliminated by the organism, the internal stability is also expected. The latter translates the fact that the state components of the uncontrolled system converge to 0. These properties of the system are stated in the propositions below.

⁽¹⁾See Identity (6.3.2) on Page 119.

Proposition 1.3.1 The PK system given by (1.3.5)-(1.3.7) is nonnegative.

Proof. This is a direct consequence of Lemma 1.1.1, since A is a Metzler matrix and b is a nonnegative matrix. \square

Proposition 1.3.2 The PK system given by (1.3.5)-(1.3.6) is internally (exponentially) stable.

Proof. Any vector $\mu = (\mu_1 \ \mu_2 \ \mu_3 \ \cdots \ \mu_n \ \mu_a)^T \gg 0$ such that $\mu_1 < \mu_a$,
 $\mu_2 = \mu_3 = \cdots = \mu_n > 0$,

and $k\mu_2 < \mu_1 < \mu_2$, where

$$k := \frac{k_{12} + k_{13} + \cdots + k_{1n}}{k_{10} + k_{12} + k_{13} + \cdots + k_{1n}} \in (0, 1),$$

verifies $A^T \mu \ll 0$. The conclusion follows by Lemma 1.1.2. \square

A Lyapunov function of this internally stable system is given, for all $x \in [0, \infty)^n$, by

$$V(x) = \mu^T x$$

where the vector μ is a positive vector as determined in the previous proof. This function can be interpreted as the weighted total mass of the system. We directly have that $V(0) = 0$ and $V(x) > 0$ for all $x \in [0, \infty)^n \setminus \{0\}$. The derivative of $V(x)$ along the zero-input state trajectories is given by

$$\dot{V}(x) = \mu^T Ax = (A^T \mu)^T x.$$

Since μ is such that $A^T \mu \ll 0$, $\dot{V}(x) < 0$ for all $x \in [0, \infty)^n \setminus \{0\}$ (Chellaboina et al., 2009, Proposition 7).

Since A is asymptotically stable, all its eigenvalues λ_i are in the left half-plane; thus, each mode of the system $e^{\lambda_i \cdot} v_i$ converges towards 0. The *dominant mode* is the slowest mode, associated to the most right eigenvalue. By Proposition 1.1.4, the most right eigenvalue of the state matrix (1.3.6) is real. The dominant mode is therefore the real exponential function $e^{\lambda_F \cdot} v_F$, where $v_F > 0$ is the right eigenvector associated to the Frobenius eigenvalue λ_F . Its absolute value $|\lambda_F|$ corresponds to the *decreasing rate* of the terminal zero-input state and output trajectories subject to exponential decay. The quantity $\tau := |1/\lambda_F|$ is called the (terminal) *time constant* or *mean lifetime*. After a period of one time constant, the dominant mode is reduced to $\pm 37\%$ of its initial value ($e^{\lambda_F \tau} = e^{-1} = 0.367\dots$). A more widespread parameter used to quantify the exponential decay is the (elimination) *half-life*, see, e.g., Toutain and Bousquet-Mélou (2004) and Gidal et al. (2017). Elimination half-life is defined as the time required for the drug concentration to reduce by half during the terminal phase and is denoted by $t_{1/2}$:

$$e^{\lambda_F t_{1/2}} = \frac{1}{2}$$

$$t_{1/2} = \frac{\ln(2)}{|\lambda_F|} = \tau \ln(2)$$

In the case of a one-compartment model,

$$t_{1/2} = \frac{\ln(2)}{k_e} = \frac{V}{CL} \ln(2)$$

is also the effective half-live since $x(t) = e^{\lambda_F t} x_0$, for all $t \geq 0$.

Figure 1.8 shows the influence of the PK parameters on the Frobenius eigenvalue. We can observe that the Frobenius eigenvalue is mostly influenced by the clearance, and seems not be affected by the volume of distribution.

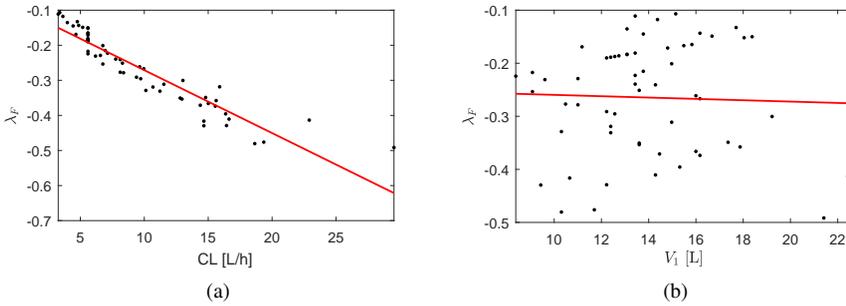


Figure 1.8 – Frobenius eigenvalue vs. **(a)** clearance and **(b)** central volume of distribution, using the popPK model developed for meropenem in Chapter 4. Squares correspond to the 60 patients included in the model building dataset. Red lines are linear regression lines.⁽²⁾

In what follows, the right eigenvectors of the state matrix (1.3.6) are assumed to be normalized, i.e., for all $i \in \{1, \dots, n\}$, $\|v_i\| = 1$. The right and left eigenvectors are biorthogonal, i.e., for all $i, j \in \{1, \dots, n\}$, $\langle v_i, w_j \rangle = \delta_{ij}$ (see Remark 1).

Proposition 1.3.3 Consider the PK system given by (1.3.5)-(1.3.6) with an initial condition x_0 . Then, for all $t \geq t^*$ where

$$t^* [\text{h}] = \frac{\ln(0.01) - \ln\left(\sum_{i=1}^n \|w_i\|\right)}{\lambda_F} \geq 0, \quad (1.3.9)$$

the zero-input state trajectory is reduced to 1% of its initial value, i.e.,

$$\|x(t)\| \leq 0.01 \|x_0\|.$$

⁽²⁾The regression has been performed using the *polyfit* function of MATLAB.

Proof. From (1.1.3), we have, for all $t \geq 0$,

$$\|x(t)\| \leq e^{\lambda_F t} \sum_{i=1}^n |c_i| \|v_i\| = e^{\lambda_F t} \sum_{i=1}^n |c_i|$$

By the Cauchy-Schwarz inequality,

$$|c_i| = | \langle w_i, x_0 \rangle | \leq \|w_i\| \|x_0\|,$$

for all $i \in \{1, \dots, n\}$. Therefore,

$$\sum_{i=1}^n |c_i| \leq \sum_{i=1}^n \|w_i\| \|x_0\|$$

and thus

$$\begin{aligned} \|x(t)\| &\leq e^{\lambda_F t} \sum_{i=1}^n \|w_i\| \|x_0\| & (1.3.10) \\ &\leq 0.01 \|x_0\| \end{aligned}$$

for all $t \geq t^*$. □

Since the observed concentrations seem to be accurate at the most to the hundredth, we can reasonably assume that the zero-input state trajectory has fallen to zero when it reaches 1% of its initial value. The time t^* in (1.3.9) could be approximated by the time t required for the dominant mode to be reduced to 1% of its initial value:

$$\begin{aligned} e^{\lambda_F t} &= 0.01 \\ t &= \frac{\ln(0.01)}{\lambda_F} = -\frac{\ln(0.01)}{\ln(2)} t_{1/2} \simeq 6.64 \cdot t_{1/2}. \end{aligned}$$

This is equivalent to assuming that

$$\sum_{i=1}^n \|w_i\| = 1.$$

Evaluating (1.3.10) at $t = 0$ yields

$$\sum_{i=1}^n \|w_i\| \geq 1.$$

Hence, for all $t \geq 0$,

$$e^{\lambda_F t} \leq e^{\lambda_F t} \sum_{i=1}^n \|w_i\|;$$

thus, $6.64 \cdot t_{1/2}$ is an **underestimation** of t^* and the smaller the sum of the norms of the left eigenvectors is, the better the approximation is.

1.3.4 Mixed effects model and covariates

Random effects are added to the structural model parameters in order to describe the interindividual variability observed in concentrations. The PK parameters in the population of interest are therefore characterized by a fixed-effect component and a random-effect component (Bauer (2019a), Nguyen et al. (2017), Owen and Fiedler-Kelly (2014)). Interindividual variability is also called between-subject or intersubject variability. The IIV can partly be explained by the patient's characteristics (covariates). The remaining variability is said to be *unexplained* and is modeled using random variables.

Deviation of the PK parameters from the nominal/central value is assumed to be normally distributed with zero mean. The normal random variable is most often included into an exponential model to ensure that the individual's parameter value is positive, whatever the realization of the random variable (Bauer (2019a)). If P denotes a PK parameter, the individual's parameter value is given by

$$P = TVP \cdot \exp(\eta_P) \quad (1.3.11)$$

where TVP is the individual *typical value* (fixed effect) and η_P is a normal random variable $\sim N(0, \omega_P^2)$ (random effect). The individual parameter P is therefore log-normally distributed, with parameters $\ln(TVP) =: \mu$ and ω_P^2 . Indeed,

$$\ln(P) = \ln(TVP) + \eta_P \sim N(\ln(P), \omega_P^2).$$

The median of this log-normal distribution is $e^\mu = TVP$, which corresponds to the nominal value. IIV can be expressed by the *coefficient of variation* (CV) of the related log-normal distribution. The CV is defined as the ratio of the standard deviation to the mean. In the case of a log-normal distribution (Nist-Sematech (2013)), the %CV is given by

$$\sqrt{e^{\omega_P^2} - 1} \cdot 100\%$$

which, for sufficiently small variance, is commonly approximated as

$$\sqrt{\omega_P^2} \cdot 100\%$$

as stated in Mould and Upton (2013). A fundamental challenge in the individual drug dosing (see Part II) is to deal with this variability and the *a priori* unknown realization of the random variables.

The typical value TVP of a PK parameter P can be expressed as a function of a patient's characteristic, which is then called a *covariate*. In a population model, a covariate is defined as a patient's characteristic (e.g., weight, body surface area, age, sex, creatinine clearance...) that affects the pharmacokinetic of a drug. In the case of an exponential model for the IIV, it is convenient to use a power/allometric model to describe the relationship between a continuous covariate and the parameter fixed effect (Bauer (2019a)):

$$TVP = \theta_P \left(\frac{COV}{COV_{med}} \right)^{\theta_{cov}} \quad (1.3.12)$$

where θ_{COV} is called the *allometric weight coefficient*, COV is the individual value of the covariate, normalized by its median value COV_{med} in the model building dataset (or an average value for a typical population); in this way, θ_P is interpreted as the parameter typical value of the *typical* patient, i.e., when $COV = COV_{med}$ (Bauer (2019a)).

1.3.5 Residual error model

The residual error (or prediction error) is the offset between the observed concentrations and the model predictions, because of model approximation, intra-individual variability and noise of the experiment (from assay errors to human recording errors). Residual error models are proportional and/or additive:

$$Y_{ij} = F_{ij} (1 + \varepsilon_{p_{ij}}) + \varepsilon_{a_{ij}}$$

where Y_{ij} and F_{ij} stand for the j^{th} observed and predicted concentrations in the i^{th} individual, respectively, and $\varepsilon_{p_{ij}}$ and $\varepsilon_{a_{ij}}$ are the individual realizations of the independent random variables $\varepsilon_p \sim N(0, \sigma_p^2)$ and $\varepsilon_a \sim N(0, \sigma_a^2)$, respectively. The proportional error can be expressed in terms of coefficient of variation (%CV) given by $\sigma_p \cdot 100\%$; ⁽³⁾ the additive error is commonly reported in term of standard deviation (σ_a , expressed in the concentration unit).

Usually, proportional, additive, and combined additive and proportional models are investigated to describe the residual variability. The residual variability model is developed until the regression line of the weighted residuals versus the predictions is sufficiently without trends (see Section 1.5).

1.3.6 Bayes estimates

The *Bayes estimates*, or individual parameter estimates, are the most likely values for an individual's parameter given the population model parameters and the observed concentrations Y_{ij} in the i^{th} individual. They are obtained by considering the following weighted least-squares objective function (OF):

$$OF_i = \sum_{j=1}^{N_i} \frac{(Y_{ij} - F_{ij})^2}{\text{Var}(Y_{ij})} + \sum_P \frac{(P_i - TVP_i)^2}{\omega_P^2} \quad (1.3.13)$$

called *Bayes objective function*, see, e.g., Mould and Upton (2013) and (Owen and Fiedler-Kelly, 2014, Chapter 7). In (1.3.13), N_i is the total number of observations in the i^{th} individual, F_{ij} are the individual model-predicted concentrations, and, for each PK parameter P , P_i is the individual's parameter estimate, TVP_i is the typical value for the i^{th} individual given its covariates, and $\omega_P^2 > 0$ is the variance of the related random variable η_P . The individual PK parameter, obtained by Bayesian estimations, are referred to as *posthoc estimates* or *empirical Bayes estimates* (EBEs). The vector of the realizations of the random variables η_P is denoted $\hat{\eta}_i$ and its components are often referred to as EBEs as well.

⁽³⁾We use the fact that, if X is a random variable with mean μ and variance σ^2 , then the random variable $Y := aX + b$, where a and b are constants, has mean $a\mu + b$ and variance $a^2\sigma^2$. This rule is applied to $Y = F\varepsilon_p + F$.

1.4 Model development

The usual process to build a popPK model consists in a step-by-step approach. The aim is to identify the model which provides the best fit of the data. The NONMEM software (Icon Development Solutions, Ellicott City, MD, USA) is widely used for this purpose. It is a well-known computer program in the PK/PD modeling community, used for more than 30 years to perform population analysis of pharmacokinetic clinical data (Bauer (2019a), Lindbom et al. (2005)). In few words, NONMEM⁽⁴⁾ uses a series of statistical methods to compute the parameter estimates and their statistical uncertainties. The assessment of the model and the estimation of its parameters is guided by numerical and graphical model fitting performances to (internal and external) data, see Section 1.5. The developed models are called *nonlinear mixed effects models* (NLMEMs). Since the structural model is linear (see Equation 1.3.5), the term “nonlinear” must be interpreted with respect to the random effects (Nguyen et al. (2017)).

For a practical use of NONMEM (formatting a data file, creating of a control stream to give instructions to the software, evaluating the report file), the reader is referred to the didactic and user-friendly textbook of working with NONMEM by Owen and Fiedler-Kelly (2014) and to the two-part NONMEM tutorial published in a journal of the American Society for Clinical Pharmacology and Therapeutics (ASCPT) (Bauer (2019a) and Bauer (2019b)).

1.4.1 Parameter estimation method

The values of the model parameters are estimated by minimizing an objective function. The default objective function is an extended least-square OF and the minimization algorithm, which consists in a numerical search in the parameter space, is a derivative-free quasi-Newton type iterative method (see the NONMEM user guide, part I (1989)). The extended least-square objective function is derived from the likelihood function of the independent normal random variables Y_{i1}, \dots, Y_{iN_i} ($i \in 1, \dots, m$), where N_i is the total number of observations in the i^{th} individual and m is the number of individuals in the dataset. For all $i \in \{1, \dots, m\}$, we define the j^{th} observation by

$$Y_{ij} = F_{ij} + F_{ij}\varepsilon_{pij} + \varepsilon_{aij} =: f(X_{ij}, \Theta, \eta_i^*) + h(X_{ij}, \Theta, \eta_i^*, \varepsilon_{ij}^*) \quad (1.4.1)$$

where $h = f\varepsilon_p + \varepsilon_a$, f corresponds to the model prediction, X_{ij} is the vector of the values taken by the independent variables (time and covariates), Θ is the vector of the fixed components, η_i^* and ε_{ij}^* are the vectors of the individual realizations of the random variables (η_P , for each PK parameter P , and $\varepsilon^{P,a}$) (Hooker et al. (2007)). The variance-covariance matrix of the random variables η_P is denoted by Ω . The covariances between the random variables η_P are often assumed to be zero, such that Ω is diagonal. The INTER(ACTION) option in the *estimation* step (\$EST) of NONMEM

⁽⁴⁾NONMEM stands for NONlinear Mixed Effects Modeling; computer program implemented in Fortran90/95, originally developed by Lewis Sheiner and Stuart Beal at the University of California (Bauer (2019a)).

means that we take into account the interaction between IIV and residual error variability. When no interaction between η and ε is assumed, the model prediction F_{ij} is evaluated at $\eta_i^* = 0$ in the term multiplied to $\varepsilon_{p_{ij}}$, i.e., $\eta_i^* = 0$ in the term h of (1.4.1) (Bauer (2019a)).

The likelihood function for the i^{th} individual is the following joint density function, considered as a function of the parameters:

$$L(\theta_{\bullet}, \omega_{\bullet}^2, \sigma_{a,p}^2; Y_{i1}, \dots, Y_{iN_i}) = \prod_{j=1}^{N_i} \frac{1}{\sqrt{2\pi \cdot \text{Var}(Y_{ij})}} e^{-\frac{(Y_{ij} - \text{E}(Y_{ij}))^2}{2\text{var}(Y_{ij})}}.$$

Finding the maximum likelihood is equivalent to minimizing the *extended least-square objective function* defined as minus two times the natural logarithm of the likelihood function L without the constant term $N_i \ln(2\pi)$, i.e.,

$$OF_i := -2\ln(L) = \sum_{j=1}^{N_i} \left(\ln(\text{Var}(Y_{ij})) + \frac{(Y_{ij} - \text{E}(Y_{ij}))^2}{\text{Var}(Y_{ij})} \right). \quad (1.4.2)$$

NONMEM offers different methods for approaching $\text{E}(Y_{ij})$ and $\text{Var}(Y_{ij})$ by linearization of the model (1.4.1), see Hooker et al. (2007) and Nguyen et al. (2017). The first-order conditional estimation with interaction (FOCEI) is the standard method to estimate the model parameters (Bauer (2019a)).

The very first method (and simplest method) used for NLMEM development was the **first-order (FO) method**. In this approach, the model $f + h$ is linearized, using a Taylor development, around the zero mean of the random variables η and σ :

$$Y_{ij} \simeq f(X_{ij}, \Theta, \eta_i^* = 0) + \left[\frac{\partial f(X_{ij}, \Theta, \eta_i^* = 0)}{\partial \eta} \right]^T \eta + f(X_{ij}, \Theta, \eta_i^* = 0)\varepsilon_p + \varepsilon_a$$

where η is the vector of the IIV random variables η_p and $\partial f/\partial \eta$ is the gradient of f with respect to η . That yields

$$\text{E}(Y_{ij}) \simeq f(X_{ij}, \Theta, \eta_i^* = 0) =: \text{PRED}_{ij} \quad (1.4.3)$$

and

$$\text{Var}(Y_{ij}) \simeq \frac{\partial f(X_{ij}, \Theta, \eta_i^* = 0)}{\partial \eta} \Omega \frac{\partial f(X_{ij}, \Theta, \eta_i^* = 0)}{\partial \eta} + f^2(X_{ij}, \Theta, \eta_i^* = 0)\sigma_p^2 + \sigma_a^2 \quad (1.4.4)$$

where *PRED* stands for (typical) population PREDiction.

In the **first-order conditional estimation (FOCE) method** without $\eta - \varepsilon$ interaction, the model $f + h$ is linearized around the individual's Bayes estimates of the IIV random variables η and around the zero mean of the residual error random variables ε :

$$Y_{ij} \simeq f(X_{ij}, \Theta, \eta_i^* = \hat{\eta}_i) + \left[\frac{\partial f(X_{ij}, \Theta, \eta_i^* = \hat{\eta}_i)}{\partial \eta} \right]^T (\eta - \hat{\eta}_i) + f(X_{ij}, \Theta, \eta_i^* = 0)\varepsilon_p + \varepsilon_a.$$

That yields

$$E(Y_{ij}) \simeq f(X_{ij}, \Theta, \eta_i^* = \hat{\eta}_i) - \left[\frac{\partial f(X_{ij}, \Theta, \eta_i^* = \hat{\eta}_i)}{\partial \eta} \right]^T \hat{\eta}_i =: CPRED_{ij} \quad (1.4.5)$$

and

$$Var(Y_{ij}) \simeq \frac{\partial f(X_{ij}, \Theta, \eta_i^* = \hat{\eta}_i)}{\partial \eta} \Omega \frac{\partial f(X_{ij}, \Theta, \eta_i^* = \hat{\eta}_i)}{\partial \eta} + f^2(X_{ij}, \Theta, \eta_i^* = 0) \sigma_p^2 + \sigma_a^2 \quad (1.4.6)$$

where *CPRED* stands for Conditional population PREDiction.

1.4.2 Likelihood ratio test and covariate selection

The OF values of two *nested* models can be compared using the likelihood ratio test (LRT). Under the hypothesis that both models provide the same description of the data, minus two times the logarithm of the ratio of their likelihood is assumed to follow a chi-squared distribution with k degree of freedom, where k is the number of additional parameters in the second model, i.e.,

$$-2 \ln(L_1/L_2) = \underbrace{OFV_2 - OFV_1}_{\Delta OF} \sim \chi_k^2$$

where OFV stands for objective function value, see Mould and Upton (2013) and Fisher and Shafer (2007). For nested models differing by one parameter, a decrease in $OFV > 3.84$ (resp. > 10.83) is considered as statistically significant (resp. highly significant). Indeed, the corresponding p-value is < 0.05 (resp. < 0.01) based on the χ_1^2 distribution. The LRT is used as the principal model selection criterion, to choose between two structural models or to select the model covariates.

The covariate model building can be performed using a forward inclusion phase and a backward elimination phase. In each step of the forward phase, covariate-parameter relationships are tested one at a time. The most significant relationship, given that it is statistically significant ($\Delta OF > 3.84$), is retained in the next step. Each remaining covariate-parameter relationship is again added one at a time to the model and the most significant is retained. This process is repeated until no more relationship is significant, at which point the full model is established. The full model is subsequently subjected to a stepwise backward elimination of relationships. Each covariate-parameter relationship is omitted from the model one at a time. The least significant relationship, given that it is not statistically highly significant ($\Delta OF > 10.83$), is removed from the model. This is repeated until no more relationship could be removed, at which point the final model was established. A covariate may also be included for clinical reasons: change of at least 20% in the parameter value at the extremes of the covariate (Mould and Upton (2013)).

1.5 Evaluation tools

In this section, a series of numerical and graphical tools for NLMEM evaluation are presented. They aim to assess the fitting and predictive performances of the model or identify model misspecification. The interested reader is referred to the suggested references for further information of each tool.

Minimization successful

The very first criteria for accepting the NONMEM parameter estimates is the “minimization successful” statement in the output report file. It indicates the convergence of the maximum likelihood estimation (Bauer (2019a)).

(Final) gradients See, e.g., (Owen and Fiedler-Kelly, 2014, Chapter 3).

Standard error of estimates (see, e.g., Bauer (2019a), Owen and Fiedler-Kelly (2014)) Standard error (SE) of estimates provide information on the precision of the parameter estimations. They are generally reported as a percentage (relative standard error of estimate, %RSE). During the so-called *covariance* step (\$COV) of NONMEM, the standard error of estimates are computed. It is derived from the shape of the OF surface around the final parameter estimate (FPEs) (Mould and Upton (2013)). If the shape is broad and shallow, there are more values of the parameters that describe the data, and, therefore, the estimations are uncertain. It is illustrated in Figure 1.9.

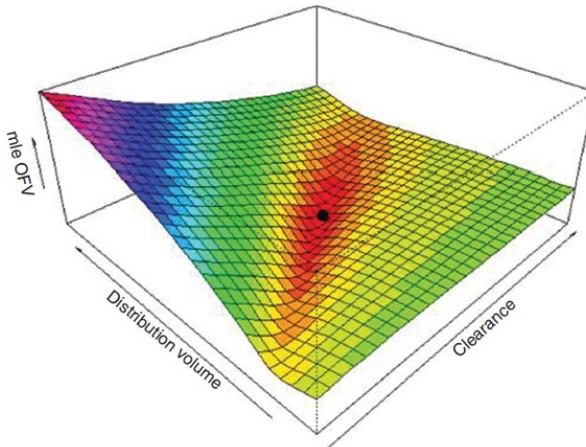


Figure 1.9 – Surface of the maximum likelihood extended (mle) objective function for a model with only two parameter to estimate. Illustration taken from Mould and Upton (2012).

The relative standard error (RSE) of estimate is defined as the SE divided by the final parameter estimate and is generally reported as a percentage, i.e.,

$$\%RSE = \frac{SE}{FPE} \cdot 100\%.$$

The 95% confidence interval⁽⁵⁾ is given by

$$CI = [FPE - 2 \cdot SE, FPE + 2 \cdot SE]$$

Usually, the accepted level of precision is $RSE < 30\%$ for the fixed-effect components Θ and $RSE < 50\%$ for the random-effect components ω_p^2 and $\sigma_{p,a}^2$ (Mould and Upton (2013)).

The reliability of the SEs provided by NONMEM is widely discussed in the literature and by NONMEM users on online forums. They argue that the SEs are used to compute confidence intervals based on the assumption that they are symmetrical around the parameter estimates (normal distribution), see Holford, N (2015) and Mould and Upton (2013). There exist alternative methods, e.g., the log likelihood profile (LLP) method⁽⁶⁾ and resampling methods such as the bootstrap (see, e.g., Lindbom et al. (2005) and Holford, N (2015)).

Bootstrap (see, e.g., Lindbom et al. (2005) and the online PsN documentation (GitHub-PsN (2018)))

Bootstrap is a re-sampling method to assess the uncertainty/precision of the estimations. It is an alternative tool to the standard error of estimates, since NONMEM \$COV step may failed even if the model adequately fits the data. A bootstrap consists in generating a large number of new datasets (e.g., 1000), including the same number of individuals as the original one, by sampling (with replacement) individuals from the original dataset (Holford, N (2015)). For each new dataset, the population model parameters are re-estimated by fitting the model to the data. Statistics can then be computed based on the parameter bootstrapped distributions. The minimum required number of samples with minimization successful (without estimates near the fixed boundary) depends on the desired percentile confidence interval, called *bootstrap confidence interval*. E.g., for a CI at 95% (i.e., based on the 2.5th and 97.5th percentiles of the bootstrapped distribution), 39 successful samples are required (see (GitHub-PsN (2018))). On contrary to the CIs based on the SEs of estimates, the bootstrap CIs do not assume a symmetric/normal distribution of the parameters (Mould and Upton (2013)).

Population predictions (see, e.g., Nguyen et al. (2017))

Population predicted concentrations correspond to the expectation of the model, i.e., $E(Y_{ij})$, approximated by either *PRED* (see (1.4.3)) or *CPRED* (see (1.4.5)). The scatter plot of the observations vs. the population predictions is a powerful diagnostic tool for model evaluation. If the model adequately fits the data, the regression line should be close to the line of identity.

Population residuals (see, e.g., Hooker et al. (2007) and Nguyen et al. (2017))

Population residuals *RSE* are the differences between the observations and the population predictions, i.e.,

$$RES_{ij} := Y_{ij} - E(Y_{ij}).$$

⁽⁵⁾A confidence interval at 95% is intended to contain the true value of the parameter 95% of the time (Mould and Upton (2013)).

⁽⁶⁾The LLP method is based on the likelihood ratio test (LRT).

These are correlated within each subject. Population *weighted residuals*, defined as

$$WRES_{ij} := \frac{Y_{ij} - E(Y_{ij})}{\sqrt{\text{Var}(Y_{ij})}}, \quad (1.5.1)$$

are decorrelated and should be normally distributed $\sim N(0, 1)^{(7)}$ as long as the model adequately fits the data. That means that 95% of the data should be evenly distributed between -2 and 2. NONMEM computes the above basic residuals using the FO approximation, i.e.,

$$WRES_{ij} := \frac{Y_{ij} - PRED_{ij}}{\sqrt{\text{Var}(Y_{ij})}} \quad (1.5.2)$$

where $\text{Var}(Y_{ij})$ is given by (1.4.4).

This diagnostic tool can be misleading when using the FOCE method for the parameter estimation (Hooker et al. (2007)). In that case, it is better to use the *conditional weighted residuals* $CWRES$, that correspond to (1.5.1) calculated with the FOCE approximation, i.e.,

$$CWRES_{ij} := \frac{Y_{ij} - CPRED_{ij}}{\sqrt{\text{Var}(Y_{ij})}} \quad (1.5.3)$$

where $\text{Var}(Y_{ij})$ is given by (1.4.6).

Note that the (conditional) weighted residuals correspond to the second term of the OF (1.4.2). The population predictions and residuals ($CPRED$ and $CWRES$) are computed from the FOCE approximation of (1.4.1) without the $\eta - \varepsilon$ interaction considered in the FOCEI objective function. But, at this stage, when using the FOCEI method for the parameter estimation, $CPRED$ and $CWRES$ are the best tools to assess the goodness-of-fit of the model (Hooker et al. (2007)).

Individual predictions and residuals (see, e.g., Nguyen et al. (2017))

Individual predicted concentrations are the model predictions given the EBEs $\hat{\eta}_i$:

$$IPRED_{ij} := f(X_{ij}, \Theta, \eta_i^* = \hat{\eta}_i) \quad (1.5.4)$$

The individual weighted residuals are defined as

$$IWRES_{ij} = \frac{Y_{ij} - IPRED_{ij}}{\sigma} \quad (1.5.5)$$

where

$$\sigma = f(X_{ij}, \Theta, \eta_i^* = \hat{\eta}_i)\sigma_p + \sigma_a$$

is the standard deviation of the the residual variability (Nguyen et al. (2017) and Savic and Karlsson (2009)). The scatter plot of the observations vs. the individual predictions enables to verify if the model is able to describe the individual data. It is similar to the corresponding graph of observations vs. (C)PRED, but with less variability.

Shrinkages (see, e.g., Savic and Karlsson (2009) and Nguyen et al. (2017))

It is obvious from the Bayes OF (1.3.13) that, for an individual with $N_i = 0$ observed

⁽⁷⁾We use the fact that, if $X \sim N(\mu, \sigma^2)$, $Y := (X - \mu)/\sigma \sim N(0, 1)$

concentration, the individual's posthoc estimates P_i are equal to the typical values TVP_i . The smaller the number of available observations is, the more the individual's Bayes estimates are close to the typical values. The variance of the EBE distributions *shrinks* therefore to 0. For a random-effect component $\eta \sim N(0, \omega)$, where ω^2 is the estimated population variability, η -shrinkage sh_η is calculated using

$$sh_\eta = 1 - \frac{SD(EBE_\eta)}{\omega^2}$$

where $SD(EBE_\eta)$ is the standard deviation of the EBE distribution of η . In the case of a high shrinkage ($> 20 - 30\%$), posthoc analyses based on the EBEs are assumed to be uninformative.

Moreover, a phenomenon called *overfitting* may occur. It is observed when the individual predicted concentrations *IPRED* *shrink* to the individual observations. This is quantified by the so-called ϵ -shrinkage sh_ϵ , which is calculated using

$$sh_\epsilon = 1 - SD(IWRES)$$

where $SD(IWRES)$ is the standard deviation of the distribution of the individual weighted residuals. In the case of a high shrinkage ($> 20 - 30\%$), diagnostic plots based on individual predicted concentrations *IPRED* are assumed to be uninformative.

Visual predictive check and prediction-corrected visual predictive check (see, e.g., (Owen and Fiedler-Kelly, 2014, Section 8.8), Nguyen et al. (2017) and Bergstrand et al. (2011))

Visual predictive check (VPC) is a simulation-based tool for model diagnostic and consists in a graphical comparison of simulated and observed concentrations. VPCs rely on the principle that a model derived from a dataset should be able to simulate concentrations similar to the original ones. During the *simulation* step (\$SIM), NONMEM uses the final model to perform simulations, called *Monte Carlo* (MC) *simulations*, in order to replicate the original dataset a high number of times (e.g., $N_{\text{repl}}=1000$, where N_{repl} stands for the number of replicates). For this purpose, it selects realizations of the random-effect components η_P for each subject in the dataset and realizations of the random variables $\epsilon_{p,a}$ (residual error) for each data to be simulated and repeats this process until the number of replicates is reached (Owen and Fiedler-Kelly (2014)). Then, a *prediction interval* (PI) of the concentration-time profiles can be compared with the observed concentrations. It is common to display the median PK profile and the 90% PI (i.e., the area between the 5th and 95th percentiles of the simulated PK profiles). A good overlap between the simulated and observed drug concentrations confirms that the model is adequately adjusted to the data.

An alternative way to present the MC simulations is to display the prediction intervals (also called VPC confidence intervals) of the median and the chosen percentiles. To do so, the median and the percentiles are computed for each replicate (simulated dataset). The prediction intervals are derived from the distribution of the N_{repl} computed medians and percentiles.

A third alternative is the prediction-corrected VPC (pcVPC). This method assumes a data binning with respect to one or more independent variable(s) (here time) and the

data are corrected before calculating the statistics (Bergstrand et al. (2011)). The observed and simulated concentrations are corrected by the median of the typical population predictions ($PRED$) in the specific bin of independent variable(s):

$$pcY_{ij} = Y_{ij} \frac{PRED_{bin}}{PRED_{ij}}$$

where $PRED_{ij}$ is the typical population prediction of the j^{th} concentration in the i^{th} individual and $PRED_{bin}$ is the median of the typical population predictions in the specific bin.

Normalized prediction distribution errors (see, e.g., Nguyen et al. (2017))

Normalized prediction distribution errors (NPDEs) is another simulation-based tool for model evaluation. For each observation Y_{ij} , the predictive distribution is based on MC simulations of the original dataset (or any validation dataset). The *prediction discrepancy* (pd) is defined as the percentile corresponding to this observation in the predictive distribution, i.e., $pd = P(Y_{sim} < Y_{ij})$. After a decorrelation step (PDE)⁽⁸⁾, the NPDE are computed using the inverse function of the normal cumulative density function $N(0,1)$. If the model adequately describes the data, the NPDEs follow a normal $N(0,1)$ distribution (Brendel et al. (2007), S. Critea (2019)).

There exist many other diagnostic tools in the pharmacometric literature, such as the ones based on the EBEs, see, e.g., Nguyen et al. (2017) and Savic and Karlsson (2009).

Internal validation

Internal evaluation consists in assessing the fitting performances of the model using prediction-based and simulation-based tools. Standard methods for internal validation include:

- (1) Visual inspection of diagnostic scatter plots, also called *goodness-of-fit* (GOF) *plots*. They usually include the observations (DV)⁽⁹⁾ vs. the individual and/or population predictions ($IPRED$ and $CPRED$) and the residual ($CWRES$) vs. the population predictions and/or time.
- (2) Visual predictive checks (VPCs).
- (3) Assessment of the estimates precision using the standard error of estimates or by bootstrap (CI).

External validation

External validation consists in assessing the predictive performances of the final model on external and independent data. These data can, for example, be generated from

⁽⁸⁾Performing the same computations but from the decorrelated observations and simulations (see (1.5.1)) will produce the prediction discrepancy errors (see Nguyen et al. (2017)).

⁽⁹⁾The acronym DV stands for dependent variable.

published models. Simulated concentration-time profile are produced on the basis of the study design used in the external dataset (dosing regimen and demographic information (distribution of covariates)). The simulation process (using NONMEM or a customized MATLAB script) selects realizations of the random variables η_P for each subject and for each replicate of the external dataset. However, in contrast to the VPC described above, the residual error is not taken into account, i.e., we consider model predictions only. The 90% PI computed after, e.g., $N_{\text{repl}} = 1000$ simulations, is displayed. A good overlap between the simulations and the observed concentrations in independent but similar patients and settings establishes that the model has good predictive performances.

1.6 Physiologically based pharmacokinetic modeling

A (whole-body) physiologically based model is a mechanistic model, based on a “bottom-up” approach (Jones and Rowland-Yeo (2013)), contrarily to a data-driven popPK model, based on a “top-down” approach. Indeed, in popPK modeling, the structural model (number of compartments), the parameter estimates and the retained covariates are based on the data (concentrations) collected in a particular group of patients.

In physiologically based pharmacokinetic modeling, there is a distinction between drug- and patient-related parameters. Model structure and parameter values are based on physiological considerations and drug’s properties. This approach is much less dependent on the available data than the population approach. Despite the high degree of complexity of such models (large number of parameters, need of experimental data, etc.), PBPK modeling in drug development have risen dramatically in the last 15 years, as well as the development of user-friendly software such as Simcyp (Sager et al. (2015)).

CHAPTER 2

Population pharmacokinetic model of hydroxychloroquine in COVID-19 patients

The aim of this chapter is to characterize the pharmacokinetics of hydroxychloroquine in COVID-19 patients, using prospectively collected pharmacokinetic data from patients either enrolled in a clinical trial or treated with hydroxychloroquine as part of standard of care. A model-based approach is used for this purpose. The content of this chapter is reported in Thémans et al. (2020a). In Chapter 5, simulations of different scenarios are performed to illustrate how the model can be used for dosing rationale.

Hydroxychloroquine (**Plaquenil**[®], HCQ sulfate) is a drug approved and used for decades for the treatment of malaria (Lim et al. (2009)), rheumatoid arthritis (RA) (Carmichael et al. (2003)), and cutaneous lupus erythematosus (CLE) (Morita et al. (2016)). During the first peak of the COVID-19 pandemic, HCQ was extensively used off-label. Based on the results of *in vitro* studies showing antiviral activity of HCQ on SARS-CoV-2 (e.g., Yao et al. (2020) and Liu et al. (2020)) and on some preliminary results from small clinical studies (e.g., Gautret et al. (2020b), Gautret et al. (2020a)), interim guidelines in several countries recommended treating hospitalized patients suffering from moderate to severe COVID-19 with HCQ at various dosing regimens (see, e.g., Sciensano (2020)). The doses implemented were inconsistent across publications, national guidelines, and clinical uses.

The pharmacokinetics of HCQ was already described in inflammatory indications but not so far in COVID-19-disease. Therefore, reference pharmacokinetic exposures in COVID-19 patients were unknown and so were clinical target exposures for disease cure. There was an urgent need for HCQ pharmacokinetic characterization in COVID-19-disease, as acknowledged in several publications (Martin-Blondel et al. (2020), Morrisette et al. (2020), Thémans et al. (2020b)). Population pharmacokinetic modeling and simulation were considered as the most appropriate approach to ob-

tain relevant pharmacokinetic information during the pandemic crisis. Indeed, popPK modeling is able to perform acceptable analysis from sparse blood samples, overcoming the need for large sampling (needed with traditional individual pharmacokinetics), that would have been very complicated to implement in the context of an outbreak.

A population approach was also used to describe the pharmacokinetics of HCQ in inflammatory diseases. Two population pharmacokinetic models have been published in patients with rheumatoid arthritis and lupus erythematosus using whole-blood HCQ concentrations (Carmichael et al. (2003) and Morita et al. (2016)). Four additional models describe plasma concentrations or merged blood and plasma concentrations in healthy volunteers (Tett et al. (1989)) and patients (Lim et al. (2009), Morita et al. (2016)), including pregnant women (Balevic et al. (2019)). These models have been used to simulate COVID-19 patient exposures at different doses in recent publications, under the unverified assumption that the pharmacokinetics of HCQ would be similar in other diseases and in COVID-19 (see, e.g., Martin-Blondel et al. (2020), Thémans et al. (2020b) and Garcia-Cremades et al. (2020)).

2.1 Study design and data

The pharmacokinetic data (blood concentrations) originated from 33 patients enrolled in an open-label, single-arm prospective study evaluating the pharmacokinetics, safety, and efficacy of HCQ in COVID-19 patients in Saint-Luc University Hospital, a tertiary hospital in Brussels (Belgium). This study was planned to enroll 50 patients with COVID-19 infection. The 33 patients were supplemented by concentrations collected from 23 patients as part of standard of care at Saint-Luc Hospital and at Saint-Pierre Hospital, another tertiary hospital in Brussels (Belgium).

HCQ therapy was administered as per the Belgian national protocol guidance: 400 mg twice daily (BID) on day 1, followed by 200 mg BID the subsequent days for a 5-day total duration of treatment. Patients received Plaquenil® tablets by oral administration, each tablet having 200 mg of racemic HCQ sulfate, equivalent to 155 mg of racemic HCQ base. Pharmacokinetic assessment of HCQ required at least one scheduled blood sampling and one optional blood sampling. At least one blood sampling was performed by patient. It was drawn within the first 4 hours after dose administration, after an accurate record of the drawing time. This sample was possibly supplemented by a blood sample at the end of treatment or at the time of treatment interruption for safety reasons.

The model building dataset was composed of data collected during the study (33 patients) supplemented by additional data from routine clinical practice (15 patients). A total of 84 whole-blood concentrations samples were obtained and are shown in Figure 2.1. The remaining patients were used for external validation. The characteristics of the patients included in the model building and validation datasets are summarized in Table 2.1, together with their baseline clinical symptoms. Body weight values were missing for 2 patients. They were replaced by the median value.

2.1 Study design and data

Table 2.1 – Baseline characteristics of the patients included in the model building and external validation datasets

	Model building dataset (N=48)	Number of missing data	External validation dataset (N=8)	Number of missing data	Total (N=56)	Number of missing data
Demographic and clinical data						
Sex (Males/females)	26/22		5/3		31/25	
Weight (kg) Median [min;max]	80 [50,122]	2	86.5 [52;108]		81.5 [50;122]	2
Age (years) Median [min;max]	58.5 [21;93]		57.5 [38;75]		58.5 [21;93]	
Fever/chills N (y/n) ^a	29/19		7/1		36/20	
Cough N (y/n)	25/23		7/1		32/24	
Dyspnea N (y/n)	21/27		5/3		26/30	
Conjunctivitis N (y/n)	0/48		0/8		0/56	
Sore throat N (y/n)	9/39		1/7		10/46	
Nasal discharge N (y/n)	8/40		3/5		11/45	
Headache N (y/n)	12/36		2/6		14/42	
General weakness N (y/n)	23/24	1	5/3		28/27	1
Myalgia N (y/n)	16/31	1	4/4		20/35	1
Nausea/vomiting N (y/n)	4/44		4/4		8/48	
Diarrhea N (y/n)	8/40		3/5		11/45	
Anosmia N (y/n)	4/43	1	0/1	7	4/44	8
Ageusia N (y/n)	6/42		0/1	7	6/43	7
Cardiovascular pathology N (y/n)	20/28		4/4		24/32	
Arterial hypertension N (y/n)	18/30		4/4		22/34	
CRP (mg/dL) Median [min;max]	69.4 [3.2,231.4]		57.4 [22.5,190.3]		67.9 [3.2,231.4]	
White blood cells (1000/mm ³) Median [min;max]	5.88 [3.14,13.62]	2	4.73 [2.55,10.01]		5.76 [2.55,13.62]	2
Lymphocytes (1000/mm ³) Median [min;max]	0.9 [0.19,2.13]		0.94 [0.31,1.57]		0.90 [0.19,2.13]	
LDH (U/L) Median [min;max]	313 [162,2555]	1	333 [296,429]		316 [162,2555]	1
AST (U/L) Median [min;max]	32 [13,968]	2	34.5 [14,46]		32.5 [13,968]	2
ALT (U/L) Median [min;max]	28.5 [8,604]	2	30 [13,42]		28.5 [8,604]	2
Creatinine (mg/dL) Median [min;max]	1.02 [0.55,2.77]		1.13 [0.62,3.33]		1.04 [0.55,3.33]	
Haemoglobin (mg/dL) Median [min;max]	13.2 [9.4,16.5]	2	13.1 [8.9,16.2]		13.2 [8.9,16.5]	2
Saturation (%) Median [min;max]	95 [83,98]	1	92.5 [84,100]		95 [83,100]	1

^a Number of patients (yes/no)

CRP, C-reactive proteine; LDH, lactate deshydrogenase; AST, aspartate aminotransferase; ALT, alanine aminotransferase

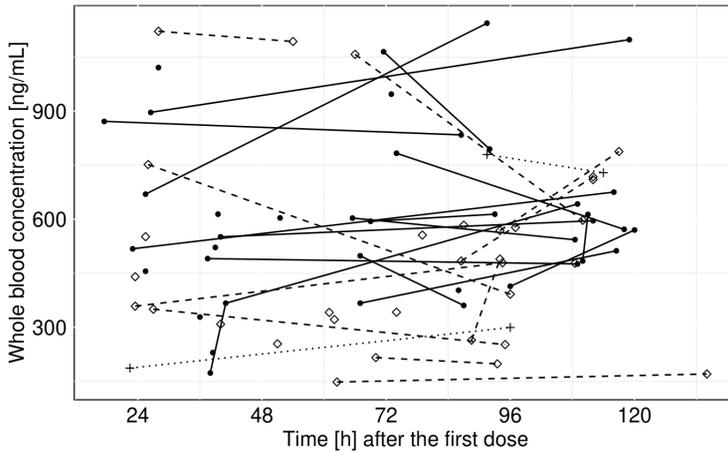


Figure 2.1 – Observed whole-blood concentrations of HCQ in the 48 patients included in the model building dataset. Filled circles, $WT \leq 80$ kg; open squares, $WT > 80$ kg; crosses, missing WT.

2.2 Population model building

Data were analyzed using nonlinear mixed effects modeling of NONMEM software, version 7.3.0. The first-order conditional estimation method with interaction was used. Base and final model selection were based on the results of likelihood ratio tests.

Based on previously published population pharmacokinetic models in malaria, RA, and CLE, one- and two-compartment structural models with first-order absorption and elimination were tested. The need for an absorption lag time parameter was tested. Finally, a one-compartment model with first-order absorption and elimination was retained to describe the observed data. The addition of a lag time component did not improve the model fitting performance, so this parameter was not kept in the model for the subsequent steps. The structural model is schematically represented in Figure 2.2. Random components on the structural model were introduced to describe the IIV in the PK parameters. They were retained provided that the estimates were neither very small⁽¹⁾ nor caused instability in the model-fitting procedure.

Correlation was visually tested between the candidate covariates (see Figure 2.3). Good correlation was found between body weight and sex. Age does not seem to be correlated with body weight (Pearson correlation coefficient: -0.12) or sex. During the covariate model building, an allometric model was used to describe the influence of body weight and age on the PK parameters, and a linear model was used to describe the influence of sex. Body weight and sex were found to significantly influence the clearance, with a higher drop in the objective function value for the body weight effect. Besides, because of the correlation between both, only body weight was kept in

⁽¹⁾A random component is considered very small if the estimated variance is less than the order of magnitude 10^{-3} .

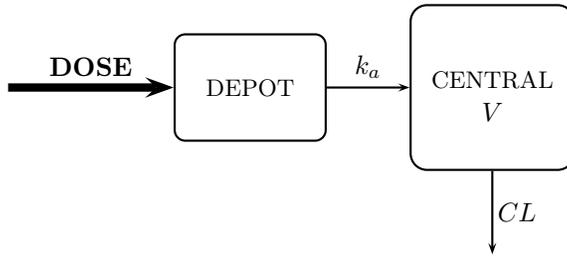


Figure 2.2 – Schematic representation of a one-compartment population pharmacokinetic model with oral administration. k_a , absorption rate constant; V , volume of distribution; CL , clearance.

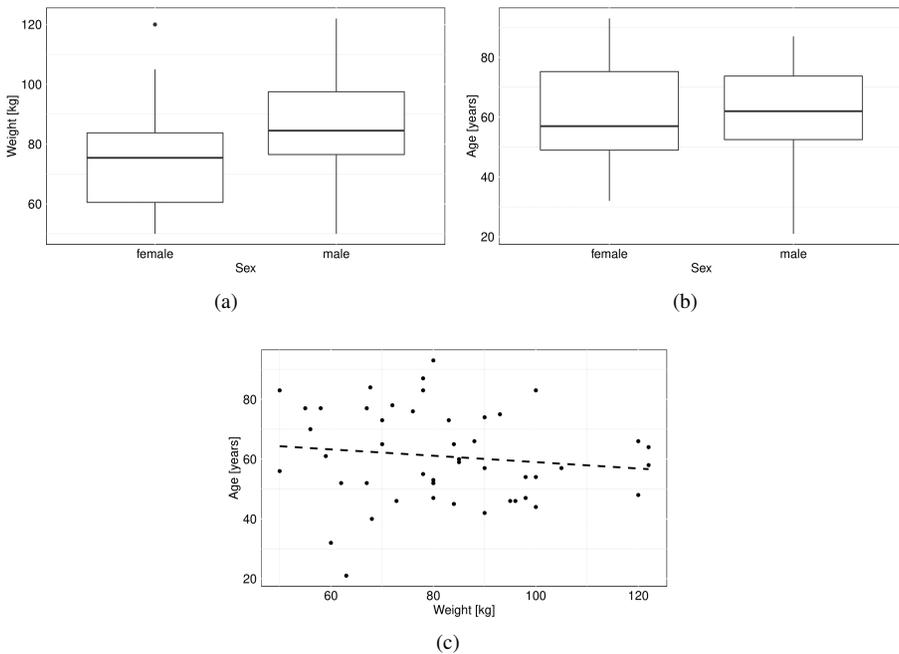


Figure 2.3 – Visual inspection of correlation between the patient characteristics. **(a)** Boxplot of weight vs. sex, **(b)** boxplot of age vs. sex, **(c)** age vs. weight. In the boxplots, the ends of the box are the 1st and the 3rd quartiles (comprise 50% of the observations), the central line represents the median and the whiskers correspond to at most 1.5 times the interquartile range (dots are the outliers).

the model. The influence of age on clearance did not reach the predefined statistical significance level to be kept in the model.

The parameter estimates of the final model are summarized in Table 2.2. The number of significant digits in the final estimations is 3.1. That means that, between the last two iterations of the estimation algorithm, none of the parameters differed in the first 3 significant digits (see the NONMEM user guide, part V (2013)). Table 2.2 also includes the corresponding estimates in the previously published model in RA (Carmichael et al. (2003)), for comparison.

This model still carries a moderate to high unexplained variability on the volume of distribution (CV: 52 %) and clearance (CV: 39 %). This can be explained by untested covariates, such as concomitant use of CYP2D6 modulators⁽²⁾ and underlying renal impairment. An important difference with the previously published models is the estimate of the absorption rate constant k_a . Our high value can be explained by tablet crunching and administration through nasogastric tubes in some of the patients who were in intensive care unit (ICU) or unable to swallow the tablets. However, this information was not consistently collected and could therefore not be adequately tested during the covariate analysis.

2.3 Model validation

All the parameters were adequately estimated as supported by the bootstrapped distributions shown in Figure 2.4. The bootstrap medians and confidence intervals at 95% are reported in Table 2.2 along with the parameter estimations and the shrinkages provided by NONMEM. Observe that the latter are quite high. The model adequately fits the observed data, as shown by the basic goodness-of-fit plots (Figure 2.5(a-d)), the NPDEs plots (Figure 2.5(e-f)), and the pcVPCs with binning on time based on 1000 simulations of the model building dataset (Figure 2.6).

The predictive performances of our model are confirmed on additional (external) data from 8 patients, collected as part of standard of care and not used for model building (Figure 2.7).

⁽²⁾HCQ is partly metabolized by CYP enzymes (Lee et al. (2016)) and CYP2D6 modulators are drugs able to either stimulate or inhibit the production of CYP2D6.

Table 2.2 – PopPK model of hydroxychloroquine: parameter estimates

Parameter	Estimate	bootstrap [median (95% CI)] ^a	shrinkage [%]	Corresponding estimated value in Carmichael et al. (2003)
k_a (h ⁻¹)	9.30	7.31 (1.81-9.44)		0.765
IIV on k_a [ω^2]	ne			0.94
V (L)	861	869 (679-1130)		605
IIV on V [ω^2]	0.272	0.257 (0.129-0.385)	27.6	0.25
CL (L/h)	15.7	15.4 (12.1-17.6)		9.89
WT effect on CL [θ_{WT}] ^b	1.38	1.40 (0.563-2.52)		-
IIV on CL [ω^2]	0.149	0.129 (0.0384-0.215)	23.3	0.127
F	0.746	<i>fixed</i>		0.746
IIV on CL [ω^2]	ne			0.004
T_{lag} (h)	ne			0.445
IIV on T_{lag} [ω^2]	ne			ne
Eprop plasma conc. [σ_p^2]	0.0286	0.0280 (0.0096-0.0455)	40.7	0.044
Eadd plasma conc. [σ_a^2]	ne			0.000365

^a Median of the bootstrapped distributions generated from 300 resampled datasets and confidence interval based on the 2.5th and 97.5th percentiles

^b Allometric covariate model, normalized to a WT of 80 kg

ne, not estimated; k_a , absorption rate constant; V , volume of distribution; CL , clearance; F , bioavailability; T_{lag} , lag time; IIV, interindividual variability; ω^2 , variance of the related random variable; WT, weight; Eprop, proportional error; $\sigma_{p,a}^2$, variances of the related random variables.

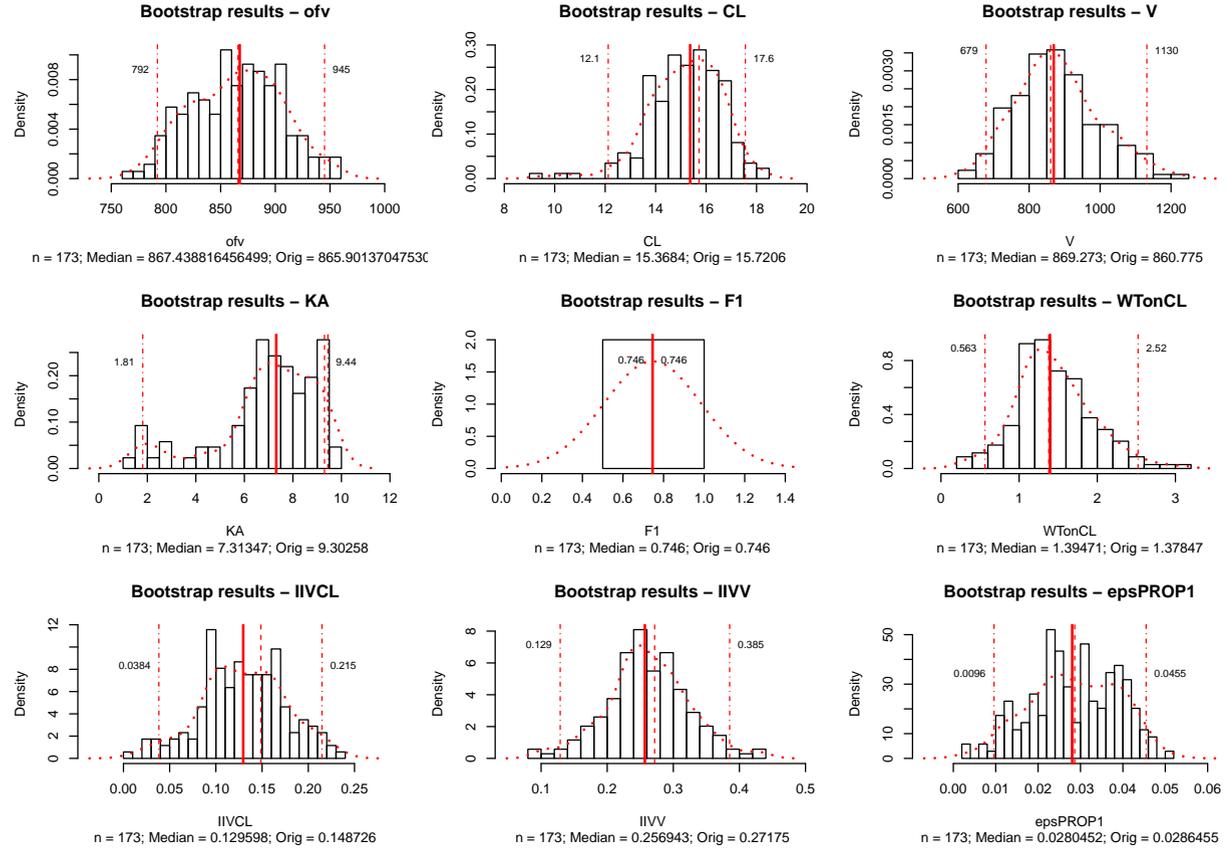


Figure 2.4 – Bootstrapped distribution of the model parameters

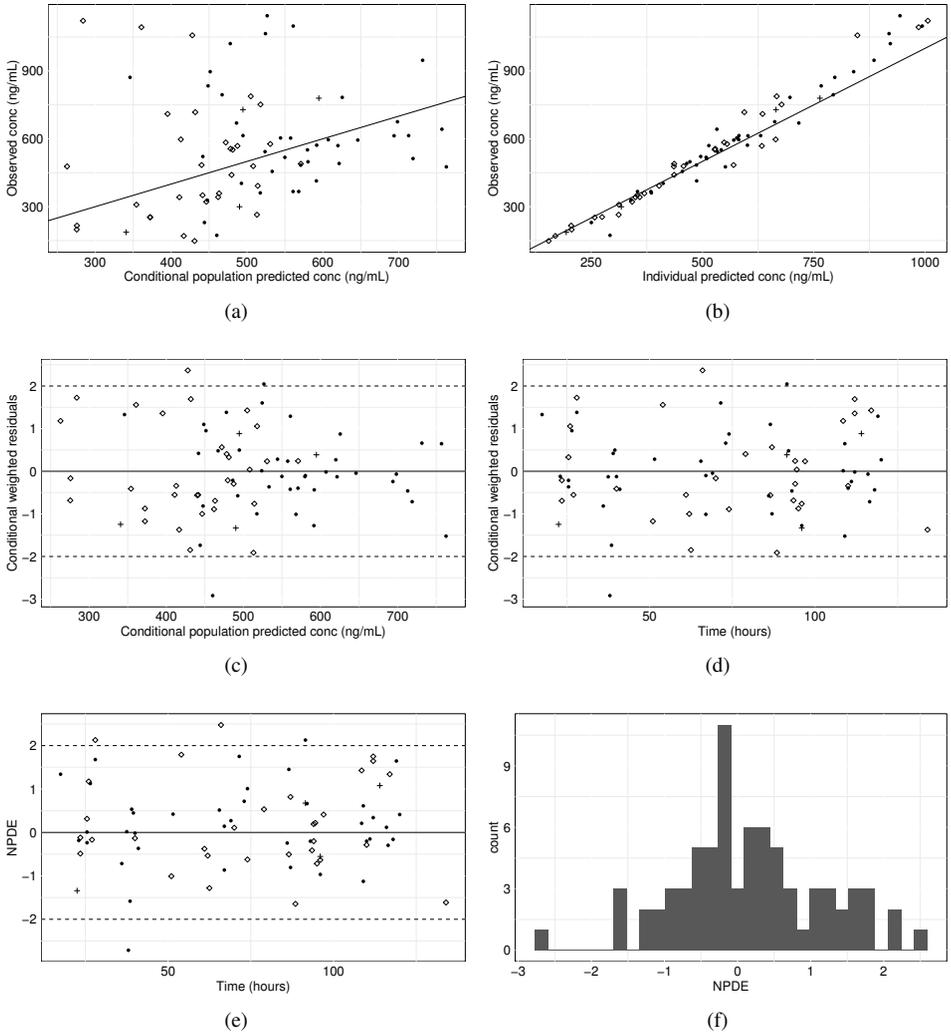


Figure 2.5 – Basic goodness-of-fit plots and normalized prediction distribution errors (NPDEs) plots. **(a)-(b)** Observations vs. population predictions and individual predictions; **(c)-(d)** residuals vs. population predictions and time; **(e)** NPDEs vs. time; **(f)** histogram of NPDEs. Filled circles, $WT \leq 80$ kg; open squares, $WT > 80$ kg; crosses, missing WT; solid lines are either the line of identity **(a,b)** or the line $x = 0$ **(c-e)**.

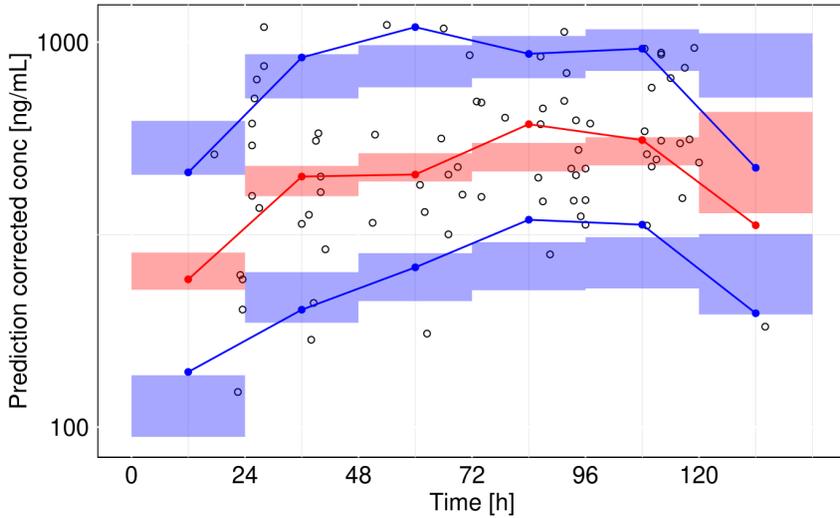


Figure 2.6 – Prediction-corrected VPC, with binning on time, of whole-blood concentrations. Width of each bin is 24 hours. Red and blue lines are the median and the 5th and 95th percentiles of the prediction-corrected observed concentrations in each bin. Red and blue areas are the simulation-based 90% confidence interval of the median and 5th and 95th percentiles in each bin. Open circles are the prediction-corrected observations.

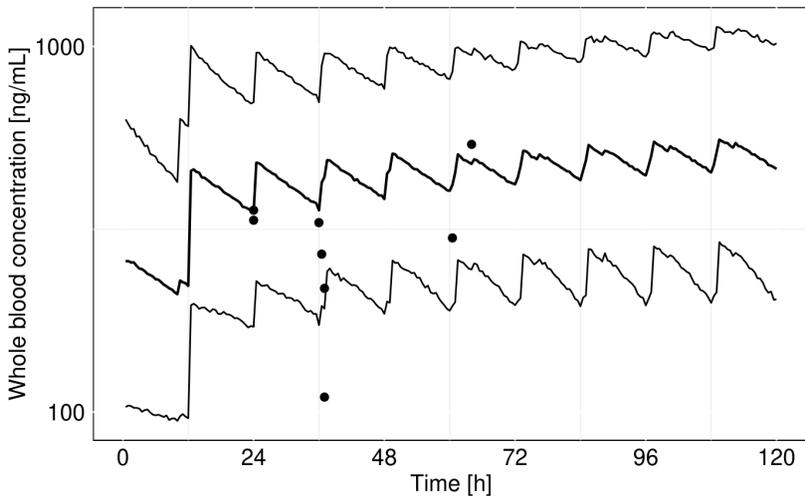


Figure 2.7 – Model predictions of HCQ blood concentrations for eight external patients (treated as part of standard of care). The lines represent the median and the 90% prediction interval. Points are the observations.

CHAPTER 3

Population pharmacokinetic model of temocillin in patients with pneumonia

This chapter aims to describe the population pharmacokinetics of temocillin administered via continuous or intermittent infusion in critically ill patients with pneumonia. The results presented in this chapter, along with the PTA analysis detailed in Chapter 5, are reported in N. Layios, C. Visée, P. Thémans, et al. (2021, submitted).

Temocillin (**Negaban**[®]) is a penicillin active against most Gram-negative microorganisms and Enterobacteriaceae, including extended spectrum β -lactamase-producing bacteria and some carbapenemase-producing bacteria (Kuch et al. (2020)). In the current era of increasing resistance to antibiotics, temocillin is an interesting alternative to carbapenems such as meropenem (see Chapter 4). According to the European Committee on Antimicrobial Susceptibility Testing (EUCAST) rationale document (EUCAST (2019)), temocillin is currently licensed in UK, Belgium, Luxembourg, France and Germany. It is mainly used for the treatment of serious infections caused by ESBL-producing Enterobacterales such as complicated urinary tract infection (UTI), bloodstream infection, and lower respiratory tract infection (LRTI), at a common dosage of 2g twice daily by intravenous infusion.

Previous pharmacokinetic studies of temocillin have been undertaken in healthy volunteers (Alexandre and Fantin (2018), Hampel et al. (1985)), in critically ill patients (De Joung et al. (2008), Laterre et al. (2015)), and in haemodialysis patients (Miranda Bastos et al. (2018) Vandecasteele et al. (2015)). . For the population analysis reported below, concentrations at the pulmonary site of infection are available. That will provides additional insight for establishing PK/PD breakpoint in pneumonia.

3.1 Study design and data

The concentrations of the model building dataset were collected as part of the single-center, open-label, randomized prospective TIC⁽¹⁾ study. This study was conducted in six intensive care units at the Centre Hospitalier Universitaire (CHU) du Sart-Tilman, Liège (Belgium) between March 2016 and February 2017. Patients were diagnosed with ventilator-associated pneumonia (VAP) or hospital-acquired pneumonia, and infected by a pathogen showing a sensitivity to temocillin ≤ 8 mg/L.⁽²⁾

Patients received temocillin by IV infusion either by intermittent infusion (II; 2g every 8h over 0.5h) or by continuous infusion (CI; 6g over 24h). The patient characteristics are summarized in Table 3.1. Thirty-one percent of the patients had augmented renal clearance (ARC), characterized by a creatinine clearance normalized to a body surface area of 1.73 m^2 ($Cl_{CR \text{ BSA}} > 120 \text{ mL/min/1.73m}^2$ (7/23 in the II versus 3/9 in the CI group, respectively).

Concentrations were measured in plasma (serum) and at the site of infection (epithelial lining fluid) after at least 24h of infusion in the CI group and at least three doses in the II group; they were supposed to be steady-state concentrations. ELF concentrations were measured by mini-bronchoalveolar lavage (mini-BAL). One mini-BAL was performed by patient, while between three and five plasma samples were collected per patient.

In the following PK analysis, we aim to describe the concentration of the free AB in plasma and the total AB in ELF. The protein level is much lower in ELF than plasma, such that the ELF protein binding is negligible (Kiem and Schentag (2008)). The observations are shown in Figure 3.1 (spaghetti plot for the plasma concentrations and scatter plot for the ELF concentrations). A high IIV can be observed in the plasma and ELF concentrations in both groups.

3.2 Population model building

A popPK model of temocillin was developed using a nonlinear mixed effects modeling approach with NONMEM program, version 7.4.3. The first-order conditional estimation method with interaction was used.

One- and two-compartment structural models were fitted to the free serum and total ELF concentrations. The interindividual variability in the PK parameters was estimated with the use of exponential models. Additive, proportional and mixed error models were tested to describe the residual variability. A full model approach was implemented for the covariate model building. Weight, body surface area (BSA), and creatinine clearance (Cl_{CR}) were tested as covariates on the volumes of distribution or clearance. Allometric functions were used for this purpose.

⁽¹⁾TIC stands for **T**emocillin **I**ntermittent versus **C**ontinuous

⁽²⁾MICs were first determined using the automated system Vitek-2®.

Table 3.1 – Demographic and clinical characteristics of the 32 patients included in the model building dataset

	All (N=32)	CI group (N=9)	II group (N=23)
Demographic and clinical data			
Age (years) mean±SD ^a	64.9 ± 11.4	66.1 ± 7.0	64.4 ± 12.8
Male N ^b (%)	24 (75.0)	8 (88.9)	16 (69.6)
Weight (kg) mean±SD	74.4 ± 13.7	75.6 ± 16.7	73.9 ± 12.8
BMI (kg/m ²) mean±SD	25.1 ± 4.6	25.1 ± 4.5	25.1 ± 4.7
Hospital stay before onset of pneumonia (days) mean±SD	15.6 ± 15.0	18.3 ± 13.9	14.5 ± 15.6
ICU stay before onset of pneumonia (days) mean±SD	10.3 ± 10.1	13.8 ± 12.9	9.0 ± 8.8
Simplified CPIS mean±SD	7.8 ± 1.0	8.1 ± 1.2	7.7 ± 0.93
SAPS III mean±SD	72.2 ± 12.7	74.8 ± 11.9	71.3 ± 13.2
SOFA score mean±SD	9.7 ± 3.3	10.0 ± 3.7	9.6 ± 3.2
APACHE II mean±SD	28.6 ± 8.6	28.3 ± 9.6	28.7 ± 8.4
Septic shock N (%)	12 (37.5)	5 (55.6)	7 (30.4)
Concomitant bacteraemia with the targeted bacteria N (%)	5 (15.6)	3 (33.3)	2 (8.7)
MDRD ^c N (%)			
> 60 mL/min	27 (84.4)	8 (88.9)	19 (82.6)
59-30 mL/min	5 (15.6)	1 (11.1)	4 (17.4)
Cl _{CR} (mL/min) ^d mean±SD	115.6 ± 51.7	119.2 ± 33.2	114.2 ± 58.0
>120 mL/min	14 (43.7)	6 (66.7)	8 (35.8)
90 – 119 mL/min	8 (25.0)	2 (22.2)	6 (26.1)
60 – 89 mL/min	3 (9.4)	0 (0.0)	3 (13.0)
30 – 59 mL/min	7 (21.9)	1 (11.1)	6 (26.1)
CVVH N(%)	0 (0.0)	0 (0.0)	0 (0.0)
Cl _{CR BSA} (mL/min/1.73m ²) ^e mean±SD	107.1 ± 49.4	112.2 ± 40.7	105.2 ± 53.2
In-hospital mortality N(%)	13 (40.6)	4 (44.4)	9 (39.1)
ICU mortality N(%)	8 (25.0)	3 (33.3)	5 (21.7)

^a SD, standard deviation^b N, Number of patients^c Estimation of the creatinine clearance using the MDRD formula^d Creatinine clearance based on 24h collection of urine^e Cl_{CR} normalized to a body surface area of 1.73 m²CI, continuous infusion; II, intermittent infusion; Cl_{CR}, creatinine clearance; BMI, body mass index; ICU, intensive care unit; MDRD, modification of diet in renal disease; CVVH, continuous veno-venous haemofiltration

CPIS, clinical pulmonary infection score; SAPS II, simplified acute physiology score; SOFA, sepsis-related organ failure assessment; APACHE, acute physiology and chronic health evaluation

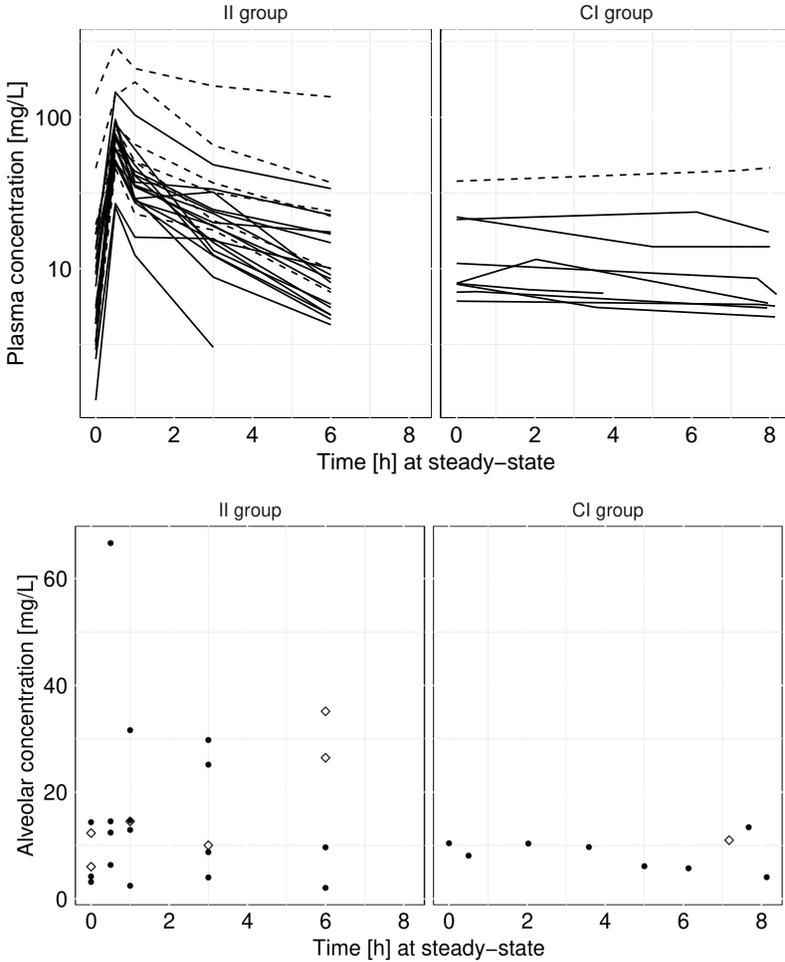


Figure 3.1 – Observed free and total concentration of temocillin in plasma and ELF, respectively, in the 32 patients included in the model building dataset. II, intermittent infusion; CI, continuous infusion. Solid lines and filled circles, $Cl_{CR} \geq 60$ mL/min; dashed lines and open squares, Cl_{CR} : 30-59 mL/min.

A two-compartment model best fitted the plasma concentrations and an additional compartment was added to describe the ELF concentrations. The structural model is schematically represented in Figure 3.2. Body surface area was retained as a significant covariate on the volumes of distribution of the central and additional ELF compartments whereas creatinine clearance (Cl_{CR}) was a significant covariate on total clearance. The PK parameters estimates, and related covariates and IIV are summarized in Table 3.2. The number of significant digits in the final estimations is 3.4, i.e., between the last two iterations of the estimation algorithm, none of the parameters differed in the first 3 significant digits.

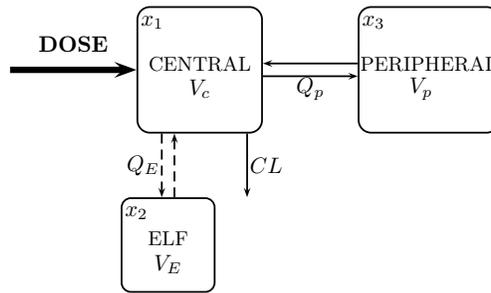


Figure 3.2 – Schematic representation of a (2+1)-compartment population pharmacokinetic model. CL , clearance; V_c , volume of distribution of the central compartment; Q_E , inter-compartmental clearance between the central and ELF compartments; V_E , volume of distribution of the ELF compartment; Q_p , inter-compartmental clearance between the central and peripheral compartments; V_p , volume of distribution of the peripheral compartment.

Using (1.3.8), the ELF-to-plasma penetration ratio is given by

$$K_t = \frac{usv_2}{usv_1} = 0.712$$

which is in line with the penetration ratio calculated on the basis of Monte Carlo simulations and derived steady-state AUC_{0-24} in N. Layios, C. Visée, P. Thémans, et al. (2021, submitted).

3.3 Model internal validation

The bootstrap confidence intervals at 95% are reported in Table 3.2 along with the parameter estimations and the standard error of estimates provided by NONMEM. We observe that the model seems to be overparametrized. Indeed, the covariate BSA on the volume of distribution is not supported by the data (high RSE and bootstrap CI that crosses 0). Nevertheless, this covariate was retained in the model for physiological considerations, based on previous PK analyses; see, e.g., Miranda Bastos et al. (2018)

Vandecasteele et al. (2015), where the body weight is identified to affect the clearance. Statistical analyses (based on the LRT) led us to include BSA, instead of WT, as a covariate in our own population model of temocillin.

Diagnostic scatter plots, based on model predictions and residuals, are displayed in Figure 3.3. They indicate adequate fitting performances of the model, as well as the VPC in Figure 3.4.

Table 3.2 – PopPK model of temocillin: parameter estimates

Parameter	Estimate	%RSE ^a	bootstrap 95% CI ^b
CL (L/h)	15.9	10.1	13.4 - 19.5
Cl _{CR} effect on CL [$\theta_{Cl_{CR}}$] ^(c)	1.04	24.3	0.487 - 1.57
IIV on CL [ω_{CL}^2 (%CV)]	0.290 (53.9)	21.9	0.146 - 0.395
V_c (L)	24.3	14.0	8.35 - 30.4
BSA effect on V _c [θ_{BSA}] ^(d)	1.56	49.4	-0.326 - 3.42
IIV on V _c [$\omega_{V_c}^2$ (%CV)]	0.289 (53.8)	34.6	0.967 - 1.20
Q_E (L/h)	38.5	22.8	24.4 - 124
V_E (L)	21.5	24.0	13.3 - 36.3
BSA effect on V _E [θ_{BSA}] ^(d)	4.46	59.1	0.574 - 12.5
IIV on V _E [$\omega_{V_E}^2$ (%CV)]	0.423 (65.0)	47.8	0.0776 - 0.976
Q_p (L/h)	4.75	12.2	3.29 - 10.7
V_p (L)	35.3	60.5	11.2 - 56200
usv_E (V _E /S _E)	712	12.1	649 - 913
Eprop plasma conc. [σ_p^2]	0.0309	21.4	0.0146 - 0.0407
Eadd plasma conc. [σ_a^2]	0.495	39.4	0.0424 - 1.39
Eprop ELF conc. [σ_p^2]	0.421	20.8	0.253 - 0.588

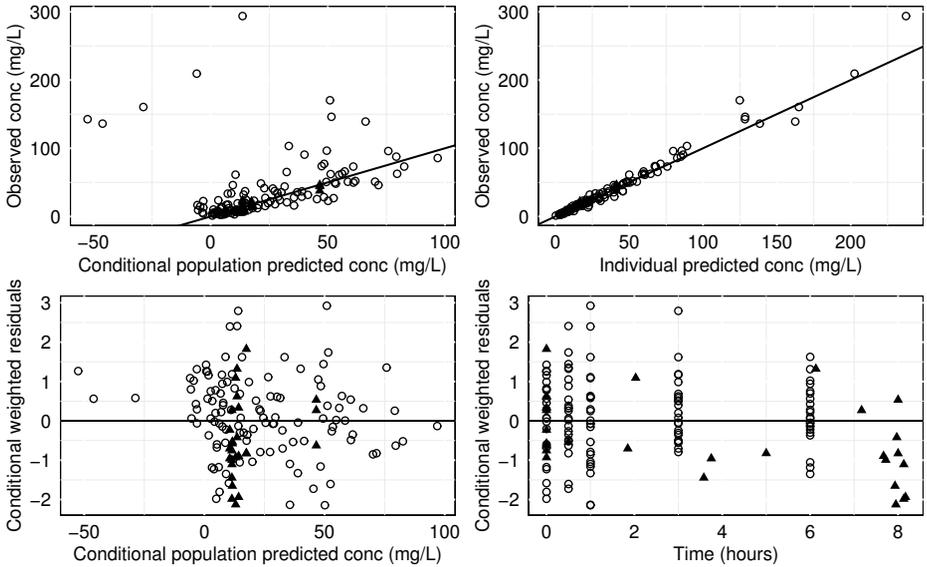
^a relative standard error of estimates

^b confidence interval based on the 2.5th and 97.5th percentiles of the bootstrapped distributions generated from 1000 resampled datasets

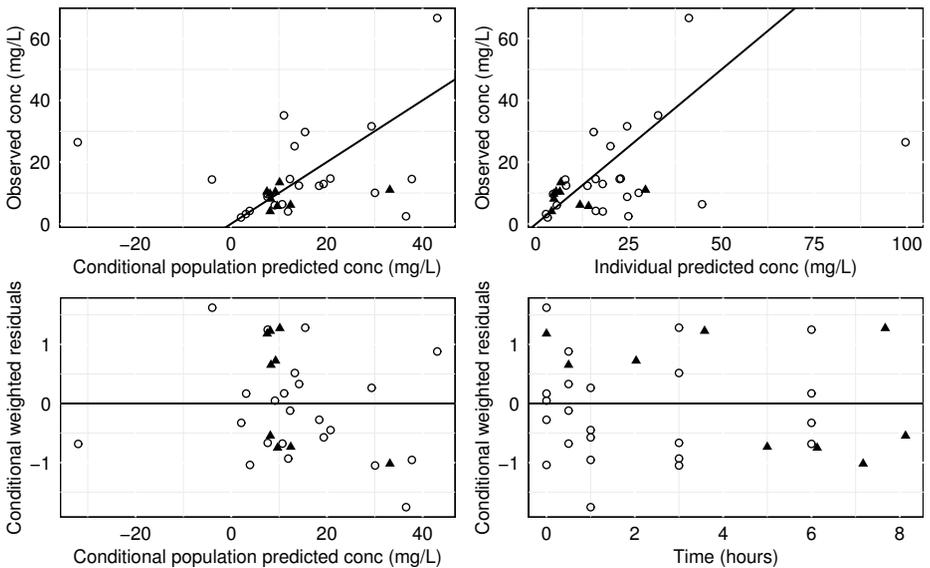
^c Allometric covariate model, normalized to a Cl_{CR} level of 117 mL/min

^d Allometric covariate model, normalized to a BSA of 2 m²

CL, clearance; Cl_{CR}, creatinine clearance based on 24h collection of urine; V_c, volume of distribution of the central compartment; BSA, body surface area; Q_E, inter-compartmental clearance between the central and ELF compartments; V_E, volume of distribution of the ELF compartment; Q_p, inter-compartmental clearance between the central and peripheral compartments; V_p, volume of distribution of the peripheral compartment; IIV, interindividual variability; ω_a^2 , variance of the related random variable; usv; unitless scalar value; S, scaling factor; Eprop, proportional error; Eadd, additional error, $\sigma_{p,a}^2$, variances of the related random variables.

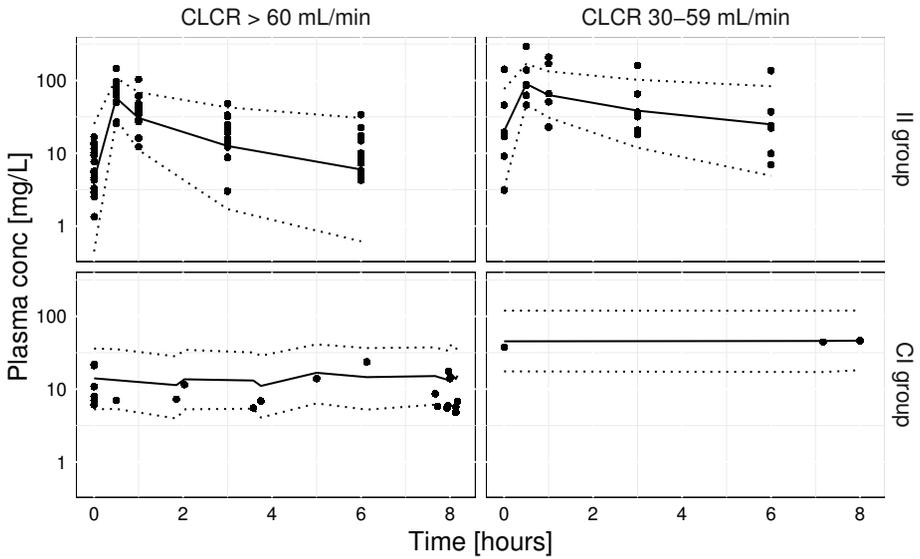


(a) Free plasma concentrations

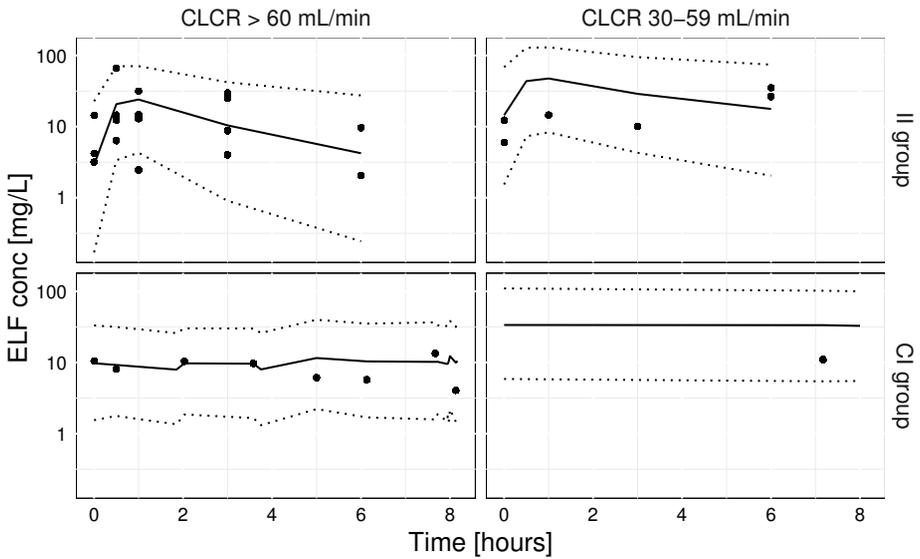


(b) Total ELF concentrations

Figure 3.3 – Basic goodness-of-fit plots. Observations vs. population predictions and individual predictions; residuals vs. population predictions and time. Open circles correspond to intermittent infusion (2g/8h over 0.5h-infusion); filled triangles correspond to continuous infusion (6g/24h). Solid lines are either the line of identity [upper rows] or the line $x = 0$ [lower rows].



(a) Free plasma concentrations



(b) Total ELF concentrations

Figure 3.4 – Visual predictive checks. Solid lines are the medians. Dotted lines correspond to the 90 % prediction intervals. Filled circles are the observed concentrations. II, intermittent infusion; CI, continuous infusion; CLCR, creatinine clearance.

Pharmacokinetic models of meropenem in patients with pneumonia

This chapter intends to develop both a population model and a physiologically based model of meropenem in patients with pneumonia. The physiologically based pharmacokinetic model presented in Section 4.3 was published in Thémans et al. (2019).

Meropenem (**Meronom**[®]) is a carbapenem with a broad antibacterial spectrum. It is a well-tolerated antibiotic with good organ and tissue penetration (see, e.g., Binder et al. (2013)), and can be used in the treatment of both Gram-positive and Gram-negative infections (EUCAST (2009)). It is used for the treatment of critical bacterial infections such as severe nosocomial pneumonia or sepsis (see, e.g., Mattioli et al. (2016) and Chow et al. (2018)). Meropenem is a time-dependent antibiotic like temocillin (see Chapter 3). In critically ill patients, it can be required to reach a $100\%T > MIC$ to ensure optimal clinical outcome (see, e.g., Goncalves-Pereira et al. (2014), Sime et al. (2015), and Burger et al. (2018)).

The pharmacokinetics of meropenem has already been studied in different populations, including paediatric patients (Du et al. (2006), Padari et al. (2012)), healthy volunteers (Krueger et al. (2005)), (noninfected) morbidly obese patients (Wittau et al. (2015)), patients with various degrees of renal functions (Chimata et al. (1993)), and patients with severe bacterial infection and/or sepsis (Li et al. (2006), Karjagin et al. (2008), Lodise et al. (2011), Binder et al. (2013), Goncalves-Pereira et al. (2014), Fripiat et al. (2015), Jaruratanasirikul et al. (2015), Kees et al. (2016), Mattioli et al. (2016), Sjövall et al. (2018), and Burger et al. (2018)).

There is a lack of consensus regarding the dosing of this drug in the scientific literature. The UK Medicines and Health Products Regulatory Agency (MHRA) recommends in their *Summary of Product Characteristics* the infusion of 500 mg or 1 g every 8 hours (every 12 hours for patients with renal impairment) over 15-30

minutes as common dosage (MHRA (2017)). Some publications report that alternative dosing regimens have been found to be more (cost-)effective in clinical practice: Some authors compared the PD and clinical outcomes of the traditional dosing to a smaller dose with shorter interval (see Perrott et al. (2010) and Chow et al. (2018)), whereas other publications state that a better PK profile (higher %T>MIC) is obtained by extended or continuous infusion (see, e.g., Veiga and Paiva (2018) and Gonçalves-Pereira and Póvoa (2011)).

4.1 Patient data

Data from five published models of meropenem were used for model development and validation (Fripiat et al. (2015), Lodise et al. (2011), Karjagin et al. (2008), Li et al. (2006) and Chimata et al. (1993)). Patient characteristics are summarized in Table 4.1. The data from the PROMESSE⁽¹⁾ study (Fripiat et al. (2015)) were available at patient level and used for model building. The four other studies were used for external validation.

Patients included in the model building dataset were diagnosed with severe nosocomial pneumonia. They received meropenem by IV infusion either by intermittent infusion (II; 1g every 8h over 0.5h) or by extended infusion (EI; 1g every 8h over 3h). The observed concentrations consist of plasma and (sparse) ELF samples and are shown in Figure 4.1. They are supposed to be steady-state concentrations. The studies by Karjagin et al. (2008) and Chimata et al. (1993) provided the relevant patients' characteristics, namely the weight and the creatinine clearance, at patient level. In the studies by Lodise et al. (2011) and Li et al. (2006), the demographic characteristics were presented at a summary level. In that case, we derived a set of individual patients using online databases from the National Health and Nutrition Examination Survey (see NHANES (2005-2006)), taking into account the proportion of males and females and the range of the different variables as described by the authors.

Data from an additional publication (Wittau et al. (2015)) were used to investigate the predictive performances of the PBPK model in morbidly obese patients. Patient characteristics are also reported, at a summary level, in Table 4.1. Given that the patients' characteristics were not reported at individual level in the publication, we generated a set of virtual patients, that matched the summary-level characteristics, using the population tab of Simcyp (Certara Inc., Princeton, NJ, USA). Simcyp virtual populations are created based on real patient populations; the actual covariance structure between patients' characteristics in the population is therefore conserved in the simulations. This very different population with regard to body weight distribution is presented as an extrapolation group, compared to the other available data.

⁽¹⁾PROMESSE stands for **PRO**toocol **ME**roopenem **S**tady **S**tate **E**valuation.

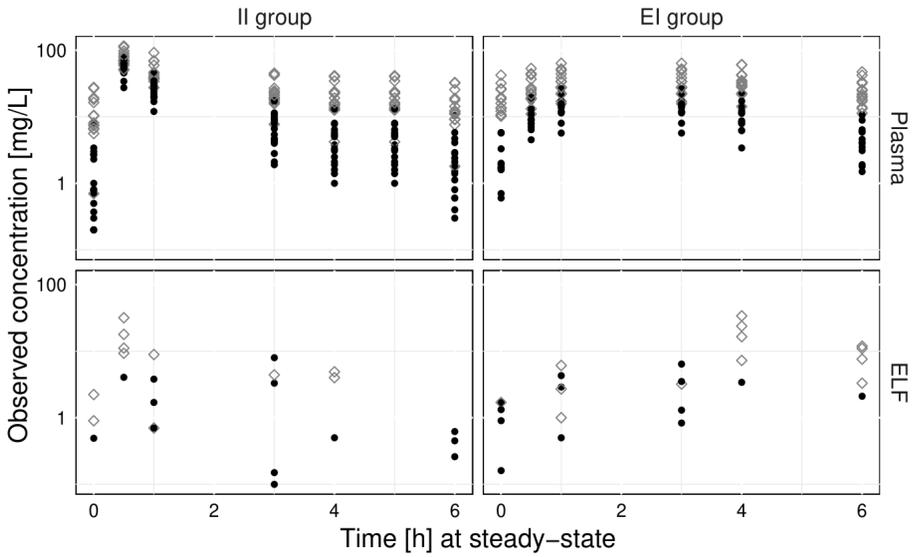


Figure 4.1 – Observed plasma and ELF meropenem concentrations in the 60 patients included in the model building dataset. Filled circles, GFR > 60 mL/min; open squares, GFR < 60 mL/min.

Table 4.1 – Demographic information from previously published studies

	Model building dataset		(External) validation datasets			Extrapolation dataset	
	Frippiat et al. (2015)		Lodise et al. (2011)	Karjagin et al. (2008)	Li et al. (2006)	Chimata et al. (1993)	Wittau et al. (2015)
	II group (n = 33)	EI group (n = 27)	(n = 39)	(n = 4)	(n = 79)	(n = 13)	(n = 5)
Type of patients	Severe nosocomial pneumonia (HAP or VAP)		Ventilator-associated pneumonia (VAP)	Severe peritonitis associated with septic shock	Intra-abdominal infections, community-acquired pneumonia, or VAP	Various degrees of renal impairment	Hospitalized morbidly obese patients
Sex (male/female)	11/22	8/19		3/1	61/18	5/8	2/3
Age (years)	15–18	41–84	20–85	52–81	18–93	30–76	31–49
Height (cm)			144–185		147–185.4		155–190
Weight (kg)	49–128	45–108	46–140	50–70	40.6–127	34–85	116–203
BSA (m ²)							2.23–3.19
GFR (mL/min)	19–401*	20–212*					
Serum creatinine (μmol/L)				47–123	35.37–610.1	44.21–618.94	64–80
Creatinine clearance (mL/min)				30–135		4.3–68.0	

The values are presented with the range.

BSA, body surface area.; GFR, glomerular filtration rate.

* GFR calculated according to the four-variable Modification of Diet in Renal Disease formula or by measurement of creatinine clearance based on 24h urine.

4.2 Population model

4.2.1 Model building

A nonlinear mixed effects modeling approach was used and model parameters were estimated using the NONMEM program, version 7.3.0. The first-order conditional estimation method with interaction was used. A two-compartment model provided an adequate fit to the observed plasma concentrations. An additional *dummy* compartment was added to describe the (sparse) available data in the site of infection (ELF) (see Figure 3.2).

Based on known physiological relationships and a previously published model (Fripiat et al. (2015)), two covariates were considered and retained in the model: the weight on the volumes of distribution and the renal function (quantified by the glomerular filtration rate (GFR)) on the clearance. An allometric model was used to describe the influence of continuous variables on the PK parameters. The weight was not a statistically relevant covariate, but has been retained in the model as a covariate because of its clinical relevance.

The model parameter estimates are reported in Table 4.2. The number of significant digits in the final estimations is 3.6, i.e., between the last two iterations of the estimation algorithm, none of the parameters differed in the first 3 significant digits. The high unexplained variability on the ELF volume of distribution may be due to the scarcity of observations and technical factors in the method of measurement (BAL, see Kiem and Schentag (2008)).

4.2.2 Model evaluation

Internal validation

The precision of the estimations were evaluated by the bootstrapped distribution of the model parameters. Satisfactory bootstrap CI are reported in Table 4.2 along with the standard error of estimates computed by NONMEM. Goodness-of-fit plots and VPCs are presented in Figures 4.2 and 4.3, respectively. The absence of inadequate trends in the displayed GOF plots and an acceptable agreement between the predicted and observed data over the dosing interval in the VPC, for both plasma and ELF concentrations, indicate adequate fitting performances of the model to the data.

Table 4.2 – PopPK model of meropenem: parameter estimates

Parameter	Estimate	%RSE ^a	bootstrap 95% CI ^b
CL (L/h)	7.94	4.95	7.34 - 8.54
GFR effect on CL [θ_{GFR}] ^(c)	0.722	8.82	0.581 - 0.816
IIV on CL [ω^2 (%CV)]	0.126 (35.5)	18.8	0.0817 - 0.157
V_c (L)	13.6	6.26	11.5 - 15.4
WT effect on V _c [θ_{WT}] ^(d)	0.949	30.1	0.609 - 1.68
IIV on V _c [ω^2 (%CV)]	0.140 (37.4)	33.6	0.0827 - 0.235
Q_E (L/h)	6.73	18.3	4.02 - 14.4
V_E (L)	4.08	33.3	1.17 - 5.87
WT effect on V _E [θ_{WT}] ^(d)	1.04	114	-5.39 - 3.02
IIV on V _E [ω^2 (%CV)]	1.76 (133)	41.1	0.909 - 4.89
Q_p (L/h)	8.22	18.3	5.70 - 11.5
IIV on Q _p [ω^2 (%CV)]	0.187 (43.2)	56.1	0.0206 - 0.349
V_p (L)	10.1	15.5	7.75 - 13.5
usv_E (V _E /S _E)	249	9.68	233 - 324
Eprop plasma conc. [σ_p^2 (%CV)]	0.0240 (15.5)	11.8	0.0170 - 0.0292
Eadd plasma conc. [σ_a^2 (mg/L)]	0.208 (0.456)	32.5	0.114 - 0.379
Eprop ELF conc. [σ_p^2 (%CV)]	0.404 (63.6)	21.3	0.254 - 0.547

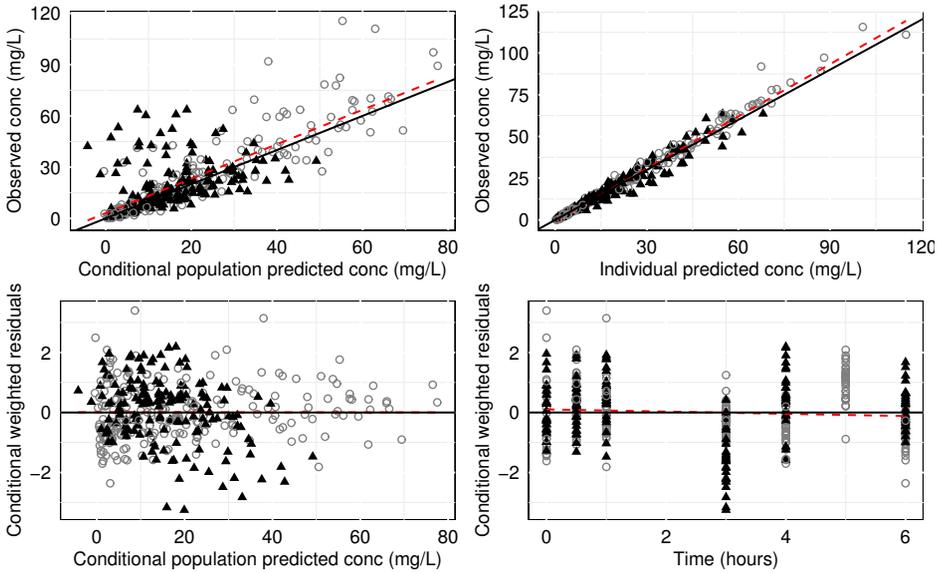
^a relative standard error of estimates

^b confidence interval based on the 2.5th and 97.5th percentiles of the bootstrapped distributions generated from 1000 resampled datasets

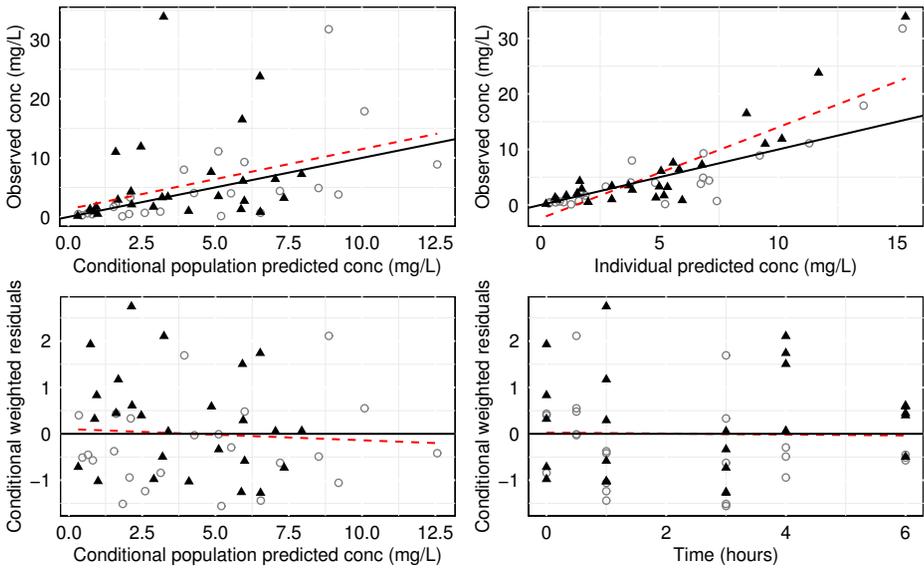
^c Allometric covariate model, normalized to a GFR level of 65 mL/min

^d Allometric covariate model, normalized to a body weight of 75 kg

CL, clearance; GFR, glomerular filtration rate; V_c, volume of distribution of the central compartment; WT, body weight; Q_E, inter-compartmental clearance between the central and ELF compartments; V_E, volume of distribution of the ELF compartment; Q_p, inter-compartmental clearance between the central and peripheral compartments; V_p, volume of distribution of the peripheral compartment; IIV, interindividual variability; ω^2 , variance of the related random variable; usv; unitless scalar value; S, scaling factor; Eprop, proportional error; Eadd, additional error; $\sigma_{p,a}^2$, variances of the related random variables.

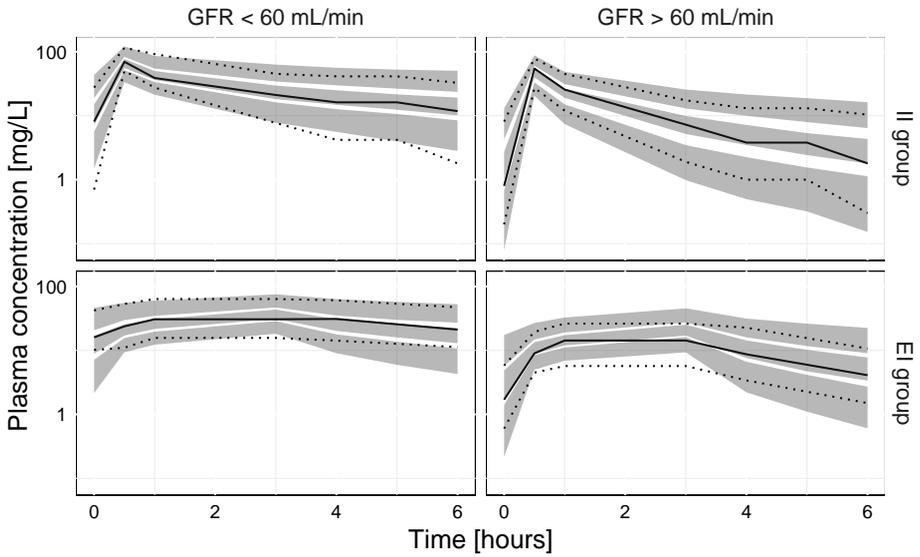


(a) Plasma concentrations

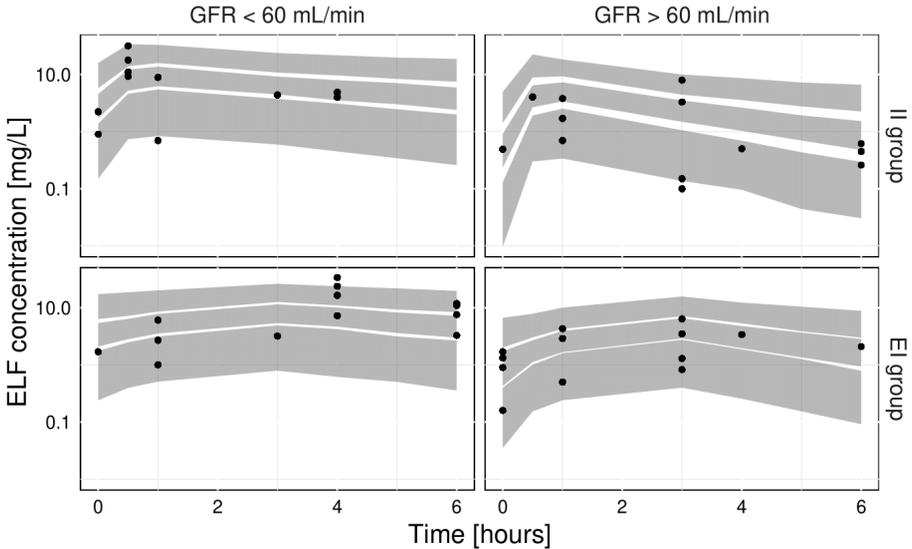


(b) ELF concentrations

Figure 4.2 – PopPK model of meropenem: basic goodness-of-fit plots. Open circles, intermittent infusion (over 30 min); filled triangles, extended infusion (over 3 hours). Dashed red lines are the linear regression lines. Solid lines are either the line of identity [upper rows] or the line $x = 0$ [lower rows]



(a) Plasma concentrations



(b) ELF concentrations

Figure 4.3 – PopPK model of meropenem: visual predictive checks. Grey areas are the 90% confidence intervals of the median and the 5th and 95th percentiles. Continuous and dotted lines correspond to the median and the 5th and 95th percentiles of the observations in plasma [(a)]; filled circles are the observations in ELF [(b)]. II, intermittent infusion; EI, extended infusion; GFR, glomerular filtration rate.

External validation

The results of external validation on data from independent patients with severe infections (Karjagin et al. (2008), Lodise et al. (2011), Li et al. (2006)) were also overall acceptable and are shown in figures 4.4, 4.5, and 4.6. Either the creatinine clearance values were used for the GFR model covariate or GFR was computed using the Modification of Diet in Renal Disease formula (MDRD) formula from the serum creatinine (Levey et al. (2000)). It should be noted that observed data were not reported in the publication by Lodise et al. (2011), but the authors performed simulations of concentration-time profiles in plasma and ELF. Figures A.1(a)-(d) of Appendix A provide individual plots for the Karjagin et al.'s patients. Separated plots for each dosing regimen reported in Li et al. (2006) are also provided in Figures A.2(a)-(f).

Figure 4.7 shows the predictions for the patients taken from Chimata et al. (1993) and allocated to three groups: group 1 (four patients with $CL_{CR} \geq 50$ mL/min), group 2 (four patients with $30 \text{ mL/min} \leq CL_{CR} \leq 50$ mL/min) and group 3 (five patients with $CL_{CR} \leq 30$ mL/min). Simulations display good agreement between observed and predicted concentrations, especially in groups 2 and 3. Figures A.3(a)-(c) of Appendix A provide the separated plots for each group.

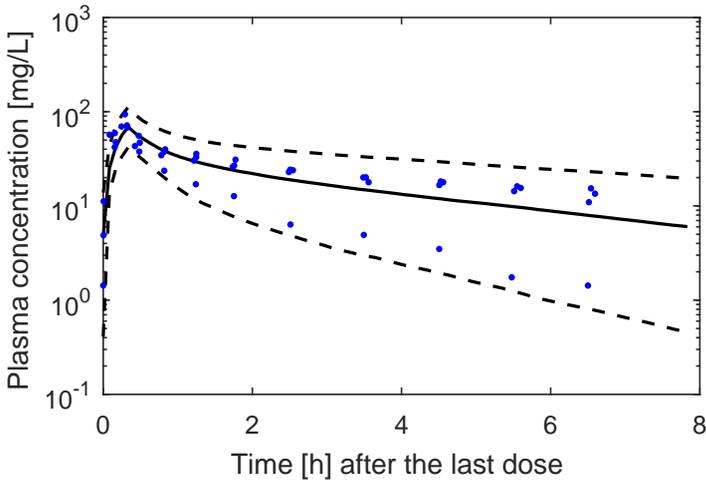
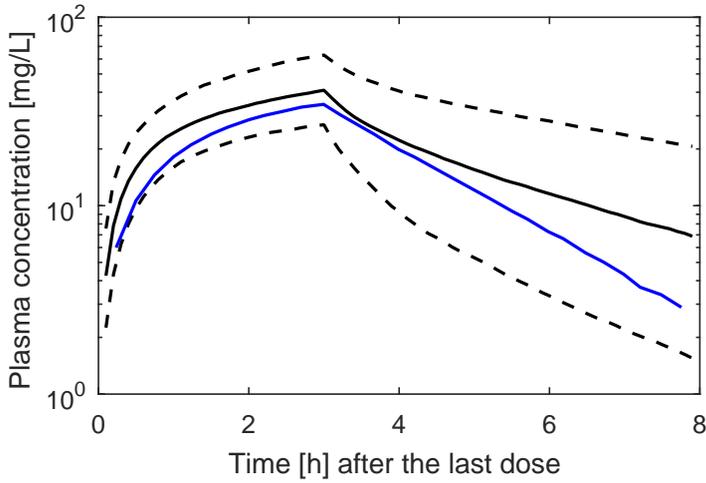
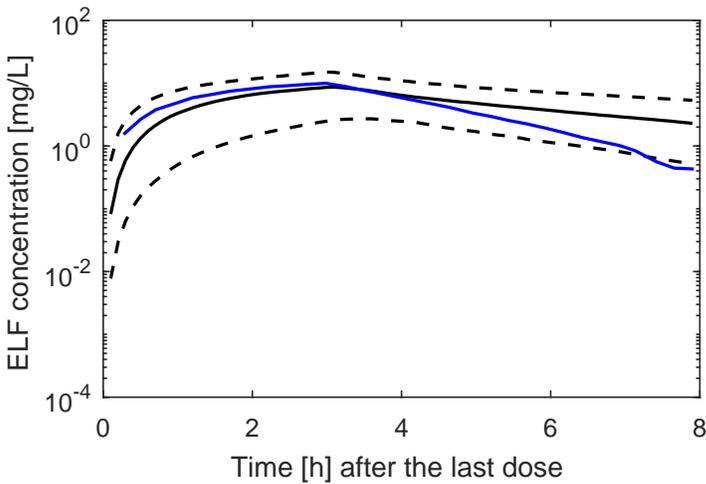


Figure 4.4 – PopPK model of meropenem: simulated plasma PK profiles (median and 90% PI) for 500 replicates of four of the patients described in Karjagin et al. (2008). Dosage of 1g every 8h over a 20min-infusion. Points are the observed plasma concentrations in Karjagin et al. (2008). Time is time after the second dose.



(a) plasma concentrations



(b) ELF concentrations

Figure 4.5 – PopPK model of meropenem: simulated **(a)** plasma and **(b)** infection-site PK profiles (median and 90% PI) for 1000 patients from the NHANES databases and consistent with the the study design of Lodise et al. (2011). Dosage of 2g over a 3h-infusion. Blue lines are the digitized simulated concentration-time profiles in Lodise et al. (2011). Time is time after the first dose.

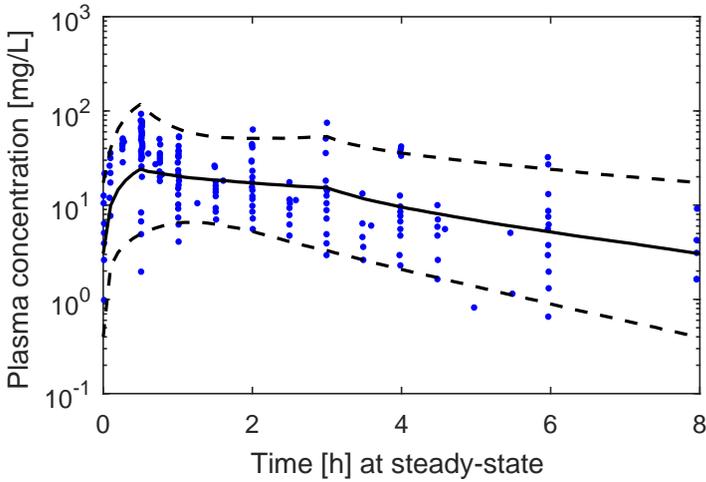


Figure 4.6 – PopPK model of meropenem: simulated steady-state plasma PK profiles (median and 90% PI) for 1000 patients from the NHANES databases and consistent with the study design of Li et al. (2006). Simulation of 6 different dosing regimens: 0.5, 1 or 2 g every 8h over a 30min- or 3h-infusion. Points are the observed plasma concentrations in Li et al. (2006).

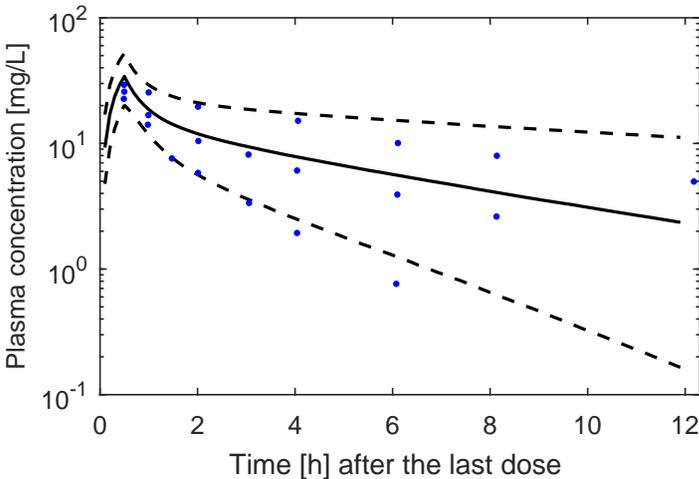


Figure 4.7 – PopPK model of meropenem: simulated plasma PK profiles (median and 90% PI) for 1000 replicates of the 13 patients described in Chimata et al. (1993). Dosage of 0.5g over a 30min-infusion. Points are (the medians of) the observed plasma concentrations in the three groups. Time is time after the first dose.

4.3 Physiologically based model

4.3.1 Structural model

The reduced PBPK model of meropenem consists of six compartments including three organs (lungs/site of infection, kidneys and liver), and two blood compartments to distinguish arterial and venous blood. All the other tissues and organs (stomach, spleen, intestine, heart, muscles, bones...) are lumped together in one compartment called “rest of the body”. The model is built on physiological considerations and includes realistic organ blood flows and organ volumes, obtained from the literature in Jones et al. (2006) and reported in Table 4.3. The compartments representing the different organs and tissues are connected in parallel between those representing the arterial and venous blood. As detailed on page 23, the systemic circulation provides arterial blood supply to all organs and tissues, and blood from the tissues flows into the venous pool. The lung compartment closes the circulation loop in the model and receives venous blood at a flow rate equal to that of the cardiac output (pulmonary circulation). The architecture of the structural PBPK model is schematized in Figure 4.8.

In the model, the organs are represented as single well-mixed compartments and the distribution of meropenem is assumed to be perfusion rate limited (in contrast to permeability rate limited, see, e.g., Jones and Rowland-Yeo (2013) and (Rowland and Tozer, 2011, Fig. p. 87)). In line with the known pharmacology of meropenem (see MHRA (2017)), the elimination of meropenem is modeled as occurring in the kidneys and the liver. Renal elimination is assumed to represent approximately 70% of total clearance. Non-renal clearance is assumed to be entirely hepatic (metabolism by hydrolysis). Other tissues are assumed to have no effect on the drug clearance. The intravascular administration is assumed to be intra-arterial in the modeling approach presented here.

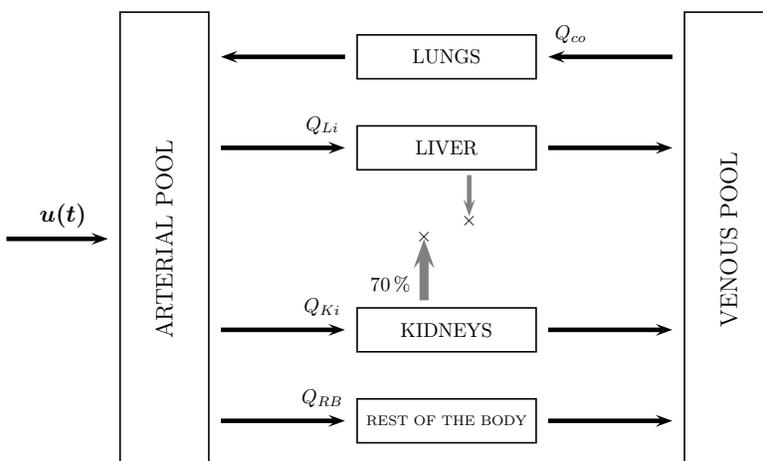


Figure 4.8 – Schematic representation of the physiologically based pharmacokinetic model of meropenem

Table 4.3 – Physiological parameters used in the model, taken from Jones et al. (2006)

Organ/tissue	Volume ^a	Blood flow rate ^a
Arterial blood	0.0257	-
Lungs	0.0076	1
Venous blood	0.0514	-
Liver	0.0257	0.25 ^b
Kidneys	0.0044	0.19
“Rest of the body”	$WT - V_a - V_{Lu} - V_v - V_{Li} - V_{Ki}$	$CO - Q_{Li} - Q_{Ki}$

^a Volumes and blood flow rates are expressed as a fraction of total body-weight (WT) and cardiac output (CO), respectively

^b The blood flow of the liver is the sum of the blood flows of the portal vein and the hepatic artery

The affinity of each tissue for the drug is modeled by a *tissue-to-plasma partition coefficient* K_p , which is defined by the ratio of the organ concentration to the efferent plasma concentration, i.e.,

$$c_t = K_p \cdot c_p$$

where c_t and c_p stand for the concentrations in the tissue/organ and in the efferent plasma. The mathematical description of this model consists in a mass balance equation for each compartment:

1. *Non-eliminating organs and tissues* (lungs and rest of the body)

$$V_{RB} \frac{dc_{RB}}{dt} = Q_{RB} \left(c_a - \frac{c_{RB}}{K_{pRB}} \right)$$

and

$$V_{Lu} \frac{dc_{Lu}}{dt} = Q_{co} \left(c_v - \frac{c_{Lu}}{K_{pLu}} \right)$$

where c_a and c_v represent the drug concentration in the arterial and venous compartments, respectively, c_{Lu} and c_{RB} denote the global drug concentration in the lungs and the “rest of the body”, respectively, V_{Lu} and V_{RB} are the corresponding volumes, Q_{co} and Q_{RB} are the cardiac output (blood flow rate of the lungs) and the blood flow rate of the rest of the body, and K_{pLu} and K_{pRB} denote the partition coefficients between the lung and the rest of the body (resp.) and the efferent plasma.

2. *Eliminating organs* (an additional term is needed to describe the elimination process)

$$V_{Li} \frac{dc_{Li}}{dt} = Q_{Li} \left(c_a - \frac{c_{Li}}{K_{pLi}} \right) - CL_H \frac{c_{Li}}{K_{pLi}}$$

and

$$V_{Ki} \frac{dc_{Ki}}{dt} = Q_{Ki} \left(c_a - \frac{c_{Ki}}{K_{pKi}} \right) - CL_R \frac{c_{Ki}}{K_{pKi}}$$

where c_{Li} and c_{Ki} represent the drug concentration in the liver and the kidneys, respectively, V_{Li} and V_{Ki} are the corresponding volumes, Q_{Li} and Q_{Ki} are the blood flow rates of the liver and the kidneys, respectively, CL_R and CL_H are the renal and hepatic clearances, and K_{pLi} and K_{pKi} denote the partition coefficients between the liver and the kidneys (resp.) and the efferent plasma. We assume that the partition coefficients of the non-fat tissues (liver and kidneys) are equivalent/equal, as described in Pilari and Huisinga (2010).

3. Blood compartments

$$V_a \frac{dc_a}{dt} = Q_{co} \frac{c_{Lu}}{K_{pLu}} - Q_{co}c_a + u$$

and

$$V_v \frac{dc_v}{dt} = \sum_i Q_i \frac{c_i}{K_{pi}} - Q_{co}c_v$$

where $u(\cdot)$ represents the intravascular rate of infusion [g/h], and c_i denotes successively the drug concentration in the the liver, the kidneys and the rest of the body ($i \in \{Li, Ki, RB\}$).

These equations can be written in matrix notation by

$$\begin{cases} \dot{x}(t) = Ax(t) + bu(t) \\ y(t) = Cx(t) \end{cases} \quad t \geq 0 \quad (4.3.1)$$

where

$$A = \begin{pmatrix} -\frac{Q_{co}}{V_a} & \frac{Q_{co}}{K_{pLu}V_a} & 0 & 0 & 0 & 0 \\ 0 & -\frac{Q_{co}}{K_{pLu}V_{Lu}} & \frac{Q_{co}}{V_{Lu}} & 0 & 0 & 0 \\ 0 & 0 & -\frac{Q_{co}}{V_v} & \frac{Q_{Li}}{K_{pLi}V_v} & \frac{Q_{Ki}}{K_{pKi}V_v} & \frac{Q_{RB}}{K_{pRB}V_v} \\ \frac{Q_{Li}}{V_{Li}} & 0 & 0 & -\frac{Q_{Li} + CL_H}{K_{pLi}V_{Li}} & 0 & 0 \\ \frac{Q_{Ki}}{V_{Ki}} & 0 & 0 & 0 & -\frac{Q_{Ki} + CL_R}{K_{pKi}V_{Ki}} & 0 \\ \frac{Q_{RB}}{V_{RB}} & 0 & 0 & 0 & 0 & -\frac{Q_{RB}}{K_{pRB}V_{RB}} \end{pmatrix} \quad (4.3.2)$$

and

$$b = \begin{pmatrix} \frac{1}{V_a} & 0 & 0 & 0 & 0 & 0 \end{pmatrix}^T, \quad C = \begin{pmatrix} 1000 & 0 & 0 & 0 & 0 & 0 \\ 0 & 1000 & 0 & 0 & 0 & 0 \end{pmatrix} \quad (4.3.3)$$

where $CL_H + CL_R$ equals the total clearance (CL) and $CL_R = 0.7 \cdot CL$. The state vector $x = (c_a \ c_{Lu} \ c_v \ c_{Li} \ c_{Ki} \ c_{RB})^T \in \mathbb{R}^6$ corresponds to the drug concentration [g/L] in each compartment and the output vector $y = (y_1 \ y_2)^T \in \mathbb{R}^2$ represents the drug concentrations [mg/L] in the plasma and at the infection site.

4.3.2 System analysis

As the state variables of (4.3.1) represent concentrations of drug, it is expected that the state trajectories stay in the nonnegative orthant of \mathbb{R}^6 for all nonnegative initial conditions and nonnegative admissible input functions. Since A and b are Metzler and nonnegative matrices, respectively, it is indeed the case by Lemma 1.1.1, like the popPK system (see Proposition 1.3.1). Besides, as the popPK system, it is expected that the PBPK model is stable.

Proposition 4.3.1 The PBPK system given by (4.3.1)-(4.3.3) is nonnegative.

Proposition 4.3.2 The PBPK system given by (4.3.1)-(4.3.3) is internally (exponentially) stable.

Proof. Let the Lyapunov function defined, for all $x \in [0, \infty)^6$, by

$$L(x) = V^T x$$

where $V = (V_A \ V_{Lu} \ V_v \ V_{Li} \ V_{Ki} \ V_{RB})^T$ is the vector of the volumes. The Lyapunov function corresponds therefore to the total mass/amount of drug in the system. The conditions $L(0) = 0$ and $L(x) > 0$ for all $x \in [0, \infty)^6 \setminus \{0\}$ are easily verified since all the volumes are positive. Furthermore, the derivative along the zero-input state trajectories reads as

$$\begin{aligned} \dot{L}(x) &= V^T \dot{x} = V^T A x \\ &= -Q_{co} c_a + \frac{Q_{co}}{K_{pLu}} c_{Lu} - \frac{Q_{co}}{K_{pLu}} c_{Lu} + Q_{co} c_v - Q_{co} c_v + \frac{Q_{Li}}{K_{pLi}} c_{Li} + \\ &\quad \frac{Q_{Ki}}{K_{pKi}} c_{Ki} + \frac{Q_{RB}}{K_{pRB}} c_{RB} + Q_{Li} c_a - \frac{Q_{Li} + CL_H}{K_{pLi}} c_{Li} + \\ &\quad Q_{Ki} c_a - \frac{Q_{Ki} + CL_R}{K_{pKi}} c_{Ki} + Q_{RB} c_a - \frac{Q_{RB}}{K_{pRB}} c_{RB} \\ &= -\frac{CL_H}{K_{pLi}} c_{Li} - \frac{CL_R}{K_{pKi}} c_{Ki} \\ &= -c_v (CL_H + CL_R) \end{aligned}$$

using $CO = Q_{Li} + Q_{Ki} + Q_{RB}$ and the definition of the tissue-to-plasma partition coefficients $K_{p\bullet}$. For any positive initial condition $x_0 > 0$, $\dot{L}(x)$ is negative along the state trajectory. In fact, it turns out that the resolvent function $(sI - A)^{-1}$ has non-zero entries on the third row, ensuring the positivity of the corresponding entries of e^{At} for all $t > 0$, since the nonnegativity is guaranteed by the Metzler property of A (see Proposition 1.1.2). Hence the matrix A is stable (by the proof of (Chellaboina et al., 2009, Proposition 7)). The numerators of the elements (3,1) to (3,6) of the matrix $(sI - A)^{-1}$ were computed using the Symbolic Math Toolbox of MATLAB and are reported in Appendix B. \square

4.3.3 Model parameter estimation

Total clearance and tissue-to-plasma partition coefficients were estimated by a “top-down” data-driven approach, using a mixed effects modeling to describe the interindividual variability. Moreover, the individual typical value of the total clearance $TVCL$ was assumed to be influenced by the renal function through an allometric relationship. Thus,

$$\begin{aligned} CL &= TVCL \cdot \exp(\eta) \\ &= \theta_{CL} \left(\frac{GFR}{GFR_{med}} \right)^{\theta_{GFR}} \cdot \exp(\eta) \end{aligned}$$

where $\eta \sim N(0, \omega^2)$. The parameter estimates of the reduced PBPK model are reported in Table 4.4. The number of significant digits in the final estimations is 2.6, i.e., between the last two iterations of the estimation algorithm, none of the parameters differed in the first 2 significant digits.

It should be noted that the organ volumes and organ blood flows are not consistently reported in previously published PBPK models, see, e.g., Nestorov et al. (1998) or Edginton et al. (2006). A sensitivity analysis, reported in Appendix C, was therefore performed and revealed that organ volumes and blood flows had little influence on the final model predictions.

The partition coefficients estimates indicate that, when target concentrations (MIC) are determined by *in vitro* evaluation, the dose should be discussed on the basis of the concentrations to reach in the target tissue rather than in plasma only. Furthermore, it is interesting to note that the ELF-to-plasma partition coefficient (penetration ratio) is similar to that calculated with the popPK approach. Indeed, as stated by Equation (1.3.8), the latter is given by

$$K_t := \frac{c_t}{c_p} = \frac{usv_2}{usv_1} = \frac{249}{1000} \simeq 0.24.$$

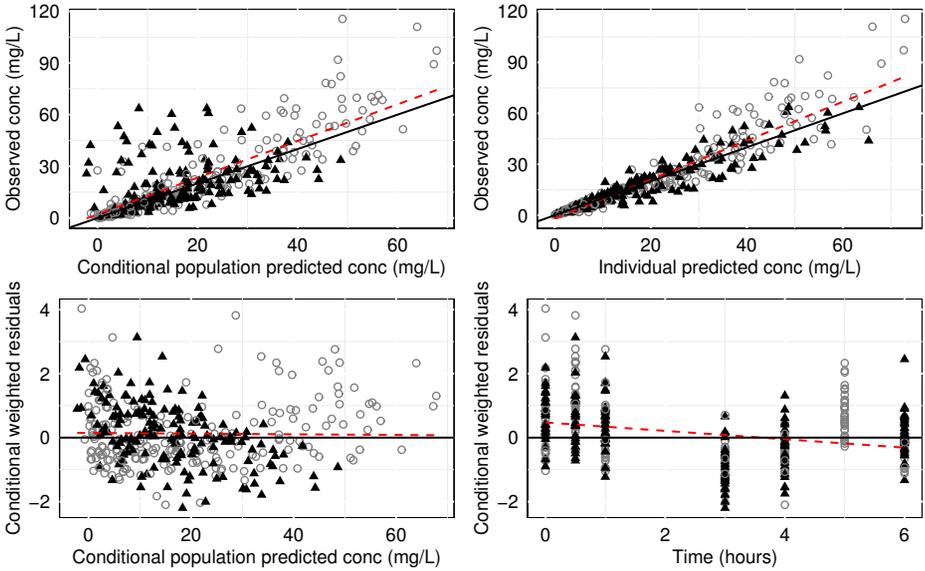
while $K_{pLu} = 0.26$ in Table 4.4. That means that the concentration in the site of infection is four times lower than the plasma concentration.

4.3.4 Model evaluation

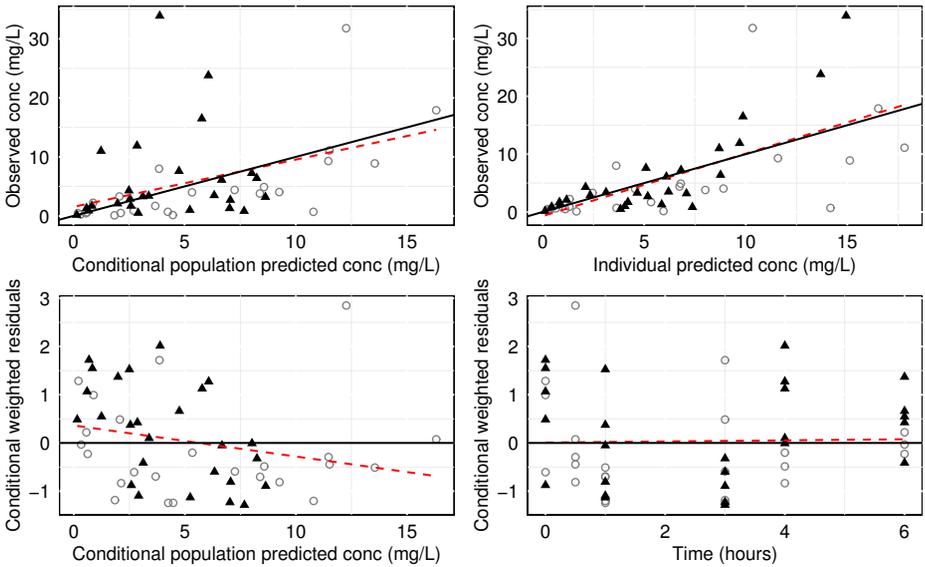
Internal validation

The bootstrap results, included in Table 4.4, give satisfactory results for the precision of the estimations. The model was also validated by GOF plots in Figure 4.9 and VPCs in Figure 4.10. We observe no inadequate trend and an acceptable agreement between predicted and observed concentration over the dosing interval.

4.3 Physiologically based model

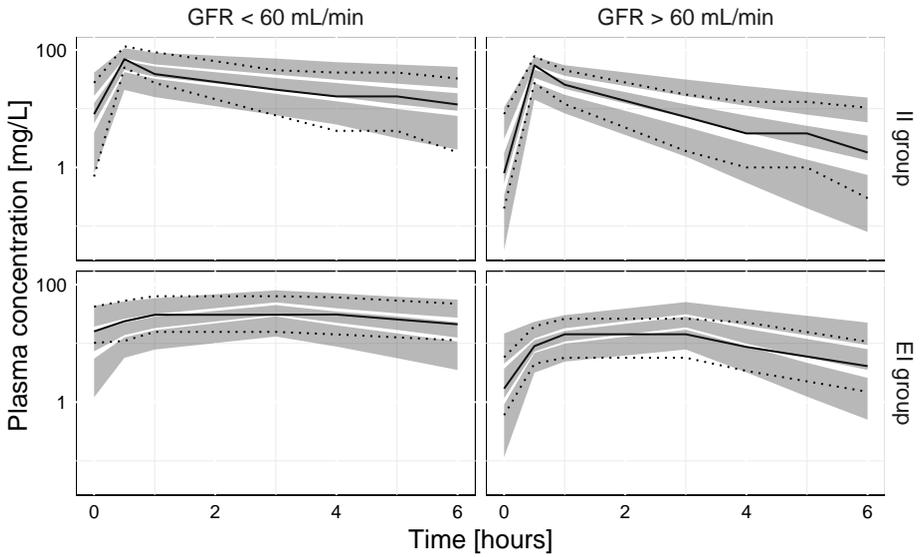


(a) plasma concentrations

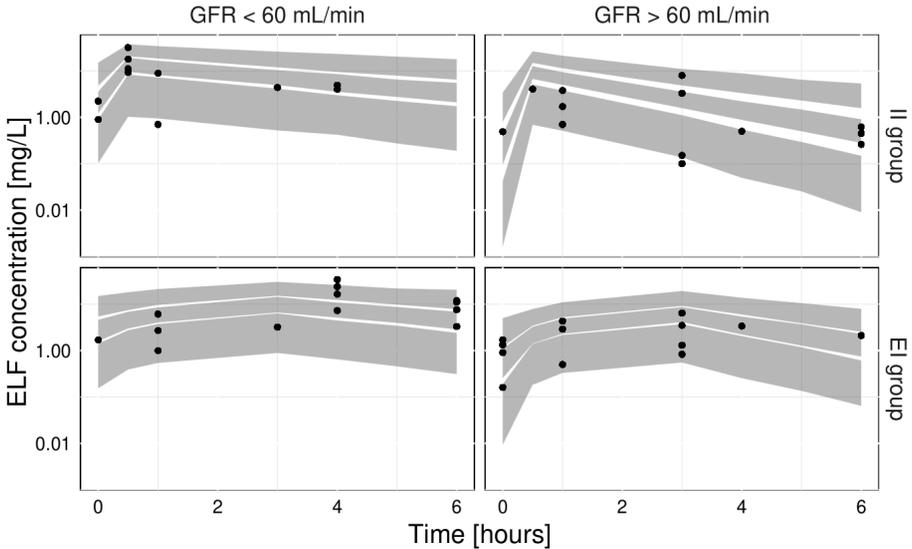


(b) ELF concentrations

Figure 4.9 – PBPK model of meropenem: basic goodness-of-fit plots. Open circles, intermittent infusion (over 30 min); filled triangles, extended infusion (over 3 hours). Dashed red lines are the linear regression lines. Solid lines are either the line of identity [upper rows] or the line $x = 0$ [lower rows]



(a) plasma concentrations



(b) ELF concentrations

Figure 4.10 – PBPK model of meropenem: visual predictive checks. Grey areas are the 90% confidence intervals of the median and the 5th and 95th percentiles. Continuous and dotted lines correspond to the median and the 5th and 95th percentiles of the observations in plasma [(a)]; filled circles are the observations in ELF [(b)]. II, intermittent infusion; EI, extended infusion; GFR, glomerular filtration rate.

Table 4.4 – PBPK model of meropenem: parameter estimates

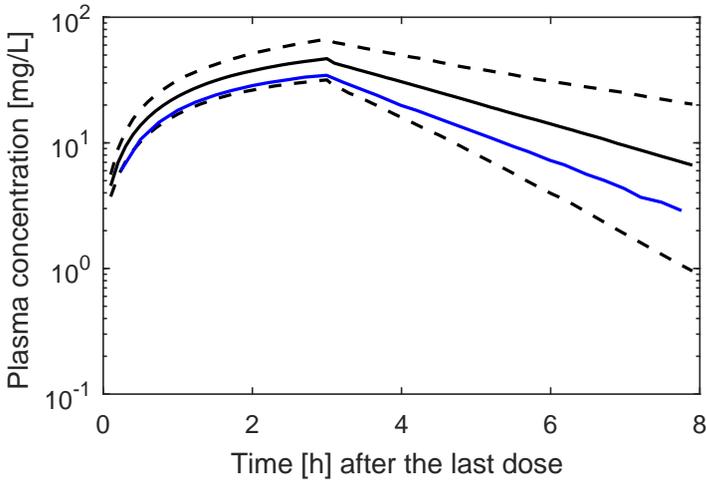
Parameter	Estimate	bootstrap CI ^a
CL	8.2	7.7 - 8.9
Allometric exponent of GFR effect on CL [θ_{GFR}]	0.722 (fixed)	-
IIV on CL [ω^2 (%CV)]	0.11 (33)	0.093 - 0.16
K_{pLu}	0.26	0.22 - 0.32
$K_{pLi} = K_{pKi}$	0.19	0.12 - 0.20
K_{pRB}	0.25	0.24 - 0.29
Eprop plasma conc. [σ_p^2 (%)]	0.086 (29)	0.076 - 0.11
Eadd plasma conc. [σ_a^2 (mg/L)]	0.036 (0.19)	0.032 - 0.049
Eprop ELF conc. [σ_p^2 (%)]	0.48 (69)	0.42 - 0.65

^a confidence interval based on the 5th and 95th percentiles of the bootstrapped distributions generated from 500 resampled datasets
CL, (renal) clearance; GFR, glomerular filtration rate; IIV, interindividual variability; $K_{p\bullet}$, tissue-to-plasma partition coefficient; ω^2 , variance of the related random variable; Eprop, proportional error; Eadd, additional error; $\sigma_{p,a}^2$, variances of the related random variables.

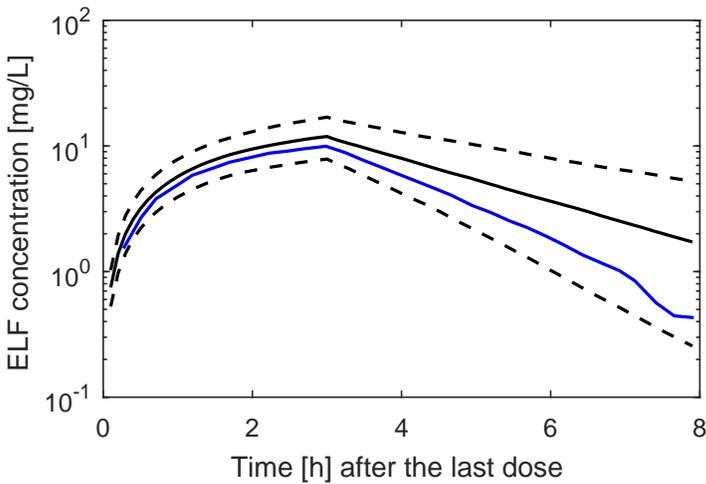
External validation

The results of external validation on data from independent patients are shown in Figures 4.11, 4.12, and 4.13. In all cases, the prediction of external data using the final PBPK model was acceptable. Figures A.4(a)-(d) of Appendix A provide individual plots for Karjagin et al.'s patients. Separated plots for each dosing regimen reported in Li et al. (2006) are also provided in Figures A.5(a)-(f).

Figure 4.14 shows the predictions for the 13 patients in Chimata et al. (1993) with various degrees of renal function. Simulations displayed good agreement between observed and predicted concentrations. Figures A.6(a)-(c) of Appendix A provide separated plots for each group.



(a) Plasma concentrations



(b) ELF concentrations

Figure 4.11 – PBPK model of meropenem: simulated (a) plasma and (b) infection-site PK profiles (median and 90% PI) for 1000 patients from the NHANES databases and consistent with the the study design of Lodise et al. (2011). Dosage of 2g over a 3h-infusion. Blue lines are the digitized simulated concentration-time profiles in Lodise et al. (2011). Time is time after the first dose.

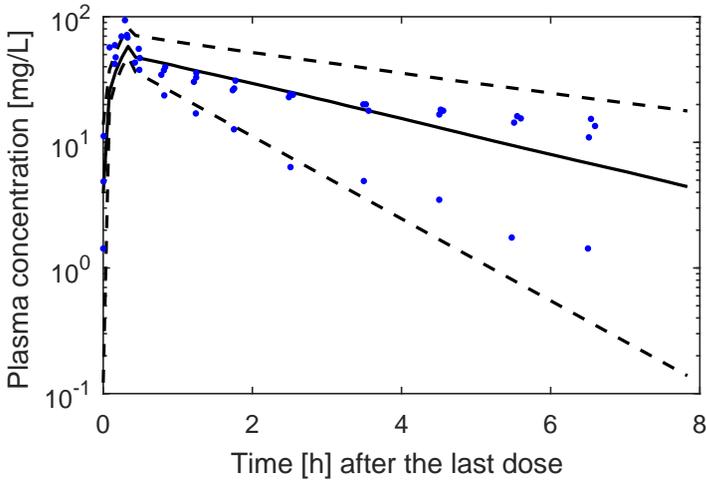


Figure 4.12 – PBPK model of meropenem: simulated plasma PK profiles (median and 90% PI) for 500 replicates of four of the patients described in Karjagin et al. (2008). Dosage of 1g every 8h over a 20min-infusion. Points are the observed plasma concentrations in Karjagin et al. (2008). Time is time after the second dose.

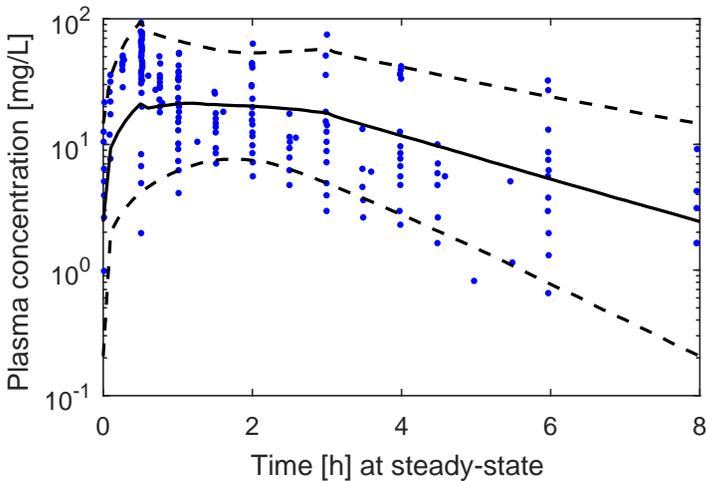


Figure 4.13 – PBPK model of meropenem: simulated steady-state plasma PK profiles (median and 90% PI) for 1000 patients from the NHANES databases and consistent with the the study design of Li et al. (2006). Simulation of 6 different dosing regimens: 0.5, 1 or 2 g every 8h over a 30min- or 3h-infusion. Points are the observed plasma concentrations in Li et al. (2006).

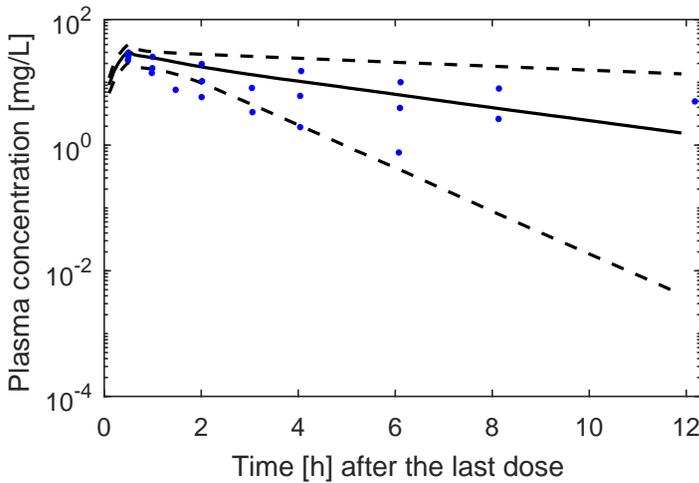


Figure 4.14 – PBPK model of meropenem: simulated plasma PK profiles (median and 90% PI) for 385 replicates of the 13 patients described in Chimata et al. (1993). Dosage of 0.5g over a 30min-infusion. Points are (the medians of) the observed plasma concentrations in the three groups. Time is time after the first dose.

4.3.5 Extrapolation in morbidly obese individuals

We investigated the extrapolation performances of the model by comparing model predictions to digitized concentrations from a previously published study on meropenem in morbidly obese patients (Wittau et al. (2015)). This study included five patients. Individual characteristics (sex, age, weight, height, body surface area and serum creatinine) were generated for 1000 virtual patients from the population tab of Simcyp and matched the summary-level characteristics in the publication. Obese patients constitute an interesting population to consider, especially because weight is an important covariate of the model (see Table 4.3).

Figure 4.15 shows that the digitized observed concentrations from the few patients of Wittau et al. (2015) seem to be overestimated by the model predictions (although the points are in the prediction interval). We can identify possible explanations. The renal elimination is assumed to account for 70% of the total clearance, which could not be a valid assumption for obese patients. Indeed, it is shown that obesity is associated with kidney diseases, and, in that case, the nonrenal clearance become the main route of elimination (see, e.g., Ververs et al. (2000)). Moreover, there is also the fact that the glomerular filtration rates of the simulated patients were estimated using the Modification of Diet in Renal Disease formula, that is misleading in obese patients (Wuerzner et al. (2011)). Having the real creatinine clearance (measured on 24 hours) would maybe improve the results. In conclusion, the model could be acceptable for extrapolation in other groups of patients, but may require additional external evaluations with consideration of alternative clearance parameterizations.

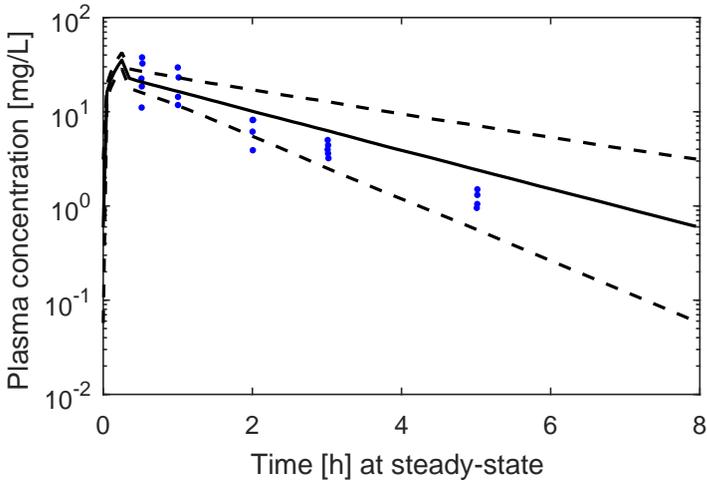


Figure 4.15 – PBPK model of meropenem: extrapolation in morbidly obese patients. Simulated steady-state plasma PK profiles (median and 90% PI) for 1000 patients from the Simcyp virtual populations and consistent with the study design of Wittau et al. (2015). Dosage of 1g every 8h over a 15min-infusion. Points are the observed plasma concentrations in Wittau et al. (2015).

Part II

Drug dosing

Simulations and probability of target attainment

This chapter aims to present how Monte Carlo simulations are used to compare different scenarios and inform dose selection. In particular, we illustrate on the popPK model of temocillin the PTA-based methodology currently used in the scientific literature for model-based AB drug dosing (see, e.g., Musuamba et al. (2017)).

5.1 Simulations: application to HCQ dosage

In Yao et al. (2020), the authors have shown by *in vitro* evaluations that the half-maximal effective concentration (EC50) for treatment and prophylactic effects on SARS-COV-2 were 0.72 and 5.85 μM , respectively, 48h post-infection. Both studies were conducted using Vero cells infected at a multiplicity of infection (MOI)⁽¹⁾ of 0.01. Higher antiviral EC50 values have also been reported by other research groups, e.g., 4.51 μM (MOI: 0.01) by Liu et al. (2020).

The final popPK model developed in Chapter 2 was used to simulate different dosing scenarios (see Table 5.1). Simulations were performed using virtual patients with extreme values of body weight: 50 and 150 kg. Each scenario was simulated for 5 and 10 days. The median PK profiles are reported in Figure 5.1. For graphical comparative purposes, EC50 values by Yao et al. (2020) and Liu et al. (2020) were scaled to total whole-blood concentrations⁽²⁾ and included in Figure 5.1. The proportion of

⁽¹⁾Multiplicity of infection is the ratio of the number of virus particles to the number of target cells in the *in vitro* experiment.

⁽²⁾The scaling was performed as following. The EC50 [μM] was multiplied by the molecular weight of HCQ (336 g/mol). Assuming 50 % protein binding in patients (McLachlan et al. (1993)), the result was multiplied by 2 to obtain the total plasma/serum concentration, and then divided by 0.53, the serum to whole-blood concentration ratio (Blanchet et al. (2019)).

simulated patients that reach the EC50 at the end of treatment (probability of target attainment (PTA%)) are provided in Table 5.1. It should be noted that, for most of the proposed dosing regimens, the simulated concentrations are below the concentrations expected for antiviral effects of HCQ, especially in over-weight patients who would need higher doses due to body weight effect on clearance. This should be taken into account for dosing recommendations for HCQ in COVID-19 patients.

It should also be noted that the immunomodulatory effects of hydroxychloroquine could also contribute to the overall clinical effects in addition to the potential antiviral effects. Characterizing the PK/PD and exposure-response is beyond the scope of this thesis, but adequately conducted exposure-response analyses are essential to characterize the target concentrations for drug efficacy and safety.

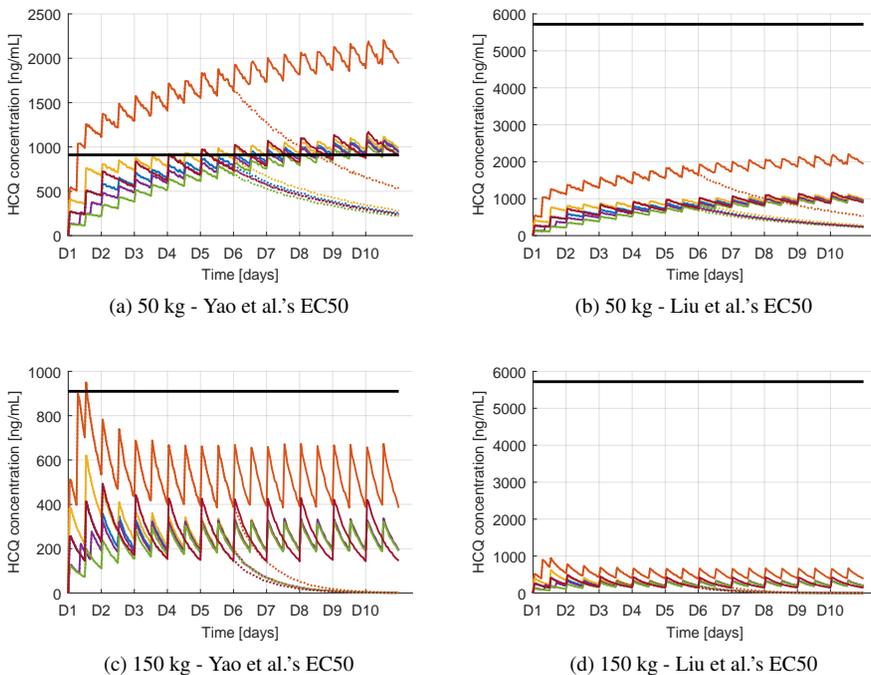


Figure 5.1 – Median PK profiles of HCQ blood concentrations after simulations ($n_{sim} = 1000$) of alternative dosing regimens (see Table 5.1) for two representative patients of 50 kg and 150 kg, resp. The horizontal lines represent the projected target total whole blood concentrations based on the EC50 values from Yao et al. (2020) ($0.72 \mu\text{M}$) and Liu et al. (2020) ($4.51 \mu\text{M}$). Solid lines, treatment for 10 days; dotted lines, treatment for 5 days.

Table 5.1 – Description of alternative dosing regimens and percentage of simulated subjects of 50 kg and 150kg achieving the *in vitro* EC50 at the end of the treatment

Dosing regimen (color)	Loading dose (D1) ^a HCQ sulfate	Maintenance dose	Duration of treatment	PTA [%] (50 kg)		PTA [%] (150 kg)	
				EC50: 0.72 μ M	EC50: 4.51 μ M	EC50: 0.72 μ M	EC50: 4.51 μ M
Blue (Belgian protocol)	400 mg BID	200 mg BID	5 days	34.4	0.0	0.0	0.0
			10 days	55.8	0.0	0.1	0.0
Orange	800 mg followed by 800 mg 6 h later, and 400 mg 6 h later	400 mg BID	5 days	93.3	0.0	2.7	0.0
			10 days	96.1	0.0	3.4	0.0
Yellow	600 mg TID	200 mg BID	5 days	43.3	0.0	0.0	0.0
			10 days	57.9	0.0	0.1	0.0
Purple	200 mg TID	200 mg BID	5 days	29.2	0.0	0.0	0.0
			10 days	54.3	0.0	0.1	0.0
Black red	400 mg BID	400 mg daily	5 days	28.7	0.0	0.0	0.0
			10 days	48.9	0.0	0.1	0.0
Green	-	200 mg BID	5 days	21.7	0.0	0.0	0.0
			10 days	50.1	0.0	0.0	0.0

^a Dx, day x

BID, twice a day; TID, three times a day

5.2 PTA-based method for AB dosing

A PK/PD target is defined on the basis of the minimum inhibitory concentration (MIC) and the PD index. The latter depends on the AB category (time- or concentration-dependent) as illustrated in Figure 5.2 (see, e.g., Abdul-Aziz et al. (2015) or Nielsen et al. (2011)). Monte Carlo simulations are then performed to determine the probability of target attainment (PTA), estimated by the proportion of simulated patients that reaches the target. The highest MIC value for which the PTA exceeds 90% is defined as the *PK/PD breakpoint* (Musuamba et al. (2017) and Usman et al. (2017)). The PK/PD breakpoints can then be compared between alternative dosing regimens in order to select the most efficient one in the studied population. This investigation of the PTAs is naturally referred to as a *PTA analysis*. In this work, we focus on time-dependent AB such that the PD index is the %T>MIC (see Figure 5.2).

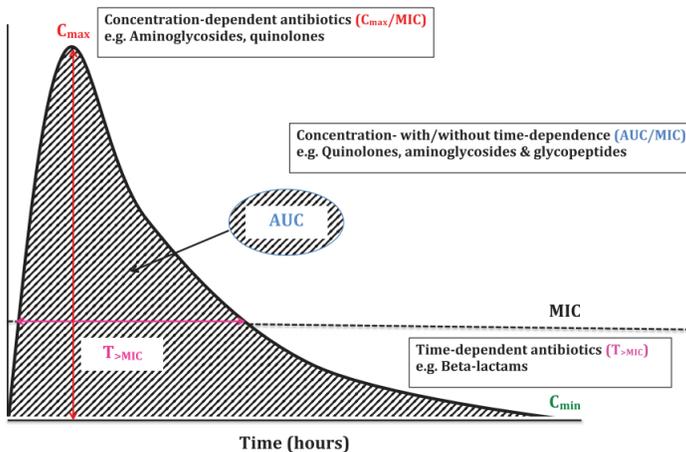


Figure 5.2 – Fundamental PK/PD indexes of antibiotics on a hypothetical concentration-time curve. AUC, area under the concentration-time curve; C_{\max} , maximal drug concentration; C_{\min} , minimum drug concentration; MIC, minimum inhibitory concentration; $T_{>MIC}$, time that drug concentration remains above MIC. Illustration taken from Abdul-Aziz et al. (2015).

A model-based PTA analysis giving a renal function-based dosage is carried out for meropenem in elderly patients in Usman et al. (2017). Below, we present a PTA analysis of temocillin in patients with nosocomial pneumonia.

5.2.1 Time-dependent antibiotics

The β -lactam antibiotics are time-dependent antibiotics, meaning that inhibitory and bactericidal activity depends on the time that the (free) drug concentration exceeds the MIC during the dosing interval (PD index). Figure 5.3 represents a hypothetical pharmacokinetic profile at steady-state, denoted by y_j^∞ below ($j = 1$ for systemic PK

profile, $j = 2$ for PK profile at the site of infection). The exponent ∞ indicates that this is an asymptotic PK profile. If we consider a high number of simulations denoted by n_{sim} , the probability of reaching $100\%T > \text{MIC}$ is estimated by:

$$\frac{\#\{y_j^\infty \mid y_j^\infty(T) > \text{MIC}\}}{n_{\text{sim}}}.$$

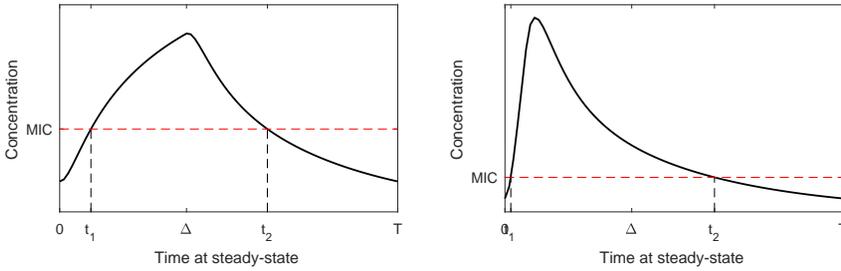


Figure 5.3 – Hypothetical PK profiles

Let t_1 and t_2 be the time points such that $t_1 < t_2$ and $y_j^\infty(t_1) = \text{MIC} = y_j^\infty(t_2)$. The probability of reaching $50\%T > \text{MIC}$ should, strictly speaking, be estimated by:

$$\frac{\#\{y_j^\infty \mid t_2 - t_1 \geq T/2\}}{n_{\text{sim}}}.$$

However, it turns out that the latter probability is often approximated by

$$\frac{\#\{y_j^\infty \mid y_j^\infty(T/2) > \text{MIC}\}}{n_{\text{sim}}}.$$

That means that the length of $[0, t_1]$ is assumed to be zero, which this is clinically acceptable. The longer the infusion time is, the poorer the approximation is.

5.2.2 PTA analysis: application to temocillin dosage

The following PTA analysis is reported in N. Layios, C. Visée, P. Thémans, et al. (2021, submitted).

Using the final popPK model of temocillin built in Chapter 3, simulations can be performed. Steady-state concentrations of temocillin were simulated in plasma and ELF for 10,000 virtual subjects for each of the two dosing scenarios (intermittent and continuous infusion). Individual characteristics (covariates) of the virtual patients were generated using their distributions in the model building dataset. Subsequently, the PTAs for different PD targets ($50\%T > \text{MIC}$ and $100\%T > \text{MIC}$) against a range of MICs were computed. They are reported in Figure 5.4. As the steady-state PK profile following continuous infusion (at constant rate) is constant, only the PD index of

100%T>MIC is of interest. The same targets were considered after dichotomization of creatinine clearance between ≥ 60 mL/min and < 60 mL/min as shown in Figures 5.5 and 5.6. The PTA analysis has also been performed in case of ARC patients.

A visual inspection of Figures 5.4-5.6 enables to draw up Table 5.2 of PK/PD breakpoints. The breakpoints are determined using a probability of success of 90%. We can observe that continuous infusion (CI) offers better PK/PD indexes than intermittent infusion (II). For the minimal pharmacodynamic targets of 50%T>1X MIC in II group and 100%T>1X MIC in CI group, the PK/PD breakpoints were 2 and 4 mg/L respectively, both in plasma and ELF. These values remain well below the British Society for Antimicrobial Chemotherapy (BSAC) breakpoints (8 mg/L) and, moreover, below the mean MIC of 9.94 mg/L of the pathogens isolated in this cohort of patients. At best, an MIC of 8 mg/L is achieved for the less stringent PD targets in ELF for both II and CI in patients with moderate renal impairment (30-60 ml/min).

Measured ELF concentrations of antibiotics may be misleading (as explained, e.g., in Kiem and Schentag (2008)). Indeed, technical errors during the bronchoalveolar lavage (BAL), such as a prolonged dwelling time, or contamination from lysis of cells during the AB measurement, could artificially increase the true ELF concentrations. However, without further clinical data, our results suggest that temocillin should not be recommended in severe nosocomial pneumonia.

Table 5.2 – PK/PD breakpoints in plasma (free conc.) and ELF (total conc.) for specific PD targets according to different modes of administration using a probability of success $\geq 90\%$

	II (2g/8h 0.5h-inf)		CI (6g/24h)	
	plasma	ELF	plasma	ELF
50% T > 1x MIC	2	2	na	
Cl _{CR} ≥ 60 mL/min	2	1		
Cl _{CR} < 60 mL/min	8	8		
Cl _{CR} > 120 mL/min/1.73m ² *	0.5	0.5		
50% T > 4x MIC	0.5	0.5		
Cl _{CR} ≥ 60 mL/min	0.5	0.25		
Cl _{CR} < 60 mL/min	2	2		
Cl _{CR} > 120 mL/min/1.73m ²	0.125	0.125		
100% T > 1x MIC	0.5	0.5	4	4
Cl _{CR} ≥ 60 mL/min	0.5	0.5	4	4
Cl _{CR} ≥ 60 mL/min	4	4	16	8
Cl _{CR} > 120 mL/min/1.73m ²	0.25	0.25	4	2
100% T > 4x MIC	0.125	0.125	1	1
Cl _{CR} ≥ 60 mL/min	0.125	0.125	1	1
Cl _{CR} ≥ 60 mL/min	1	1	4	2
Cl _{CR} > 120 mL/min/1.73m ²	0.0625	0.0625	1	0.5

na: not applicable; II, intermittent infusion (inf); CI, continuous infusion
Cl_{CR}, creatinine clearance

* These patients are included in the group of patients with Cl_{CR} ≥ 60 mL/min

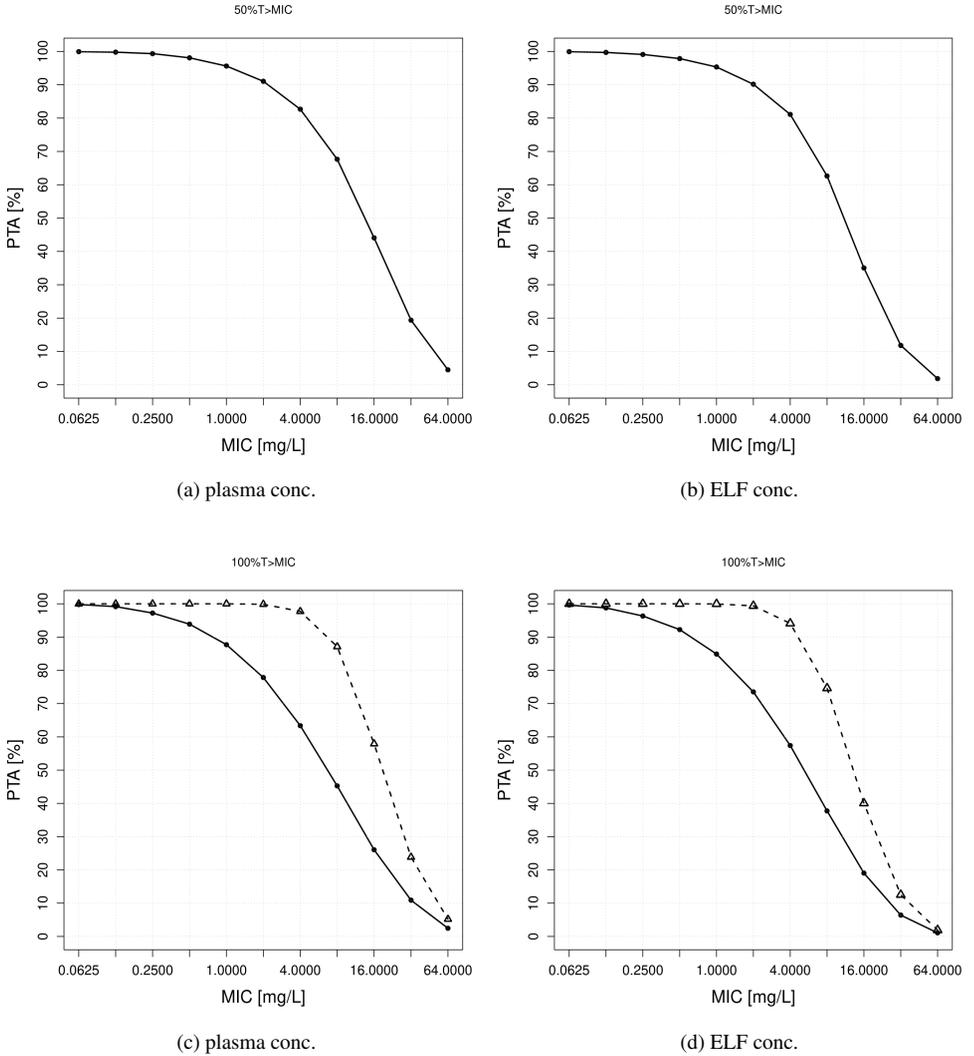


Figure 5.4 – Probability of target attainment (obtained with Monte Carlo simulations, $n_{\text{sim}} = 10,000$) for free plasma concentrations (left) and total ELF concentrations (right) for different dosing regimens. Continuous lines with filled circles correspond to intermittent infusion (2g/8h over 0.5h-infusion); broken lines with open triangles correspond to continuous infusion (6g/24h)

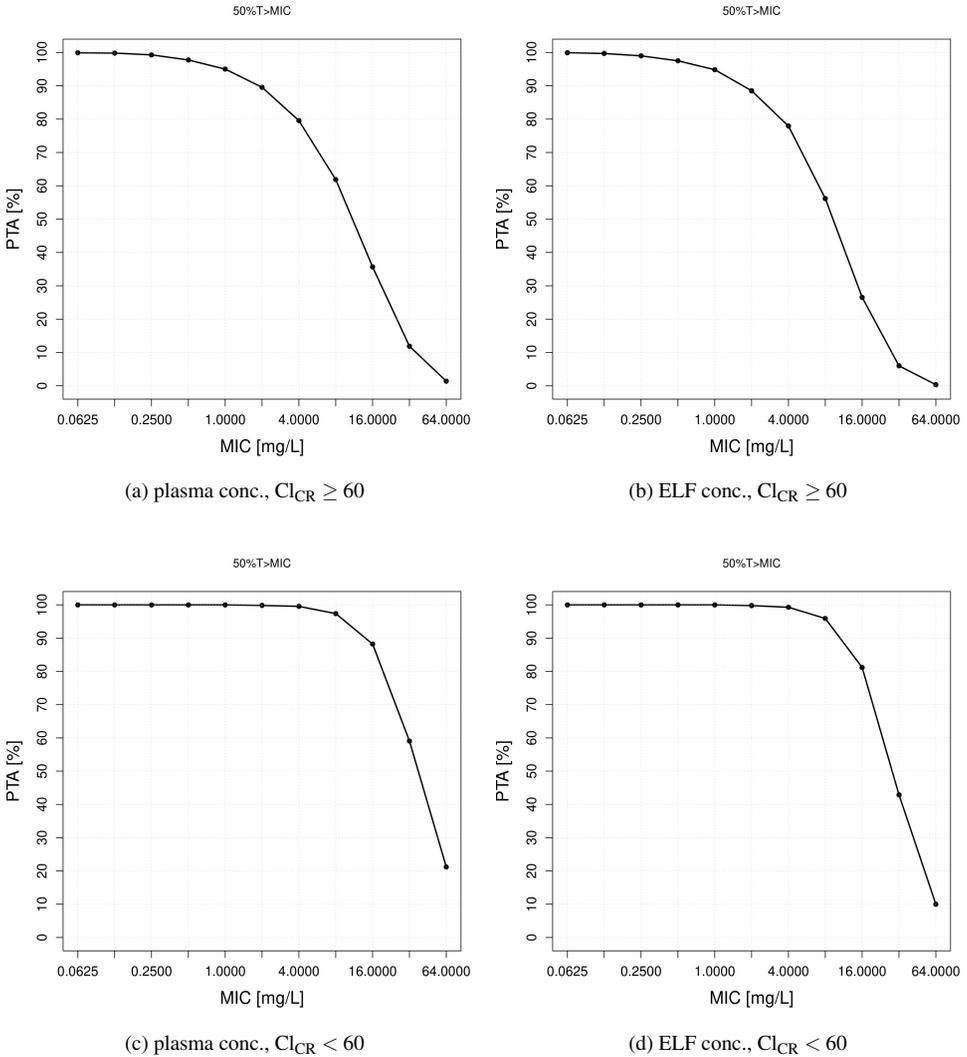


Figure 5.5 – Probability of target attainment (obtained with Monte Carlo simulations) for free plasma concentrations (left) and total ELF concentrations (right) for intermittent infusion (2g/8h over 0.5h-infusion). (a)-(b) $Cl_{CR} \geq 60$ mL/min ($n_{sim} \approx 6000$); (c)-(d) $Cl_{CR} < 60$ mL/min ($n_{sim} = 4000$)

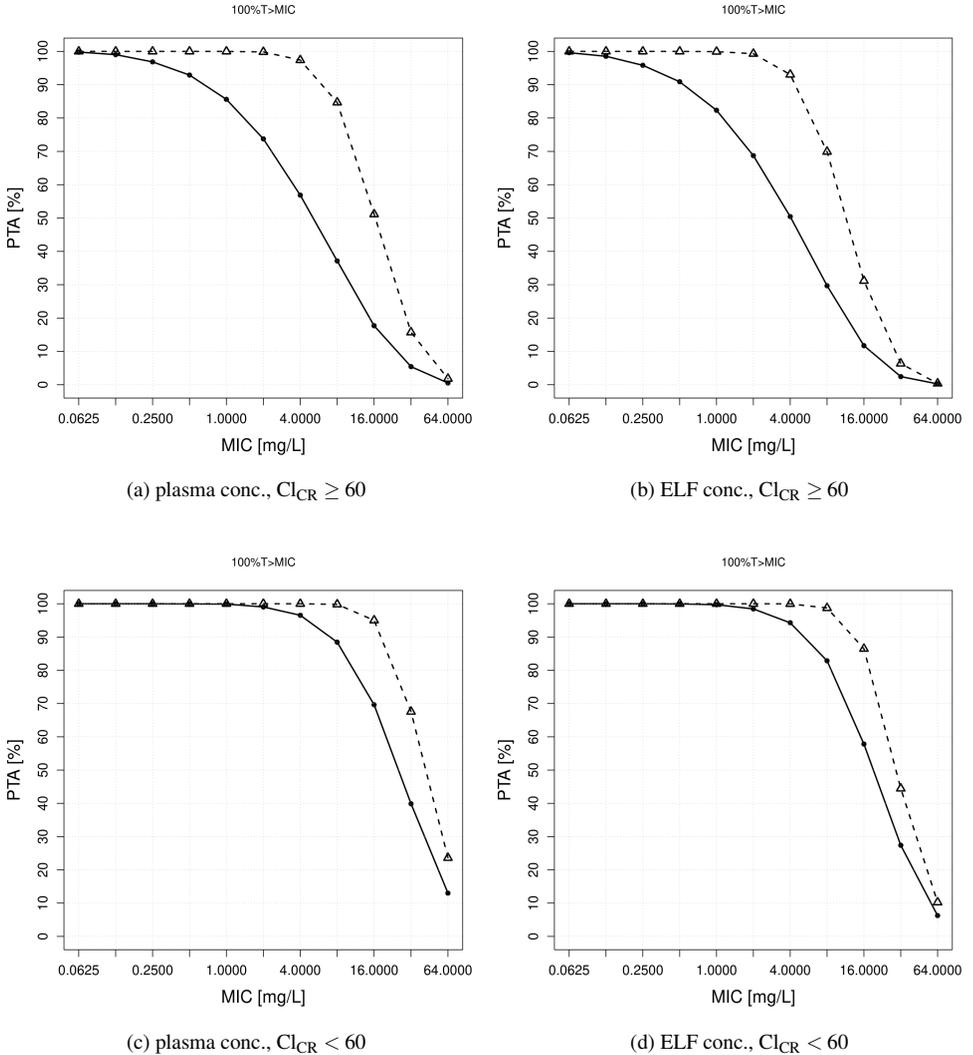


Figure 5.6 – Probability of target attainment (obtained with Monte Carlo simulations) for free plasma concentrations (left) and total ELF concentrations (right) for different dosing regimens. Continuous lines with filled circles correspond to intermittent infusion (2g/8h over 0.5h-infusion); broken lines with open triangles correspond to continuous infusion (6g/24h). **(a)-(b)** $Cl_{CR} \geq 60$ mL/min ($n_{sim} \approx 6000$); **(c)-(d)** $Cl_{CR} < 60$ mL/min ($n_{sim} = 4000$)

CHAPTER 6

Open-loop control law

In contrast with the empirical methods presented in Chapter 5, we report here an analytical strategy for the dosing of drugs (particularly antibiotics) administered by intravenous infusion at regular dosing intervals. This new approach is based on basic tools from systems and control theory, and aims at improving dosing recommendations at individual level while sparing computational time due to MC simulations. The content of this chapter is reported in Thémans et al. (2020c).

A deterministic input-output analysis of a particular class of LTI systems (in which are included the PK models, see Appendix D) yields an open-loop control law which enables to compute an appropriate dosage for the individual nominal patient. This approach is then incorporated into the “*worst-case*” system based on the monotony of the state trajectories with respect to the clearance. Thanks to numerical simulations, these methods are successively illustrated on the popPK model of meropenem (time-dependent β -lactam AB) developed in Chapter 4, Section 4.2.

6.1 State-space model

In the present and subsequent chapters, we consider pharmacokinetic systems described by LTI state-space representation of the general form:

$$\begin{cases} \dot{x}(t) = Ax(t) + bu(t) \\ y(t) = Cx(t) \end{cases} \quad t \geq 0 \quad (6.1.1)$$

where $A \in \mathbb{R}^{n \times n}$ is a Metzler and (asymptotically) stable matrix, and $b \in \mathbb{R}^{n \times 1}$ is nonnegative. In a mixed effects modeling approach, the model parameters can include random components. Unless otherwise stated, the PK parameters are assumed to be

fixed to their nominal values. The state vector $x = (x_1 \ x_2 \ x_3 \ \cdots \ x_n)^T \in \mathbb{R}^n$ corresponds to the drug amounts [g] or the drug concentrations [g/L] in well-defined compartments. Without loss of generality, x_1 and x_2 correspond to the plasma and the site of infection, respectively. The input function $u(\cdot)$ represents the administration [g/h] of the drug into the first compartment and the output vector $y = (y_1 \ y_2)^T \in \mathbb{R}^2$ corresponds to the drug concentrations [mg/L] in the plasma and, if described by the model, at the site of infection. Consequently, the input matrix $b \in \mathbb{R}^{n \times 1}$ is a column vector filled by $(n-1)$ zeros and one non-zero (positive) value in the first component and the output matrix $C \in \mathbb{R}^{2 \times n}$ has non-zero elements at positions (1,1) and (2,2) (as it is the case in (1.3.7) and (4.3.3)), i.e.,

$$b = (b_1 \ 0 \ \cdots \ 0)^T, \quad C = \begin{pmatrix} 1/S_1 & 0 & 0 & \cdots & 0 \\ 0 & 1/S_2 & 0 & \cdots & 0 \end{pmatrix} \quad (6.1.2)$$

where, for all $j \in \{1, 2\}$, S_j converts the state component x_j in concentration (e.g., [mg/L]) both in plasma ($j = 1$) and at the site of infection ($j = 2$). This results in a strictly proper transfer function $\hat{G}(s) := C(sI - A)^{-1}b = (\hat{g}_1(s) \ \hat{g}_2(s))^T \in \mathbb{R}_{p,0}(s)^{2 \times 1}$.

Remark 3 By the proof of Proposition 1.1.3, $A = VDW^*$, where $D = \text{diag}[\lambda_i]$, with, for all $i \in \{1, \dots, n\}$, $\lambda_i \in \sigma(A)$, and V and W are the matrices of the associated right and left eigenvectors, respectively ($W^*V = I$). Therefore, $W^*(sI - A)V = sI - D$. Given that $(sI - D)^{-1} = \text{diag}\left[\frac{1}{s - \lambda_i}\right]$,

$$\begin{aligned} (sI - A)^{-1} &= V(sI - D)^{-1}W^* \\ &= \sum_{i=1}^n \frac{1}{s - \lambda_i} v_i w_i^*. \end{aligned}$$

Using the form of the matrices C and b above, the transfer function is given by

$$\begin{aligned} \hat{g}_j(s) &= \sum_{i=1}^n \frac{1}{s - \lambda_i} (C_j v_i) (w_i^* b) \\ &= \sum_{i=1}^n \frac{1}{s - \lambda_i} \frac{1}{S_j} (v_i)_j (w_i^*)_1 b_1 \end{aligned}$$

where C_j denotes the j^{th} row of the output matrix C .

6.1.1 Input function

Intravascular infusion of a fixed dose (called *maintenance dose*) at regular intervals is recommended for the administration of β -lactam antibiotics in ICUs. Consequently, the input function/infusion rate $u(\cdot)$ is a right-continuous piecewise constant function that depends on three parameters: the **dose** [g] denoted by D , the **duration of the infusion** [h] denoted by Δ , and the time between two doses (**dosing interval**) [h] denoted by T . For all $t \geq 0$,

$$u(t) [\text{g/h}] = \begin{cases} D/\Delta & \text{if } (t \bmod T) < \Delta \\ 0 & \text{if } (t \bmod T) \geq \Delta \end{cases} \quad (6.1.3)$$

If required, an initial *loading dose* D_L (higher than the maintenance dose) is given at the first administration. In this case, for all $t \in [0, \Delta]$, $u(t) = D_L/\Delta$ and, for all $t \in [iT, iT + \Delta[$ ($i \in \mathbb{N}_0$), $u(t) = D/\Delta$. The duration of the infusion is necessarily shorter than the dosing interval ($\Delta < T$). These functions are represented in Figure 6.1. Besides, continuous administration for treating severe infection has been studied recently, see, e.g., Veiga and Paiva (2018) and Sjövall et al. (2018). The latter can be seen as a limit case of the mode of administration considered here ($\Delta = T$).

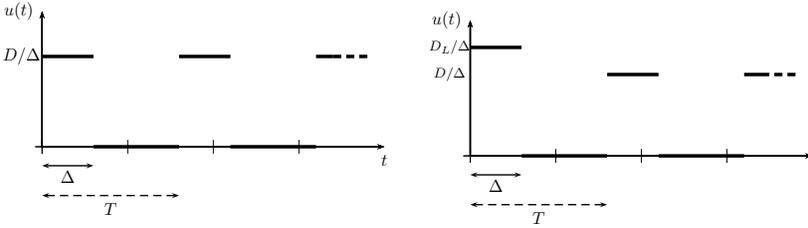


Figure 6.1 – System input function: drug infusion rate vs. time (left: maintenance dose, right: additional loading dose)

6.1.2 Input-output analysis

In the following, the state matrix $A \in \mathbb{R}^{n \times n}$ in (6.1.1) is assumed to have n **distinct** and **real** eigenvalues. Moreover, the system $[A, b, C]$ corresponds to an individual patient. Indeed, the model parameters are computed on the basis of the patient characteristics according to the covariate-parameter models (1.3.12), and/or the real physiological parameters (Table 4.3).

Proposition 6.1.1 (System response) Consider the PK system (6.1.1)-(6.1.2) with an input function of the form (6.1.3). The zero-state system response $y(\cdot)$ is given as follows, where $N_t := \lfloor t/T \rfloor$ denotes the number of administrations already received at time t (including the ongoing administration, if appropriate): for all $j \in \{1, 2\}$ and for all $t \geq 0$,

- if $(t \bmod T) < \Delta$ (during infusion)

$$y_j(t) = \frac{D}{\Delta} \left[\sum_{l=0}^{N_t-2} \sum_{i=1}^n \frac{F_{ji}}{\lambda_i} e^{\lambda_i(t-lT)} (1 - e^{-\lambda_i \Delta}) + \sum_{i=1}^n \frac{F_{ji}}{\lambda_i} (e^{\lambda_i(t-(N_t-1)T)} - 1) \right]$$

- if $(t \bmod T) \geq \Delta$ (after infusion)

$$y_j(t) = \frac{D}{\Delta} \sum_{l=0}^{N_t-1} \sum_{i=1}^n \frac{F_{ji}}{\lambda_i} e^{\lambda_i(t-lT)} (1 - e^{-\lambda_i \Delta}).$$

The symbol $\lfloor \cdot \rfloor$ denotes the integer part of a real number. The coefficients F_{ji} and

λ_i ($i \in \{1, 2, 3, \dots, n\}$, $j \in \{1, 2\}$) are directly related to the model parameters: λ_i denote the eigenvalues of the matrix A and F_{ji} are the residuals of the transfer functions $\hat{g}_j(s)$ in λ_i , i.e., $F_{ji} = \lim_{s \rightarrow \lambda_i} (\hat{g}_j(s) (s - \lambda_i)) = \frac{1}{S_j} (v_i)_j (w_i^*)_1 b_1$.

Proof. See Appendix D for a detailed proof. It consists in computing the inverse Laplace transform of $\hat{y}(s) = \hat{G}(s)\hat{u}(s)$ to derive the zero-state response in the time domain. The j^{th} component of the transfer function can be written in partial fraction expansion as:

$$\hat{g}_j(s) = \sum_{i=1}^n \frac{F_{ji}}{s - \lambda_i}.$$

To compute the Laplace transform $\hat{u}(s)$, the input function should be considered as a superposition of functions of the form

$$U_i(t) = K \mathbf{1}_{[iT, iT+\Delta]}(t), \quad t \geq 0$$

where $i \in \mathbb{N}$ and $\mathbf{1}_I$ is the characteristic function of the subset I . □

Let us denote by $y^N(\tilde{t})$ ($\tilde{t} \in [0, T]$) the system response on the N^{th} dosing interval. So, for all $t \in [(N-1)T, NT[$, $y(t) = y^N(\tilde{t})$ where $\tilde{t} = t \bmod T$, i.e., $t = \tilde{t} + (N-1)T$. The new variable \tilde{t} indicates the position in the dosing interval after N administrations. Due to system stability, the concentration trajectory converges to an equilibrium trajectory denoted by y^∞ , which will be called *steady output* (known in the pharmacology literature as the steady-state PK profile or “plateau”), i.e.,

$$\lim_{N \rightarrow \infty} y^N(\tilde{t}) = y^\infty(\tilde{t})$$

as illustrated in Figure 6.2. Proposition 6.1.2 provides its analytical expression.

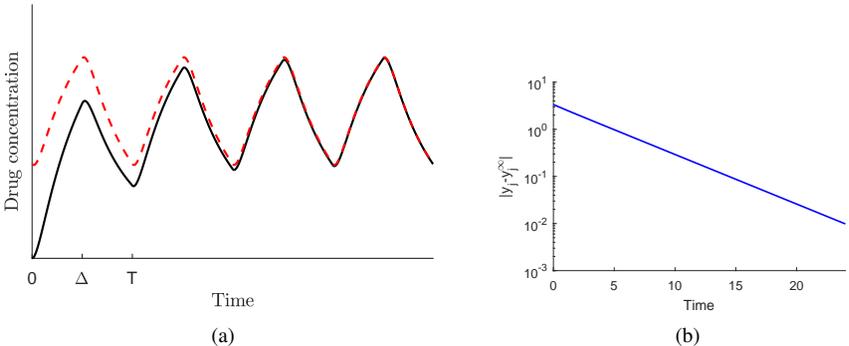


Figure 6.2 – (a) Hypothetical PK profiles. Continuous curve, system response y_j ; dashed red curve, repeated equilibrium trajectory y_j^∞ . (b) Absolute error $|y_j^N - y_j^\infty|$.

Proposition 6.1.2 (Asymptotic response) Consider the PK system (6.1.1)-(6.1.2) with an input function of the form (6.1.3). The output trajectory converges to an equilibrium trajectory, i.e., for all $\tilde{t} \in [0, T[$,

$$y^N(\tilde{t}) - y^\infty(\tilde{t}) \xrightarrow{N \rightarrow \infty} 0$$

where the plateau y^∞ is given, for all $j \in \{1, 2\}$, by

- if $\tilde{t} \in [0, \Delta]$,

$$y_j^\infty(\tilde{t}) = \frac{D}{\Delta} \left[\sum_{i=1}^n \frac{F_{ji}}{\lambda_i} \frac{e^{\lambda_i \tilde{t}} (1 - e^{-\lambda_i \Delta})}{e^{-\lambda_i T} - 1} + \sum_{i=1}^n \frac{F_{ji}}{\lambda_i} (e^{\lambda_i \tilde{t}} - 1) \right]$$

- if $\tilde{t} \in [\Delta, T]$,

$$y_j^\infty(\tilde{t}) = \frac{D}{\Delta} \sum_{i=1}^n \frac{F_{ji}}{\lambda_i} \frac{e^{\lambda_i(\tilde{t}-T)} (1 - e^{-\lambda_i \Delta})}{e^{-\lambda_i T} - 1}$$

Proof. See Appendix D.

As shown in Figure 6.2, the system response exponentially converges towards the equilibrium trajectory. A similar exercise has been carried out in (Koch, 2012, Section 3.3) for multiple dosing by oral or IV bolus administration.

It follows from Proposition 6.1.2 that, at steady-state, the concentrations at the end and beginning of the dosing interval are equal:

$$\lim_{\tilde{t} \rightarrow T^+} y^\infty(\tilde{t}) = y^\infty(0).$$

We can therefore define

$$y^\infty(T) := y^\infty(0).$$

The concentration $y_1^\infty(T)$ corresponds to the minimal *plasma* concentration on the dosing interval (the lowest concentration (c_{trough}) observed just before a new administration). However, if there is a time disconnect between systemic and infection-site concentrations, i.e., if c_{max} and c_{trough} are reached later at the site of infection than in the plasma (due to, e.g., delayed/slow tissue penetration), $y_2^\infty(T)$ does not correspond to the minimal concentration at the site of infection, as illustrated on the hypothetical cases shown in Figure 6.3.

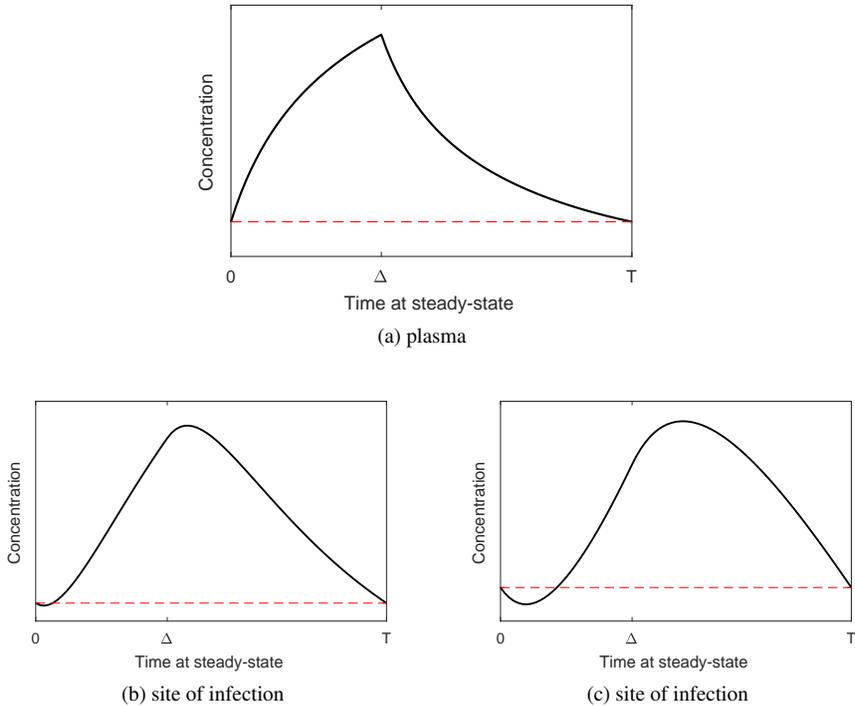


Figure 6.3 – Hypothetical PK profiles (a) y_1^∞ , (b) y_2^∞ with slight time disconnect, (c) y_2^∞ with important time disconnect.

In control theory, we call *settling time* the time needed for the output trajectory to enter and remain within a band of arbitrary width around the asymptotic trajectory. It can be interpreted in the PK field as the time needed to reach the steady state.

Proposition 6.1.3 Consider the PK system (6.1.1)-(6.1.2) with an input function of the form (6.1.3). Then, for all $N \geq N^*$ where $N^* = \max\{N_1, N_2\}$ and, for all $j \in \{1, 2\}$,

$$N_j = \max \left\{ \left\lceil \frac{\ln(0.01) - \ln(\Sigma_j)}{\lambda_F \cdot T} \right\rceil + 2, 0 \right\} \quad (6.1.4)$$

and

$$\Sigma_j(D, \Delta, T) = \frac{D}{\Delta} \sum_{i=1}^n \left| \frac{F_{ji}}{\lambda_i} \right| \frac{1 - e^{-\lambda_i \Delta}}{1 - e^{-\lambda_i T}} > 0 \quad (6.1.5)$$

where λ_F is the Frobenius eigenvalue of A , the zero-state output trajectory y^N is within an error bound of 0.01 around the steady output.

Proof. For all $N \in \mathbb{N}_0$, $j \in \{1, 2\}$, and $\tilde{t} \in [0, T]$,

$$\begin{aligned} |y_j^N(\tilde{t}) - y_j^\infty(\tilde{t})| &= \frac{D}{\Delta} \left| \sum_{i=1}^n \frac{F_{ji}}{\lambda_i} e^{\lambda_i \tilde{t}} \frac{1 - e^{-\lambda_i \Delta}}{1 - e^{-\lambda_i T}} e^{\lambda_i (N-1)T} \right| \quad (\text{see proof of Proposition D.3.1.}) \\ &\leq \frac{D}{\Delta} \sum_{i=1}^n \left| \frac{F_{ji}}{\lambda_i} \right| e^{\lambda_i \tilde{t}} \frac{1 - e^{-\lambda_i \Delta}}{1 - e^{-\lambda_i T}} e^{\lambda_i (N-1)T} \end{aligned}$$

Such that the *distance* between y_j^N and y_j^∞ induced by the uniform norm is upper bounded:

$$\begin{aligned} e(y_j^N, y_j^\infty) &:= \sup_{\tilde{t} \in [0, T]} |y_j^N(\tilde{t}) - y_j^\infty(\tilde{t})| \leq \frac{D}{\Delta} \sum_{i=1}^n \left| \frac{F_{ji}}{\lambda_i} \right| \frac{1 - e^{-\lambda_i \Delta}}{1 - e^{-\lambda_i T}} e^{\lambda_i (N-1)T} \\ &\leq \underbrace{\frac{D}{\Delta} \sum_{i=1}^n \left| \frac{F_{ji}}{\lambda_i} \right| \frac{1 - e^{-\lambda_i \Delta}}{1 - e^{-\lambda_i T}} e^{\lambda_i (N-1)T}}_{=:\Sigma_j(D, \Delta, T)} \quad (6.1.6) \end{aligned}$$

Indeed, on the one hand, the real modes $e^{\lambda_i \cdot}$ are decreasing exponential functions, such that the least upper bound on $[0, T]$ is reached at $\tilde{t} = 0$, and, on the other hand, $e^{\lambda_F \cdot}$ is the slowest mode (for all $i \in \{1, \dots, n\}$, $\lambda_i \leq \lambda_F$). If

$$\begin{aligned} \Sigma_j \cdot e^{\lambda_F (N-1)T} &\leq 0.01 \\ N &\geq \frac{\ln(0.01) - \ln(\Sigma_j)}{\lambda_F T} + 1 \end{aligned}$$

then, for all $\tilde{t} \in [0, T]$,

$$|y_j^N(\tilde{t}) - y_j^\infty(\tilde{t})| \leq 0.01. \quad \square$$

Numerical tests, using the (deterministic) popPK model of meropenem and the covariate values observed in the patients included in the PROMESSE dataset, show that $\Sigma_1(D, \Delta, T) > \Sigma_2(D, \Delta, T)$. That would mean that

$$\max\{N_1, N_2\} = N_1$$

and that the steady-state is reached more rapidly for the ELF concentrations than plasma concentrations. At equal infusion duration and dosing interval, the higher the dose is, the higher Σ_j is, and the higher the number of administrations needed to reach the steady state is. Besides, under the reasonable⁽¹⁾ assumption that $\Sigma_j \geq 0.01$, at equal dose and infusion duration, the shorter the dosing interval is, the smaller the number of administrations needed to reach the steady state is.

We can also determine a more conservative settling time by observing that

$$\Sigma_j(D, \Delta, T) \leq \frac{D}{\Delta} \sum_{i=1}^n \left| \frac{F_{ji}}{\lambda_i} \right| =: \tilde{\Sigma}_j$$

⁽¹⁾according to the values observed during the numerical tests.

since $\Delta \leq T$. This way, we observe that, at equal dose and dosing interval, the higher the infusion duration is, the lower $\tilde{\Sigma}_j$ is, and the lower the number of administrations needed to ensure the steady-state is.

The number of administrations N_j ($j \in \{1, 2\}$) needed to reach the steady-state may be approximated by

$$N_j \simeq \left\lceil \frac{\ln(0.01)}{\lambda_F \cdot T} \right\rceil + 2. \quad (6.1.7)$$

This approximation is exact if $\Sigma_j(D, \Delta, T) = 1$. Let observe, in (6.1.6), that $\Sigma_j(D, \Delta, T)$ is an upper bound of the *initial error* $e(y_j^1, y_j^\infty)$ between the zero-state response and the equilibrium trajectory. Therefore, if the initial error is bigger than 1 mg/L,

$$\Sigma_j(D, \Delta, T) > 1.$$

Hence (6.1.7) is an **underestimation** of (6.1.4). The bigger Σ_j is, the worst the approximation is. Higher dose, longer dosing interval and shorter infusion duration make this approximation still worse. On the contrary, if

$$\Sigma_j(D, \Delta, T) < 1,$$

(6.1.7) is an **overestimation** of N_j .

6.2 Dose selection for time-dependent AB

In this section, $y(t)$ and $y^\infty(\tilde{t})$ are denoted by $y(D, \Delta, T; t)$ and $y^\infty(D, \Delta, T; \tilde{t})$, respectively, in order to highlight the dependence with respect to the input parameters. The *mode of administration*, i.e., the infusion duration Δ [h] and the length of the dosing interval T [h], is assumed to be fixed. The following reasoning aims to determine the appropriate maintenance dose D needed to meet the PK/PD target given these practical constraints. For antibiotics with a (narrow) therapeutic window, it is necessary to either determine the maximum dose not to be exceeded, or to allow a second degree of freedom to prevent toxicity (see Section 6.3). In the later case, we need to fine-tune one of the two other input parameters, in addition to the dose.

6.2.1 Input-output formula

A simple and natural approach to determine the dose needed to reach a (systemic - $j = 1$, or infection-site - $j = 2$) target concentration α at a given time $t^* \in [0, T]$ of the steady-state dosing interval consists in solving the following equation with respect to D :

$$y_j^\infty(D, \Delta, T; \tilde{t} = t^*) = \alpha \quad (6.2.1)$$

The relevant time t^* depends on the PD index. For a concentration-dependent AB, it is the time corresponding to the maximal concentration (c_{\max}), and for a time-dependent AB, it is the time which corresponds to the desired %T>MIC. E.g., to

ensure $100\%T > \text{MIC}$, t^* should be the time of c_{trough} . Besides, if it is necessary to reach the PK/PD target after the very first infusion, a loading dose can be found by solving the following equation with respect to D :

$$y_j(D, \Delta, T; t = t^*) = \alpha.$$

Note the difference with (6.2.1).

Proposition 6.2.1 and Corrolary 6.2.3 below are established for the most stringent PD index ($100\%T > \text{MIC}$) of a time-dependent AB without clinically relevant time disconnect between systemic and infection-site concentrations. Consequently, the time t^* corresponds to c_{trough} and is T whatever the compartment.

Proposition 6.2.1 (I/O formula) Consider the PK system (6.1.1)-(6.1.2) with an input function of the form (6.1.3). For any target concentration level $\alpha > 0$ [mg/L], the maintenance dose [g] required to maintain the steady output trajectory y_j^∞ above the threshold α is given by

$$D = \frac{\alpha \Delta}{\sum_{i=1}^n \frac{F_{ji}}{\lambda_i} \frac{1 - e^{-\lambda_i \Delta}}{e^{-\lambda_i T} - 1}}. \quad (6.2.2)$$

The loading dose [g] is given by

$$D_L = \frac{\alpha \Delta}{\sum_{i=1}^n \frac{F_{ji}}{\lambda_i} e^{\lambda_i T} (1 - e^{-\lambda_i \Delta})}.$$

For all $i \in \{1, 2, 3, \dots, n\}$, $\lambda_i \in \sigma(A)$ and $F_{ji} = \frac{1}{S_j} (v_i)_j (w_i^*)_1 b_1$.

Formula 6.2.2 is called *input-output (I/O) formula*. It can be adapted to alternative PD target, provided that the relevant time t^* is well-determined. The block diagram in Figure 6.4 represents the resulting open-loop system.

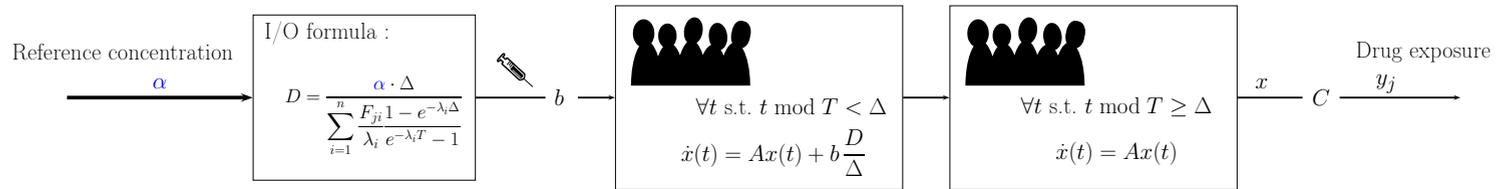


Figure 6.4 – Block diagram representing the open-loop system. $[A, b, C]$, model specific to the individual patient; α , target (minimal) concentration; y_j , system output (concentration in the plasma - $j = 1$, or at the site of infection - $j = 2$). The coefficients F_{ji} and λ_i ($i \in \{1, 2, 3, \dots, n\}$) are directly related to the model parameters.

The parameters F_{ij} and λ_i are directly related to the PK parameters and, consequently, to the realization of the random effects. However, these realizations are, *a priori*, unknown. A way to overcome this difficulty is to incorporate the I/O formula into a worst-case analysis. In the meantime, if the PK parameters including a random component are set to their nominal/typical value, Formula (6.2.2) provides a successful dosage for the nominal PK profile, as well as the median PK profile of the MC simulations (see Figure 6.5).

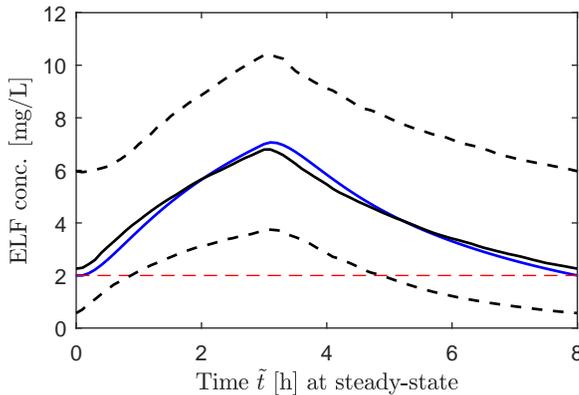


Figure 6.5 – Monte Carlo simulations of the typical patient (WT, 75 kg; GFR, 65 mL/min; $n_{\text{sim}} = 1000$) for a typical dose obtained by the I/O formula in the nominal case. Dashed black lines represent the 90 % prediction interval; solid black line, median PK profile; blue line, nominal PK profile; horizontal dashed red line, target concentration level.

6.2.2 “Worst-case” analysis

A sensitivity analysis was performed on the popPK model described in Section 4.2 (see Appendix E) and revealed that, among all the PK parameters including IIV components, the clearance has the most important influence on the model predictions. Given the individual characteristics/covariates, we call *worst-case system*, the virtual patient $[A, b, C]$ corresponding to the worst realization of the clearance regarding the PK/PD target, all the other parameters set to their nominal value.

Below, the state trajectory $x(t)$ and the steady output trajectory $y^\infty(\tilde{t})$ are denoted by $x(t; CL)$ and $y^\infty(\tilde{t}; CL)$. We prove here the monotony of the state trajectories with respect to the clearance.

Proposition 6.2.2 Consider the PK system (6.1.1), where A is either (1.3.6) or (4.3.2) and $b \in \mathbb{R}^{n \times 1}$ is any nonnegative matrix. The state trajectory $x(\cdot; CL)$ is decreasing with respect to the clearance parameter, i.e., if $0 < CL_1 \leq CL_2$ and if $x(0; CL_1) \geq x(0; CL_2)$, then, for all $t \geq 0$, $x(t; CL_1) \geq x(t; CL_2)$.

Remark 4 Clearance is the only model parameter with a random-effect component in the physiologically based model built in Section 4.3.

Proof. Using the physiological parametrization, the state matrix of the popPK model (1.3.6) reads as:

$$A = \begin{pmatrix} -\frac{CL}{V_1} - \sum_{j=2}^n \frac{Q_j}{V_1} & \frac{Q_2}{V_2} & \frac{Q_3}{V_3} & \cdots & \cdots & \frac{Q_n}{V_n} \\ \frac{Q_2}{V_1} & -\frac{Q_2}{V_2} & 0 & 0 & \cdots & 0 \\ \frac{Q_3}{V_1} & 0 & -\frac{Q_3}{V_3} & 0 & \cdots & \vdots \\ \vdots & \vdots & 0 & \ddots & \ddots & \vdots \\ \vdots & \vdots & \vdots & \ddots & \ddots & 0 \\ \frac{Q_n}{V_1} & 0 & 0 & \cdots & 0 & -\frac{Q_n}{V_n} \end{pmatrix}$$

Remember that the state matrix of the PBPK model (4.3.2) is given by:

$$A = \begin{pmatrix} -\frac{Q_{co}}{V_a} & \frac{Q_{co}}{K_{pLu}V_a} & 0 & 0 & 0 & 0 \\ 0 & -\frac{Q_{co}}{K_{pLu}V_{Lu}} & \frac{Q_{co}}{V_{Lu}} & 0 & 0 & 0 \\ 0 & 0 & -\frac{Q_{co}}{V_v} & \frac{Q_{Li}}{K_{pLi}V_v} & \frac{Q_{Ki}}{K_{pKi}V_v} & \frac{Q_{RB}}{K_{pRB}V_v} \\ \frac{Q_{Li}}{V_{Li}} & 0 & 0 & -\frac{Q_{Li} + CL_H}{K_{pLi}V_{Li}} & 0 & 0 \\ \frac{Q_{Ki}}{V_{Ki}} & 0 & 0 & 0 & -\frac{Q_{Ki} + CL_R}{K_{pKi}V_{Ki}} & 0 \\ \frac{Q_{RB}}{V_{RB}} & 0 & 0 & 0 & 0 & -\frac{Q_{RB}}{K_{pRB}V_{RB}} \end{pmatrix}$$

where $CL = CL_H + CL_R$.

Below, A is denoted by A_{CL} to highlight the dependence with respect to the clearance parameter. The state trajectories $x(t; CL_1) =: x(t)$ and $x(t; CL_2) =: \tilde{x}(t)$ (where $CL_1 \leq CL_2$) are the solutions of the two following Cauchy problems, respectively:

$$\begin{cases} \dot{x} = A_{CL_1}x + bu, & x(0) = x_0 \\ \dot{\tilde{x}} = A_{CL_2}\tilde{x} + bu, & \tilde{x}(0) = \tilde{x}_0 \end{cases}$$

where $0 \leq \tilde{x}_0 \leq x_0$. For the popPK model, the state matrix A_{CL_2} can be written as

$$A_{CL_2} = A_{CL_1} + \begin{pmatrix} -\varepsilon & 0 & \cdots \\ 0 & 0 & \cdots \\ \vdots & \vdots & \ddots \end{pmatrix}$$

where $\varepsilon = \frac{CL_2 - CL_1}{V_1} \geq 0$, and, for the PBPK model, the state matrix A_{CL_2} can be written as

$$A_{CL_2} = A_{CL_1} + \begin{pmatrix} \ddots & 0 & \cdots & \cdots & \cdots \\ 0 & -\varepsilon_1 & 0 & \cdots & \cdots \\ \vdots & \vdots & -\varepsilon_2 & 0 & \cdots \\ \vdots & \vdots & 0 & 0 & \cdots \\ \vdots & \vdots & \vdots & \vdots & \ddots \end{pmatrix}$$

where $\varepsilon_1 = \frac{CL_{H_2} - CL_{H_1}}{V_{Li}K_{pLi}} \geq 0$ and $\varepsilon_2 = \frac{CL_{R_2} - CL_{R_1}}{V_{Ki}K_{pKi}} \geq 0$.

Besides, we have

$$\frac{d}{dt}(x - \tilde{x}) = A_{CL_1}(x - \tilde{x}) + (A_{CL_1} - A_{CL_2})\tilde{x},$$

which obviously describes a nonnegative system (A_{CL_1} is Metzler and $A_{CL_1} - A_{CL_2}$ is nonnegative). Since its initial condition $x_0 - \tilde{x}_0 \geq 0$ and its input function \tilde{x} verifies $\tilde{x}(t) \geq 0$ for all $t \geq 0$,

$$x(t) - \tilde{x}(t) \geq 0$$

for all $t \geq 0$ (see Chapter 1, Definition 4). Consequently, $x(t; CL_1) \geq x(t; CL_2)$ for all $t \geq 0$. \square

Proposition 6.2.2 holds also for the steady output trajectory. In particular, whenever $0 < CL_1 \leq CL_2$, for all $\tilde{t} \in [0, T]$, $y^\infty(\tilde{t}; CL_1) \geq y^\infty(\tilde{t}; CL_2)$. It is illustrated in Figure 6.6. Given that the PK/PD target is to maintain the steady output trajectory $y_j^\infty(\cdot; CL)$ ($j \in \{1, 2\}$) sufficiently high, the worst clearance corresponds to its highest value. However, theoretically, the clearance may take any value on the real axis. Indeed, according to Equation (1.3.11),

$$CL = TVCL \cdot \exp(\eta), \quad \eta \sim N(0, \omega^2)$$

where, given the covariates, $TVCL$ is the individual typical value of the parameter. We define the *worst-case realization* at $p \cdot 100\%$, where $0 < p < 1$ and $p = k/q$, as its k^{th} q -quantile. For example, the worst-case realization at 90% ($p = 0.9$) of CL corresponds to its 9th deciles associated to $\eta^* = 1.28 \cdot \omega$ (see Figure 6.7).

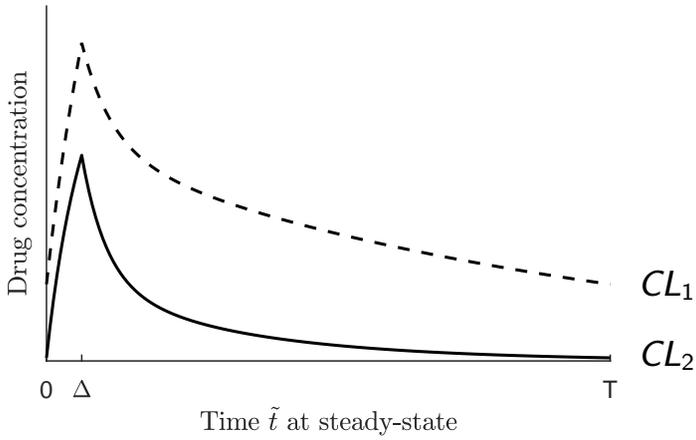


Figure 6.6 – Hypothetical PK profiles $y_j^\infty(\cdot; CL)$. $CL_1 < CL_2$.

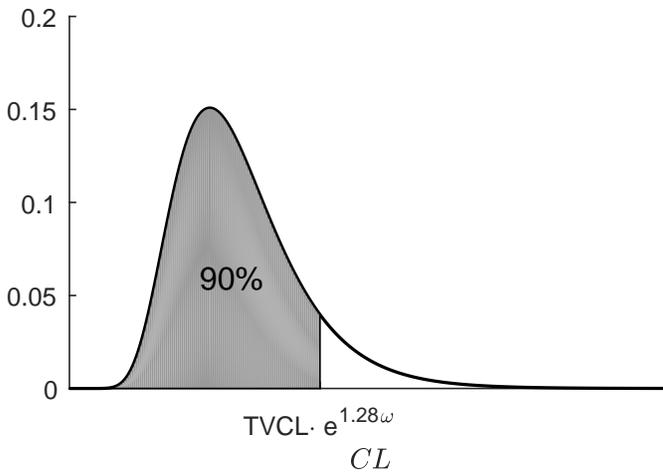


Figure 6.7 – Density function of the log-normally distributed clearance parameter. TVCL, individual typical value.

The following Corollary is an application of Proposition 6.2.1 to the “worst case” system.

Corollary 6.2.3 Consider the PK system (6.1.1)-(6.1.2) with an input function of the form (6.1.3). Assume that the PK parameters including a random-effect component are set to their nominal values, except the clearance whose value is its worst-case realization at $p \cdot 100\%$ (“worst-case” system). Then, for any target concentration level $\alpha > 0$ [mg/L], the maintenance dose [g] computed according to the I/O formula (6.2.2) enables to maintain the steady output trajectory y_j^∞ above the threshold α in $p \cdot 100\%$ of simulated patients, provided that all their PK parameters, except the clearance, are fixed to their nominal value.

An application of this result is illustrated in Figure 6.8.

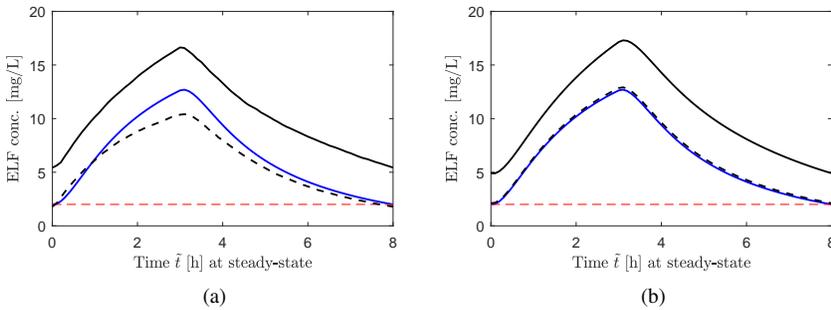


Figure 6.8 – Monte Carlo simulations of the typical patient (WT, 75 kg; GFR, 65 mL/min; $n_{\text{sim}} = 1000$) for a “worst-case” dose obtained by the I/O formula. For the graph (b), all the PK parameters were set to their median value, except the clearance. Dashed black lines, 10th percentile of the predictions; solid black line, median of the predictions; blue line, “worst-case” PK profile; horizontal dashed red line, target concentration level.

6.2.3 Drawbacks and advantages

The main drawbacks are related to the open-loop nature of the method, and the deterministic approach of a problem including variability. However, the I/O formula could be used to update the dose after concentration measurements (see feedback control law, Chapter 7). An additional weakness is the determination of the relevant time t^* in Equation (6.2.1), $j = 2$, in the case of an AB with important time disconnect between systemic and local concentrations.

This I/O formula for dose selection has several advantages. It is an analytical method in contrast to the empirical PTA-based method using on MC simulations at population level. Besides, if the individual characteristics of the patient are known, the described approach provides a dose at the individual level.

6.2.4 Application to meropenem dosage: a PTA-based comparison

A PTA analysis can be used to compare different dosing regimens. Two dosages were obtained by the I/O formula ($j = 2$), in the nominal case and in the “worst case” at 90 %, for a hypothetical target concentration (α , 2 mg/L)⁽²⁾, given the mode of administration (T , 8 hours; Δ , 30 min) and the patient’s characteristics (typical patient: WT, 75 kg; GFR, 65 mL/min). The respective dosing regimens (1.52g/8h over 30’ and 4.34g/8 over 30’) were compared using steady-state MC simulations of the typical patient. Figure 6.9 represents the PTA against a range of MICs for two PD indexes: 100%T>MIC and 50%T>MIC. They are compared with the common dosage recommended by the provider for adult patients with pneumonia: 1g by IV infusion over 30-minutes every 8h (see MHRA (2017) and FAMHP (2020))

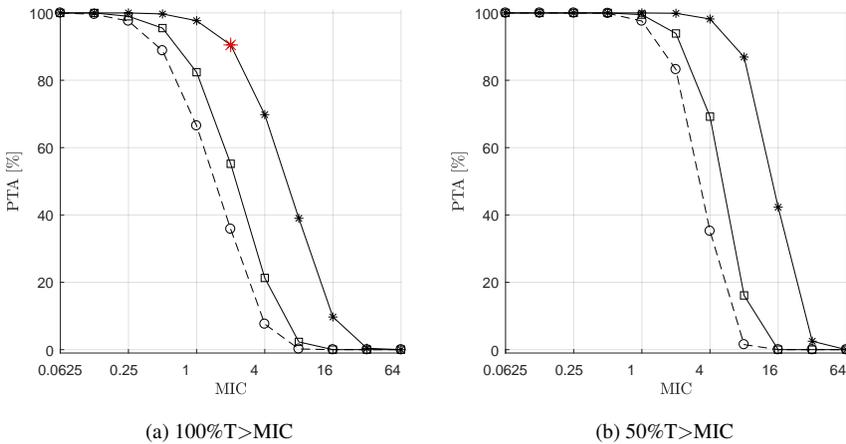


Figure 6.9 – Probability of target attainment for ELF concentrations based on MC simulations of the typical patient (WT, 75 kg; GFR, 65 mL/min; $n_{\text{sim}} = 1000$). Continuous lines with squares correspond to the typical dose (nominal case); continuous lines with stars correspond to the “worst-case” dose; dashed lines with circles correspond to the provider recommendation.

As expected, the dose associated to the “worst-case” system provides a probability of success of about 90% for a minimal inhibitory concentration of 2mg/L, see the red point in Figure 6.9(a). This conservative dose (4.34g) is obviously higher than the typical one (1.52g). However, this dosing strategy enables to ensure a larger proportion of patients meeting the PK/PD target.

⁽²⁾MICs of the drug against the antimicrobial agents are the results of *in vitro* analysis that are beyond the scope of this work.

6.3 Therapeutic window

Some patients are at risk of drug toxicity when receiving meropenem, see, e.g., Beumier et al. (2015). We suggest here two strategies to decrease costs and risks of drug accumulation and toxicity while ensuring drug efficacy. Both deserve to be deepened. The first one consists in using an adapted form of the I/O formula in order to identify the maximum dose not to be exceeded. The second assumes a second degree of freedom on the control variable, i.e., we can design the other input parameters to address the control problem. For this purpose, we introduce a well-known PD index: the *area under the concentration–time curve* (AUC).

6.3.1 Input-output formula

Proposition 6.3.1 below is established to determine the dose achieving a given maximal concentration α_{\max} for an AB without clinically relevant time disconnect between systemic and infection-site concentrations. Consequently, the time t^* in (6.2.1) should correspond to c_{\max} and is Δ whatever the compartment.

Proposition 6.3.1 (I/O formula) Consider the PK system (6.1.1)–(6.1.2) with an input function of the form (6.1.3). For any concentration $\alpha_{\max} > 0$ [mg/L], the maximum maintenance dose [g] for the steady output trajectory y_j^∞ not to exceed α_{\max} is given by

$$D = \frac{\alpha_{\max} \Delta}{\sum_{i=1}^n \frac{F_{ji}}{\lambda_i} \frac{e^{\lambda_i \Delta} - 1}{1 - e^{\lambda_i T}}}.$$

For all $i \in \{1, 2, 3, \dots, n\}$, $\lambda_i \in \sigma(A)$ and $F_{ji} = \frac{1}{S_j} (v_i)_j (w_i^*)_1 b_1$.

A worst-case approach is needed to deal with the unknown realization of the random effects. In that case, the target is to prevent the output trajectory to exceed a given threshold, such that the “worst-case” system corresponds to a low clearance, e.g., the worst-case system at 5%.

6.3.2 Area under the concentration-time curve

A short development using the analytical expression of the steady output trajectory y_j^∞ (see Proposition 6.1.2) enables to show that, for a n -compartment pharmacokinetic model, the steady-state AUC, denoted by AUC_j^∞ , is given by

$$AUC_j^\infty = \int_0^T y^\infty(\tilde{t}) d\tilde{t} = \int_0^\Delta y^\infty(\tilde{t}) d\tilde{t} + \int_\Delta^T y^\infty(\tilde{t}) d\tilde{t} = -D \sum_{i=1}^n \frac{F_{ji}}{\lambda_i}. \quad (6.3.1)$$

where, for all $i \in \{1, \dots, n\}$ F_{ji} is the residuals of the transfer function $\hat{g}_j(s)$ in the eigenvalue λ_i , i.e.,

$$F_{ji} = \frac{1}{S_j} (v_i)_j (w_i^*)_1 b_1.$$

Let apply this formula on the one- and two-compartment models.

- *One-compartment model* ($n = 1$). The state-space representation reads, for all $t \geq 0$, as

$$\dot{x}(t) = -k_{10}x(t) + u(t), \quad y(t) = \frac{1}{S}x(t)$$

where $S = V/usb$. Its transfer function $\hat{G}(s) \in \mathbb{R}_{p,0}(s)^{1 \times 1}$ is given by

$$\hat{g}_1(s) = \frac{usb/V}{s + k_{10}}.$$

Thus, using (6.3.1),

$$AUC_1^\infty = D \frac{usb}{k_{10}V} = \frac{D}{CL}usb$$

since

$$\lambda_1 = -k_{10} \quad \text{and} \quad F_{11} = \frac{usb}{V}.$$

- *Two-compartment model* ($n = 2$). The state-space representation reads, for all $t \geq 0$, as

$$\dot{x}(t) = \begin{pmatrix} -k_{10} - k_{12} & k_{21} \\ k_{12} & -k_{21} \end{pmatrix} x(t) + \begin{pmatrix} 1 \\ 0 \end{pmatrix} u(t), \quad y(t) = \begin{pmatrix} 1/S_1 & 0 \\ 0 & 1/S_2 \end{pmatrix} x(t)$$

Its transfer function $\hat{G}(s) \in \mathbb{R}_{p,0}(s)^{2 \times 1}$ is given by

$$\begin{cases} \hat{g}_1(s) = \frac{usb_1}{V_1} \frac{s + k_{21}}{(s - \lambda_1)(s - \lambda_2)} = \frac{F_{11}}{s - \lambda_1} + \frac{F_{12}}{s - \lambda_2} \\ \hat{g}_2(s) = \frac{usb_2}{V_2} \frac{k_{12}}{(s - \lambda_1)(s - \lambda_2)} = \frac{F_{21}}{s - \lambda_1} + \frac{F_{22}}{s - \lambda_2} \end{cases}$$

where

$$F_{11} = \frac{usb_1}{V_1} \frac{\lambda_1 + k_{21}}{\lambda_1 - \lambda_2}, \quad F_{12} = \frac{usb_1}{V_1} \frac{\lambda_2 + k_{21}}{\lambda_2 - \lambda_1}$$

and

$$F_{21} = \frac{usb_2}{V_2} \frac{k_{12}}{\lambda_1 - \lambda_2}, \quad F_{22} = \frac{usb_2}{V_2} \frac{k_{12}}{\lambda_2 - \lambda_1}.$$

Thus,

$$AUC_1^\infty = -D \left(\frac{F_{11}}{\lambda_1} + \frac{F_{12}}{\lambda_2} \right) = D \frac{usb_1}{V_1 k_{10}} = \frac{D}{CL}usb_1$$

and

$$AUC_2^\infty = D \left(\frac{F_{21}}{\lambda_1} + \frac{F_{22}}{\lambda_2} \right) = D \frac{usv_2}{V_2} \frac{k_{12}}{k_{10}k_{21}} = D \frac{usv_2}{V_1k_{10}} = \frac{D}{CL} usv_2$$

using $\lambda_1\lambda_2 = k_{10}k_{21}$. The following relationship holds:

$$\frac{AUC_2^\infty}{AUC_1^\infty} = \frac{usv_2}{usv_1} \quad (6.3.2)$$

which is the penetration ratio (see (1.3.8)).

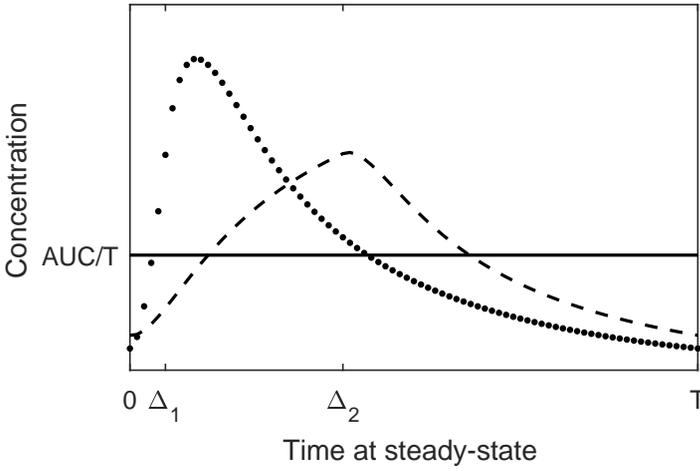


Figure 6.10 – Hypothetical PK profiles $y_j^\infty(D, \Delta, T; \bar{t})$ for different modes of administration, but equal dose. Dotted line, intermittent infusion ($\Delta = \Delta_1$); dashed line, extended infusion ($\Delta = \Delta_2$); continuous line, continuous infusion ($\Delta = T$).

We observe in (6.3.1) that the AUC^∞ is independent of the mode of administration, i.e., Δ and T , contrary to the amount D . Indeed, the parameters F_{ji} and λ_i depend only on the transfer function $\hat{G}(s) = C(sI - A)^{-1}b$ and the state matrix A , i.e., to the system $[A, b, C]$. In particular, at equal dose, the average concentrations over the steady-state dosing interval, given by

$$\frac{AUC_j^\infty}{T} = \frac{D}{T} \hat{g}_j(0),$$

are the same regardless of the value of Δ (Figure 6.10). Consequently, the dose needed for the concentration to reach a PK/PD target is expected to be higher if given by intermittent infusion rather than by extended or continuous infusion. This is consistent with the PK literature; e.g., it is stated in Zhou et al. (2017) that exposure may be improved by (1) “increasing the dose while retaining the same dosage interval,” (2) “reducing the dosage interval while retaining the same dose,” or (3) “increasing the duration of IV infusion.”

Table 6.1 provides the doses computed by the I/O formula (in the nominal case) for different modes of administration, but the same PK/PD target. Figure 6.11 shows the corresponding nominal PK profiles. For a given therapeutic window, i.e., a constraint on the maximal concentration in addition to the MIC constraint, the appropriate infusion duration, or length of the dosing interval (equivalent to the number of daily doses), can be determined by numerical resolution of Equation (6.2.1) with respect to Δ , or T .

Table 6.1 – Typical maintenance doses [g] obtained with the I/O formula for different modes of administration ($j = 2$; target concentration level α , 2 mg/L; T , 8 hours; WT, 75 kg)

	poor renal function GFR = 30 mL/min	typical/median patient GFR = 65 mL/min	good renal function GFR = 120 mL/min
II $\Delta = 0.5\text{h}$	0.545	1.52	4.21
EI $\Delta = 3\text{h}$	0.448	1.10	2.62
CI $\Delta = 8\text{h} = T$	0.292	0.510	0.794

II, intermittent infusion; EI, extended infusion; CI, continuous infusion

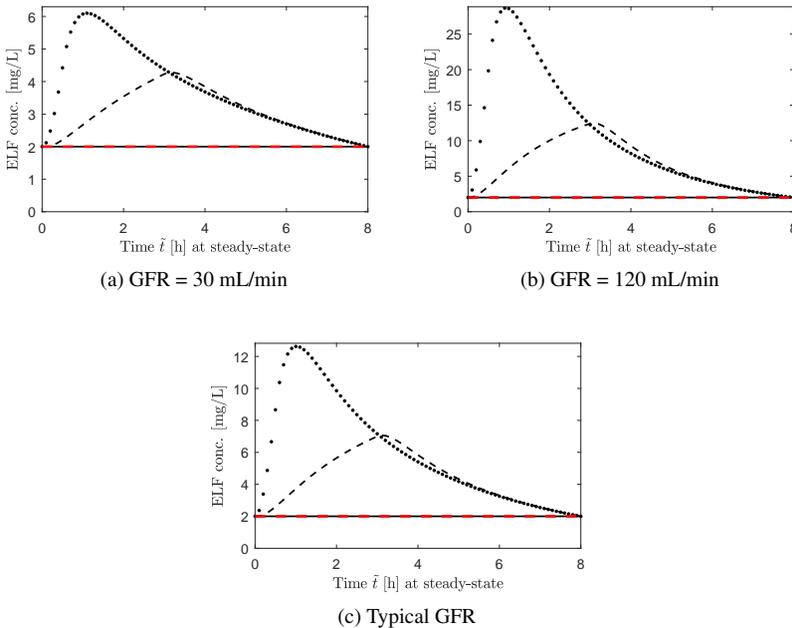


Figure 6.11 – Nominal PK profiles for different dosing scenarios as described in Table 6.1. Dotted line, intermittent infusion; dashed line, extended infusion; continuous line, continuous infusion (confused with the horizontal red line $y = 2$ that represents the target concentration level).

State estimation and feedback control law

This chapter deals with a heuristic feedback control in order to adjust the individual dosing after Bayes estimations. The control law is based on the estimated state and uses the I/O formula. It is also part of Thémans et al. (2020c)).

7.1 Discrete-time state estimator

In this chapter, we distinguish the observed output (y_1) and the regulated output (y_1 or y_2) using distinct output matrices:

$$C_{\text{mes}} = (1/S_1 \quad 0 \quad 0 \quad \dots \quad 0) \in \mathbb{R}^{1 \times n}$$

and

$$C_{\text{reg}} = (1/S_1 \quad 0 \quad 0 \quad \dots \quad 0) \in \mathbb{R}^{1 \times n} \quad \text{or} \quad C_{\text{reg}} = (0 \quad 1/S_2 \quad 0 \quad \dots \quad 0) \in \mathbb{R}^{1 \times n}$$

where, for all $j \in \{1, 2\}$, S_j converts the state component x_j in concentration both in plasma ($j = 1$) and at the site of infection ($j = 2$).

Since the plasma concentration is *not* continually measured, we need to transform the continuous-time dynamical system (6.1.1) in a discrete-time setting. Let h be the *sample time*, also called discretization step, and $N := \frac{T}{h} \in \mathbb{N}_0$ the number of sampling intervals of any dosing interval $[iT, (i+1)T[$ ($i \in \mathbb{N}$). Consider $x[k] := x(kh)$ and $u[k] := u(kh)$. The discrete-time state-space representation (recurrence equations) is given, for all $k \in \mathbb{N}$, by

$$\begin{cases} x[k+1] = A_d x[k] + b_d u[k], & x[0] = 0 \\ y[k] = C_{\text{mes}} x[k] \end{cases} \quad (7.1.1)$$

The matrices A_d and b_d can be derived from the integral form of the state trajectory

$$x(t) = e^{A(t-t_0)}x(t_0) + \int_{t_0}^t e^{A(t-\tau)}bu(\tau)d\tau, \quad \forall t \geq 0 \quad (7.1.2)$$

where the control input $u(\cdot)$ is assumed constant on the sampling intervals (zero-order hold), i.e., for all $k \in \mathbb{N}$,

$$u(t) = u(kh), \quad \forall t \in [kh, (k+1)h].$$

With $t \leftarrow (k+1)h$ and $t_0 \leftarrow kh$ in (7.1.2), we obtain

$$x[k+1] = \underbrace{e^{Ah}}_{A_d} x[k] + \underbrace{\int_0^h e^{As} ds}_{b_d} u[k].$$

Since the continuous-time input function is a piecewise constant function, the solution $x[k]$ of (7.1.1) is exactly the continuous-time solution $x(\cdot)$ at the sampling time $t = kh$. The discrete-time input function is given, for all $k \in \mathbb{N}$, by

$$u[k] [g/h] = \begin{cases} D_i/\Delta & \text{if } (k \bmod N) < N_1 \quad (i = \lfloor k/N \rfloor) \\ 0 & \text{if } (k \bmod N) \geq N_1 \end{cases}$$

where $N_1 := \frac{\Delta}{h} \in \mathbb{N}_0$ is the number of sampling intervals of any administration interval $[iT, iT + \Delta]$ ($i \in \mathbb{N}$), and D_i denotes the dose administrated on the $(i+1)$ th dosing interval (see, e.g., Figure 8.1). We necessarily have

$$\frac{T}{\Delta} = \frac{N}{N_1}. \quad (7.1.3)$$

W.l.o.g., let N_1 and N be the smallest integers verifying (7.1.3). The nonnegativity and internal stability are directly derived from the nonnegativity and internal stability of the continuous-time system, see (Haddad et al., 2010, Chapter 2).

Let assume, in line with the clinical practice, that the plasma concentration is measured at the end of each dosing interval, just before a new administration. Therefore, the time scale of the state estimator will be larger than the one of the dynamics. For all $i \in \mathbb{N}$, $\tilde{x}[i]$ denotes the estimated state of $x[iN] = x(iT)$ and $u_i := u[iN] = D_i/\Delta$. A state estimator is therefore described by the following system:

$$\begin{cases} \tilde{x}[i+1] = \mathcal{A}\tilde{x}[i] + \mathcal{B}u_i + \mathcal{L}(\tilde{y}[i] - y[iN]), & \tilde{x}[0] = 0 \\ \tilde{y}[i] = C_{\text{mes}}\tilde{x}[i] \end{cases}$$

where

$$\mathcal{A} = A_d^N \text{ and } \mathcal{B} = \sum_{l=1}^{N_1} A_d^{N-l} b_d.$$

The matrix \mathcal{L} is called (*output error injection matrix*) and has to be designed such that $\mathcal{A} + \mathcal{L}C_{\text{mes}}$ is stable, i.e., for all $\lambda \in \sigma(\mathcal{A} + \mathcal{L}C_{\text{mes}})$, $|\lambda| < 1$. Standard methods, such as pole placement or Kalman filter,⁽¹⁾ can be used to determine \mathcal{L} .

⁽¹⁾This is beyond the scope of the thesis.

7.2 Dose adjustment: heuristic method

In this section, we derive a feedback dosing strategy from the superposition principle stating that the state trajectory of the system $[A, b, C]$ is linear with respect to the input level. Therefore, for any doses $D_1, D_2 > 0$ and for all $\tilde{t} \in [0, T]$,

$$y^\infty(D_1 + D_2, \Delta, T; \tilde{t}) = y^\infty(D_1, \Delta, T; \tilde{t}) + y^\infty(D_2, \Delta, T; \tilde{t}).$$

The I/O formula is used to update the dose and fill the *gap* between the target concentration and the estimated or measured concentration in the compartment of interest. The feedback control law for individual dosing adjustment is reported below as an algorithm.

Algorithm (Estimated state feedback)

Data: The mode of administration (T and Δ); the target level (*reference* α) of the regulated output; the typical value of the parameters and the patient's characteristics (\rightarrow nominal or “worst-case” system $[A, b, C_{\text{mes}}/C_{\text{reg}}]$); the dosing interval of the first dose adjustment (e.g., $m_0 := N^* + 1$, see Remark 6 below).

The individual realizations of the random-effect component are unknown.

Base step: The first dose D_0 is computed by the I/O formula (6.2.2). The output injection matrix \mathcal{L} and the discrete-time state estimator are determined. For all $i \in \{0, \dots, m_0 - 1\}$, $D_i = D_0$. We define by

$$GAP := \alpha - C_{\text{reg}} \tilde{x}[m_0 - 1]$$

the “gap” at the beginning of the m_0^{th} dosing interval.

Intermediate step: The individual parameter estimates (EBEs) are computed (see Remark 5). The output injection matrix \mathcal{L} and the discrete-time state estimator are also updated. Replacing $\alpha \leftarrow GAP$ in (6.2.2) yields the following estimated state feedback law:

$$\begin{aligned} D_1 &= D_0 + \tilde{D} \\ D_i &= D_1 \end{aligned}$$

for all $i \in \{m_0, \dots, m_1 - 1\}$, where

$$\tilde{D} = \frac{GAP \cdot \Delta}{\sum_{i=1}^n \frac{F_i}{\lambda_i} \frac{1 - e^{-\lambda_i \Delta}}{e^{-\lambda_i T} - 1}}. \quad (7.2.1)$$

where, for all $i \in \{1, \dots, n\}$, λ_i is the i^{e} eigenvalue of the (updated) state matrix A and $F_i := \lim_{s \rightarrow \lambda_i} (\hat{g}(s)(s - \lambda_i))$ denotes the residual in λ_i of the transfer function \hat{g} corresponding to the system $[A, b, C_{\text{reg}}]$.

The dosing intervals of the next dose adjustments are updated (see Remark 6).

$q \leftarrow 1$.

Recurrence step: While $|GAP| \geq 0.01$: let

$$GAP := \alpha - C_{\text{reg}}\tilde{x}[m_q - 1].$$

The dose is updated following:

$$\begin{aligned} D_q &= D_{q-1} + \tilde{D} \\ D_i &= D_q \end{aligned}$$

for all $i \in \{m_{q-1}, \dots, m_q - 1\}$, where \tilde{D} is given by (7.2.1). $q \leftarrow q + 1$.

The block diagram in Figure 7.2 represents the resulting closed-loop system.

Remark 5 A Bayesian analysis (see Figure 7.1) can be easily implemented via the \$EST step of NONMEM with the option MAXEVAL=0 (Simon (2020)). It will provide the most likely values of the model random variables given observed concentrations in a particular patient. This procedure is automated, e.g., in the website *TDMx* by Wicha (2018). The updated model describes then how the drug is behaving in that patient (Vinks (2002)).

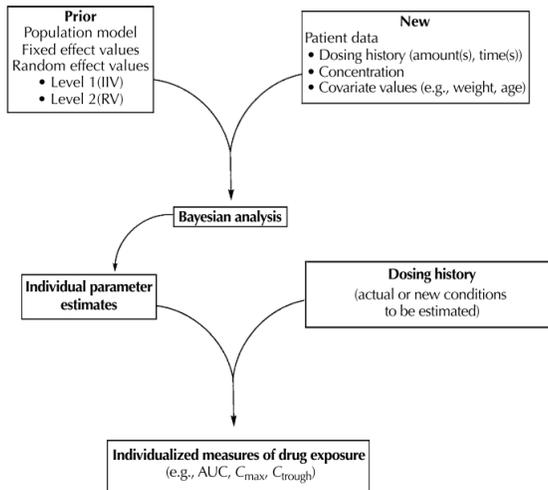


Figure 7.1 – Overview of the parameter Bayesian estimation in a typical PK project. IIV, interindividual variability; RV, residual variability; AUC, area under the concentration versus time curve; C_{max} , maximal concentration; C_{trough} , minimal concentration. Illustration taken from Owen and Fiedler-Kelly (2014).

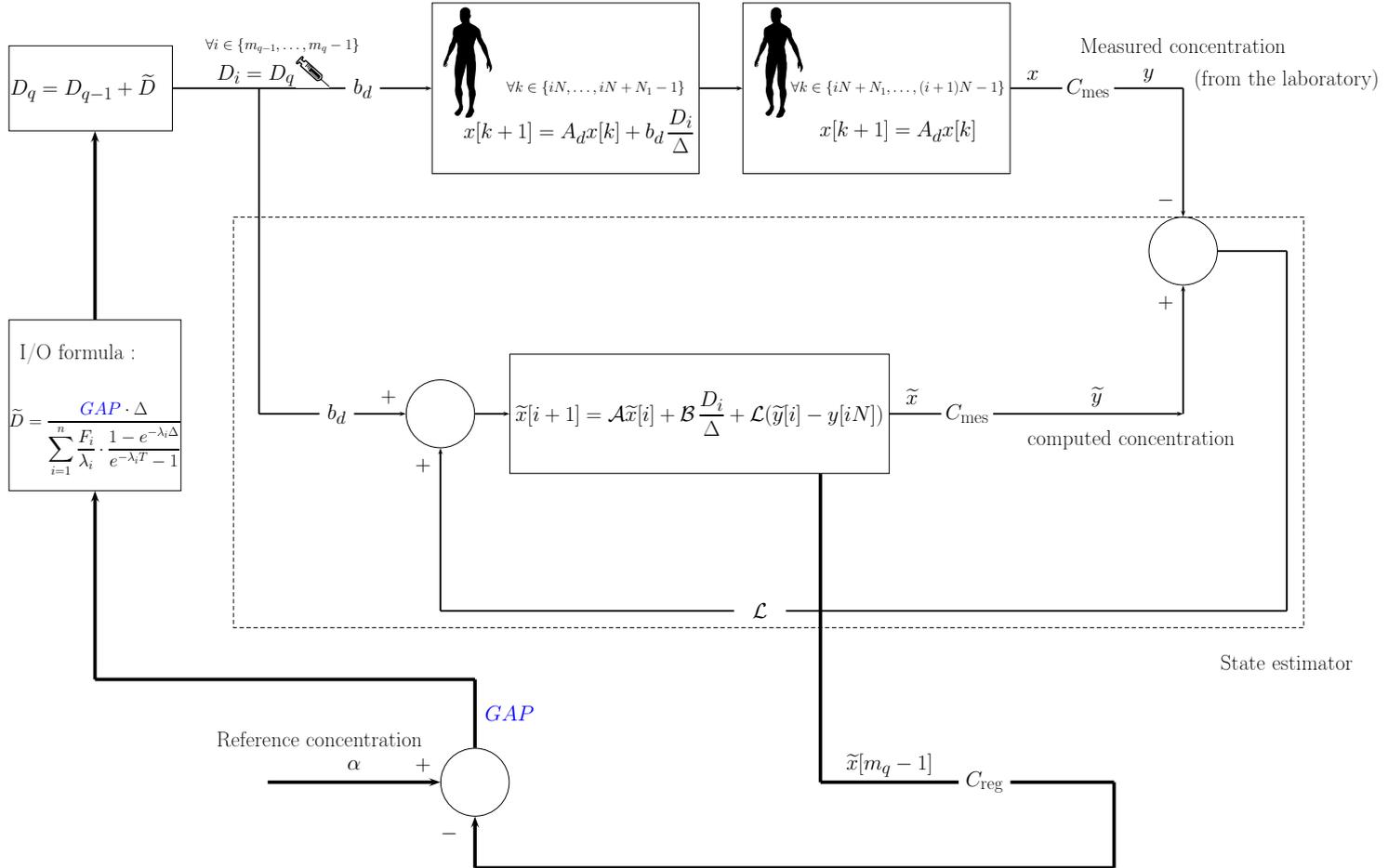


Figure 7.2 – Block diagram representing the closed-loop system (recurrence step, $q \in \mathbb{N}_0$). $[A_d, b_d, C_{mes}]$, (discrete-time) model specific to the individual patient. The coefficients F_i and λ_i ($i \in \{1, 2, 3, \dots, n\}$) are directly related to the parameters of the continuous-time model specific to the individual patient $[A, b, C_{reg}]$.

Remark 6 Since the I/O formula is established to reach the PK/PD target at steady state, “gap” evaluation and dose adjustment (state feedback) should be performed when the output trajectory is sufficiently close to the equilibrium trajectory. Combining the time needed for the zero-input state trajectory to reach zero (Propositions 1.3.3) and the number of administrations for the output trajectory y_j to reach the steady output (Proposition 6.1.3), the number of dosing intervals to assume that the system $[A, b, C_{\text{mes}}/C_{\text{reg}}]$ has reached the steady state is given by

$$\max \{N^*, \lfloor t^*/T \rfloor + 1\}$$

where

$$N^* [\text{adm}] = \max \left\{ \left\lfloor \frac{\ln(0.01) - \ln(\Sigma)}{\lambda_F \cdot T} \right\rfloor + 2, 0 \right\},$$

$$\Sigma(D, \Delta, T) = \frac{D}{\Delta} \sum_{i=1}^n \left| \frac{F_i}{\lambda_i} \right| \frac{1 - e^{-\lambda_i \Delta}}{1 - e^{-\lambda_i T}}$$

where D corresponds to D_0 in the base step and to the successive \tilde{D} in the recurrence step, and

$$t^* [\text{h}] = \frac{\ln(0.01) - \ln \left(\sum_{i=1}^n \|w_i\| \right)}{\lambda_F}$$

where $\{w_j : j \in \underline{n}\}$ are the left eigenvectors of the state matrix A , associated to normalized right eigenvectors.

7.3 Application to meropenem dosage

Given a hypothetical target concentration (α , 2 mg/L), the mode of administration (T , 8 hours; Δ , 30 min), and the patient’s characteristics (typical patient: WT, 75 kg; GFR, 65 mL/min), Figures 7.3(a)-(b) show the evolution of the input function and the PK profile attributable to this feedback control law. The error injection matrix \mathcal{L} was designed using the *place* function of MATLAB and an arbitrary closed-loop pole location ($p = [-1/3, 0, 1/3]$). The number of dosing intervals needed to reach the steady state was approximated by

$$N^* \simeq \left\lfloor \frac{\ln(0.01)}{\lambda_F \cdot T} \right\rfloor + 2 < \left\lfloor \frac{5\tau}{T} \right\rfloor + 2$$

where τ is the terminal time constant, such that

$$\begin{cases} m_0 = \lfloor 5\tau_0/T \rfloor + 2 \\ m_q = m_{q-1} + \lfloor 5\tau/T \rfloor + 2, \quad \forall q \in \mathbb{N}_0 \end{cases}$$

where τ_0 is the time constant *before* the Bayesian analysis.

The initial AB treatment was ~ 1.10 g over 3 hours every 8 hours. The Bayesian analysis to recalculate the model parameters was performed at the beginning of the 4th dosing interval (m_0). The time constant was then re-evaluated for the updated model. The successive doses were 5.18 g, 4.60 g and 3.94 g, updated every four infusions (m). In this illustration, the control law was based on the estimated state at the infection site, i.e.,

$$C_{\text{reg}} = (0 \quad 1/S_2 \quad 0 \quad \cdots \quad 0),$$

while the measures were plasma samples, as indicated by C_{mes} . The terminal half-life $\lambda_{1/2}$ of the nominal system and the updated one were 2.86 hours and 2.75 hours, respectively.

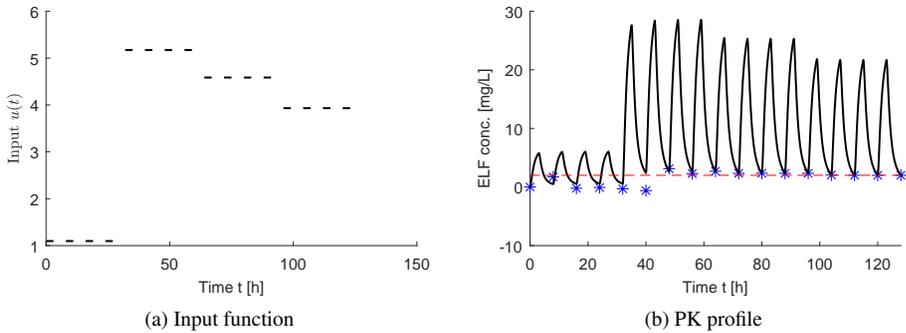


Figure 7.3 – Illustration of the state feedback algorithm. **(a)** Rate of infusion of the drug (D_i/Δ) w.r.t. time. **(b)** Continuous line, actual concentration-time curve; blue stars, estimated output $C_{\text{reg}}\hat{x}[i]$ at the beginning of each dosing interval, horizontal dashed red line, target concentration level.

Remark 7 This illustration of the heuristic feedback method for dosing adjustment was performed with customized MATLAB scripts. Three different systems were used: the “real” system corresponding to the virtual patient, the nominal system and the updated system after the Bayesian analysis. We assume that enough measurements have been taken to correctly determine the EBEs, such that the updated system and the “real” system coincide. The models were converted from continuous to discrete time using the *c2d* function of MATLAB.

Optimal control approach

This chapter deals with an optimal control approach for dosing recommendation. This approach aims at improving the drug dosing by optimizing a criteria under input and state constraints. The characterization of the optimal solution is derived from the minimum principle in discrete-time setting and formally proved by verifying the conditions of the Pontryagin's maximum principle as it is presented in Beauthier (2011) and Hartl et al. (1995). The numerical experimentations were performed using the nominal popPK model of meropenem for a typical patient (WT, 75 kg; GFR, 65 mL/min).

8.1 Continuous-time finite-horizon setting

Let consider the n -compartment pharmacokinetic system with finite horizon

$$\begin{cases} \dot{x}(t) = Ax(t) + bu(t) \\ y(t) = Cx(t) \end{cases} \quad t \in [0, t_f]$$

where $t_f = mT$ and $m \in \mathbb{N}_0$ corresponds to the (fixed) number of dosing intervals. The state matrix $A \in \mathbb{R}^{n \times n}$ is compartmental and the input matrix $b \in \mathbb{R}^{n \times 1}$ has the form

$$b = (b_1 \quad 0 \quad \dots \quad 0)^T \tag{8.1.1}$$

where $b_1 > 0$. Let assume the general form of the output matrix to be

$$C = \begin{pmatrix} 1/S_1 & 0 & 0 & \dots & 0 \\ 0 & 1/S_2 & 0 & \dots & 0 \end{pmatrix} \in \mathbb{R}^{2 \times n}$$

where, for all $j \in \{1, 2\}$, S_j converts the state component x_j in concentration (e.g., [mg/L]) both in plasma ($j = 1$) and at the site of infection ($j = 2$). The input function

$u(\cdot)$ (rate of infusion) is assumed to be constant but not necessarily the same on each dosing interval, i.e., for all $t \geq 0$,

$$u(t) [\text{g/h}] = \begin{cases} \bar{u}_i = D_i/\Delta & \text{if } (t \bmod T) < \Delta \quad (i = \lfloor t/T \rfloor) \\ 0 & \text{if } (t \bmod T) \geq \Delta \end{cases} \quad (8.1.2)$$

where D_i denotes the dose administered on the $(i + 1)^{\text{th}}$ dosing interval. Therefore, the control variable can be expressed as a vector $u = (u_1, \dots, u_{m-1})$. The function u is represented in Figure 8.1.

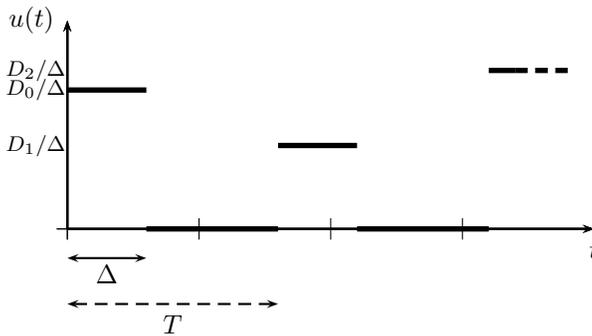


Figure 8.1 – System input function: drug infusion rate vs. time

Remark 8 As previously mentioned, the mode of infusion (length of the dosing interval T and infusion duration Δ) is fixed. We exclude the limit case $\Delta = T$ (continuous infusion). Instead, the drug is administrated by intermittent infusion, i.e., $\Delta < T$.

The studied OC problem consists in minimizing the squared L_2 -norm of the input function, i.e., the cost functional

$$J_1(u) = \int_0^{t_f} u^2(t) dt \quad (8.1.3)$$

or, equivalently, the quadratic functional

$$J_2(u) = \sum_{i=0}^{m-1} \bar{u}_i^2 \quad (8.1.4)$$

for the system dynamics $\dot{x} = Ax + bu$ with a fixed initial condition $x_0 = 0$, and under the following input and state constraints:

$$\begin{cases} u(t) = 0 & \forall t \text{ s.t. } (t \bmod T) \geq \Delta \\ u(t) = \bar{u}_i & \forall t \in [0, t_f[\text{ s.t. } (t \bmod T) < \Delta \quad (i = \lfloor t/T \rfloor) \\ \bar{u}_i \geq 0 & \forall i \in \{0, \dots, m-1\} \\ e_j^T x(t) \geq \alpha S_j & \forall t \in [n_{\text{adm}}T, t_f] \end{cases} \quad (8.1.5)$$

where the vector $e_j = (0 \ \cdots \ 0 \ 1 \ 0 \ \cdots \ 0)^T$ is the j^{th} vector of the canonical basis, $\alpha > 0$ is the target lower bound [mg/L] of the concentration trajectory y_j , e.g., the (systemic or infection-site) threshold for drug efficacy, and $n_{\text{adm}} \in \{1, \dots, m\}$ corresponds to the number of administrations required to reach and maintain the output trajectory above this lower bound.

The natural choice of the L_2 -norm enables to express the OC problem as a standard linear-quadratic problem under linear equality and convex inequality constraints. We state the conjecture that the input function that minimizes the L_2 -norm will also minimize the L_1 -norm. The L_1 -norm is interpreted as the area under the curve of u , i.e., the total amount of drug. This is relevant from a clinical point of view, since the solution will provide the lowest effective dosing (given the dosing interval and the infusion duration).

In Paragraph 8.2.2 and Section 8.3, the rate of infusion is assumed to be not necessarily constant on the dosing intervals, i.e., the second constraint is relaxed. This results in the following *simplified* constraints

$$\begin{cases} u(t) = 0 & \forall t \text{ s.t. } (t \bmod T) \geq \Delta \\ u(t) \geq 0 & \forall t \in [0, t_f] \text{ s.t. } (t \bmod T) < \Delta \\ e_j^T x(t) \geq \alpha S_j & \forall t \in [n_{\text{adm}}T, t_f] \end{cases} \quad (8.1.6)$$

Only the latter set of constraints is considered for the resolution of the continuous-time setting. For comparison purposes, the numerical implementations (discrete-time setting) were performed for both sets of constraints.

8.2 Discrete-time setting

Let h be the sample time. Following a reasoning similar to Section 7.1, the recurrence equations describing the state dynamics are

$$x[k+1] = A_d x[k] + b_d u[k], \quad \forall k \in \{iN, \dots, iN + N_1 - 1 | i = 0, \dots, m-1\} \quad (8.2.1)$$

$$x[k+1] = A_d x[k], \quad \forall k \in \{iN + N_1, \dots, (i+1)N - 1 | i = 0, \dots, m-1\} \quad (8.2.2)$$

where

$$A_d = e^{Ah}, \quad b_d = \int_0^h e^{As} ds b$$

and $N := T/h$ and $N_1 := \Delta/h$ are the number of sampling intervals of any dosing interval and sub-interval of administration, respectively. We can observe that the first constraint of (8.1.5) is directly expressed in the dynamics, i.e.,

$$u[k] = 0, \quad \forall k \in \{iN + N_1, \dots, (i+1)N - 1 | i = 0, \dots, m-1\}.$$

The OC problem consists in minimizing the quadratic function

$$\tilde{J}_1(u) = \sum_{i=0}^{m-1} \sum_{k=iN}^{iN+N_1-1} u^2[k] \quad (8.2.3)$$

or, equivalently,

$$\tilde{J}_2(u) = \sum_{i=0}^{m-1} u^2[iN] \quad (8.2.4)$$

for the system dynamics (8.2.1)-(8.2.2) with a fixed initial condition $x[0] = 0 \in \mathbb{R}^n$, and under the constraints equivalent to (8.1.5):

$$\begin{cases} u[k] = u[iN] & \forall k \in \{iN + 1, \dots, iN + N_1 - 1 \mid i = 0, \dots, m - 1\} \\ u[iN] \geq 0 & \forall i \in \{0, \dots, m - 1\} \\ e_j^T x[k] \geq \alpha S_j & \forall k \in \{n_{\text{adm}}N, \dots, mN\} \end{cases} \quad (8.2.5)$$

The first constraint will be omitted under the relaxed constraints, and, in that case, the objective function (8.2.3) should be used.

8.2.1 Minimum principle

The *Karush-Kuhn-Tucker (KKT) conditions* are necessary conditions for (local) optimality. Since the present problem is convex, they are also sufficient optimality conditions (Bierlaire (2015)).

The Lagrangian function is given by

$$\begin{aligned} \mathcal{L}(x, u, p, \mu, v, \bar{v}) = & \sum_{i=0}^{m-1} u^2[iN] + p[-1]^T (x[0] - 0) + \\ & \sum_{i=0}^{m-1} \sum_{k=iN}^{iN+N_1-1} p[k]^T (x[k+1] - A_d x[k] - b_d u[k]) + \\ & \sum_{i=0}^{m-1} \sum_{k=iN+N_1}^{(i+1)N-1} p[k]^T (x[k+1] - A_d x[k]) + \\ & \sum_{i=0}^{m-1} \sum_{k=iN+1}^{iN+N_1-1} \mu_k (u[k] - u[iN]) + \\ & \sum_{i=0}^{m-1} v_i (-u[iN]) + \sum_{k=n_{\text{adm}}N}^{mN} \bar{v}_k (-e_j^T x[k] + \alpha S_j) \end{aligned}$$

where $x := (x[0]^T \ \dots \ x[mN]^T)^T$ and $u := (u[0] \ \dots \ u[mN - 1])^T$ are the state and control variables. The $p[k] \in \mathbb{R}^n$ are the *adjoint state variables*, $\mu_k \in \mathbb{R}$ are the multipliers associated with the equality constraints and $v_i, \bar{v}_k \in \mathbb{R}$ are the multipliers associated with the inequality constraints, on the input and state variables, respectively.

The KKT conditions are given by the four following groups of conditions.

Stationarity conditions:

$$\partial \mathcal{L} / \partial x[k] = 0, \quad \forall k \in \{0, \dots, mN\} \quad (\text{a})$$

$$\partial \mathcal{L} / \partial u[k] = 0 \quad \forall k \in \{iN, \dots, iN + N_1 - 1 \mid i = 0, \dots, m - 1\} \quad (\text{b})$$

i.e.,

$$(\text{a}) \begin{cases} p[k-1] - A_d^T p[k] = 0 & \forall k \in \{iN, \dots, (i+1)N - 1 \mid i = 0, \dots, n_{\text{adm}} - 1\} \\ p[k-1] - A_d^T p[k] - \bar{v}_k e_j = 0 & \forall k \in \{iN, \dots, (i+1)N - 1 \mid i = n_{\text{adm}}, \dots, m - 1\} \\ p[mN - 1] - \bar{v}_{mN} e_j = 0 \end{cases}$$

$$(\text{b}) \begin{cases} 2u[iN] - b_d^T p[iN] - \sum_{k=iN+1}^{iN+N_1-1} \mu_k - v_i = 0 & \forall i \in \{0, \dots, m - 1\} \\ -b_d^T p[k] + \mu_k = 0 & \forall k \in \{iN + 1, \dots, iN + N_1 - 1 \mid i = 0, \dots, m - 1\} \end{cases}$$

Primal feasibility:

- Dynamics:

$$\begin{aligned} x[k+1] &= A_d x[k] + b_d u[k] & \forall k \in \{iN, \dots, iN + N_1 - 1 \mid i = 0, \dots, m - 1\} \\ x[k+1] &= A_d x[k] & \forall k \in \{iN + N_1, \dots, (i+1)N - 1 \mid i = 0, \dots, m - 1\} \\ x[0] &= 0 \end{aligned}$$

- Equality constraints:

$$u[k] = u[iN], \quad \forall k \in \{iN + 1, \dots, iN + N_1 - 1 \mid i = 0, \dots, m - 1\}$$

- Inequality constraints:

$$\begin{aligned} u[iN] &\geq 0 & \forall i \in \{0, \dots, m - 1\} \\ e_j^T x[k] - \alpha S_j &\geq 0 & \forall k \in \{n_{\text{adm}}N, \dots, mN\} \end{aligned}$$

Dual feasibility (sign constraints on the multipliers):

$$\begin{aligned} v_i &\geq 0 & \forall i \in \{0, \dots, m - 1\} \\ \bar{v}_k &\geq 0 & \forall k \in \{n_{\text{adm}}N, \dots, mN\} \end{aligned}$$

Complementarity conditions:

$$\begin{aligned} v_i \cdot u[iN] &= 0 & \forall i \in \{0, \dots, m - 1\} \\ \bar{v}_k \cdot (e_j^T x[k] - \alpha S_j) &= 0 & \forall k \in \{n_{\text{adm}}N, \dots, mN\} \end{aligned}$$

An educated guess leads us to anticipate that the positivity constraint on the input variables is inactive, i.e.,

$$u[iN] > 0, \quad \forall i \in \{0, \dots, m - 1\}$$

meaning that drug administration occurs on each dosing interval. Using the complementarity conditions, the associated multipliers are therefore zero, i.e.,

$$v_i = 0, \quad \forall i \in \{0, \dots, m - 1\}.$$

From (b), we derive a necessary form of the control, expressed as a function of the adjoint state:

$$u[iN] = \frac{1}{2} b_d^T \sum_{k=iN}^{iN+N_1-1} p[k], \quad \forall i \in \{0, \dots, m-1\}.$$

Proposition below includes all the (necessary and sufficient) KKT conditions, formatted to express the control law as a feedback of the adjoint state (minimum principle). Note that we have renamed the adjoint state variables: for all $k \in \{0, \dots, mN\}$,

$$p[k-1] \leftarrow p[k].$$

Proposition 8.2.1

The discrete-time OC problem (8.2.4) has a solution

$$(x[0]^T \quad \dots \quad x[mN]^T \quad u[0] \quad \dots \quad u[mN-1])^T$$

if and only if there exist an adjoint state

$$(p[0]^T \quad \dots \quad p[mN]^T)^T$$

and multipliers \bar{v}_k ($k \in \{n_{\text{adm}}N, \dots, mN\}$) such that

$$\begin{cases} u[iN] = \frac{1}{2} b_d^T \sum_{k=iN}^{iN+N_1-1} p[k+1] & \forall i \in \{0, \dots, m-1\} \\ u[k] = 0 & \forall k \in \{iN+N_1, \dots, (i+1)N-1 \mid i = 0, \dots, m-1\} \\ u[k] = u[iN] & \forall k \in \{iN, \dots, iN+N_1-1 \mid i = 0, \dots, m-1\} \end{cases}$$

where $(x[0]^T \quad \dots \quad x[mN]^T \quad p[0]^T \quad \dots \quad p[mN-1]^T)^T$ is the solution of (joint state and adjoint state dynamics)

$$\begin{cases} p[k] = A_d^T p[k+1] & \forall k \in \{iN, \dots, (i+1)N-1 \mid i = 0, \dots, n_{\text{adm}}-1\} \\ p[k] = A_d^T p[k+1] + \bar{v}_k e_j & \forall k \in \{iN, \dots, (i+1)N-1 \mid i = n_{\text{adm}}, \dots, m-1\} \\ x[k+1] = A_d x[k] + b_d u[k] & \forall k \in \{iN, \dots, iN+N_1-1 \mid i = 0, \dots, m-1\} \\ x[k+1] = A_d x[k] & \forall k \in \{iN+N_1, \dots, (i+1)N-1 \mid i = 0, \dots, m-1\} \end{cases}$$

where (state initial condition and adjoint state final condition)

$$\begin{cases} p[mN] = \bar{v}_{mN} e_j \\ x[0] = 0 \end{cases}$$

and (inequality constraints and complementarity conditions)

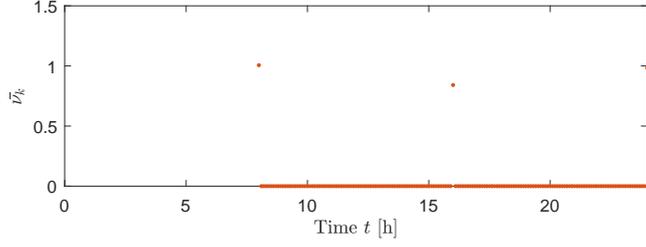
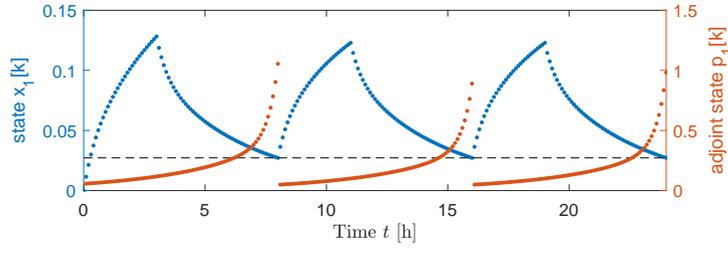
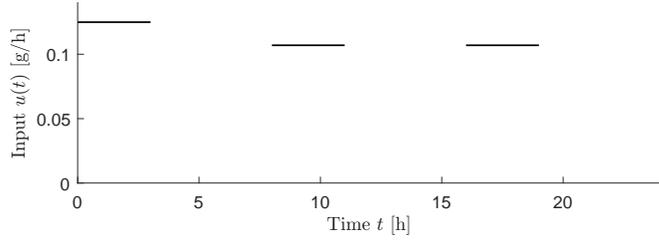
$$\begin{cases} u[iN] > 0 & \forall i \in \{0, \dots, m-1\} \\ e_j^T x[k] \geq \alpha S_j & \forall k \in \{n_{\text{adm}}N, \dots, mN\} \\ \bar{v}_k \geq 0 & \forall k \in \{n_{\text{adm}}N, \dots, mN\} \\ \bar{v}_k \cdot (e_j^T x[k] - \alpha S_j) = 0 & \forall k \in \{n_{\text{adm}}N, \dots, mN\} \end{cases}$$

A numerical study of the discrete-time OC problem (8.2.4), with the state constraint imposed successively on the first ($j = 1$, plasma) and the second ($j = 2$, ELF) state component, was performed for the following parameters:

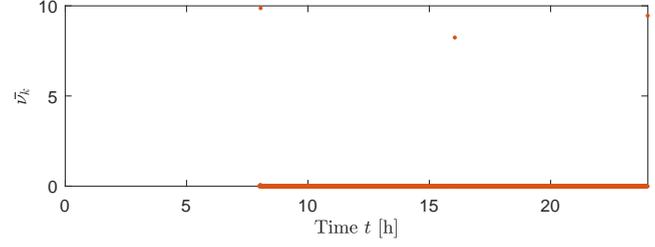
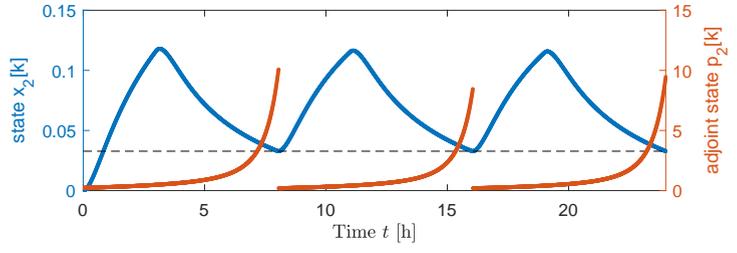
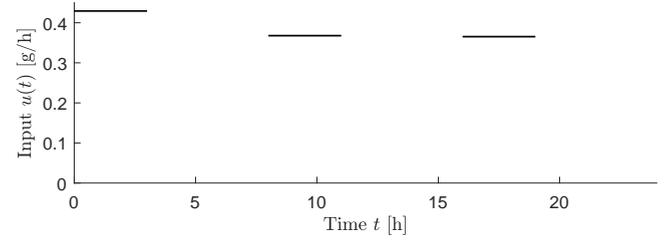
- T , 8 hours; Δ , 3 hours;
- m , 3 dosing intervals;
- n_{adm} , 1 administration; α , 2 mg/L.

The results are shown in Figure 8.2. The *quadprog* MATLAB function was used for the computations. The MATLAB algorithm is based on the interior-point method (see the documentation in MathWorks (2021)). A numerical validation of the minimum principle was performed by verifying that the solution and the multipliers provided by *quadprog* satisfy the equations in Proposition 8.2.1 above.

When the threshold of 2 mg/L is imposed in the plasma (Fig. 8.2(a)), the successive doses are 3.75 g, 3.21 g, and 3.21 g. They correspond exactly to the loading and maintenance doses computed by the I/O formula, see Proposition 6.2.1. However, when the same target concentration level is imposed at the site of infection (Fig. 8.2(b)), the first (loading) dose of 1.29 g is slightly higher than the I/O loading dose (1.28 g). This is explained by the time disconnect between systemic and infection-site concentrations. Indeed, while Proposition 6.2.1 neglects the time disconnect for dose selection, the OC approach ensures the concentration to stay above the concentration threshold whatever the importance of the time disconnect. The PK profiles following the I/O and OC approaches are shown on Figure 8.3. Let recall that the meropenem has no significant time disconnect.



(a) $j = 1$



(b) $j = 2$

Figure 8.2 – Numerical resolution of the discrete-time OC problem using *quadprog.m*.

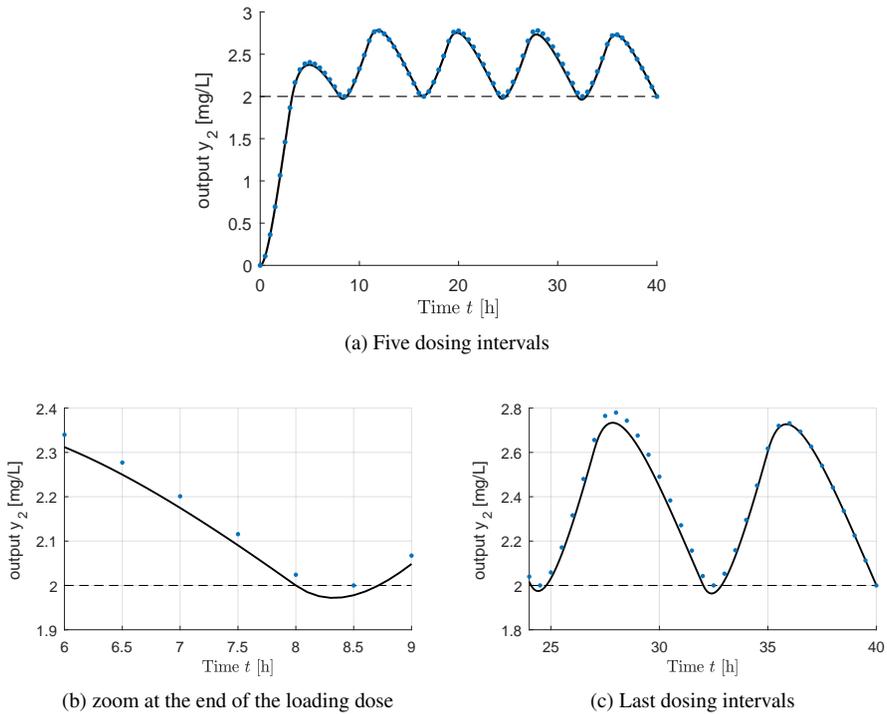


Figure 8.3 – PK profiles in ELF for different dosing strategies: continuous line, I/O approach with loading dose; blue points, OC approach in discrete-time setting using *quadprog.m* ($j = 2$, $m = 5$). The PK parameter Q_E was modified to amplify the time disconnect.

8.2.2 Relaxed constraints

Let relax the constraint stating that the rate of infusion is constant over the administration intervals. This constraint relaxation yields a simplified solution of the optimization problem under constraints, and makes it easier to extend to continuous time. The (1) OC problem, (2) KKT conditions, and (3) minimum principle are written as follows.

(1) *Discrete-time OC problem:*

$$\tilde{J}_1(u) = \sum_{i=0}^{m-1} \sum_{k=iN}^{iN+N_1-1} u^2[k] \longrightarrow \min \quad (8.2.6)$$

for the system dynamics (8.2.1)-(8.2.2) with a fixed initial condition $x[0] = 0 \in \mathbb{R}^n$, and under the following constraints:

$$\begin{cases} u[k] \geq 0 & \forall k \in \{iN, \dots, iN + N_1 - 1 \mid i = 0, \dots, m - 1\} \\ e_j^T x[k] \geq \alpha S_j & \forall k \in \{n_{\text{adm}}N, \dots, mN\} \end{cases} \quad (8.2.7)$$

Figure 8.4 compares the optimal input with and without the constraint relaxation.

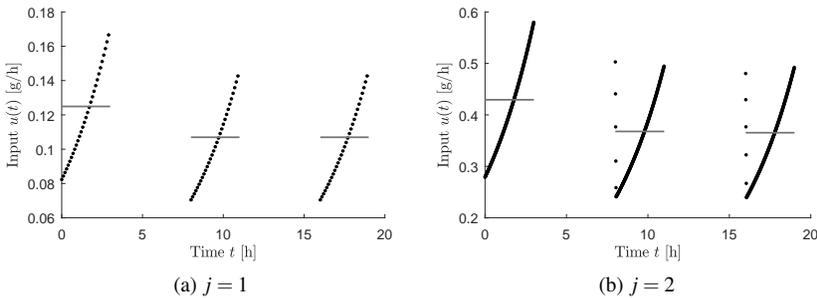


Figure 8.4 – Numerical resolution of the discrete-time OC problem using *quadprog.m*. Gray, OC problem with constraints (8.2.5); black, OC problem with relaxed constraints (8.2.7).

(2) *Lagrangian function:*

$$\begin{aligned}
 \mathcal{L}(x, u, p, \mu, v, \bar{v}) = & \sum_{i=0}^{m-1} \sum_{k=iN}^{iN+N_1-1} u^2[k] + p[-1]^T (x[0] - 0) + \\
 & \sum_{i=0}^{m-1} \sum_{k=iN}^{iN+N_1-1} p[k]^T (x[k+1] - A_d x[k] - b_d u[k]) + \\
 & \sum_{i=0}^{m-1} \sum_{k=iN+N_1}^{(i+1)N-1} p[k]^T (x[k+1] - A_d x[k]) + \\
 & \sum_{i=0}^{m-1} \sum_{k=iN}^{iN+N_1-1} v_k (-u[k]) + \sum_{k=n_{\text{adm}}N}^{mN} \bar{v}_k (-e_j^T x[k] + \alpha S_j)
 \end{aligned}$$

Stationarity conditions:

$$\partial \mathcal{L} / \partial x[k] = 0, \quad \forall k \in \{0, \dots, mN\} \quad (\text{a})$$

$$\partial \mathcal{L} / \partial u[k] = 0 \quad \forall k \in \{iN, \dots, iN + N_1 - 1 \mid i = 0, \dots, m-1\} \quad (\text{b})$$

i.e.,

$$(\text{a}) \begin{cases} p[k-1] - A_d^T p[k] = 0 & \forall k \in \{iN, \dots, (i+1)N-1 \mid i = 0, \dots, n_{\text{adm}}-1\} \\ p[k-1] - A_d^T p[k] - \bar{v}_k e_j = 0 & \forall k \in \{iN, \dots, (i+1)N-1 \mid i = n_{\text{adm}}, \dots, m-1\} \\ p[mN-1] - \bar{v}_{mN} e_j = 0 \end{cases}$$

$$(\text{b}) \quad 2u[k] - b_d^T p[k] - v_k = 0, \quad \forall k \in \{iN, \dots, iN + N_1 - 1 \mid i = 0, \dots, m-1\}$$

Primal feasibility:

- Dynamics:

$$x[k+1] = A_d x[k] + b_d u[k] \quad \forall k \in \{iN, \dots, iN + N_1 - 1 \mid i = 0, \dots, m-1\}$$

$$x[k+1] = A_d x[k] \quad \forall k \in \{iN + N_1, \dots, (i+1)N - 1 \mid i = 0, \dots, m-1\}$$

$$x[0] = 0$$

- Inequality constraints:

$$u[k] \geq 0 \quad \forall k \in \{iN, \dots, iN + N_1 - 1 \mid i = 0, \dots, m-1\}$$

$$e_j^T x[k] - \alpha S_j \geq 0 \quad \forall k \in \{n_{\text{adm}}N, \dots, mN\}$$

Dual feasibility (sign constraints on the multipliers):

$$v_k \geq 0 \quad \forall k \in \{iN, \dots, iN + N_1 - 1 \mid i = 0, \dots, m-1\}$$

$$\bar{v}_k \geq 0 \quad \forall k \in \{n_{\text{adm}}N, \dots, mN\}$$

Complementarity conditions:

$$v_k \cdot u[k] = 0 \quad \forall k \in \{iN, \dots, iN + N_1 - 1 \mid i = 0, \dots, m-1\}$$

$$\bar{v}_k \cdot (e_j^T x[k] - \alpha S_j) = 0 \quad \forall k \in \{n_{\text{adm}}N, \dots, mN\}$$

(3) Minimum principle: for all $k \in \{0, \dots, mN\}$,

$$p[k-1] \leftarrow p[k].$$

Proposition 8.2.2

The discrete-time OC problem (8.2.6) has a solution

$$(x[0]^T \quad \dots \quad x[mN]^T \quad u[0] \quad \dots \quad u[mN-1])^T$$

if and only if there exist an adjoint state

$$(p[0]^T \quad \dots \quad p[mN]^T)^T$$

and multipliers \bar{v}_k ($k \in \{0, \dots, mN\}$) such that

$$\begin{cases} u[k] = \frac{1}{2} b_d^T p[k+1] & \forall k \in \{iN, \dots, iN + N_1 - 1 \mid i = 0, \dots, m-1\} \\ u[k] = 0 & \forall k \in \{iN + N_1, \dots, (i+1)N - 1 \mid i = 0, \dots, m-1\} \end{cases}$$

where $(x[0]^T \quad \dots \quad x[mN]^T \quad p[0]^T \quad \dots \quad p[mN]^T)^T$ is the solution of the Hamiltonian system, for all $k \in \{0, \dots, mN-1\}$,

$$\begin{bmatrix} x[k+1] \\ p[k] \end{bmatrix} = \begin{bmatrix} A_d & \frac{1}{2} b_d b_d^T \mathcal{X}_{\{k: (k \bmod N) < N_1\}}(k) \\ 0 & A_d^T \end{bmatrix} \begin{bmatrix} x[k] \\ p[k+1] \end{bmatrix} + \begin{bmatrix} 0 \\ e_j \end{bmatrix} \bar{v}_k$$

where $\bar{v}_k = 0$ for all $k \in \{0, \dots, n_{\text{adm}}N - 1\}$, and (state initial condition and adjoint state final condition)

$$\begin{cases} p[mN] = \bar{v}_{mN} e_j \\ x[0] = 0 \end{cases}$$

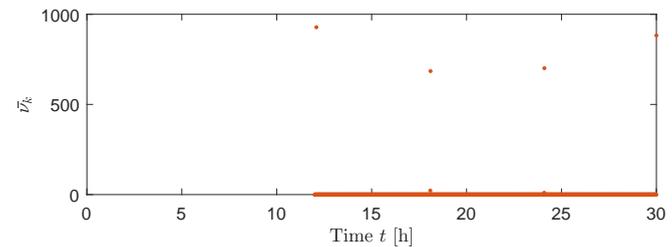
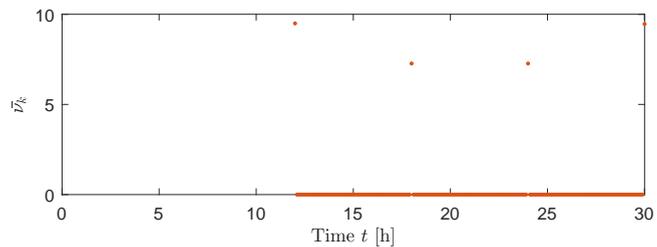
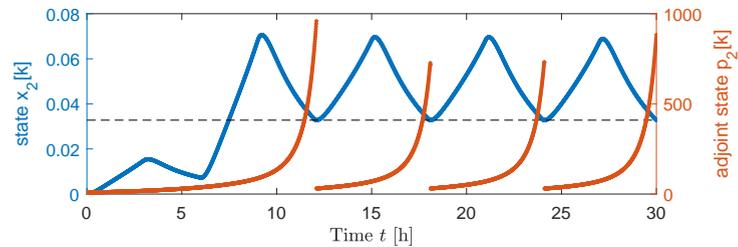
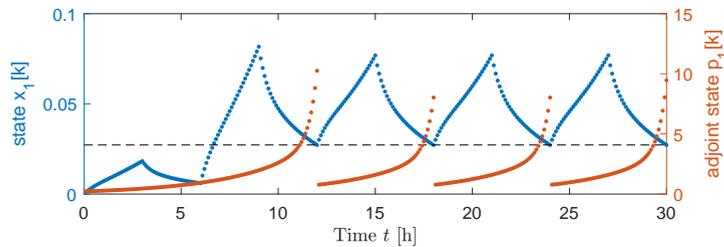
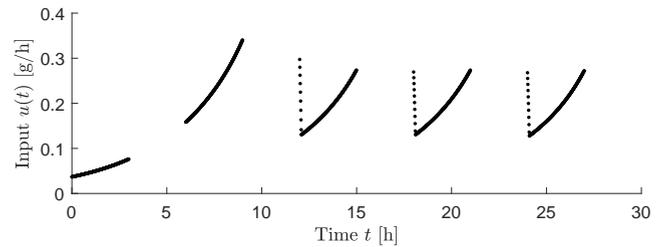
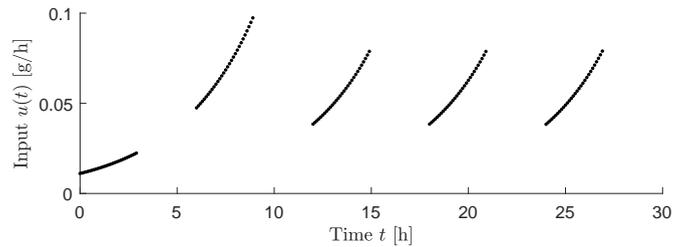
and (inequality constraints and complementarity conditions)

$$\begin{cases} u[k] > 0 & \forall k \in \{iN, \dots, iN + N_1 - 1 \mid i = 0, \dots, m-1\} \\ e_j^T x[k] \geq \alpha S_j & \forall k \in \{n_{\text{adm}}N, \dots, mN\} \\ \bar{v}_k \geq 0 & \forall k \in \{n_{\text{adm}}N, \dots, mN\} \\ \bar{v}_k \cdot (e_j^T x[k] - \alpha S_j) = 0 & \forall k \in \{n_{\text{adm}}N, \dots, mN\} \end{cases}$$

Figure 8.5 shows the solution of the discrete-time OC problem with constraint relaxation (8.2.6) for the following parameters:

- T , 6 hours; Δ , 3 hours;
- m , 5 administrations;
- n_{adm} , 2 dosing intervals; α , 2 mg/L.

We observe that the j^{th} component of the adjoint state trajectory has $m - n_{\text{adm}} = 3$ discontinuity points.



(a) $j = 1$

(b) $j = 2$

Figure 8.5 – Numerical resolution of the discrete-time OC problem with constraint relaxation using *quadprog.m*. The number of administrations to reach the state constraint is set to $n_{\text{adm}} = 2$.

Remark 9 As highlighted in Figure 8.6, the *discontinuity* points of the adjoint state trajectory coincide with the time points at which the state constraint is active, i.e., times τ such that the j^{th} component of the state trajectory reaches the boundary ($x_j(\tau) = \alpha S_j$). We observe that the state trajectory just reaches the boundary: for a time t just before and just after τ , $x_j(t) > \alpha S_j$. Such a point τ is called *contact time* (Hartl et al. (1995)). Due to time disconnect, when the state constraint is imposed on the second state component x_2 (i.e., at the site of infection), the contact times are not reached at the end of the dosing intervals iT ($i \in \{n_{\text{adm}}, \dots, m-1\}$), but slightly after. Let τ_i , $i \in \{1, \dots, m - n_{\text{adm}}\}$, be the contact times on $[n_{\text{adm}}T, t_f[$.

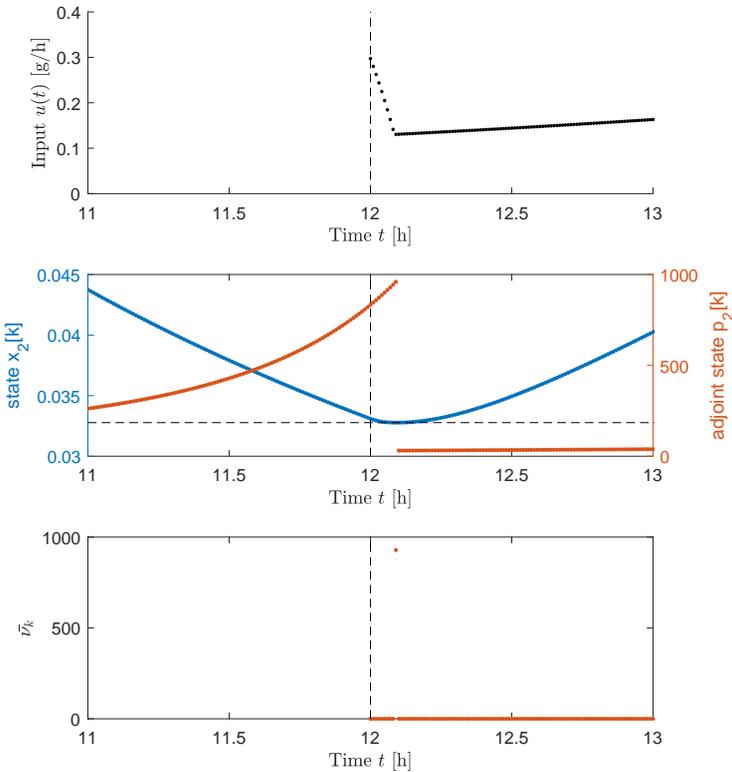


Figure 8.6 – Numerical resolution of the discrete-time OC problem with constraint relaxation using *quadprog.m* ($j = 2$): zoom on a contact time

8.3 Extension to the continuous-time setting

Proposition 8.3.1 below extends the minimum principle to the continuous-time setting on the basis of the necessary and sufficient conditions of optimality presented in Proposition 8.2.2. The continuous-time solution is then formally validated in the proof.

Numerical tests in the discrete-time setting showed that the contact times are invariant with respect to the sample time. We can therefore reasonably assume that they coincide with the contact times in the continuous-time setting.

Proposition 8.3.1 The continuous-time OC problem (8.1.3) with the relaxed constraints (8.1.6) has a solution

$$\begin{aligned} u(t) : [0, t_f] &\longrightarrow \mathbb{R}^+ \\ x(t) : [0, t_f] &\longrightarrow \mathbb{R}_+^n \end{aligned}$$

if and only if there exist an adjoint state $p : [0, t_f] \longrightarrow \mathbb{R}_+^n$ and a multiplier function $\bar{v} : [0, t_f] \longrightarrow \mathbb{R}^+$ such that (adjoint state feedback)

$$\begin{cases} u(t) = \frac{1}{2} b^T p(t) \stackrel{(8.1.1)}{=} \frac{b_1}{2} p_1(t) & \forall t \in [0, t_f[\text{ s.t. } (t \bmod T) < \Delta \\ u(t) = 0 & \forall t \text{ s.t. } (t \bmod T) \geq \Delta \end{cases}$$

where $x(\cdot)$ and $p(\cdot)$ are the solution of the family of Hamiltonian systems defined, for all $t \in [\tau_{i-1}, \tau_i[$ ($i \in \{1, \dots, m - n_{\text{adm}}\}$) and for all $t \in [\tau_{m-n_{\text{adm}}}, t_f]$, by

$$\begin{bmatrix} \dot{x}(t) \\ \dot{p}(t) \end{bmatrix} = \begin{bmatrix} A & \frac{1}{2} b b^T \chi_{\{t : (t \bmod T) < \Delta\}}(t) \\ 0 & -A^T \end{bmatrix} \begin{bmatrix} x(t) \\ p(t) \end{bmatrix} \quad (8.3.1)$$

where, $\tau_0 := 0$ and, for any $i \in \{1, \dots, m - n_{\text{adm}}\}$, $\tau_i \geq n_{\text{adm}}T$ is a contact time on $[n_{\text{adm}}T, t_f]$. The state initial condition and adjoint state final condition are

$$\begin{cases} x(0) = 0 \\ p(t_f) = \bar{v}(t_f) e_j, \quad \text{where } \bar{v}(t_f) > 0. \end{cases}$$

[Jump conditions] At any contact time $\tau_i \in [n_{\text{adm}}T, t_f]$, the final condition is updated using

$$p(\tau_i^-) = p(\tau_i^+) + \bar{v}(\tau_i) e_j \quad (8.3.2)$$

where e_j is the j^{th} vector of the canonical basis and $\bar{v}(\cdot)$ is such that

$$\begin{cases} \bar{v}(t) > 0 & \forall t \in \{\tau_i : i = 1, \dots, m - n_{\text{adm}}\} \\ \bar{v}(t) = 0 & \forall t \in [0, t_f] \setminus \{\tau_i : i = 1, \dots, m - n_{\text{adm}}\} \end{cases}$$

Furthermore, the state constraint is active at the final time, i.e.,

$$e_j^T x(t_f) - \alpha S_j = 0.$$

The state complementarity condition

$$\bar{v}(t) \cdot (e_j^T x(t) - \alpha S_j) = 0 \quad \forall t \in [0, t_f] \quad (8.3.3)$$

is then necessarily verified since, by definition of contact time,

$$e_j^T x(\tau_i) - \alpha S_j = 0.$$

Besides (inequality constraints),

$$\begin{cases} u(t) > 0 & \forall t \in [0, t_f[\text{ s.t. } (t \bmod T) < \Delta \\ e_j^T x(t) \geq \alpha S_j & \forall t \geq n_{adm} T \end{cases}$$

Remark 10 Since A is Metzler, the system $\dot{p} = -A^T p$ is nonnegative in inverse time. In particular, for all final condition $p_f \geq 0$,

$$p(t) = e^{-A^T(t-t_f)} p_f = e^{A^T(t_f-t)} p_f \geq 0$$

for all $t \in [0, t_f]$, since $e^{A^T \tau} \geq 0$ for all $\tau \geq 0$ (see Proposition 1.1.2).

Proof. Here, we prove that the form of the solution provided in Proposition 8.3.1 satisfies the necessary and sufficient optimality conditions of the Pontryagin's maximum principle. The studied OC problem with state and relaxed input constraints is stated below. The right-hand sides of the identities below are explicitly related to the notations used in the formalism of Hartl et al. (1995).

$$J = \int_0^{t_f} -u^2(t) dt =: \int_0^{t_f} F(u(t)) dt \longrightarrow \max$$

for the system dynamics

$$\dot{x}(t) = Ax(t) + bu(t) =: f(x(t), u(t))$$

under the constraints

$$0 \leq u(t) =: g_1(u(t))$$

$$0 \leq -u(t) \chi_{\{t: (t \bmod T) \geq \Delta\}} =: g_2(u(t), t)$$

$$0 \leq (e_j^T x(t) - \alpha S_j) \chi_{\{t: t \geq n_{adm} T\}} =: h(x(t), t)$$

The *Hamiltonian* \mathcal{H} and *Lagrangian* \mathcal{L} are given by:

$$\mathcal{H}(x, u, \lambda_0, \lambda) := \lambda_0 F(u) + \lambda f(x, u) = -\lambda_0 u^2 + \lambda^T (Ax + bu)$$

and

$$\begin{aligned}\mathcal{L}(x, u, \lambda_0, \lambda, \mu, \nu, t) &:= \mathcal{H}(x, u, \lambda_0, \lambda) + \mu g(u, t) + \nu h(x, t) \\ &= -\lambda_0 u^2 + \lambda^T (Ax + bu) + \mu_1 u(t) - \mu_2 u \chi_{\{t: (t \bmod T) \geq \Delta\}} \\ &\quad + \nu(e_j^T x - \alpha S_j) \chi_{\{t: t \geq n_{\text{adm}} T\}}\end{aligned}$$

where $\lambda_0 \geq 0$ is a constant, $\lambda \in \mathbb{R}^n$ is the co-state (or adjoint state) of the system, and $\mu_1, \mu_2, \nu \in \mathbb{R}$ are the multipliers. Let's define the control region:

$$\Omega(t) := \{u \in \mathbb{R} : g(u, t) \geq 0\} = \{u \geq 0 \in \mathbb{R} : u \chi_{\{t: (t \bmod T) \geq \Delta\}} = 0\}.$$

The control region is independent of x since the input constraints g_1 and g_2 do not depend on the state x .

Necessary conditions.

What follows is based on (Hartl et al., 1995, Informal theorem 4.1), also reported in (Beauthier, 2011, Appendix B).

The Pontryagin's maximum principle states that, if the state trajectory x^* (with finite number of junction times)⁽¹⁾ and the control u^* (right-continuous with left-hand limits) correspond to an optimal solution, then there exists

- $\lambda_0 \geq 0$
- $\lambda : [0, t_f] \rightarrow \mathbb{R}^n$ piecewise absolutely continuous
- $\mu_1, \mu_2, \mu : [0, t_f] \rightarrow \mathbb{R}$ piecewise continuous
- $\gamma \in \mathbb{R}$
- $\eta(\tau_i) \in \mathbb{R}$ for each point of discontinuity of $\lambda(\cdot)$

that satisfy almost everywhere the conditions (4.4)-(4.14) set out in Hartl et al. (1995) and listed below:

$$(4.4) \quad u^*(t) = \arg \max_{u \in \Omega(x^*(t), t)} \mathcal{H}(x^*(t), u, \lambda_0, \lambda(t))$$

$$(4.5) \quad \frac{\partial \mathcal{L}}{\partial u}(x^*(t), u^*(t), \lambda_0, \lambda(t), \mu(t), \nu(t), t) = 0$$

$$(4.6) \quad \dot{\lambda}(t) = -\frac{\partial \mathcal{L}}{\partial x}(x^*(t), u^*(t), \lambda_0, \lambda(t), \mu(t), \nu(t), t)$$

$$(4.7) \quad \mu(t) \geq 0, \quad \mu(t)g(u^*(t), t) = 0$$

$$(4.8) \quad \nu(t) \geq 0, \quad \nu(t)h(x^*(t), t) = 0$$

⁽¹⁾Junction times include the contact times, as well as the entry and exit times that are the extremities of the boundary intervals. A boundary interval $[\tau_1, \tau_2]$, with $\tau_1 < \tau_2$, is such that, for all $t \in [\tau_1, \tau_2]$, $h(x(t), t) = 0$ (Hartl et al. (1995)).

$$(4.9) \quad \frac{d\mathcal{H}^*}{dt}(t) = \frac{d\mathcal{L}^*}{dt}(t) = \frac{\partial \mathcal{L}}{\partial t}(x^*(t), u^*(t), \lambda_0, \lambda(t), \mu(t), v(t), t)$$

where $\mathcal{H}^* = \mathcal{H}(x^*, u^*, \lambda_0, \lambda)$ and $\mathcal{L}^* = \mathcal{L}(x^*, u^*, \lambda_0, \lambda, \mu, v, t)$.

At the terminal time T , the transversality conditions:

$$(4.10) \quad \lambda(T^-) = \gamma \frac{\partial h}{\partial x}(x^*(T), T)$$

$$(4.11) \quad \gamma \geq 0, \quad \gamma h(x^*(T), T) = 0.$$

For any time τ in a boundary interval and for any contact time τ , the costate trajectory λ may have a discontinuity given by the following jump conditions:

$$(4.12) \quad \lambda(\tau^-) = \lambda(\tau^+) + \eta(\tau) \frac{\partial h}{\partial x}(x^*(\tau), \tau)$$

$$(4.13) \quad \mathcal{H}^*(\tau^-) = \mathcal{H}^*(\tau^+) - \eta(\tau) \frac{\partial h}{\partial t}(x^*(\tau), \tau)$$

$$(4.14) \quad \eta(\tau) \geq 0, \quad \eta(\tau) h(x^*(\tau), \tau).$$

Note that the qualification constraints hold only for all t such that $(t \bmod T) < \Delta$. The optimal input $u^*(t)$ is set to 0 for all t such that $(t \bmod T) \geq \Delta$. The right-continuity of u^* in Proposition 8.3.1 is guaranteed by the integrating intervals of p that are open on the right. By choosing the following multipliers, the conditions hold:

- $\lambda_0 = 1$ (normal case)
- $\lambda(\cdot) = p(\cdot)$ described in Proposition 8.3.1 above, which is piecewise C^∞
- $\mu_1(\cdot), \mu_2(\cdot) \geq 0$ s.t., for all $t \in [0, t_f[$ s.t. $(t \bmod T) < \Delta$,

$$\mu_1(t) = 0 = \mu_2(t)$$
- $v(\cdot) = \bar{v}(\cdot)$ described in Proposition 8.3.1 above
- $\gamma = \bar{v}(t_f)$ (see the transversality conditions below)
- $\eta(\tau_i) = \bar{v}(\tau_i)$

Indeed:

(4.4): For all $t \in [0, t_f[$ such that $(t \bmod T) < \Delta$,

$$u^*(t) = \arg \max_{u \in \Omega(t)} \mathcal{H}(x^*(t), u, p(t))$$

since $u^*(t) = \frac{1}{2} b^T p(t)$ verifies the necessary and sufficient KKT conditions of the optimization problem

$$\mathcal{H}(x^*(t), u, p(t)) \longrightarrow \max$$

under the constraint $u \geq 0$.

(4.5): For all $t \in [0, t_f[$ such that $(t \bmod T) < \Delta$,

$$\frac{\partial \mathcal{L}}{\partial u}(x^*(t), u^*(t)) = 0$$

since

$$\frac{\partial \mathcal{L}}{\partial u} = -2u + b^T p + \mu_1 - \mu_2 \chi_{\{t: (t \bmod T) \geq \Delta\}} = -2u + b^T p$$

using $\mu_1(t) = 0$.

(4.6): For all $t \in [0, t_f[\setminus \{\tau_i : i = 0, \dots, m - n_{\text{adm}}\}$,

$$\dot{p}(t) = -\frac{\partial \mathcal{L}}{\partial x}(x^*(t), u^*(t)).$$

Indeed,

$$\frac{\partial \mathcal{L}}{\partial x} = A^T p + \bar{v} e_j \chi_{\{t: t \geq n_{\text{adm}} T\}} = A^T p$$

almost everywhere since $\bar{v}(\cdot)$ is the null function almost everywhere (except at contact times), and, on each integrating interval,

$$\dot{p} = -A^T p = -\frac{\partial \mathcal{L}}{\partial x}(x^*, u^*)$$

(see the Hamiltonian systems in Proposition 8.3.1).

(4.7): For all $t \in [0, t_f[$ such that $(t \bmod T) < \Delta$, the conditions

$$\begin{aligned} \mu_1(t) &\geq 0, & \mu_1(t) g_1(u^*(t)) &= 0 \\ \mu_2(t) &\geq 0, & \mu_2(t) g_2(u^*(t), t) &= 0 \end{aligned}$$

are obviously verified since $\mu_1(t) = 0 = \mu_2(t)$. Observe that, for all t such that $(t \bmod T) < \Delta$, $g_2(u^*(t), t) = -u^*(t) \chi_{\{t: (t \bmod T) \geq \Delta\}} = 0$, such that $\mu_2(t)$ may be any nonnegative real number.

(4.8): For all $t \in [0, t_f[$ such that $(t \bmod T) < \Delta$, (except at contact times,)

$$\bar{v}(t) \geq 0, \quad \bar{v}(t) h(x^*(t), t) = 0$$

hold by (8.3.3).

(4.9): For almost all $t \in [0, t_f[$ such that $(t \bmod T) < \Delta$,

$$\frac{d\mathcal{H}^*}{dt}(t) = \frac{d\mathcal{L}^*}{dt}(t) = \frac{\partial \mathcal{L}}{\partial t}(x^*(t), u^*(t))$$

where $\mathcal{H}^* = \mathcal{H}(x^*, u^*, p)$ and $\mathcal{L}^* = \mathcal{L}(x^*, u^*, p, \mu_1, \mu_2, \bar{v}, t)$. Indeed, \mathcal{L} is, almost everywhere, not explicitly time-dependent, such that

$$\frac{\partial \mathcal{L}}{\partial t} = 0$$

almost everywhere, and, for all $t \in [0, t_f[$ such that $(t \bmod T) < \Delta$,

$$\mathcal{H}^*(t) = -\left(\frac{1}{2}b^T p(t)\right)^2 + p^T(t)Ax^*(t) + \frac{1}{2}p^T(t)bb^T p(t).$$

Therefore

$$\begin{aligned} \frac{d\mathcal{H}^*}{dt}(t) &= \dot{p}^T(t)Ax^*(t) + p^T(t)A\dot{x}^*(t) + \frac{1}{2}\dot{p}^T(t)bb^T p(t) \\ &= -p^T(t)AAx^*(t) + p^T(t)A(Ax^*(t) + bu^*(t)) - p^T(t)Abu^*(t) \\ &= 0. \end{aligned}$$

Furthermore, for all $t \in [0, t_f[$ such that $(t \bmod T) < \Delta$,

$$\mathcal{L}^*(t) = \mathcal{H}^*(t) + \mu_1(t)u^*(t) + \bar{v}(t)(e_j^T x^*(t) - \alpha S_j)\chi_{\{t:t \geq n_{\text{adm}}T\}}.$$

Hence

$$\mathcal{L}^*(t) = \mathcal{H}^*(t)$$

using $\mu_1(t) = 0$ and the state complementary condition (8.3.3).

Transversality conditions.

(4.10): At the terminal time t_f ,

$$p(t_f^-) = \bar{v}(t_f) \frac{\partial h}{\partial x}(x^*(t_f), t_f).$$

Indeed,

$$\frac{\partial h}{\partial x} = e_j \chi_{\{t:t \geq n_{\text{adm}}T\}}$$

such that

$$\frac{\partial h}{\partial x}(x^*(t_f), t_f) = e_j.$$

And

$$p(t_f^-) = \bar{v}(t_f)e_j$$

by the adjoint state final condition in Proposition 8.3.1.

(4.11): At the terminal time t_f , the conditions

$$\bar{v}(t_f) \geq 0, \quad \bar{v}(t_f)h(x^*(t_f), t_f) = 0$$

are satisfied since

$$\bar{v}(t_f) > 0 \quad \text{and} \quad e_j^T x^*(t_f) - \alpha S_j = 0.$$

Jump conditions.

(4.12): For any contact time $\tau_i \in [n_{\text{adm}}T, t_f]$, $i \in \{1, \dots, m - n_{\text{adm}}\}$,

$$p(\tau_i^-) = p(\tau_i^+) + \bar{v}(\tau_i) \frac{\partial h}{\partial x}(x^*(\tau_i), \tau_i).$$

Indeed, since $\tau_i \geq n_{\text{adm}}T$,

$$\frac{\partial h}{\partial x}(x^*(\tau_i), \tau_i) = e_j$$

and

$$p(\tau_i^-) = p(\tau_i^+) + \bar{v}(\tau_i)e_j$$

by (8.3.2). That means that the j^{th} component of the adjoint state trajectory has a discontinuity at the contact times and the other components of p are continuous on $[0, t_f]$. Note that it is consistent with the discrete-time numerical tests, as illustrated in Figure 8.7.

(4.13): For any contact time $\tau_i \in [n_{\text{adm}}T, t_f]$, $i \in \{1, \dots, m - n_{\text{adm}}\}$, the condition

$$\mathcal{H}^*(\tau_i^-) = \mathcal{H}^*(\tau_i^+) - \bar{v}(\tau_i) \frac{\partial h}{\partial t}(x^*(\tau_i)) \quad (8.3.4)$$

holds. Indeed, since h is not explicitly time-dependent for all $t \geq n_{\text{adm}}T$,

$$\frac{\partial h}{\partial t} = 0$$

and (8.3.4) becomes

$$\mathcal{H}^*(\tau_i^-) = \mathcal{H}^*(\tau_i^+) \quad (8.3.5)$$

where

$$\mathcal{H}^*(t) = -(u^*(t))^2 + p^T(t)(Ax^*(t) + bu^*(t)).$$

- If $j = 2$, we can reasonably assume that $0 < (\tau_i \bmod T) < \Delta$ (see Remark 9). Since τ_i is in the interior of the administration interval and $p_1(\cdot)$ is continuous,

$$u^*(\tau_i^-) = \frac{b_1}{2} p_1(\tau_i^-) = \frac{b_1}{2} p_1(\tau_i^+) = u^*(\tau_i^+)$$

and Condition (8.3.5) can be written as the following equivalent identities

$$\begin{aligned} p^T(\tau_i^-)Ax^*(\tau_i) + b_1 p_1(\tau_i)u^*(\tau_i) &= p^T(\tau_i^+)Ax^*(\tau_i) + b_1 p_1(\tau_i)u^*(\tau_i) \\ (p^T(\tau_i^+) + \bar{v}(\tau_i)e_j^T)Ax^*(\tau_i) &= p^T(\tau_i^+)Ax^*(\tau_i) \\ \bar{v}(\tau_i)e_j^T(Ax^*(\tau_i) + bu^*(\tau_i)) &= 0 \\ e_j^T x^*(\tau_i) &= 0 \end{aligned} \quad (8.3.6)$$

using (8.3.2), $e_j^T b = 0$, and $\bar{v}(\tau_i) \neq 0$. Condition (8.3.6) holds. Indeed, if $\dot{x}_j^*(\tau_i) \neq 0$, $x_j^*(\cdot)$ is monotone on an interval around τ_i , which is not possible since x_j^* decreases just before τ_i and increases just after τ_i (contact time).

- If $j = 1$, $(\tau_i \bmod T) = 0$. Since τ_i is the lower bound of the administration interval,

$$u^*(\tau_i^-) = 0.$$

Using the right-continuity of $u^*(\cdot)$ and $p_1(\cdot)$, Condition (8.3.5) can be written as the following equivalent identities

$$\begin{aligned} p^T(\tau_i^-)Ax^*(\tau_i) &= -(u^*(\tau_i))^2 + p^T(\tau_i^+)(Ax^*(\tau_i) + bu^*(\tau_i)) \\ (p^T(\tau_i^+) + \bar{v}(\tau_i)e_j^T)Ax^*(\tau_i) &= -(u^*(\tau_i))^2 + p^T(\tau_i^+)(Ax^*(\tau_i) + bu^*(\tau_i)) \\ \bar{v}(\tau_i)e_j^T Ax^*(\tau_i) &= -\left(\frac{b_1}{2}p_1(\tau_i)\right)^2 + \frac{b_1^2}{2}p_1^2(\tau_i) \\ \bar{v}(\tau_i)\left(\dot{x}(\tau_i) - \frac{b_1^2}{2}p_1(\tau_i)\right) &= \frac{b_1^2}{4}p_1^2(\tau_i) \\ \dot{x}(\tau_i) &= \frac{1}{2}b_1^2p_1(\tau_i)\left(1 + \frac{p_1(\tau_i)}{2\bar{v}(\tau_i)}\right) \end{aligned} \quad (8.3.7)$$

using $Ax^*(\tau_i) = \dot{x}(\tau_i) - bu^*(\tau_i) = \dot{x}(\tau_i) - \frac{b_1}{2}p_1(\tau_i)b$ and $e_j^T b = b_1$. Identity (8.3.7) corresponds to the positive right-hand limit of the derivative \dot{x} at the contact time τ_i (see, e.g., Figure 8.9).

Remark. The first component of the adjoint state $p_1(\cdot)$ is non-zero on each integrating interval. Indeed, if there exists t such that $p_1(t) = 0$, then

$$\dot{p}_1(t) = -k_{12}p_2(t) - k_{13}p_3(t) - \dots - k_{1n}p_n(t) \geq 0.$$

If $\dot{p}_1(t) > 0$, then, since p_1 is C^1 , there exists an interval around t on which p_1 is increasing. This is impossible by Remark 10. If $\dot{p}_1(t) = 0$, then $p(t) = 0$ and, for all $\tau \geq t$, $p(\tau) = e^{-A^T(\tau-t)}p(t) = 0$. This is impossible since p_1 is negative at the end of the dosing interval (see final condition and jumps defined in Proposition 8.3.1).

Note that, combined with (4.9), (8.3.5) is equivalent to say that \mathcal{H}^* is constant (autonomous case), as stated in (Hartl et al., 1995, footnote 4).

(4.14): For any contact time $\tau_i \in [n_{\text{adm}}T, t_f[$, $i \in \{1, \dots, m - n_{\text{adm}}\}$,

$$\bar{v}(\tau_i) \geq 0, \quad \bar{v}(\tau_i)h(x^*(\tau_i), \tau_i) = 0$$

are satisfied since

$$\bar{v}(\tau_i) > 0 \quad \text{and} \quad e_j^T x^*(\tau_i) - \alpha S_j = 0.$$

Sufficient conditions.

For all $t \in [0, t_f[$ such that $(t \bmod T) < \Delta$, the minimized Hamiltonian

$$\begin{aligned} \mathcal{H}^0(x(t), p(t), t) &:= \min_{u \in \Omega(t)} \mathcal{H}(x(t), u, p(t), t) \\ &= - \left(\frac{1}{2} b^T p(t) \right)^2 + p^T \left(Ax(t) + \frac{1}{2} b b^T p(t) \right) \end{aligned}$$

is linear w.r.t. x . Furthermore, $g(u) = [u \ -u]^T$ is linear w.r.t. u as well as $h(x) = (e_j^T x(t) - \alpha S_j) \chi_{\{t: t \geq n_{\text{adm}} T\}}$ w.r.t. x . Based on (Hartl et al., 1995, Theorem 8.2), conditions (4.4)-(4.14) are sufficient. \square

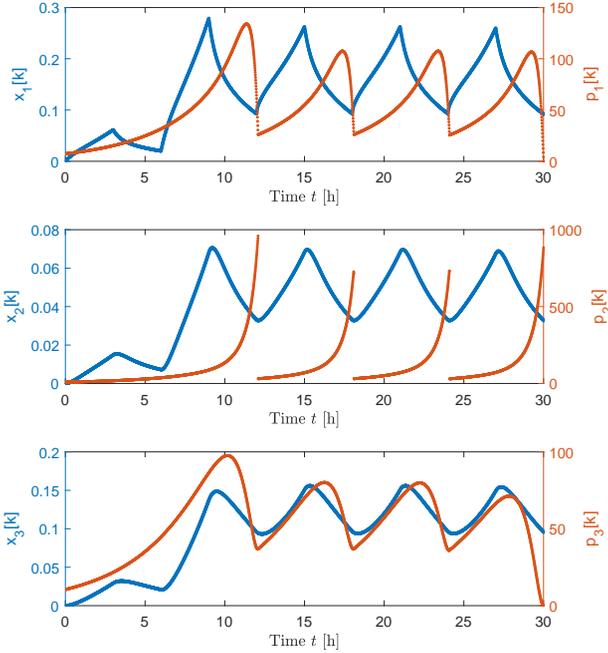


Figure 8.7 – Numerical resolution of the discrete-time OC problem with constraint relaxation using `quadprog.m` ($j = 2$, $n_{\text{adm}} = 2$): adjoint state trajectory.

8.4 Further computational explorations

Some additional numerical simulations have been carried out and open up interesting perspectives in order to gain insight in the optimal solution.

- *Adjoint state: final condition and jumps.*

A *fundamental challenge* is to determine the values of the multiplier function $\bar{v}(\cdot)$ at t_f and each contact time τ_i ($i \in \{1, \dots, m - n_{\text{adm}}\}$), that parametrize the adjoint state trajectory. In discrete-time setting, we observe in Figure 8.9 that the jumps $p_j(\tau_i^-) - p_j(\tau_i^+)$ coincide with the values of the multiplier \bar{v}_k associated with the state constraints. The notation $\bar{v}(\tau_i)$ is thus a natural choice in Proposition 8.3.1 for jumps (denoted by $\eta(\tau_i)$ in the general theory reported Hartl et al. (1995)). However, in discrete-time setting, the values of the \bar{v}_k depend on the sample time h , such that an extrapolation to the continuous-time solution is not possible on the basis of the numerical tests. An educated guess, based on a simple case, suggests that the integration of the Hamiltonian system (8.3.1) with the boundary values $x(0) = 0$ and $x(t_f) = \alpha S_j e_j$, and contact times informations should be enough to analytically determine the solution.

Indeed, assuming for simplicity a one-compartment model (so we necessarily have $j = 1$) with $b_1 = \sqrt{2}$ (modulo rescaling of the input function), Equation (8.3.1) reads as

$$\begin{bmatrix} \dot{x}(t) \\ \dot{p}(t) \end{bmatrix} = \begin{bmatrix} -k_e & \chi_{\{t:(t \bmod T) < \Delta\}}(t) \\ 0 & k_e \end{bmatrix} \begin{bmatrix} x(t) \\ p(t) \end{bmatrix}$$

where $k_e > 0$. Let consider $m = 2$ and $n_{\text{adm}} = 1$. Let τ be the only contact time. Since $j = 1$, the contact time is reached at the end of the dosing interval, i.e., $\tau = T$ (see Figure 8.8).

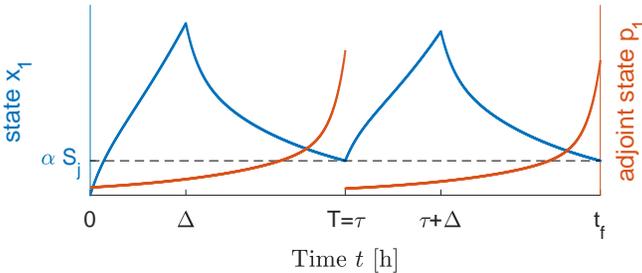


Figure 8.8 – Hypothetical state and adjoint state trajectories ($n_{\text{adm}} = 1, m = 2$)

By solving the Hamiltonian system successively on $[0, \Delta]$, $[\Delta, \tau]$, $[\tau, \tau + \Delta]$, and $[\tau + \Delta, t_f]$, we obtain a system of 8 equations and 8 unknown parameters:

- integration on $[0, \Delta]$,

$$\begin{cases} x(\Delta) = \frac{\sinh(k_e \Delta)}{k_e} p(0) \\ p(\Delta) = e^{k_e \Delta} p(0) \end{cases}$$

- integration on $[\Delta, \tau]$,

$$\begin{cases} \alpha S_j = e^{-k_e(\tau-\Delta)} x(\Delta) \\ p(\tau^-) = e^{k_e(\tau-\Delta)} p(\Delta) \end{cases}$$

- integration on $[\tau, \tau + \Delta]$,

$$\begin{cases} x(\tau + \Delta) = \alpha S_j e^{-k_e \Delta} + \frac{\sinh(k_e \Delta)}{k_e} (p(\tau^-) - \bar{v}(\tau)) \\ p(\tau + \Delta) = e^{k_e \Delta} (p(\tau^-) - \bar{v}(\tau)) \end{cases}$$

- integration on $[\tau + \Delta, t_f]$,

$$\begin{cases} \alpha S_j = e^{-k_e(t_f-\tau-\Delta)} x(\tau + \Delta) \\ \bar{v}(t_f) = e^{k_e(t_f-\tau-\Delta)} p(\tau + \Delta) \end{cases}$$

or, equivalently,

$$\begin{pmatrix} e^{-k_e(\tau-\Delta)} & 0 & 0 & 0 & 0 & 0 & 0 & 0 \\ -1 & \frac{\sinh(k_e \Delta)}{k_e} & 0 & 0 & 0 & 0 & 0 & 0 \\ 0 & -e^{k_e \Delta} & 1 & 0 & 0 & 0 & 0 & 0 \\ 0 & 0 & -e^{k_e(\tau-\Delta)} & 1 & 0 & 0 & 0 & 0 \\ 0 & 0 & 0 & 0 & e^{-k_e(t_f-\tau-\Delta)} & 0 & 0 & 0 \\ 0 & 0 & 0 & -\frac{\sinh(k_e \Delta)}{k_e} & 1 & \frac{\sinh(k_e \Delta)}{k_e} & 0 & 0 \\ 0 & 0 & 0 & -e^{k_e \Delta} & 0 & e^{k_e \Delta} & 1 & 0 \\ 0 & 0 & 0 & 0 & 0 & 0 & -e^{k_e(t_f-\tau-\Delta)} & 1 \end{pmatrix} \begin{pmatrix} x(\Delta) \\ p(0) \\ p(\Delta) \\ p(\tau^-) \\ x(\tau + \Delta) \\ \bar{v}(\tau) \\ p(\tau + \Delta) \\ \bar{v}(t_f) \end{pmatrix} = \begin{pmatrix} \alpha S_j \\ 0 \\ 0 \\ 0 \\ \alpha S_j \\ \alpha S_j e^{-k_e \Delta} \\ 0 \\ 0 \end{pmatrix}$$

which is a lower triangular linear system.

Let consider a n -compartment model, and still $j = 1$ ($\tau = T$ and Figure 8.8 is still applicable). The Hamiltonian system (8.3.1) reads as

$$\begin{bmatrix} \dot{x}(t) \\ \dot{p}(t) \end{bmatrix} = \begin{bmatrix} A & e_1 e_1^T \mathcal{X}_{\{t: (t \bmod T) < \Delta\}}(t) \\ 0 & -A^T \end{bmatrix} \begin{bmatrix} x(t) \\ p(t) \end{bmatrix}$$

which is an upper triangular by blocks system. Based on the analytical solution described in the scalar case, we state that the solution can be found by solving successive Cauchy problems:

- On $[\Delta, \tau]$, the block at position (1,2) is the zero matrix, such that the system is block diagonal. Let assume that we completely know the state x^* at the contact time τ (and at the the final time t_f). The state $x(\Delta) = x_\Delta$ is determined by solving the Cauchy problem

$$\begin{cases} \dot{x} = Ax, & \forall t \in [\Delta, \tau] \\ x(\tau) = x^* \text{ where } x_j^* = \alpha S_j. \end{cases}$$

- Knowing the states $x(0)$ and $x(\Delta)$, the resolution of the boundary values problem

$$\begin{cases} \dot{x} = Ax + e_1 e_1^T p, & \forall t \in [0, \Delta] \\ x(0) = 0, x(\Delta) = x_\Delta \end{cases}$$

should provide the adjoint state initial condition $p(0) = p_0$. We could then compute $p(\Delta) = p_\Delta$ and $p(\tau^-)$ by solving the Cauchy problems

$$\begin{cases} \dot{p} = -A^T p, & \forall t \in [0, \Delta] \\ p(0) = p_0 \end{cases}$$

and

$$\begin{cases} \dot{p} = -A^T p, & \forall t \in [\Delta, \tau] \\ p(\Delta) = p_\Delta. \end{cases}$$

- On $[\tau + \Delta, t_f]$, the block at position (1,2) is again the zero matrix. The state $x(\tau + \Delta) = x_{\tau+\Delta}$ should be determined by solving the Cauchy problem

$$\begin{cases} \dot{x} = Ax, & \forall t \in [\tau + \Delta, t_f] \\ x(t_f) = x^* \text{ where } x_j^* = \alpha S_j. \end{cases}$$

- Knowing the states $x(\tau)$ and $x(\tau + \Delta)$, the resolution of the boundary values problem

$$\begin{cases} \dot{x} = Ax + e_1 e_1^T p, & \forall t \in [\tau, \tau + \Delta] \\ x(\tau) = x^*, x(\tau + \Delta) = x_{\tau+\Delta} \end{cases}$$

should provide $p(\tau^+)$, and thus $\bar{v}(\tau) = p_j(\tau^-) - p_j(\tau^+)$. We could then compute $p(\tau + \Delta) = p_{\tau+\Delta}$ and $p(t_f) = \bar{v}(t_f)e_j$ by solving the Cauchy problems

$$\begin{cases} \dot{p} = -A^T p, & \forall t \in [\tau, \tau + \Delta] \\ p(\tau^+) = p(\tau^-) - \bar{v}(\tau)e_j \end{cases}$$

and

$$\begin{cases} \dot{p} = -A^T p, & \forall t \in [\tau + \Delta, t_f] \\ p(\tau + \Delta) = p_{\tau+\Delta}. \end{cases}$$

The $n - 1$ unknown components of x^* can be completed by the information on the adjoint state final condition:

- The integration of $\dot{p} = -A^T p$ (in inverse time) on $[\tau + \Delta, t_f]$ yields

$$p(\tau + \Delta) = e^{A^T(t_f - \tau - \Delta)} p(t_f). \quad (8.4.1)$$

- The solution of $\dot{p} = -A^T p$ (in inverse time) on the time interval $[\tau, \tau + \Delta]$ is given by

$$\begin{aligned} p(t) &= e^{A^T(\tau + \Delta - t)} p(\tau + \Delta), & \forall t \in [\tau, \tau + \Delta] \\ &\stackrel{(8.4.1)}{=} e^{A^T(t_f - t)} p(t_f), & \forall t \in [\tau, \tau + \Delta] \end{aligned} \quad (8.4.2)$$

- The integration of $\dot{x} = Ax + e_1 e_1^T p$ on $[\tau, \tau + \Delta]$ yields

$$\begin{aligned} x(\tau + \Delta) &= e^{A\Delta} x(\tau) + \int_{\tau}^{\tau + \Delta} e^{A(\tau + \Delta - s)} e_1 e_1^T p(s) ds \\ &\stackrel{(8.4.2)}{=} e^{A\Delta} x(\tau) + \int_{\tau}^{\tau + \Delta} e^{A(\tau + \Delta - s)} e_1 e_1^T e^{A^T(t_f - s)} ds p(t_f) \end{aligned} \quad (8.4.3)$$

- The solution of $\dot{x} = Ax$ on the time interval $[\tau + \Delta, t_f]$ is given by

$$\begin{aligned} x(t) &= e^{A(t - \tau - \Delta)} x(\tau + \Delta), & \forall t \in [\tau + \Delta, t_f] \\ &\stackrel{(8.4.3)}{=} e^{A(t - \tau)} x(\tau) + \int_{\tau}^{\tau + \Delta} e^{A(t - s)} e_1 e_1^T e^{A^T(t_f - s)} ds p(t_f), & \forall t \in [\tau + \Delta, t_f] \end{aligned}$$

In particular for $t = t_f$, we obtain the following equivalent identities

$$\begin{aligned} x(t_f) &= e^{A(t_f - \tau)} x(\tau) + \int_{\tau}^{\tau + \Delta} e^{A(t_f - s)} e_1 e_1^T e^{A^T(t_f - s)} ds p(t_f) \\ (I - e^{A(t_f - \tau)}) x^* &= \int_{\tau}^{\tau + \Delta} e^{A(t_f - s)} e_1 \left(e^{A(t_f - s)} e_1 \right)^T ds \bar{v}(t_f) e_j \end{aligned}$$

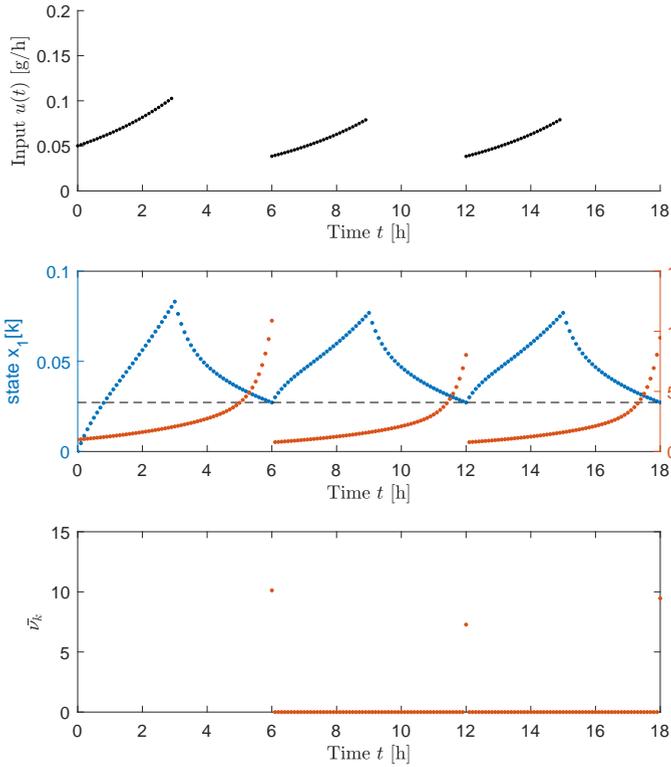
which is a system of n equations and n unknown parameters, namely the $(n - 1)$ unknown components of the state x^* at the contact and final times, and the nonzero component $\bar{v}(t_f)$ of the adjoint state at the final time.

We could easily extend the reasoning to $m > 2$.

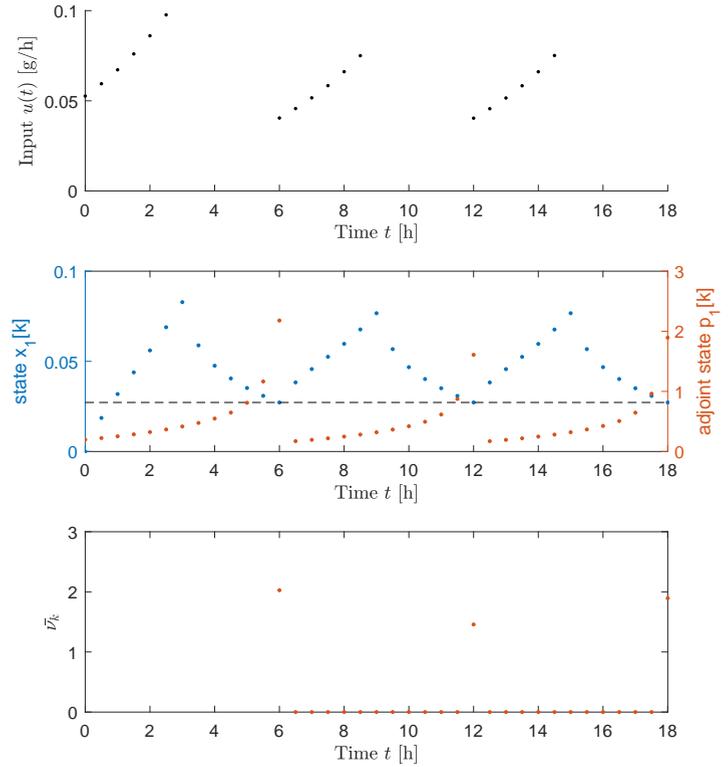
An extension to $j = 2$ could also be investigated. Due to time disconnect between systemic and tissue concentrations, the contact time τ verifies

$$T < \tau < T + \Delta.$$

In that case, we have to integrate the Hamiltonian system on five time intervals $[0, \Delta]$, $[\Delta, T]$, $[T, \tau]$, $[\tau, T + \Delta]$, and $[T + \Delta, t_f]$.



(a) $j = 1 - h = 0.1$



(b) $j = 1 - h = 0.5$

Figure 8.9 – Numerical resolution of the discrete-time OC problem with constraint relaxation using *quadprog.m* ($n_{\text{adm}} = 1$): different discretization steps

■ *Optimal total amount of drug.*

We stated the conjecture that the L_2 -norm-based optimal control $u(\cdot)$, under the constraints (8.1.5), is exactly the control that minimizes its L_1 -norm, i.e., the total amount of drug. However, it is not the case under the relaxed constraints, as illustrated in Figure 8.10. These graphs show the solution, in discrete-time setting, of the following OC problem:

$$J(u) = \int_0^{t_f} |u(t)| dt \longrightarrow \min$$

for the system dynamics $\dot{x} = Ax + bu$ with a fixed initial condition $x_0 = 0$, and under the following relaxed input and state constraints:

$$\begin{cases} u(t) = 0 & \forall t \text{ s.t. } (t \bmod T) \geq \Delta \\ u(t) \geq 0 & \forall t \in [0, t_f[\text{ s.t. } (t \bmod T < \Delta) \\ e_j^T x(t) \geq \alpha S_j & \forall t \in [n_{\text{adm}}T, t_f] \end{cases}$$

The optimal solution is not intuitive (discontinuity of the optimal state trajectory, boundary intervals) and needs to be investigated. Without going into details, we can already suggest some lines of investigation. The discrete-time objective function reads as

$$\tilde{J}_1(u) = \sum_{i=0}^{m-1} \sum_{k=iN}^{iN+N_1-1} u[k] \longrightarrow \min$$

Due to the linearity of the objective function, the optimal u does not correspond to a stationarity point of the Lagrangian function. Indeed, the following KKT condition:

$$\partial \mathcal{L} / \partial u[k] = 0, \quad \forall k \in \{iN, \dots, iN + N_1 - 1 \mid i = 0, \dots, m-1\} \quad (\text{b})$$

becomes

$$(\text{b}) \quad -b_d^T p[k] - v_k = 0, \quad \forall k \in \{iN, \dots, iN + N_1 - 1 \mid i = 0, \dots, m-1\}.$$

The optimal solution should therefore be determined by the (active) state constraints. It is expected that the state constraints are active at times of c_{trough} . For simplicity, let assume that $j = 1$ (state constraint in the plasma). Thus, at steady state, the minimal concentration (c_{trough}) is reached at the end of the dosing interval, just before a new administration. Based on the numerical tests, we assume that the optimal control u is zero everywhere, except at the end of the administration intervals, i.e.

$$u[k] = 0, \quad \forall k \notin \{iN + N_1 - 1 \mid i = n_{\text{adm}} - 1, \dots, m-1\}.$$

The solution of the dynamics (p. 139) can be expressed, for all $i \in \{0, \dots, m-1\}$ and for all $l \in \{0, \dots, N-1\}$, by

$$x[iN + N_1 + l] = \sum_{\tilde{i}=0}^i A_d^{\tilde{i}N+l} b_d u[(i-\tilde{i})N + N_1 - 1].$$

By evaluating the state inequality constraint

$$e_j^T x[k] \geq \alpha S_j$$

in $k = iN + N_1 + l$, for all $i \in \{n_{\text{adm}} - 1, \dots, m - 1\}$ and for $l = 0$, and assuming that the constraint is active at these points, we will obtain a system of equations that should provide the values of the control variable u .

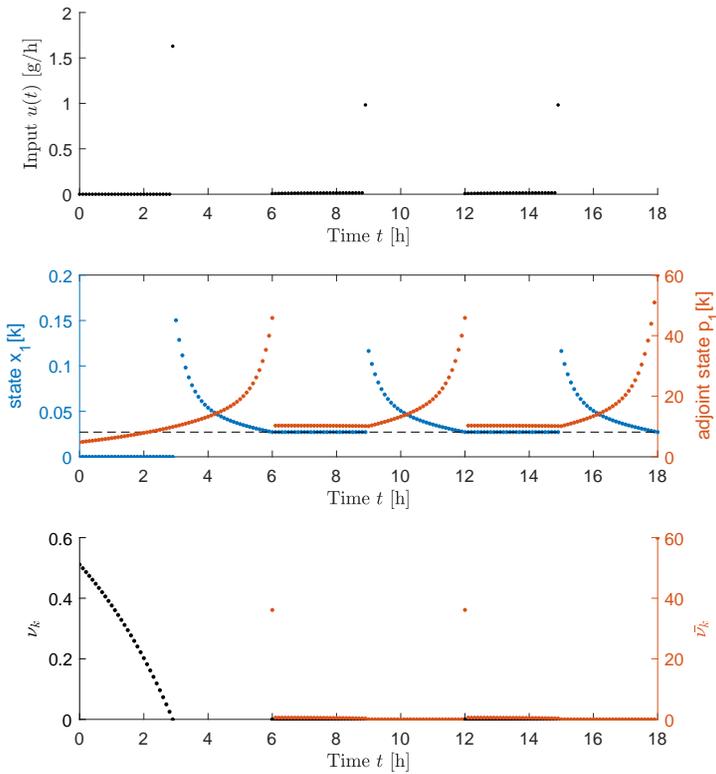


Figure 8.10 – Numerical resolution of the discrete-time L_1 -norm-based OC problem with constraint relaxation, using `linprog.m` ($j = 1, n_{\text{adm}} = 1$)

Conclusion and perspectives

“[...] dites-moi que je suis nécessaire et je vous soulève des montagnes.”

La déesse des petites victoires (2012)
Yannick Grannec

This PhD thesis is an interdisciplinary work, between life sciences and mathematics. The American mathematician William Paul Thurston said “*Mathematics is not about numbers, equations, computations, or algorithms: it is about understanding.*” Through this work, we showed that mathematics enables to describe and understand real data. Thanks to mathematical tools of dynamical systems and control theory, we shed light on still challenging research questions that concern adequate dose selection (Musuamba et al. (2017)).

Three drugs were presented and then used as case studies to exemplify the control methods for drug dosing. Meropenem and temocillin are intravenous β -lactam antibiotics used for the treatment of critically ill patients with pneumonia. As all β -lactam AB, they are time-dependent drugs, so that their PK/PD index is well-known. On the contrary, hydroxychloroquine is an oral drug used off-label during the first peak of the COVID-19 epidemic. Its PK/PD target is unknown: further studies are needed to characterize the exposure-response for both safety and efficacy (Morrisette et al. (2020)). Based on individual data collected during prospective studies and routine clinical practice, population pharmacokinetics analyses were conducted using a non-linear mixed effects modeling approach. Data were available at the site of infection for temocillin and meropenem, so that an additional compartment was added in the popPK models to describe and then predict ELF drug exposure. The developed population models of temocillin and meropenem are so-called *mechanistic-based* models, as some covariates are included based on physiological considerations, but are not necessarily supported by the data (overparametrization). In other words, the approach used is not completely an empirical (data-driven) analysis. A “middle-out” (or semi-

mechanistic) PBPK model was also developed for meropenem. Such a model is less dependent on the data and could therefore be used for extrapolation in different populations, as discussed on external data in obese patients. Models were internally validated by numerical and graphical tools and showed satisfactory fitting performances. Some patient- and population-level data digitized in already published models were used for external evaluation.

In the second part, we discussed current and studied methods for dosing rationale. An input-output analysis was conducted for a right-continuous piecewise constant input function, representing the intravenous administration of a fixed dose at regular dosing intervals. It yields a so-called I/O formula (open-loop control law). The latter enables to compute the dose needed to attain the most stringent PK/PD target for time-dependent drugs ($100\%T > MIC$), but can be easily adapted to other PK/PD target provided that the relevant time t^* in Equation (6.2.1) is known. This result can be applied to the “worst-case” system, ensuring an arbitrarily high probability of success. The I/O formula was then used to design a heuristic estimated state feedback for dosing adjustment. Finally, an OC control approach was investigated to determine the L_2 -norm-based optimal dosing under state and (relaxed) input constraints.

Therapeutic drug monitoring with feedback control is likely the best approach for individualized dosing in order to prevent AB underdosing and improve clinical outcome. From TDM data measured in clinical practice and Bayes estimations, a nominal PK model could be refined to obtain the model specific to an individual patient. Such techniques should improve patients’ treatment and costs. However, it is currently not often used in clinical routine for β -lactam antibiotics (see, e.g., Veiga and Paiva (2018)). In Darwich et al. (2017), authors regret that model-informed precision dosing is not widespread in clinical practice, staying in local collaborations between academia and healthcare. PK modelers “*need to increase awareness and transfer knowledge [...] to ensure that the application is not lost in the methodology by aligning with healthcare professionals, patient groups, industry, and regulators.*” The modeling tools, computational and analytical methods are aimed to support clinicians and physicians who have to face situations using their previous experience.

Perspectives

A few perspectives were highlighted in the manuscript. We list below the outlook and the scope for further improvement.

- The overparametrization noted in the pharmacokinetic models could be confirmed by observability tests of the augmented systems, in which the additional state components are the PK parameters to be estimated P ($\dot{P} = 0$).
- The popPK model of temocillin (Chapter 3) describes the free plasma concentrations, since only the free drug is able to diffuse through the blood-alveolar barrier. Total observed values are also available. It could be interesting to model

both total and free concentrations in order to describe the protein binding, using

$$c_t = c_u + B_{\text{lin}} \cdot c_u + B_{\text{max}} \frac{c_u}{K_m + c_u}$$

where c_t and c_u stand for total and unbound plasma concentrations, $B_{\text{lin}} \cdot c_u$ represents the linear protein binding, B_{max} is the maximal value of the nonlinear and saturable protein binding term and K_m is the unbound concentration at half-maximal binding (see, e.g., Henningsson et al. (2003)). Furthermore, as the dosing history is well-defined, we could develop the model without assuming steady-state observed concentrations.

- The PBPK model of meropenem was developed assuming that the drug was administrated in the arterial pool and that the observations were arterial samples. The estimation process could be performed again by considering that the drug is administrated in the venous pool and that the plasma observations are venous samples. Furthermore, simulations in obese patients led to identify possible model weaknesses for extrapolation, such as the fact the the renal clearance is assumed to account for 70% of the total elimination. An alternative clearance parametrization could be considered.
- Chapters 6-8 were developed based on numerical investigations from the population model of meropenem. This model has then been chosen to provide the readers with toy examples. The different established control laws and algorithms could be applied to the other models developed for IV drugs. In particular, it could be interesting to conduct an in-depth comparative analysis (I/O maintenance and loading doses and optimal dosing) between the popPK and PBPK models.
- The analyses reported in Chapters 6-8 were conducted for the dosing of intravenous drugs. In the case of a bolus injection or an oral administration, the system input u is the null function (see Section 1.3) so that the control must be performed on the initial condition. Similar developments, from the input-output to the optimal control approaches, could be done in this alternative framework. The model of HCQ could be used for the numerical tests and investigations. A result similar to Proposition 6.1.2 is presented in the PhD thesis Koch (2012). The author gives the solution of the state trajectory x for multiple dosing.
- The open-loop control law (6.2.2) is based on only one degree of freedom (dose, D). This method could fail in the case of drugs with a (narrow) therapeutic window. It could then be needed to either adapt the I/O formula in order to compute the maximum dose not to be exceeded, in addition to the dose required for efficacy, or to design two parameters, e.g., dose (D) and infusion duration (Δ). A discussion is initiated in Section 6.3 and deserves to be deepened in line with the needs in clinical practice.
- As highlighted in Section 8.4, the characterization of the optimal solution under relaxed constraints, provided in Proposition 8.3.1, seems to be complete.

Indeed, the jump values and the final condition of the adjoint state should be determined by solving the Hamiltonian system describing the dynamics of the joint state and adjoint state.

- Additional perspectives for further research include the discretization of the Pontryagin's minimum principle (Proposition 8.3.1), to verify if it will correspond to the discrete-time minimum principle derived from the KKT conditions, as well as the study of the continuous-time solution without constraint relaxation.
- A very interesting perspective from a clinical point of view could be the resolution of the OC problem developed in Chapter 8 for an alternative objective function: the L_1 -norm of the control function, representing the total amount of administrated drug. Indeed, in that case, the optimal dosing will be the minimal effective dose. An intuition of the discrete-time solution is given in Section 8.4.

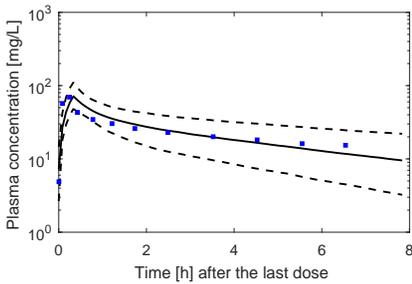
Appendices

APPENDIX **A**

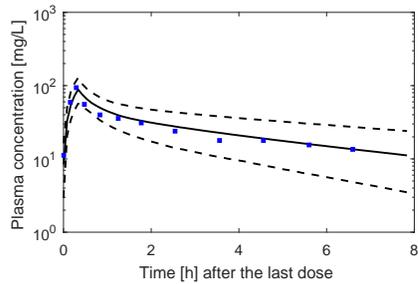
External evaluation of the models of meropenem: additional plots

This appendix provides additional external evaluation plots for the population and the physiologically based model of meropenem.

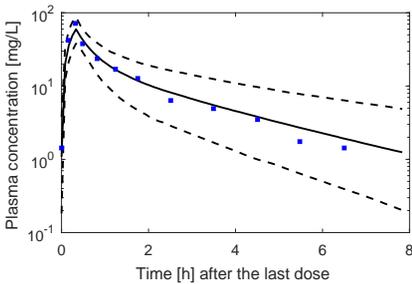
A.1 Population model



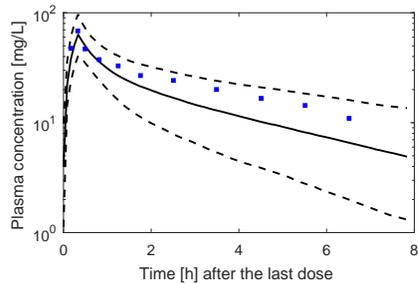
(a) Patient 1: WT, 65 kg; GFR, 35 mL/min



(b) Patient 2: WT, 50 kg; GFR, 30 mL/min



(c) Patient 5: WT, 67 kg; GFR, 135 mL/min



(d) Patient 6: WT, 70 kg; GFR, 61 mL/min

Figure A.1 – Simulated plasma PK profile (median and 90% PI) for the patients described in Karjagin et al. (2008), after two doses of 1 g over 20 minutes infusion every 8 hours. Square points, (digitized) observed plasma concentrations; GFR is approximated by Cl_{CR} .

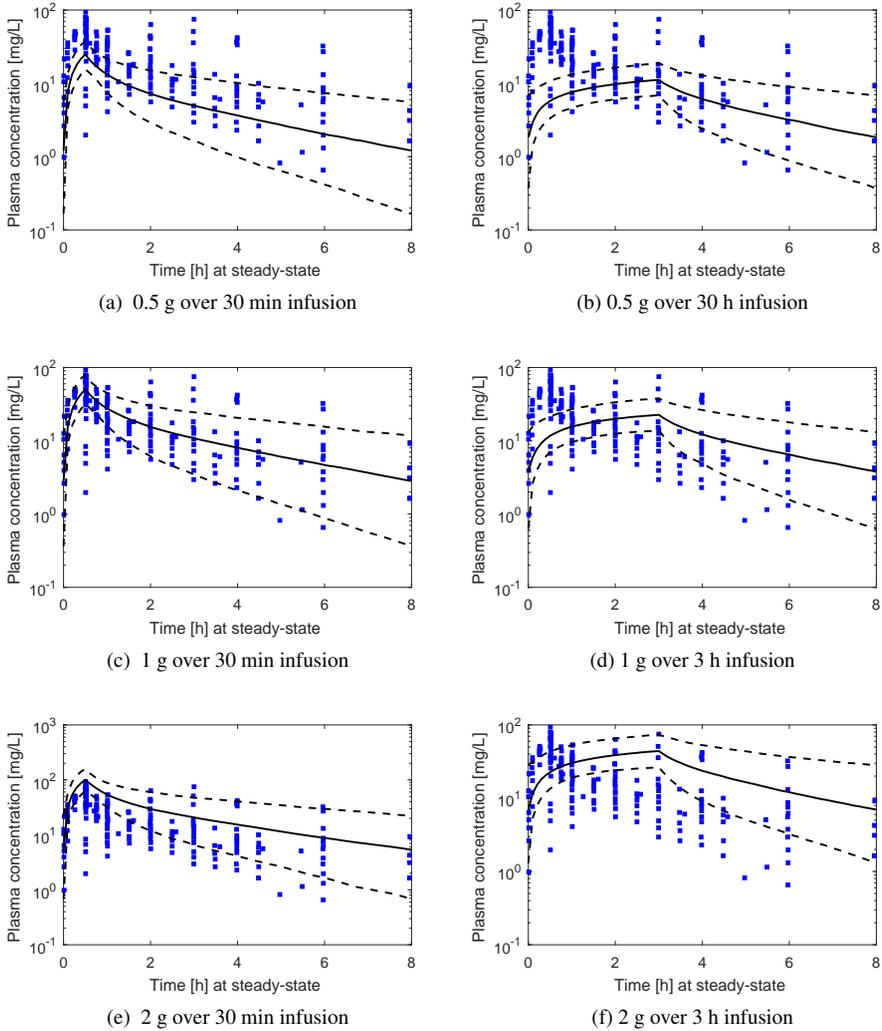


Figure A.2 – Simulated plasma PK profiles (median and 90% PI) after different dosing regimens for 1000 patients consistent with the variable ranges described in the Li et al. (2006). Square points, (digitized) observed plasma concentrations; GFR is computed with the MDRD formula.

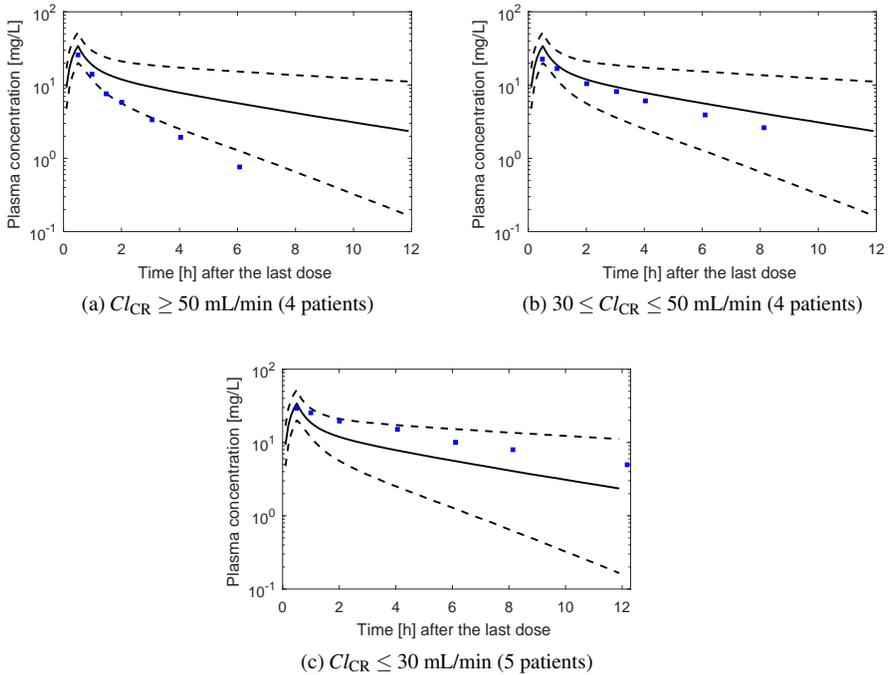
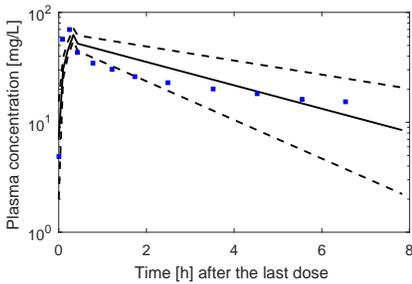
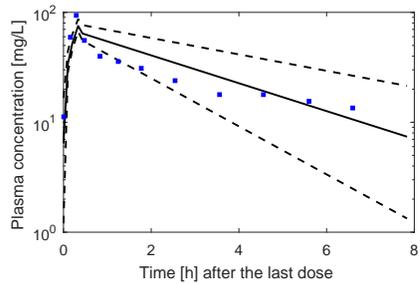


Figure A.3 – Simulated plasma PK profiles (median and 90% PI) for various degrees of renal function as described in the Chimata et al. (1993), after one dose of 0.5 g over 30 minutes infusion. Square points, (digitized) observed plasma concentrations; GFR is approximated by Cl_{CR} .

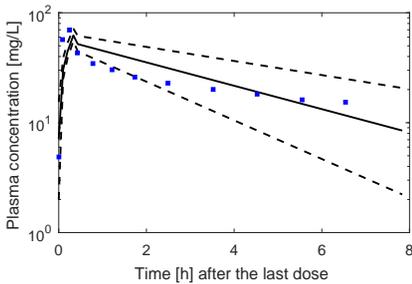
A.2 Physiologically based model



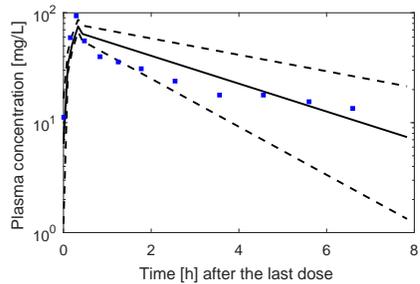
(a) Patient 1: WT, 65 kg; GFR, 35 mL/min



(b) Patient 2: WT, 50 kg; GFR, 30 mL/min



(c) Patient 5: WT, 67 kg; GFR, 135 mL/min



(d) Patient 6: WT, 70 kg; GFR, 61 mL/min

Figure A.4 – Simulated plasma PK profile (median and 90% PI) for the patients described in Karjagin et al. (2008), after two doses of 1 g over 20 minutes infusion every 8 hours. Square points, (digitized) observed plasma concentrations; GFR is approximated by Cl_{CR} .

Appendix A External validation: additional plots

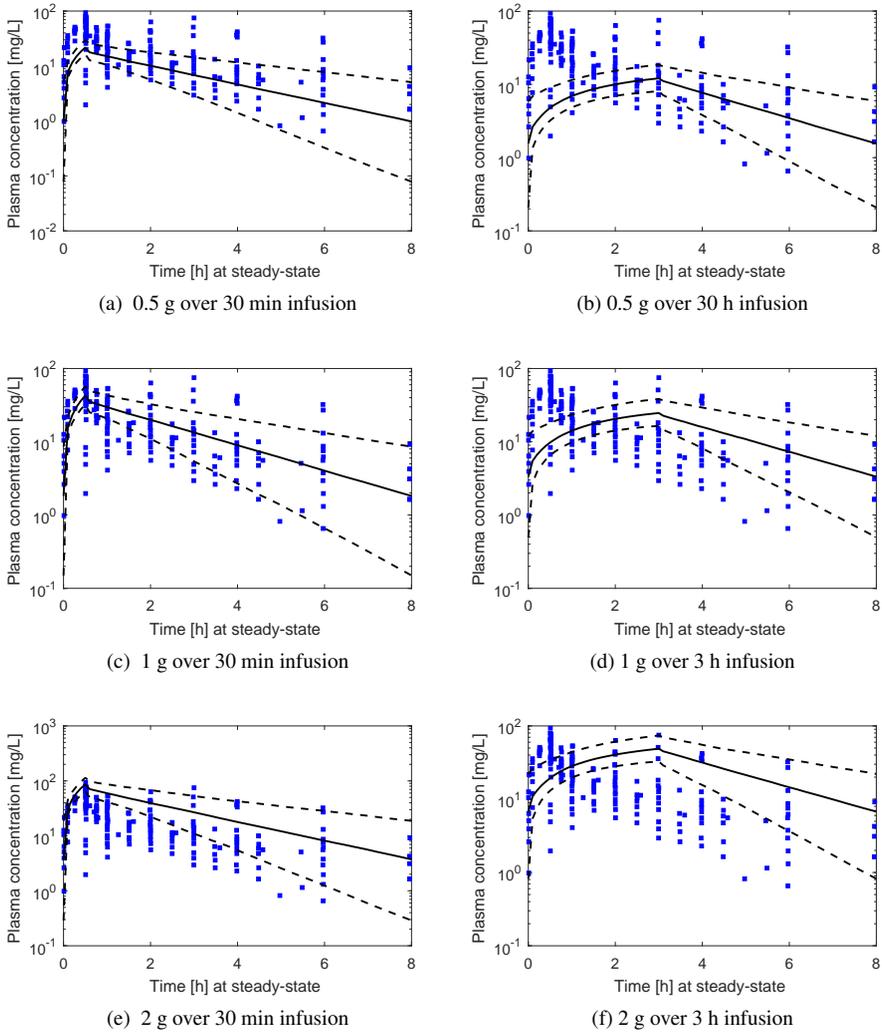


Figure A.5 – Simulated plasma PK profiles (median and 90% PI) after different dosing regimens for 1000 patients consistent with the variable ranges described in the Li et al. (2006). Square points, (digitized) observed plasma concentrations; GFR is computed with the MDRD formula.

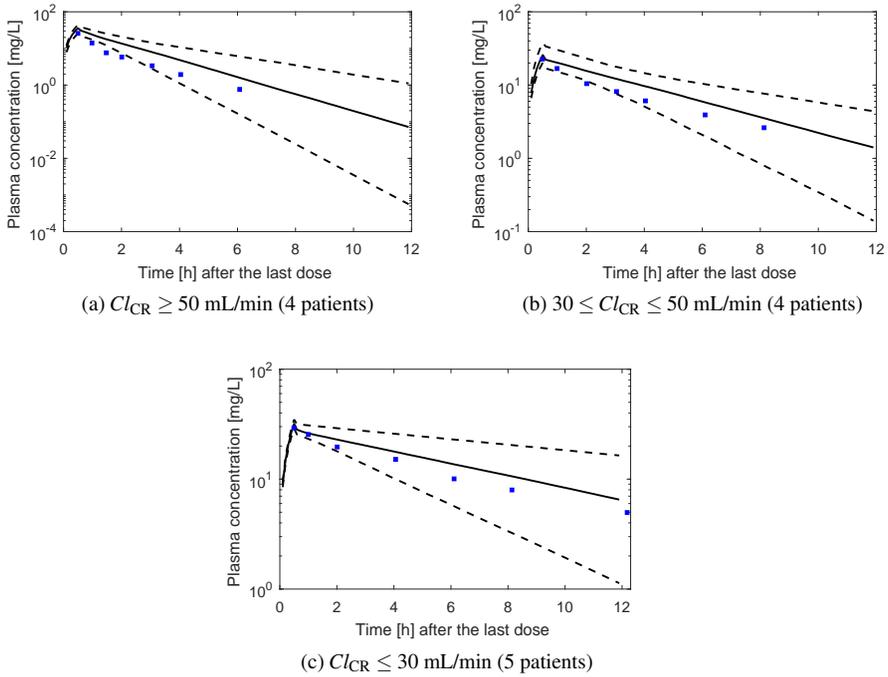


Figure A.6 – Simulated plasma PK profiles (median and 90% PI) for various degrees of renal function as described in the Chimata et al. (1993), after one dose of 0.5 g over 30 minutes infusion. Square points, (digitized) observed plasma concentrations; GFR is approximated by Cl_{CR} .

APPENDIX B

Resolvent function of the PBPK model: symbolic computations

We report here the numerators of the elements (3,1) to (3,6) of the resolvent matrix $(sI - A)^{-1}$, where A is the state matrix of the PBPK model of meropenem developed in Section 4.3.

(3, 1)

$$\begin{aligned} & (KL*VART*VLUN*(VKID*VLIV*KP^2*QRB^2 + KRB*VLIV*VRB*KP*QKID^2 + \\ & KRB*VKID*VRB*KP*QLIV^2))*s^3 + \\ & (QCO*VART*(VKID*VLIV*KP^2*QRB^2 + KRB*VLIV*VRB*KP*QKID^2 + \\ & KRB*VKID*VRB*KP*QLIV^2) + KL*VART*VLUN*(KP*QKID*QRB^2*VLIV + \\ & KP*QLIV*QRB^2*VKID + KP*QKID^2*QRB*VLIV + KP*QLIV^2*QRB*VKID + \\ & KRB*QKID*QLIV^2*VRB + KRB*QKID^2*QLIV*VRB + CLH*KP*QRB^2*VKID + \\ & CLR*KP*QRB^2*VLIV + CLH*KRB*QKID^2*VRB + \\ & CLR*KRB*QLIV^2*VRB))*s^2 + \\ & (QCO*VART*(KP*QKID*QRB^2*VLIV + KP*QLIV*QRB^2*VKID + \\ & KP*QKID^2*QRB*VLIV + KP*QLIV^2*QRB*VKID + KRB*QKID*QLIV^2*VRB + \\ & KRB*QKID^2*QLIV*VRB + CLH*KP*QRB^2*VKID + CLR*KP*QRB^2*VLIV + \\ & CLH*KRB*QKID^2*VRB + CLR*KRB*QLIV^2*VRB) + \\ & KL*VART*VLUN*(QKID^2*QLIV*QRB + CLH*QKID^2*QRB + \\ & QKID*QLIV^2*QRB + QKID*QLIV*QRB^2 + CLH*QKID*QRB^2 + \\ & CLR*QLIV^2*QRB + CLR*QLIV*QRB^2 + CLH*CLR*QRB^2))*s + \\ & QCO*VART*(QKID^2*QLIV*QRB + CLH*QKID^2*QRB + QKID*QLIV^2*QRB + \\ & QKID*QLIV*QRB^2 + CLH*QKID*QRB^2 + CLR*QLIV^2*QRB + \\ & CLR*QLIV*QRB^2 + CLH*CLR*QRB^2) \end{aligned}$$

(3, 2)

Appendix B Resolvent function PBPK model

$$\begin{aligned}
 & (QCO*VLUN*(VKID*VLIV*KP^2*QRB^2 + KRB*VLIV*VRB*KP*QKID^2 + \\
 & KRB*VKID*VRB*KP*QLIV^2))*s^2 + \\
 & (QCO*VLUN*(KP*QKID*QRB^2*VLIV + KP*QLIV*QRB^2*VKID + \\
 & KP*QKID^2*QRB*VLIV + KP*QLIV^2*QRB*VKID + KRB*QKID*QLIV^2*VRB + \\
 & KRB*QKID^2*QLIV*VRB + CLH*KP*QRB^2*VKID + CLR*KP*QRB^2*VLIV + \\
 & CLH*KRB*QKID^2*VRB + CLR*KRB*QLIV^2*VRB))*s + \\
 & QCO*VLUN*(QKID^2*QLIV*QRB + CLH*QKID^2*QRB + QKID*QLIV^2*QRB + \\
 & QKID*QLIV*QRB^2 + CLH*QKID*QRB^2 + CLR*QLIV^2*QRB + \\
 & CLR*QLIV*QRB^2 + CLH*CLR*QRB^2)
 \end{aligned}$$

(3,3)

$$\begin{aligned}
 & (KL*KP^2*KRB*VART*VKID*VLIV*VLUN*VRB*VVEN))*s^5 + \\
 & (KP*VLIV*(KP*VKID*(VART*(KRB*QCO*VRB*VVEN + KL*QRB*VLUN*VVEN) + \\
 & KL*KRB*QCO*VLUN*VRB*VVEN) + KL*KRB*VART*VLUN*VRB*VVEN*(CLR + \\
 & QKID)) + KL*KP*KRB*VART*VKID*VLUN*VRB*VVEN*(CLH + QLIV))*s^4 + \\
 & ((KP*VKID*(VART*(KRB*QCO*VRB*VVEN + KL*QRB*VLUN*VVEN) + \\
 & KL*KRB*QCO*VLUN*VRB*VVEN) + KL*KRB*VART*VLUN*VRB*VVEN*(CLR + \\
 & QKID))*(CLH + QLIV) + KP*VLIV*((VART*(KRB*QCO*VRB*VVEN + \\
 & KL*QRB*VLUN*VVEN) + KL*KRB*QCO*VLUN*VRB*VVEN)*(CLR + QKID) + \\
 & KP*VKID*(QCO*(KRB*QCO*VRB*VVEN + KL*QRB*VLUN*VVEN) + \\
 & QCO*QRB*VART*VVEN)))*s^3 + \\
 & (((VART*(KRB*QCO*VRB*VVEN + KL*QRB*VLUN*VVEN) + \\
 & KL*KRB*QCO*VLUN*VRB*VVEN)*(CLR + QKID) + \\
 & KP*VKID*(QCO*(KRB*QCO*VRB*VVEN + KL*QRB*VLUN*VVEN) + \\
 & QCO*QRB*VART*VVEN))*(CLH + QLIV) + \\
 & KP*VLIV*((QCO*(KRB*QCO*VRB*VVEN + KL*QRB*VLUN*VVEN) + \\
 & QCO*QRB*VART*VVEN)*(CLR + QKID) + KP*QCO^2*QRB*VKID*VVEN))*s^2 + \\
 & (((QCO*(KRB*QCO*VRB*VVEN + KL*QRB*VLUN*VVEN) + \\
 & QCO*QRB*VART*VVEN)*(CLR + QKID) + KP*QCO^2*QRB*VKID*VVEN)*(CLH + \\
 & QLIV) + KP*QCO^2*QRB*VLIV*VVEN*(CLR + QKID))*s + \\
 & QCO^2*QRB*VVEN*(CLR + QKID)*(CLH + QLIV)
 \end{aligned}$$

(3,4)

$$\begin{aligned}
 & (KL*KP*KRB*QLIV*VART*VKID*VLIV*VLUN*VRB))*s^4 + \\
 & (KP*VKID*(VART*(KRB*QCO*QLIV*VLIV*VRB + KL*QLIV*QRB*VLIV*VLUN) + \\
 & KL*KRB*QCO*QLIV*VLIV*VLUN*VRB) + \\
 & KL*KRB*QLIV*VART*VLIV*VLUN*VRB*(CLR + QKID))*s^3 + \\
 & ((VART*(KRB*QCO*QLIV*VLIV*VRB + KL*QLIV*QRB*VLIV*VLUN) + \\
 & KL*KRB*QCO*QLIV*VLIV*VLUN*VRB)*(CLR + QKID) + \\
 & KP*VKID*(QCO*(KRB*QCO*QLIV*VLIV*VRB + KL*QLIV*QRB*VLIV*VLUN) + \\
 & QCO*QLIV*QRB*VART*VLIV))*s^2 + \\
 & ((QCO*(KRB*QCO*QLIV*VLIV*VRB + KL*QLIV*QRB*VLIV*VLUN) + \\
 & QCO*QLIV*QRB*VART*VLIV)*(CLR + QKID) + \\
 & KP*QCO^2*QLIV*QRB*VKID*VLIV))*s + \\
 & QCO^2*QLIV*QRB*VLIV*(CLR + QKID)
 \end{aligned}$$

(3,5)

$$(KL*KP*KRB*QKID*VART*VKID*VLIV*VLUN*VRB))*s^4 +$$

$$\begin{aligned}
& (KP*VLIV*(VART*(KRB*QCO*QKID*VKID*VRB + KL*QKID*QRB*VKID*VLUN) + \\
& KL*KRB*QCO*QKID*VKID*VLUN*VRB) + \\
& KL*KRB*QKID*VART*VKID*VLUN*VRB*(CLH + QLIV))*s^3 + \\
& ((VART*(KRB*QCO*QKID*VKID*VRB + KL*QKID*QRB*VKID*VLUN) + \\
& KL*KRB*QCO*QKID*VKID*VLUN*VRB)*(CLH + QLIV) + \\
& KP*VLIV*(QCO*(KRB*QCO*QKID*VKID*VRB + KL*QKID*QRB*VKID*VLUN) + \\
& QCO*QKID*QRB*VART*VKID))*s^2 + \\
& ((QCO*(KRB*QCO*QKID*VKID*VRB + KL*QKID*QRB*VKID*VLUN) + \\
& QCO*QKID*QRB*VART*VKID)*(CLH + QLIV) + \\
& KP*QCO^2*QKID*QRB*VKID*VLIV)*s + \\
& QCO^2*QKID*QRB*VKID*(CLH + QLIV) \\
& (3,6) \\
& (KL*KP^2*QRB*VART*VKID*VLIV*VLUN*VRB)*s^4 + \\
& (KP*VLIV*(KP*VKID*(QCO*QRB*VART*VRB + KL*QCO*QRB*VLUN*VRB) + \\
& KL*QRB*VART*VLUN*VRB*(CLR + QKID)) + \\
& KL*KP*QRB*VART*VKID*VLUN*VRB*(CLH + QLIV))*s^3 + \\
& ((KP*VKID*(QCO*QRB*VART*VRB + KL*QCO*QRB*VLUN*VRB) + \\
& KL*QRB*VART*VLUN*VRB*(CLR + QKID))*(CLH + QLIV) + \\
& KP*VLIV*((QCO*QRB*VART*VRB + KL*QCO*QRB*VLUN*VRB)*(CLR + QKID) + \\
& KP*QCO^2*QRB*VKID*VRB))*s^2 + \\
& (((QCO*QRB*VART*VRB + KL*QCO*QRB*VLUN*VRB)*(CLR + QKID) + \\
& KP*QCO^2*QRB*VKID*VRB)*(CLH + QLIV) + \\
& KP*QCO^2*QRB*VLIV*VRB*(CLR + QKID))*s + \\
& QCO^2*QRB*VRB*(CLR + QKID)*(CLH + QLIV)
\end{aligned}$$

APPENDIX C

Sensitivity analysis on the PBPK model of meropenem

A sensitive analysis was performed using MC simulations of the typical patient (WT, 75 kg; GFR, 65 mL/min; CO, 360 L/h). The simulations were performed using the arbitrary dosing regimen of

1g/8h 3h-infusion.

The physiological parameters used in the PBPK model are reported in Table 4.3. Figures C.1-C.7 show the steady output trajectories y^∞ (i.e., steady-state PK profiles) if a parameter varies between -60% (P_- , blue) and 60% (P_+ , yellow) of the value indicated in Table 4.3, i.e.,

$$P_- = P - \frac{60}{100}P \quad P_+ = P + \frac{60}{100}P$$

We indicate the maximum relative error on the dosing interval with respect to the nominal one:

$$e_{P_-} := \max_{\tilde{t} \in [0, T]} \frac{|y_{P_-}^\infty(\tilde{t}) - y_P^\infty(\tilde{t})|}{y_P^\infty(\tilde{t})}, \quad e_{P_+} := \max_{\tilde{t} \in [0, T]} \frac{|y_{P_+}^\infty(\tilde{t}) - y_P^\infty(\tilde{t})|}{y_{P_+}^\infty(\tilde{t})}$$

A visual inspection of these figures reveals that organ volumes and blood flows have little influence on the model predictions.

Appendix C Sensitive analysis PBPK model

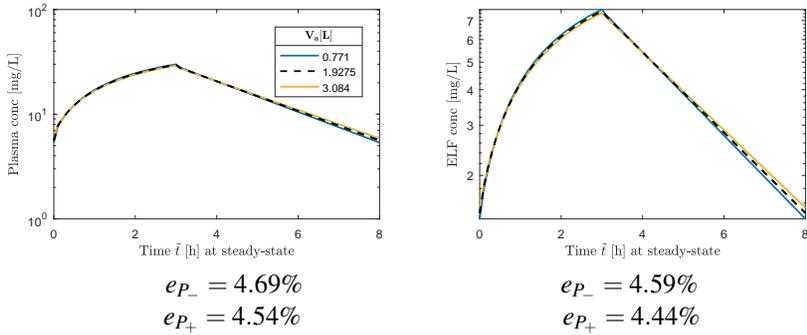


Figure C.1 – Comparison of steady-state PK profiles when the volume of the arterial blood V_a varies

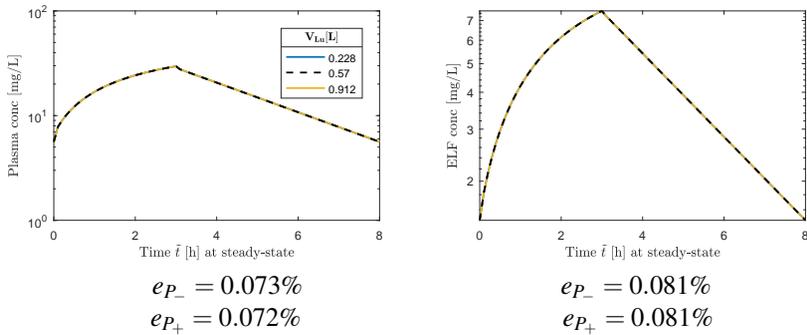


Figure C.2 – Comparison of steady-state PK profiles when the volume of the lungs V_{Lu} varies

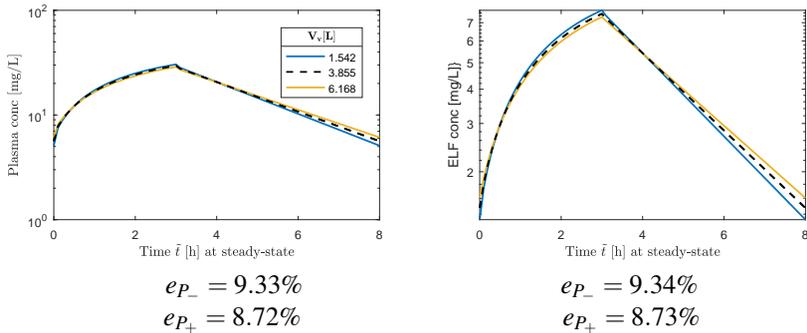


Figure C.3 – Comparison of steady-state PK profiles when the volume of the venous blood V_v varies

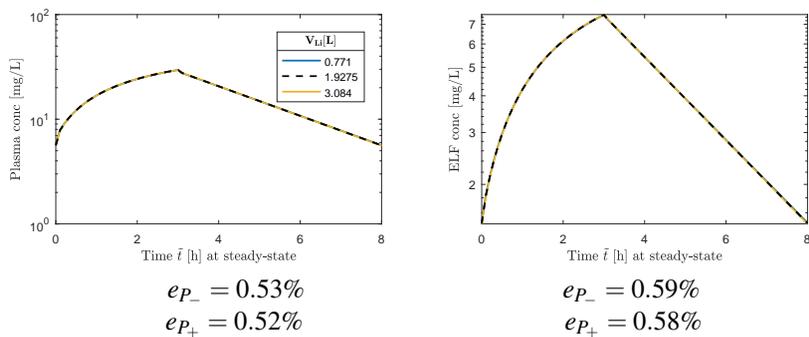


Figure C.4 – Comparison of steady-state PK profiles when the volume of the liver V_{Li} varies

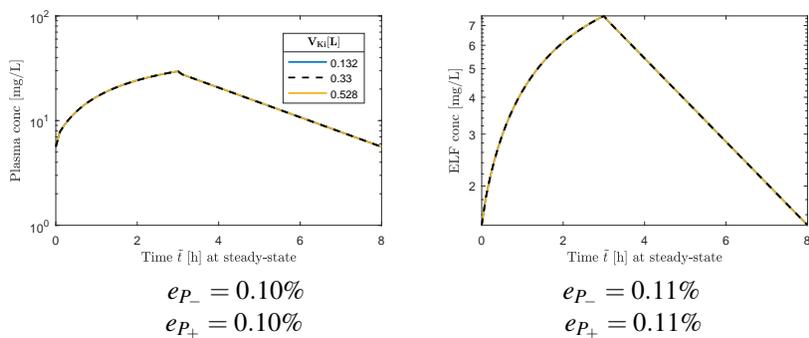


Figure C.5 – Comparison of steady-state PK profiles when the volume of the kidneys V_{Ki} varies

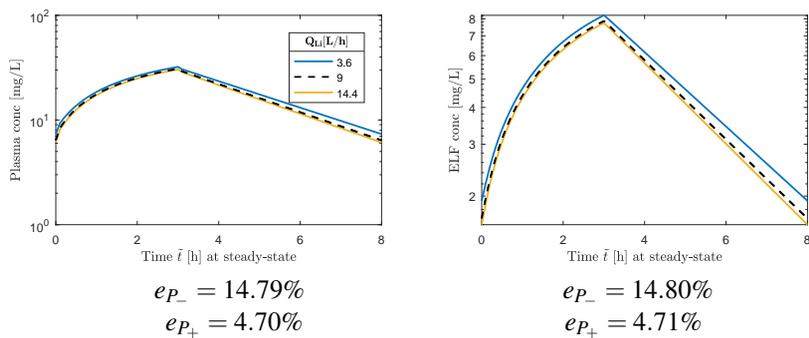
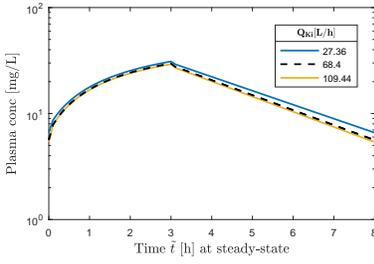
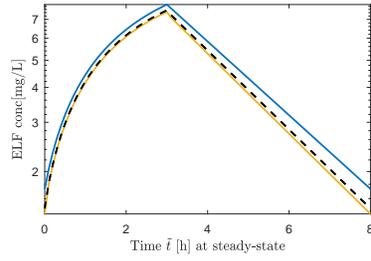


Figure C.6 – Comparison of steady-state PK profiles when the blood flow of the liver Q_{Li} varies



$$e_{P_-} = 17.41\%$$

$$e_{P_+} = 4.34\%$$



$$e_{P_-} = 17.53\%$$

$$e_{P_+} = 4.34\%$$

Figure C.7 – Comparison of steady-state PK profiles when the blood flow of the kidneys Q_{Ki} varies

APPENDIX D

System response

D.1 Context

Let consider a LTI state-space representation:

$$\begin{cases} \dot{x}(t) = Ax(t) + bu(t) \\ y(t) = Cx(t) \end{cases} \quad t \geq 0 \quad (\text{D.1.1})$$

where $A \in \mathbb{R}^{n \times n}$ is (asymptotically) stable, $b \in \mathbb{R}^{n \times 1}$ is filled by $(n - 1)$ zeros and one non-zero value, and $C \in \mathbb{R}^{p \times n}$ has 1 and only 1 non-zero element on each row. This results in a strictly proper transfer function $\hat{G}(s) = (\hat{g}_1(s) \ \dots \ \hat{g}_p(s))^T \in \mathbb{R}_{p,0}(s)^{p \times 1}$. In the following analysis, the state matrix $A \in \mathbb{R}^{n \times n}$ is assumed to have n distinct eigenvalues. The input function is a right-continuous piecewise constant function defined, for all $t \geq 0$, by

$$u(t) [g/h] = \begin{cases} D/\Delta & \text{if } (t \bmod T) < \Delta \\ 0 & \text{if } (t \bmod T) \geq \Delta \end{cases} \quad (\text{D.1.2})$$

where $\Delta \leq T$. It corresponds to the drug infusion rate when u is the input of a pharmacokinetic system.

Definition The *Laplace transform* of a function $f : \mathbb{R} \rightarrow \mathbb{C}$ with support on \mathbb{R}^+ is the function \hat{f} defined by

$$\hat{f}(s) = \mathcal{L}[f(\cdot)](s) = \int_0^{\infty} e^{-st} f(t) dt$$

for all $s \in \mathbb{C}$ such that $\text{Re}[s] > \sigma_0$, where σ_0 , called the absolute convergence abscissa, defines an existence right-half plane.

Remark 11 A delay of T units in the time domain corresponds to a multiplication by e^{-sT} in the Laplace domain, i.e.,

$$\mathcal{L}^{-1}[e^{-sT}\hat{f}(\cdot)](t) = f(t-T), \quad t \geq T.$$

Definition Let us consider the system $[A, b, C]$. Its *transfer function* $\hat{G}(s)$ is defined as the Laplace transform of the system impulse response and is given by

$$\hat{G}(s) = C(sI - A)^{-1}b.$$

The transfer function describes the relationship between inputs and outputs, i.e.,

$$\hat{y} = \hat{G}\hat{u}.$$

D.2 Zero-state system response

Proposition D.2.1 Consider the PK system (D.1.1) with an input function of the form (D.1.2). The zero-state system response $y(\cdot)$ is given as follows, where $N_t := \lfloor t/T \rfloor$ denotes the number of administrations already received at time t (including the ongoing administration, if appropriate): for all $j \in \{1, \dots, p\}$ and for all $t \geq 0$,

- if $(t \bmod T) < \Delta$ (during infusion)

$$y_j(t) = \frac{D}{\Delta} \left[\underbrace{\sum_{l=0}^{N_t-2} \sum_{i=1}^n \frac{F_{ji}}{\lambda_i} e^{\lambda_i(t-lT)} (1 - e^{-\lambda_i \Delta})}_{\text{previous administrations}} + \underbrace{\sum_{i=1}^n \frac{F_{ji}}{\lambda_i} (e^{\lambda_i(t-(N_t-1)T)} - 1)}_{\text{ongoing infusion}} \right] \quad (\text{D.2.1})$$

- if $(t \bmod T) \geq \Delta$ (after infusion)

$$y_j(t) = \frac{D}{\Delta} \underbrace{\sum_{l=0}^{N_t-1} \sum_{i=1}^n \frac{F_{ji}}{\lambda_i} e^{\lambda_i(t-lT)} (1 - e^{-\lambda_i \Delta})}_{\text{previous administrations}} \quad (\text{D.2.2})$$

where, for all $i \in \{1, 2, 3, \dots, n\}$ and $j \in \{1, \dots, p\}$, $\lambda_i \in \sigma(A)$ and

$$F_{ji} := \lim_{s \rightarrow \lambda_i} (\hat{g}_j(s) (s - \lambda_i)).$$

Proof.

Step 1: transfer function. Let $L(s)$ denote the matrix $(sI - A)$, whose characteristic polynomial is given by

$$\det(L(s)) = (s - \lambda_1)(s - \lambda_2)(s - \lambda_3) \cdots (s - \lambda_n).$$

Each component \hat{g}_j ($j \in \{1, \dots, p\}$) of the transfer function $\hat{G}(s)$ can be written in partial fraction expansion as

$$\hat{g}_j(s) = \frac{F_{j1}}{s - \lambda_1} + \frac{F_{j2}}{s - \lambda_2} + \frac{F_{j3}}{s - \lambda_3} + \cdots + \frac{F_{jn}}{s - \lambda_n},$$

where $F_{j1}, F_{j2}, F_{j3}, \dots, F_{jn}$ are the residual of $\hat{g}_j(s)$ in $\lambda_1, \lambda_2, \lambda_3, \dots, \lambda_n$, respectively.

Step 2: Laplace transform of the input function. The input function can be written as a superposition of functions of the form

$$U_i(t) = \frac{D}{\Delta} \cdot \mathbf{1}_{[iT, iT+\Delta]}(t), \quad t \geq 0,$$

where $i \in \mathbb{N}$ and $\mathbf{1}_I$ is the characteristic function of the subset I . Let $N \in \mathbb{N}_0$ be the number of administrations. The input function $u(t)$ is written as

$$u(t) = \sum_{i=0}^{N-1} U_i(t), \quad t \geq 0.$$

The reference input function, corresponding to the first administration, is denoted $U(t)$ and given by

$$U(t) = U_0(t) = \frac{D}{\Delta} \cdot \mathbf{1}_{[0, \Delta]}(t), \quad t \geq 0.$$

The Laplace transform of the latter function is given by

$$\hat{U}(s) = \frac{D}{\Delta} \left(\frac{1}{s} - \frac{e^{-\Delta s}}{s} \right).$$

The other functions $U_i(t)$ ($i \in \{1, \dots, N-1\}$) are equal to the reference input with a delay of iT time units, i.e.,

$$U_i(t) = U(t - iT), \quad t \geq iT.$$

According to Remark 11, there are expressed in the Laplace domain by

$$\hat{U}_i(s) = e^{-s iT} \hat{U}(s).$$

Using the linearity of the Laplace transformation, we finally obtain

$$\hat{u}(s) = \sum_{i=0}^{N-1} e^{-s iT} \frac{D}{\Delta} \left(\frac{1}{s} - \frac{e^{-\Delta s}}{s} \right).$$

Step 3: Time domain response. In the Laplace domain, the zero-state system response is

$$\hat{y}(s) = \hat{G}(s)\hat{u}(s).$$

For $j \in \{1, \dots, p\}$,

$$\hat{y}_j(s) = \hat{g}_j(s)\hat{u}(s) = \frac{D}{\Delta} \cdot \sum_{l=0}^{N-1} \underbrace{e^{-sIT}}_{\text{delay}} \hat{Y}_j(s), \quad (\text{D.2.3})$$

where

$$\hat{Y}_j(s) = \sum_{i=1}^n \frac{F_{ji}}{s - \lambda_i} \left(\frac{1}{s} - \frac{e^{-\Delta s}}{s} \right) = \hat{h}_j(s) - \underbrace{e^{-\Delta s}}_{\text{delay}} \hat{h}_j(s), \quad (\text{D.2.4})$$

where $\hat{h}_j(s) = \sum_{i=1}^n \frac{F_{ji}}{s - \lambda_i} \frac{1}{s}$ (proper rational function). Its partial fraction decomposition (where $\lambda_{n+1} = 0$) is given by

$$\hat{h}_j(s) = \frac{\tilde{F}_{j1}}{s - \lambda_1} + \frac{\tilde{F}_{j2}}{s - \lambda_2} + \frac{\tilde{F}_{j3}}{s - \lambda_3} + \dots + \frac{\tilde{F}_{jn}}{s - \lambda_n} + \frac{\tilde{F}_{j(n+1)}}{s - \lambda_{n+1}},$$

where $\tilde{F}_{j1}, \tilde{F}_{j2}, \tilde{F}_{j3}, \dots, \tilde{F}_{j(n+1)}$ are the residuals of $\hat{h}_j(s)$ in $\lambda_1, \lambda_2, \lambda_3, \dots, \lambda_{n+1}$, respectively. We can easily show that, for all $i \in \{1, 2, 3, \dots, n\}$,

$$\tilde{F}_{ji} = \frac{F_{ji}}{\lambda_i} \quad \text{and} \quad \tilde{F}_{j(n+1)} = - \left(\frac{F_{j1}}{\lambda_1} + \frac{F_{j2}}{\lambda_2} + \frac{F_{j3}}{\lambda_3} + \dots + \frac{F_{jn}}{\lambda_n} \right).$$

Laplace transform formulas enable us to write the inverse Laplace transform of $\hat{h}_j(s)$, as follows:

$$h_j(t) = \mathcal{L}^{-1}[\hat{h}_j(\cdot)](t) = \sum_{i=1}^{n+1} \tilde{F}_{ji} e^{\lambda_i t} = \sum_{i=1}^n \frac{F_{ji}}{\lambda_i} (e^{\lambda_i t} - 1), \quad t \geq 0.$$

Using the linearity of the Laplace transformation to (D.2.4) and Remark 11, we get

$$\begin{aligned} Y_j(t) &= \mathcal{L}^{-1}[\hat{h}_j(\cdot)](t) \\ &= h_j(t) - h_j(t - \Delta), \quad t \geq \Delta \\ &= h_j(t) - h_j(t - \Delta) \mathbf{1}_{[\Delta, +\infty[}(t), \quad t \geq 0. \end{aligned}$$

Similarly, we can deduce from (D.2.3) that, for $t \geq 0$,

$$\begin{aligned} y_j(t) &= \mathcal{L}^{-1}[\hat{y}_j(\cdot)](t) \\ &= \frac{D}{\Delta} \sum_{l=0}^{N-1} Y_j(t - lT) \mathbf{1}_{[lT, +\infty[}(t) \\ &= \frac{D}{\Delta} \sum_{l=0}^{N-1} [h_j(t - lT) \mathbf{1}_{[lT, +\infty[}(t) - h_j(t - lT - \Delta) \mathbf{1}_{[lT + \Delta, +\infty[}(t)] \end{aligned}$$

where $h_j(t) = \sum_{i=1}^n \frac{F_{ji}}{\lambda_i} (e^{\lambda_i t} - 1)$; hence, Identities (D.2.1) and (D.2.2) hold. \square

D.3 Asymptotic system response

Proposition D.3.1 Consider the system (D.1.1) with an input function of the form (D.1.2). The output trajectory converges to an equilibrium trajectory, i.e., for all $\tilde{t} \in [0, T[$,

$$y^N(\tilde{t}) - y^\infty(\tilde{t}) \xrightarrow{N \rightarrow \infty} 0$$

where y^∞ is given, for all $j \in \{1, \dots, p\}$, by

- if $\tilde{t} \in [0, \Delta]$,

$$y_j^\infty(\tilde{t}) = \frac{D}{\Delta} \left[\sum_{i=1}^n \frac{F_{ji}}{\lambda_i} \frac{e^{\lambda_i \tilde{t}} (1 - e^{-\lambda_i \Delta})}{e^{-\lambda_i T} - 1} + \sum_{i=1}^n \frac{F_{ji}}{\lambda_i} (e^{\lambda_i \tilde{t}} - 1) \right]$$

- if $\tilde{t} \in [\Delta, T[$,

$$y_j^\infty(\tilde{t}) = \frac{D}{\Delta} \sum_{i=1}^n \frac{F_{ji}}{\lambda_i} \frac{e^{\lambda_i(\tilde{t}-T)} (1 - e^{-\lambda_i \Delta})}{e^{-\lambda_i T} - 1}.$$

Proof. Let $j \in \{1, \dots, p\}$ and $t \geq 0$ such that $(t \bmod T) \geq \Delta$. Let $N \in \mathbb{N}_0$ be the number of administrations received at time t . The zero-state system response $y_j(t)$ (see (D.2.2)) is given by

$$y_j(t) = \frac{D}{\Delta} \sum_{i=1}^n \frac{F_{ji}}{\lambda_i} (1 - e^{-\lambda_i \Delta}) e^{\lambda_i t} \sum_{l=0}^{N-1} e^{-\lambda_i l T}$$

or, equivalently,

$$y_j(t) = \frac{D}{\Delta} \sum_{i=1}^n \frac{F_{ji}}{\lambda_i} (1 - e^{-\lambda_i \Delta}) e^{\lambda_i t} \frac{1 - e^{-\lambda_i N T}}{1 - e^{-\lambda_i T}}.$$

We set $t = \tilde{t} + (N-1)T$ (i.e., $\tilde{t} = t \bmod T$), hence $\Delta \leq \tilde{t} < T$ indicates the position on the dosing interval $[0, T[$ after N administrations. Consequently, $y_j(t)$ can be written

$$y_j^N(\tilde{t}) = \frac{D}{\Delta} \sum_{i=1}^n \frac{F_{ji}}{\lambda_i} (1 - e^{-\lambda_i \Delta}) \frac{e^{\lambda_i(N-1)T} - e^{-\lambda_i T}}{1 - e^{-\lambda_i T}} e^{\lambda_i \tilde{t}}.$$

Since, for all $i \in \{1, \dots, n\}$, $\text{Re}(\lambda_i) < 0$ (system stability), the asymptotic response reads

$$y_j^\infty(\tilde{t}) := \lim_{N \rightarrow \infty} y_j^N(\tilde{t}) = \frac{D}{\Delta} \sum_{i=1}^n \frac{F_{ji}}{\lambda_i} (1 - e^{-\lambda_i \Delta}) \frac{e^{-\lambda_i T}}{e^{-\lambda_i T} - 1} e^{\lambda_i \tilde{t}}.$$

A similar development can be applied for $t \geq 0$ such that $(t \bmod T) < \Delta$ (or, equivalently, $0 \leq \tilde{t} < \Delta$). Let $N \in \mathbb{N}_0$ be the number of administrations received (including the

ongoing administration) at time t . The zero-state system response $y_j(t)$ (see (D.2.1)) is given by

$$y_j(t) = \frac{D}{\Delta} \left[\sum_{i=1}^n \frac{F_{ji}}{\lambda_i} (1 - e^{-\lambda_i \Delta}) e^{\lambda_i t} \sum_{l=0}^{N-2} e^{-\lambda_i l T} + \sum_{i=1}^n \frac{F_{ji}}{\lambda_i} (e^{\lambda_i(t-(N-1)T)} - 1) \right],$$

i.e.,

$$y_j(t) = \frac{D}{\Delta} \left[\sum_{i=1}^n \frac{F_{ji}}{\lambda_i} (1 - e^{-\lambda_i \Delta}) e^{\lambda_i t} \frac{1 - e^{-\lambda_i(N-1)T}}{1 - e^{-\lambda_i T}} + \sum_{i=1}^n \frac{F_{ji}}{\lambda_i} (e^{\lambda_i(t-(N-1)T)} - 1) \right].$$

Thus, for $\tilde{t} \in [0, \Delta[$,

$$y_j^N(\tilde{t}) = \frac{D}{\Delta} \left[\sum_{i=1}^n \frac{F_{ji}}{\lambda_i} (1 - e^{-\lambda_i \Delta}) \frac{e^{\lambda_i(N-1)T} - 1}{1 - e^{-\lambda_i T}} e^{\lambda_i \tilde{t}} + \sum_{i=1}^n \frac{F_{ji}}{\lambda_i} (e^{\lambda_i \tilde{t}} - 1) \right].$$

Since, for all $i \in \{1, \dots, n\}$, $\text{Re}(\lambda_i) < 0$ (system stability), the asymptotic response reads

$$y_j^\infty(\tilde{t}) := \lim_{N \rightarrow \infty} y_j^N(\tilde{t}) = \frac{D}{\Delta} \left[\sum_{i=1}^n \frac{F_{ji}}{\lambda_i} (1 - e^{-\lambda_i \Delta}) \frac{1}{e^{-\lambda_i T} - 1} e^{\lambda_i \tilde{t}} + \sum_{i=1}^n \frac{F_{ji}}{\lambda_i} (e^{\lambda_i \tilde{t}} - 1) \right].$$

□

APPENDIX E

Sensitivity analysis on the popPK model of meropenem

A sensitive analysis was performed using MC simulations of the typical patient (WT, 75 kg; GFR, 65 mL/min). The simulations were performed using the arbitrary dosing regimen of

1g/8h 3h-infusion.

The PK parameters with a random-effect component are the clearance CL , the central volume of distribution V_c , the volume of distribution of the dummy ELF compartment V_E and the intercompartmental clearance between the central and the peripheral compartment Q_p (see Table 4.2). For each of these parameters, IIV was described by an exponential model:

$$P = TVP \cdot \exp(\eta_P)$$

where η_P is a normal random variable $\sim N(0, \omega_P^2)$ and TVP is the individual typical value of the parameter. Figures E.1-E.4 show the steady output trajectories y^∞ if a PK parameter varies between $\eta_P = -2\omega$ (blue) and $\eta_P = 2\omega$ (yellow). That represents 95.4% of the model predictions. Indeed, if a random variable η follows a normal distribution $N(0, \omega^2)$, then $z := \frac{\eta}{\omega} \sim N(0, 1)$, such that

$$\begin{aligned} P(-2\omega < \eta < 2\omega) &= P(-2 < z < 2) \\ &= P(z < 2) - P(z < -2) \\ &= 2 \cdot P(z < 2) - 1 \\ &= 0.9544 \end{aligned}$$

We indicate the maximum relative error on the dosing interval with respect to the nominal one:

$$e_{\eta=-2} := \max_{\tilde{t} \in [0, T]} \frac{|y_{\eta=-2}^{\infty}(\tilde{t}) - y_{\eta=0}^{\infty}(\tilde{t})|}{y_{\eta=0}^{\infty}(\tilde{t})}, \quad e_{\eta=2} := \max_{\tilde{t} \in [0, T]} \frac{|y_{\eta=2}^{\infty}(\tilde{t}) - y_{\eta=0}^{\infty}(\tilde{t})|}{y_{\eta=0}^{\infty}(\tilde{t})}$$

A visual inspection of these figures leads to the following conclusions:

- The drug concentration decreases when the clearance increases. It is stated and demonstrated in Proposition 6.2.2.
- The concentrations at time T (end of the dosing interval) seem to increase when the volumes of distributions V_c and V_E and the intercompartmental clearance Q_p increase. The intercompartmental clearance seems to have a lower impact on the PK profiles.

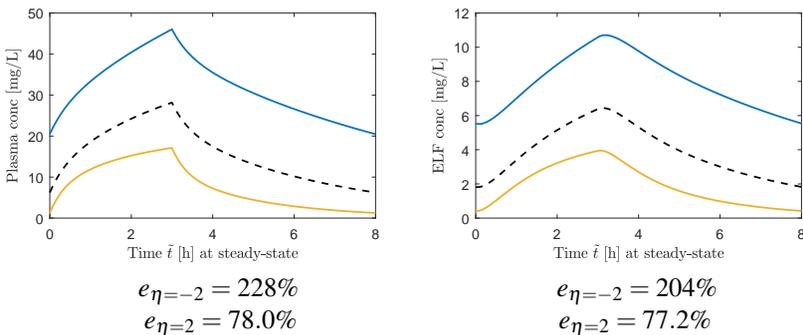


Figure E.1 – Comparison of PK profiles when the clearance CL varies, and all the other parameters are set to their typical value. Blue curve, $\eta = -2\omega$; yellow curve, $\eta = 2\omega$; dashed black curve, $\eta = 0$ (nominal PK profile).

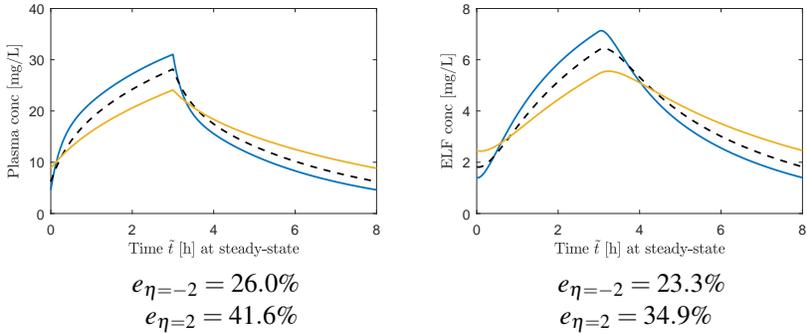


Figure E.2 – Comparison of PK profiles when the central volume of distribution V_c varies, and all the other parameters are set to their typical value. Blue curve, $\eta = -2\omega$; yellow curve, $\eta = 2\omega$; dashed black curve, $\eta = 0$ (nominal PK profile).

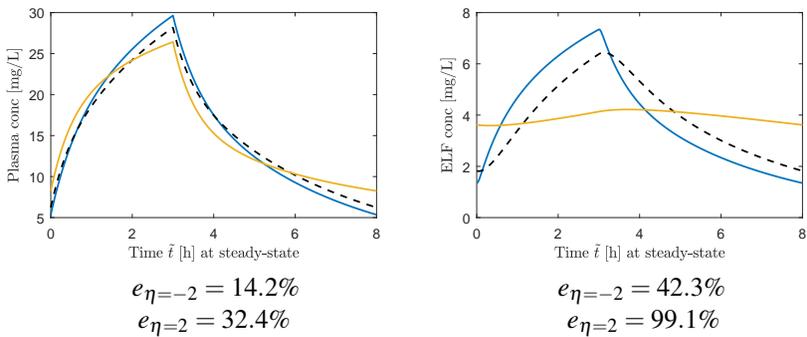


Figure E.3 – Comparison of PK profiles when the volume of distribution of the ELF compartment V_E varies, and all the other parameters are set to their typical value. Blue curve, $\eta = -2\omega$; yellow curve, $\eta = 2\omega$; dashed black curve, $\eta = 0$ (nominal PK profile).

Appendix E Sensitive analysis popPK model

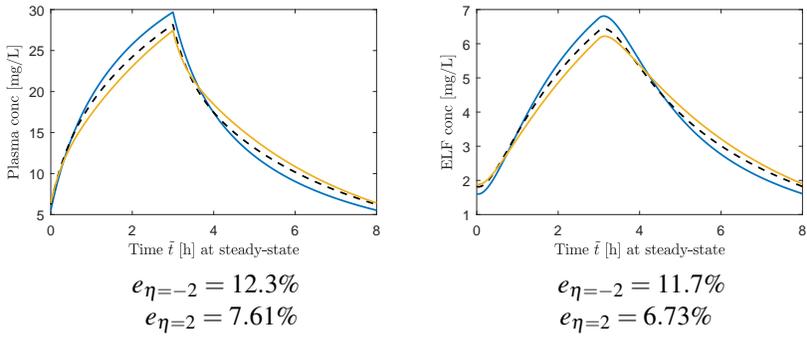


Figure E.4 – Comparison of PK profiles when the intercompartmental clearance Q_p varies, and all the other parameters are set to their typical value. Blue curve, $\eta = -2\omega$; yellow curve, $\eta = 2\omega$; dashed black curve, $\eta = 0$ (nominal PK profile).

Bibliography

- M. H. Abdul-Aziz, J. Lipman, J. W. Mouton, et al. Applying pharmacokinetic/pharmacodynamic principles in critically ill patients: Optimizing efficacy and reducing resistance development. *Semin Resp Crit Care*, 36(1):136–153, 2015. doi: 10.1055/s-0034-1398490.
- K. Alexandre and B. Fantin. Pharmacokinetics and pharmacodynamics of temocillin. *Clin Pharmacokinet*, 57(3):287–296, 2018. doi: 10.1007/s40262-017-0584-7.
- A. J. N. Anelone, M. F. Villa-Tamayo, and P. S. Rivadeneira. Oncolytic virus therapy benefits from control theory. *R Soc Open Sci*, 7:200473, 2020. doi: 10.1098/rsos.200473.
- J. M. Bailey and W. M. Haddad. Drug dosing control in clinical pharmacology. *IEEE Control Syst Mag*, 25(2):35–51, April 2005.
- S. J. Balevic, T. P. Green, M. E. Clowse, et al. Pharmacokinetics of hydroxychloroquine in pregnancies with rheumatic diseases. *Clin Pharmacokinet*, 58(4):525–533, 2019. doi: 10.1007/s40262-018-0712-z.
- R. J. Bauer. NONMEM tutorial part I: Description of commands and options, with simple examples of population analysis. *CPT Pharmacometrics Syst Pharmacol*, 8(8):525–537, 2019a. doi: 10.1002/psp4.12404.
- R. J. Bauer. NONMEM tutorial part II: Estimation methods and advanced examples. *CPT Pharmacometrics Syst Pharmacol*, 8(8):538–556, 2019b. doi: 10.1002/psp4.12422.
- C. Beauchier. *The LQ-Optimal Control Problem for Invariant Linear Systems*. PhD thesis, FUNDP, May 2011.

Bibliography

- M. Bergstrand, A. C. Hooker, J. E. Wallin, and M. O. Karlsson. Prediction-corrected visual predictive checks for diagnosing nonlinear mixed-effects models. *The AAPS J.*, 13(2):143–151, 2011. doi: 10.1208/s12248-011-9255-z.
- M. Beumier, G. S. Casu, et al. Elevated β -lactam concentrations associated with neurological deterioration in ICU septic patients. *Minerva Anesthesiol*, 81(5):497–506, 2015.
- M. Bierlaire. *Optimization: Principles and algorithms*. EPFL Press, 1st edition, 2015.
- L. Binder, H. Schwörer, S. Hoppe, et al. Pharmacokinetics of meropenem in critically ill patients with severe infections. *Ther Drug Monit*, 35(1):63–70, 2013.
- B. Blanchet, J. Moez, M. Allard, and Others. Hydroxychloroquine levels in patients with systemic lupus erythematosus: Comparison of Whole Blood and Serum Levels [abstract]. *Arthritis Rheumatol*, 2019. URL <https://acrabstracts.org/abstract/hydroxychloroquine-levels-inpatients-with-systemic-lupus-erythematosus-comparison-of-wholeblood-and-serum-levels/>.
- K. Brendel et al. Normalized prediction distribution errors for evaluation of nonlinear mixed-models. PAGANZ meeting. 2007.
- R. Burger, M. Guidi, V. Calpini, et al. Effect of renal clearance and continuous renal replacement therapy on appropriateness of recommended meropenem dosing regimens in critically ill patients with susceptible life-threatening infections. *J Antimicrob Chemother*, 73(12):3413–3422, 2018. doi: 10.1093/jac/dky370.
- S. J. Carmichael, B. Charles, and S. E. Tett. Population pharmacokinetics of hydroxychloroquine in patients with rheumatoid arthritis. *Ther Drug Monit*, 25(6):671–681, 2003. doi: 10.1097/00007691-200312000-00005.
- CDC. ESBL-producing Enterobacteriaceae in healthcare settings. In: Centers for Disease Control and Prevention(CDC)/Healthcare-associated Infections (HAI) /Diseases and Organisms, Nov 2019. URL <https://www.cdc.gov/hai/organisms/ESBL.html>. Accessed November 3, 2020.
- V. Chellaboina, S. P. Bath, et al. Modeling and analysis of mass-action kinetics. *IEEE Control Syst Mag*, 29(4):60–78, Aug. 2009.
- M. Chimata, M. Nagase, Y. Suzuki, et al. Pharmacokinetics of meropenem in patients with various degrees of renal function, including patients with end-stage renal disease. *Antimicrob Agents Chemother*, 37(2):229–233, 1993.
- I. Chow, V. Mabasa, and C. Chan. Meropenem assessment before and after implementation of a small-Dose, short-Interval standard dosing regimen. *Can J Hosp Pharm*, 71(1), 2018.

- M. O. Cotta, J. A. Roberts, and J. Lipman. Antibiotic dose optimization in critically ill patients. *Med Intensiva*, 39(9):563–572, 2015. ISSN 15786749. doi: 10.1016/j.medin.2015.07.009.
- R. Curtain and H. Zwart. *Introduction to infinite-dimensional systems theory: A state-space approach*. Springer, 2020.
- A. Darwich, K. Ogungbenro, A. Vinks, et al. Why has model-informed precision dosing not yet become common clinical reality? lessons from the past and a roadmap for the future. *Clin Pharmacol Ther*, 101(5):646–656, 2017. doi: 10.1002/cpt.659.
- R. De Jong, R. Hens, V. Basma, et al. Continuous versus intermittent infusion of temocillin, a directed spectrum penicillin for intensive care patients with nosocomial pneumonia: Stability, compatibility, population pharmacokinetic studies and breakpoint selection. *J Antimicrob Chemother*, 61(2):382–388, 2008. doi: 10.1093/jac/dkm467.
- S. A. Dhaese, A. Farkas, P. Colin, J. Lipman, V. Stove, A. G. Verstraete, J. A. Roberts, and J. J. De Waele. Population pharmacokinetics and evaluation of the predictive performance of pharmacokinetic models in critically ill patients receiving continuous infusion meropenem: A comparison of eight pharmacokinetic models. *J Antimicrob Chemother*, 74(2):432–441, 2019. doi: 10.1093/jac/dky434.
- X. Du, C. Li, J. L. Kuti, et al. Population pharmacokinetics and pharmacodynamics of meropenem in pediatric patients. *J Clin Pharmacol*, 46(1):69–75, 2006.
- A. N. Edginton, W. Schmitt, and S. Willmann. Development and evaluation of a generic physiologically based pharmacokinetic model for children. *Clin Pharmacokinet*, 45(10):1013–1034, 2006. doi: 10.2165/00003088-200645100-00005.
- EUCAST. Meropenem: rationale document. Version 1.5. European Committee on Antimicrobial Susceptibility Testing, June 2009. URL https://eucast.org/publications_and_documents/rd/.
- EUCAST. Temcollin: rationale document. Version 1.0. European Committee on Antimicrobial Susceptibility Testing, March 2019. URL https://eucast.org/publications_and_documents/rd/.
- FAMHP. Meropenem IV. In: PIL and SPC of a medicine. Federal Agency for Medicines and Health Products, 2020. URL <https://www.famhp.be/en>. Accessed November 30, 2020.
- D. Fisher and S. Shafer. Pharmacokinetic and pharmacodynamic analysis with NONMEM: **Basic concepts**. fisher/shafer NONMEM workshop, ghent, belgium, March 2007.
- F. Fripiat, F. T. Musuamba, et al. Modelled target attainment after meropenem infusion in patients with severe nosocomial pneumonia: The PROMESSE study. *J Antimicrob Chemother*, 70(1):207–216, 2015.

- M. Garcia-Cremades, B. P. Solans, E. Hughes, et al. Optimizing hydroxychloroquine dosing for patients with COVID-19: An integrative modeling approach for effective drug repurposing. *Clin Pharm Therap*, 108(2):253–263, 2020. doi: 10.1002/cpt.1856.
- P. Gautret, J.-C. Lagier, P. Parola, et al. Clinical and microbiological effect of a combination of hydroxychloroquine and azithromycin in 80 COVID-19 patients with at least a six-day follow up: A pilot observational study. *Travel Med Infect Dis*, 34, 2020a. doi: 10.1016/j.tmaid.2020.101663.
- P. Gautret, J.-C. Lagier, P. Parola, et al. Hydroxychloroquine and azithromycin as a treatment of COVID-19: results of an open-label non-randomized clinical trial. *Int J Antimicrob Agents*, 2020b. doi: 10.1016/j.ijantimicag.2020.105949.
- B. E. Gidal, A. M. Clark, B. Anders, and F. Gilliam. The application of half-life in clinical decision making: Comparison of the pharmacokinetics of extended-release topiramate (USL255) and immediate-release topiramate. *Epilepsy Res*, 129:26–32, 2017. doi: 10.1016/j.eplepsyres.2016.10.020.
- GitHub-PsN. Bootstrap user guide. In: Pearl speaks NONMEM (PsN) Documentation, 2018. URL <https://uupharmacometrics.github.io/PsN/>. Accessed April 26, 2019.
- J. Gonçalves-Pereira and P. Póvoa. Antibiotics in critically ill patients: A systematic review of the pharmacokinetics of β -lactams. *Crit Care*, 15:R206, 2011. doi: 10.1186/cc10441.
- J. Goncalves-Pereira, N. E. Silva, et al. Assessment of pharmacokinetic changes of meropenem during therapy in septic critically ill patients. *BMC Pharmacol Toxicol*, 15(1):15–21, 2014.
- I. M. Gould and F. M. MacKenzie. Antibiotic exposure as a risk factor for emergence of resistance: The influence of concentration. *J Appl Microbiol Symp Suppl*, 92(1): 78–84, 2002. doi: 10.1046/j.1365-2672.92.5s1.10.x.
- W. M. Haddad, V. Chellaboina, and Q. Hui. *Nonnegative and compartmental dynamical systems*. Princeton University Press, 2010.
- A. Haidar. The artificial pancreas: How closed-loop control is revolutionizing diabetes. *IEEE Control Syst Mag*, 36(5):28–47, 2016.
- B. Hampel, M. Feike, P. Koeppe, and H. Lode. Pharmacokinetics of temocillin in volunteers. *Drugs*, 29, 1985.
- R. Hartl, S. Sethi, and R. Vickson. A survey of the maximum principles for optimal control problems with state constraints. *SIAM Rev*, 37(2):181–218, 1995.

- A. J. Heffernan, F. B. Sime, J. Lipman, and J. A. Roberts. Individualising therapy to minimize bacterial multidrug resistance. *Drugs*, 78(6):621–641, 2018. doi: 10.1007/s40265-018-0891-9. URL <https://doi.org/10.1007/s40265-018-0891-9>.
- A. Henningsson, A. Sparreboom, et al. Population pharmacokinetic modelling of unbound and total plasma concentrations of paclitaxel in cancer patients. *Eur J Cancer*, 39(8):1105–1114, 2003. doi: 10.1016/S0959-8049(03)00126-6.
- Holford, N. Bootstrap and confidence intervals, 2015. URL <http://holford.fmhs.auckland.ac.nz/docs/bootstrap-and-confidence-intervals.pdf>. Accessed October 28, 2020.
- A. C. Hooker, C. E. Staatz, and M. O. Karlsson. Conditional weighted residuals (CWRES): A model diagnostic for the FOCE method. *Pharmaceutical Research*, 24(12):2187–2197, 2007. doi: 10.1007/s11095-007-9361-x.
- R. Horn and C. Johnson. *Matrix analysis*. Cambridge University Press, 1985.
- K. Ikawa, N. Morikawa, H. Ohge, et al. Pharmacokinetic–pharmacodynamic target attainment analysis of meropenem in Japanese adult patients. *J Infect Chemother*, 16(1):25–32, 2010.
- N. G. Jager, R. M. van Hest, J. Lipman, J. A. Roberts, and M. O. Cotta. Antibiotic exposure at the site of infection: principles and assessment of tissue penetration. *Expert Rev Clin Pharmacol*, 12(7):623–634, 2019. doi: 10.1080/17512433.2019.1621161.
- S. Jaruratanasirikul, S. Thengyai, W. Wongpoowarak, et al. Population pharmacokinetics and Monte Carlo dosing simulations of meropenem during the early phase of severe sepsis and septic shock in critically ill patients in intensive care units. *Antimicrob Agents Chemother*, 59(6):2995–3001, 2015. doi: 10.1128/AAC.04166-14.
- H. M. Jones and K. Rowland-Yeo. Basic concepts in physiologically based pharmacokinetic modeling in drug discovery and development. *CPT Pharmacometrics Syst Pharmacol*, 2(8):1–12, 2013.
- H. M. Jones, N. Parrott, K. Jorga, and T. Lavé. A novel strategy for physiologically based predictions of human pharmacokinetics. *Clin Pharmacokinet*, 45(5):511–542, 2006.
- J. Karjagin, K. O. S. Lefeuvre, et al. Pharmacokinetics of meropenem determined by microdialysis in the peritoneal fluid of patients with severe peritonitis associated with septic shock. *Clin Pharmacol Ther*, 83(3):452–459, 2008. doi: 10.1038/sj.cpt.6100312.
- M. G. Kees, I. K. Minichmayr, S. Moritz, et al. Population pharmacokinetics of meropenem during continuous infusion in surgical ICU patients. *J Clin Pharmacol*, 56(3):307–315, 2016. doi: 10.1002/jcph.600.

- S. Kiem and J. J. Schentag. Interpretation of antibiotic concentration ratios measured in epithelial lining fluid. *Antimicrob Agents Chemother*, 52(1):24–36, 2008. doi: 10.1128/AAC.00133-06.
- G. Koch. *Modeling of pharmacokinetics and pharmacodynamics with application to cancer and arthritis*. PhD thesis, Univ. Konstanz, May 2012.
- W. A. Krueger, J. Bulitta, M. Kinzig-Schippers, et al. Evaluation by Monte Carlo simulation of the pharmacokinetics of two doses of meropenem administered intermittently or as a continuous infusion in healthy volunteers. *Antimicrob Agents Chemother*, 49(5):1881–1889, 2005.
- A. Kuch, Ż. Dorota, A. Skoczy, and W. Hryniewicz. Activity of temocillin against ESBL-, AmpC-, and/or KPC-producing Enterobacterales isolated in Poland. *Eur J Clin Microbiol Infect Dis*, pages 1185–1191, 2020. doi: 10.1007/s10096-020-03844-5.
- P.-F. Laterre, X. Wittebole, S. Van De Velde, et al. Temocillin (6 g daily) in critically ill patients: Continuous infusion versus three times daily administration. *J Antimicrob Chemother*, 70(3):891–898, 2015. doi: 10.1093/jac/dku465.
- J. Y. Lee, N. Vinayagamoorthy, K. Han, et al. Association of polymorphisms of cytochrome P450 2D6 with blood hydroxychloroquine levels in patients with systemic lupus erythematosus. *Arthritis Rheumatol*, 68(1):184–190, 2016. doi: 10.1002/art.39402.
- A. Levey, T. Greene, J. Kusek, and G. Beck. A simplified equation to predict glomerular filtration rate from serum creatinine. *Journal of the American Society of Nephrology*, 11:155A, 2000. doi: 1046-6673.
- C. Li, J. L. Kuti, C. H. Nightingale, et al. Population pharmacokinetic analysis and dosing regimen optimization of meropenem in adult patients. *J Clin Pharmacol*, 46(10):1171–1178, 2006.
- H.-S. Lim, J.-S. Im, J.-Y. Cho, et al. Pharmacokinetics of hydroxychloroquine and its clinical implications in chemoprophylaxis against malaria caused by plasmodium vivax. *Antimicrob Agents Chemother*, 53(4):1468–1475, 2009. doi: 10.1128/AAC.00339-08.
- L. Lindbom, P. Pihlgren, and N. Jonsson. PsN-Toolkit - A collection of computer intensive statistical methods for non-linear mixed effect modeling using NONMEM. *Comput Methods Programs Biomed*, 79(3):241–257, 2005. doi: 10.1016/j.cmpb.2005.04.005.
- J. T. Liparulo, T. D. Knab, and R. S. Parker. Toxicity-centric cancer chemotherapy treatment design. *IFAC-PapersOnLine*, 53(2):16353–16358, 2020. ISSN 2405-8963. doi: 10.1016/j.ifacol.2020.12.666.

- J. Liu, R. Cao, M. Xu, et al. Hydroxychloroquine, a less toxic derivative of chloroquine, is effective in inhibiting SARS-CoV-2 infection *in vitro*. *Cell Discov*, 6(1): 6–9, 2020. doi: 10.1038/s41421-020-0156-0.
- T. P. Lodise, F. Sorgel, D. Melnick, et al. Penetration of meropenem into epithelial lining fluid of patients with ventilator-associated pneumonia. *J Antimicrob Chemother*, 55(4):1606–1610, 2011.
- G. Martin-Blondel, S. Ruiz, M. Murriss, et al. Hydroxychloroquine in COVID-19 patients: what still needs to be known about the kinetics. *Clin Infect Dis*, 2020. doi: 10.1093/cid/ciaa558.
- MathWorks. quadprog - Quadratic programming. In: Help Center. Support, 2021. URL <https://www.mathworks.com/support/search.html?q=quadprog&page=1>. Accessed March 9, 2021.
- F. Mattioli, C. Fucile, V. Del Bono, et al. Population pharmacokinetics and probability of target attainment of meropenem in critically ill patients. *Eur J Clin Pharmacol*, 72(7):839–848, 2016.
- A. J. McLachlan, D. J. Cutler, and S. E. Tett. Plasma protein binding of the enantiomers of hydroxychloroquine and metabolites. *Eur J Clin Pharmacol*, 44(5):481–484, 1993. doi: 10.1007/BF00315548.
- MHRA. Meropenem trihydrate. In: Medicines information: SPC & PILs. Medicines and Healthcare Products Regulatory Agency, 2017. URL <http://www.mhra.gov.uk/spc-pil/>. Accessed July 21, 2018.
- A. C. Miranda Bastos, S. J. Vandecasteele, et al. Temocillin dosing in haemodialysis patients based on population pharmacokinetics of total and unbound concentrations and Monte Carlo simulations. *J Antimicrob Chemother*, 73(6):1630–1638, 2018. doi: 10.1093/jac/dky078.
- S. Morita, T. Takahashi, et al. Population pharmacokinetics of hydroxychloroquine in Japanese patients with cutaneous or systemic lupus erythematosus. *Ther Drug Monit*, 38(2):259–267, 2016. doi: 10.1097/FTD.0000000000000261.
- T. Morrisette, T. P. Lodise, M. H. Scheetz, et al. The pharmacokinetic and pharmacodynamic properties of hydroxychloroquine and dose selection for COVID-19: Putting the cart before the horse. *Infect Dis Ther*, 9(3):561–572, 2020. doi: 10.1007/s40121-020-00325-2.
- D. R. Mould and R. N. Upton. Basic Concepts in population modeling, simulation, and model-based drug development. *CPT Pharmacometrics Syst Pharmacol*, 1(9): 1–14, 2012. doi: 10.1038/psp.2012.4.
- D. R. Mould and R. N. Upton. Basic concepts in population modeling, simulation, and model-based drug development-Part 2: Introduction to pharmacokinetic modeling methods. *CPT Pharmacometrics Syst Pharmacol*, 2(4):1–14, 2013.

- F. T. Musuamba, E. Manolis, N. Holford, et al. Advanced methods for dose and regimen finding during drug development: Summary of the EMA/EFPIA workshop on dose finding (London 4-5 December 2014). *CPT Pharmacometrics Syst Pharmacol*, 6(7):418–429, 2017. doi: 10.1002/psp4.12196.
- I. a. Nestorov, L. J. Aarons, P. a. Arundel, and M. Rowland. Lumping of whole-body physiologically based pharmacokinetic models. *Journal of pharmacokinetics and biopharmaceutics*, 26(1):21–46, 1998. doi: 10.1023/A:1023272707390.
- T. Nguyen et al. Model evaluation of continuous data pharmacometric models: metrics and graphics. *CPT Pharmacometrics Syst Pharmacol*, 6(2):87–109, 2017.
- NHANES. Questionnaires, datasets, and related documentation. In: Centers for Disease Control and Prevention(CDC)/National Center for Health Statistics/National Health and Nutrition Examination Survey(NHANES), 2005-2006. URL <http://www.cdc.gov/nchs/nhanes>. Accessed April 17, 2018.
- E. I. Nielsen, O. Cars, and L. E. Friberg. Pharmacokinetic/Pharmacodynamic (PK/PD) indices of antibiotics predicted by a semimechanistic PKPD model: A step toward model-based dose optimization. *J Antimicrob Chemother*, 55(10):4619–4630, 2011. doi: 10.1128/AAC.00182-11.
- Nist-Sematech. 1.3.6.6.9. Lognormal distribution. In: e-Handbook of statistical methods, 2013. URL <https://www.itl.nist.gov/div898/handbook/>. Accessed October 22, 2020.
- J. S. Owen and J. Fiedler-Kelly. *Introduction to population pharmacokinetic/pharmacodynamic analysis with nonlinear mixed effects models*. John Wiley & Sons, 2014.
- H. Padari, T. Metsvaht, L. T. Kõrgvee, et al. Short versus long infusion of meropenem in very-low-birth-weight neonates. *Antimicrob Agents Chemother*, 56(9):4760–4764, 2012. doi: 10.1128/AAC.00655-12.
- S. L. Parker, F. B. Sime, and J. A. Roberts. Optimizing dosing of antibiotics in critically ill patients. *Curr Opin Infect Dis*, 28(6):497–504, 2015. doi: 10.1097/QCO.0000000000000206.
- A. Y. Peleg and D. C. Hooper. Hospital-acquired infections due to gram-negative bacteria. *N Engl J Med*, 362(19):1804–1813, 2010. doi: 10.1056/NEJMr0904124.
- J. Perrott, V. H. Mabasa, and M. H. H. Ensom. Comparing outcomes of meropenem administration strategies based on pharmacokinetic and pharmacodynamic principles: A qualitative systematic review. *Ann Pharmacother*, 44(3):557–564, 2010. doi: 10.1345/aph.1M339.
- S. Pilari and W. Huisinga. Lumping of physiologically-based pharmacokinetic models and a mechanistic derivation of classical compartmental models. *J Pharmacokinetic Pharmacodyn*, 37(4):365–405, 2010.

- D. Rawat and D. Nair. Extended-spectrum β -lactamases in Gram Negative Bacteria. *J Glob Infect Dis*, 2(3):263–274, 2010. doi: 10.4103/0974-777X.68531.
- M. Rowland and T. N. Tozer. *Clinical pharmacokinetics and pharmacodynamics: Concepts and application*. Lippincott Williams and Wilkins, 4th edition, 2011.
- S. Critea. Validate your model with NPDE analysis. In: NPDE tutorial. PMX Solutions, 2019. URL <https://www.pmxsolutions.com/2019/05/21/how-to-npde/>. Accessed October 29, 2020.
- J. E. Sager, J. Yu, et al. Physiologically based pharmacokinetic (PBPK) modeling and simulation approaches: A systematic review of published models, applications, and model verification. *Drug Metab Dispos*, 43(11):1823–1837, 2015. doi: 10.1124/dmd.115.065920.
- R. M. Savic and M. O. Karlsson. Importance of shrinkage in empirical bayes estimates for diagnostics: Problems and solutions. *AAPS J*, 11(3):558–569, 2009. doi: 10.1208/s12248-009-9133-0.
- Sciensano. Interim clinical guidance for adults with suspected or confirmed Covid-19 in Belgium. 31 March; Version 6, 2020. URL https://epidemiology.wiv-isp.be/ID/Documents/Covid19/COVID19_InterimGuidelines_Treatment_ENG.pdf. Accessed April 17, 2020.
- J. E. Sereno, M. A. Caicedo, and P. S. Rivadeneira. Artificial pancreas: glycemic control strategies for avoiding hypoglycemia. *Dyna*, 85(207):198–207, 2018.
- F. B. Sime, M. S. Roberts, and J. A. Roberts. Optimization of dosing regimens and dosing in special populations. *Clin Microbiol Infect*, 21(10):886–893, 2015. doi: 10.1016/j.cmi.2015.05.002.
- N. Simon. Block ESTIMATION. In: Bienvenue dans le monde de NONMEM, 2020. URL <https://nonlin-model.org/blockestimation/>. Accessed December 18, 2020.
- F. Sjövall, S. A. Alobaid, S. C. Wallis, et al. Maximally effective dosing regimens of meropenem in patients with septic shock. *J Antimicrob Chemother*, 73(1):191–198, 2018. ISSN 14602091. doi: 10.1093/jac/dkx330.
- S. Tett, D. Cutler, et al. Bioavailability of hydroxychloroquine tablets in healthy volunteers. *Br J Clin Pharmacol*, 27(6):771–779, 1989. doi: 10.1111/j.1365-2125.1989.tb03439.x.
- P. Thémans, P. Marquet, J. J. Winkin, and F. T. Musuamba. Towards a generic tool for prediction of meropenem systemic and infection-site exposure: A physiologically based pharmacokinetic model for adult patients with pneumonia. *Drugs in R&D*, 19(2):177–189, 2019. doi: 10.1007/s40268-019-0268-x.

- P. Thémans, L. Belkhir, N. Dauby, et al. Population pharmacokinetics of hydroxy-chloroquine in COVID-19 patients: Implications for dose optimization. *Eur J Drug Metab Pharmacokinet*, 45(6):703–713, 2020a. doi: 10.1007/s13318-020-00648-y.
- P. Thémans, N. Dauby, L. Schrooyen, et al. Model informed dosing of hydroxy-chloroquine in COVID-19 patients: Learnings from the recent experience, remaining uncertainties and gaps. *Br J Clin Pharmacol*, (April):1–9, 2020b. doi: 10.1111/bcp.14436.
- P. Thémans, F. T. Musuamba, and J. J. Winkin. Model-based strategies of drug dosing for pharmacokinetic systems. *IFAC-PapersOnLine*, 53(2):16061–16068, 2020c. doi: 10.1016/j.ifacol.2020.12.421.
- G. J. Tortora and B. Derrickson. *Principes d'anatomie et de physiologie*. De Boeck, 4th edition, 2007.
- P. L. Toutain and A. Bousquet-Mélou. Plasma terminal half-life. *J Vet Pharmacol Ther*, 27(6):427–439, 2004.
- M. Usman, O. R. Frey, and G. Hempel. Population pharmacokinetics of meropenem in elderly patients: dosing simulations based on renal function. *Eur J Clin Pharmacol*, 73(3):333–342, 2017. doi: 10.1007/s00228-016-2172-4.
- S. J. Vandecasteele, A. C. Miranda Bastos, et al. Thrice-weekly temocillin administered after each dialysis session is appropriate for the treatment of serious Gram-negative infections in haemodialysis patients. *Int J Antimicrob Agents*, 46(6):660–665, 2015. doi: 10.1016/j.ijantimicag.2015.09.005.
- R. P. Veiga and J.-A. Paiva. Pharmacokinetics–pharmacodynamics issues relevant for the clinical use of beta-lactam antibiotics in critically ill patients. *Crit Care*, 22(1): 233, 2018. doi: 10.1186/s13054-018-2155-1.
- T. F. Ververs, A. Van Dijk, S. A. Vinks, et al. Pharmacokinetics and dosing regimen of meropenem in critically ill patients receiving continuous venovenous hemofiltration. *Crit Care Med*, 28(10):3412–3416, 2000. doi: 10.1097/00003246-200010000-00006.
- A. A. Vinks. The application of population pharmacokinetic modeling to individualized antibiotic therapy. *Int J Antimicrob Agents*, 19(4):313–322, 2002.
- S. G. Wicha. TDMx - model-supported therapeutic drug monitoring for precision dosing, 2018. URL <http://www.tdmx.eu/>. Accessed October 28, 2019.
- M. Wittau, J. Scheele, M. Kurlbaum, et al. Population pharmacokinetics and target attainment of meropenem in plasma and tissue of morbidly obese patients after laparoscopic intraperitoneal surgery. *Antimicrob Agents Chemother*, 59(10):6241–6247, 2015.

- G. Wuerzner, M. Bochud, et al. Measurement of glomerular filtration rate in obese patients: Pitfalls and potential consequences on drug therapy. *Obes Facts*, 4(3): 238–243, 2011. doi: 10.1159/000329547.
- X. Yao, F. Ye, M. Zhang, et al. In vitro antiviral activity and projection of pptimized dosing design of hydroxychloroquine for the treatment of severe acute respiratory syndrome coronavirus 2 (SARS-CoV-2). *Clin Infect Dis*, 2020. doi: 10.1093/cid/ciaa237.
- Q. T. Zhou, B. He, , et al. Meropenem dosing based on a population pharmacokinetic–pharmacodynamic model in elderly patients with infection of the lower respiratory tract. *Drugs Aging*, 34(2):115–121, 2017.